Titre: Title:	Radiation Properties and Antenna Developments Through Periodic and End-Fire Composite Structures
Auteur: Author:	Yifan Yin
Date:	2021
Type:	Mémoire ou thèse / Dissertation or Thesis
Référence: Citation:	Yin, Y. (2021). Radiation Properties and Antenna Developments Through Periodic and End-Fire Composite Structures [Ph.D. thesis, Polytechnique Montréal]. PolyPublie. https://publications.polymtl.ca/6271/

URL de PolyPublie: PolyPublie URL:	https://publications.polymtl.ca/6271/
Directeurs de recherche: Advisors:	Ke Wu
Programme: Program:	Génie électrique

POLYTECHNIQUE MONTRÉAL

affiliée à l'Université de Montréal

Radiation properties and antenna developments through periodic and end-fire composite structures

YIFAN YIN

Département de génie électrique

Thèse présentée en vue de l'obtention du diplôme de *Philosophiae Doctor*

Génie électrique

Mars 2021

POLYTECHNIQUE MONTRÉAL

affiliée à l'Université de Montréal

Cette thèse intitulée :

Radiation properties and antenna developments through periodic and end-fire composite structures

présentée par **Yifan YIN**

en vue de l'obtention du diplôme de *Philosophiae Doctor*

a été dûment acceptée par le jury d'examen constitué de :

Chahé NERGUIZIAN, président
Ke WU, membre et directeur de recherche
Tarek DJERAFI, membre
Halim BOUTAYEB, membre externe

ACKNOWLEDGEMENTS

I would like to thank my Ph.D. advisor, Prof. Ke Wu for giving me this opportunity to pursue my PhD study at Ecole Polytechnique de Montreal in Canada. His passion for research, persistence, and his innovative ideas helped me to understand and explore new frontiers and to accomplish this thesis.

I would like to thank the jury members for their time and reading my thesis and providing me with very helpful comments.

I would like to thank all the technical personnel at the Poly-Grames Research Center for the help in fabrication and measurement of the prototypes.

I would like to thank Mr. Jean-Sébastien Décarie for the assistance of computer problems, Mrs. Rachel Lortie and Mrs. Nathalie Lévesque for the administrative procedures of the department.

I would like to thank all my student colleagues and friends for all the professional and personal advices, they made my stay at Ecole Polytechnique de Montreal memorable.

Most importantly, I would like to thank my family, who will give me support at anytime.

I would like to end this part with a classic quote from NBA legend Kobe Bryant, which encourage me in my lowest time,

‘Those times when you get up early and you work hard, those times when you stay up late and you work hard, those times when you don't feel like working, you're too tired and you don't want to push yourself but you do it anyway. That is actually the dream.’

RÉSUMÉ

Diverses applications ont été faites diverses exigences aux antennes. Une antenne composite a plusieurs radiateurs intégrés dans une antenne, et est une bonne solution pour répondre à ces exigences. La motivation de la thèse est d'explorer les antennes composites planaires basées sur des guides d'ondes intégrés au substrat (SIW), en particulier les antennes composites planaires à polarisation circulaire (CP) end-fire sur des substrats minces à gains élevés, ce qui est supposé être difficile à concevoir. Etant donné qu'un SIW est également une structure périodique, les formules de calcul des paramètres associés aux structures périodiques sont développées, et les caractéristiques d'impédance, de réflexion et de rayonnement des structures périodiques ont été examinées. Les principales contributions de la thèse peuvent être résumées comme suit:

- Proposer et faire la démonstration de trois antennes composites CP à gain élevé basées sur SIW entièrement planes: klaxon-ALTSA, slot-ALTSA et UDR-ALTSA. Les trois antennes composites sont en fait trois types de réseaux linéaires hétérogènes à deux éléments, s'étendant respectivement dans les trois dimensions d'espace orthogonales. La corne-ALTSA est constituée de cornes SIW et d'une fente antipodale linéaire conique (ALTSA) sur un substrat, s'étendant transversalement sur le plan du substrat. Il comprend également un réseau d'alimentation plan compact avec des configurations flexibles de phase et d'amplitude, et il pourrait également être utilisé pour former un grand réseau. La fente-ALTSA est constituée de fentes sur les larges parois et d'un ALTSA, s'étendant longitudinalement sur le plan du substrat. La fente-ALTSA est également un réseau hétérogène d'un faisceau de balayage de fréquence et d'un faisceau fixe en bout, et il est censé être difficile à concevoir. En outre, le slot-ALTSA démontre également une application du rayonnement à ondes lentes dans un SIW à fente. L'UDR-ALTSA se compose d'un UDR et d'un ALTSA, s'étendant le long de la direction normale au plan du substrat. L'UDR-ALTSA a non seulement une large impédance et des largeurs de bande AR, mais aussi une très petite taille avec un substrat d'alimentation très mince de 0,05λ_0, et ces caractéristiques font de l'antenne un bon candidat pour les antennes élémentaires d'un grand réseau. Les trois réseaux linéaires pourraient être intégrés les uns aux autres pour former divers réseaux planaires, même un réseau tridimensionnel, et fournir diverses solutions flexibles aux antennes planes CP End-fire à gain élevé. De plus, l'UDR-ALTSA comprend un UDR intelligent, alimenté par une nouvelle structure d'alimentation,

pour améliorer uniquement le rayonnement VP plutôt que HP d'ALTSA. La nouvelle amélioration sélective de polarisation pourrait être appliquée à d'autres antennes CP.

- Proposer des formules complètes de forme fermée de paramètres caractéristiques dans une structure périodique (FPPS). Le FPPS peut être utilisé pour séparer les ondes avant et arrière de l'onde totale en tout point à l'intérieur d'une structure pratique, et pour calculer les coefficients de réflexion, les impédances d'onde, les constantes de phase, les constantes d'atténuation, ainsi que le nombre et les amplitudes du Bloch / Floquet modes. Comparé à la méthode de réseau équivalente et à la méthode Eigenmode Solver, le FPPS peut calculer plus de types de paramètres et peut être appliqué à des structures uniformes et périodiques, de transmission et de rayonnement, à des structures 1-D et multidimensionnelles, et pas seulement à l'électromagnétique mais aussi à l'acoustique et à la physique des solides.
- Explorer et examiner, théoriquement et à l'aide du FPPS, les caractéristiques de l'impédance et de la réflexion des ondes dans une structure périodique. Différente d'une impédance d'onde uniforme réelle dans une ligne de transmission uniforme, l'impédance d'onde dans une ligne de transmission périodique est complexe et inhomogène, de sorte qu'il y a de l'énergie stockée et des ondes réfléchies dans la région intérieure de la ligne de transmission. La réflexion interne à l'intérieur d'une structure périodique est différente de la réflexion du port, et la réflexion interne peut être importante même si la réflexion du port est faible. La réflexion interne est inhomogène et dépendante de la polarisation, et elle doit être caractérisée par un coefficient de réflexion tenseur.
- Vérifier, avec des simulations et des expériences, qu'il existe un rayonnement produit par une onde lente dans une antenne non périodique, pour l'appliquer à l'antenne à fente ALTSA proposée. En outre, pour interpréter le diagramme de rayonnement d'une antenne à ondes de fuite périodique (PLWA) avec son mode fondamental même si le mode fondamental est une onde lente, et pour clarifier que si un mode dans une structure périodique produit des rayonnements ou non, il peut ' t être identifié uniquement sur la base de ses nombres d'onde longitudinaux. À la suite de cette étude, il pourrait ne plus être une opinion inacceptable que c'est le mode fondamental dans une PLWA qui produit un rayonnement même si le mode fondamental est une onde lente. Les travaux permettront également de comprendre les phénomènes de rayonnement dans une ligne de transmission périodique telle que SIW, ligne

de transmission composite mains droite et gauche (CRLH) et spoof surface plasmon polariton (SSPP).

- Proposer et étudier des antennes composites planaires: UDR-SIW alimenté par un SIW mince de 0,05λ_0, un slot-horn. L'UDR-SIW applique la théorie de Fabry-perot pour obtenir un rayonnement unidirectionnel, a une taille compacte, un gain élevé, un grand FTBR et un motif symétrique, et pourrait être un remplacement raisonnable pour un pavillon SIW H-plan. Le cornet à fente présente un motif omnidirectionnel sur le plan E et une bonne performance de filtre.

Le travail de la thèse fournirait une base conceptuelle solide et une méthode complète pour les recherches et les applications relatives aux structures périodiques, et élargirait les antennes basées sur les SIW à diverses antennes composites planaires à incandescence.

ABSTRACT

Diverse applications have been made various requirements to antennas. A composite antenna has multiple radiators integrated in an antenna, and is a good solution to match these requirements. The motivation of the thesis is to develop antennas and to explore radiation properties through periodic and end-fire composite structures based on substrate integrated waveguide (SIW). The principal contributions of the thesis can be summarized as follows

- To propose and demonstrate three fully planar SIW-based high gain end-fire circularly polarized (CP) composite antennas: horn-ALTSA, slot-ALTSA, and UDR-ALTSA. The three composite antennas are actually three kinds of two-element heterogeneous linear arrays, stretching in the three orthogonal space dimensions respectively. The horn-ALTSA consists of SIW horns and antipodal linearly tapered slot (ALTSA) on a substrate, stretching transversely on the substrate plane. It also includes a compact planar feeding network with flexible configurations of phase and magnitude, and it could be also used to form a big array. The slot-ALTSA consists of slots on the broad walls and an ALTSA, stretching longitudinally on the substrate plane. The slot-ALTSA is also a heterogeneous array of a frequency-scanning beam and an end-fire fixed beam, and it supposed to be difficult to design. Besides, the slot-ALTSA also demonstrates an application of slow wave radiation in a slotted SIW. The UDR-ALTSA consists of UDR and an ALTSA, stretching along the direction normal to the substrate plane. The UDR-ALTSA has not only wide impedance and axial ratio bandwidths but also a very small size with a very thin feeding substrate of $0.05\lambda_0$, and these features make the antenna to be a good candidate for element antennas of a big array. The three linear arrays could be integrated with each other to form various planar arrays, even a three-dimensional array, and provide diverse flexible solutions to high gain end-fire CP planar antennas. Moreover, the UDR-ALTSA includes a smart UDR, fed by a novel feeding structure, to enhance only vertically polarized (VP) rather than horizontally polarized (HP) radiation of ALTSA. The novel polarization-selective enhancement could be applied to other CP antennas.
- To propose and investigate planar composite antennas: UDR-SIW VP antenna fed by a thin SIW of $0.05\lambda_0$, a slot-horn omnidirectional antenna. The UDR-SIW antenna applies generalized Fabry-perot principle to achieve a unidirectional radiation, has compact size, a

high gain, a large FTBR and a symmetric pattern, and could be a competitive replacement for an SIW H-plane horn. The slot-horn exhibits an omnidirectional pattern on E-plane and a good filter performance.

- To propose comprehensive closed-form formulas of characteristic parameters in a periodic structure (FPPS). The FPPS can be used to separate the forward waves and backward waves from the total wave at any point inside a practical structure, and to calculate reflection coefficients, wave impedances, phase constants, attenuation constants, and the number and amplitudes of the Bloch/Floquet modes. Compared to the equivalent network method and the Eigenmode Solver method, the FPPS can calculate more various kinds of parameters, and can be applied to uniform and periodic, transmission and radiation structure, 1-D and multi-dimensional structures, and not only to electromagnetics but also to acoustics and solid physics.
- To explore and examine, theoretically and/or using the FPPS, the characteristics of wave impedance and reflection in a periodic structure. Different from a real uniform wave impedance in a uniform transmission line, the wave impedance in a periodic transmission line is complex and inhomogeneous, so that there is stored energy and reflected waves at inner region of the transmission line. The inner reflection inside a periodic structure is different from the port reflection, and the inner reflection could be large even the port reflection is little. The inner reflection is inhomogeneous and polarization dependant, and it should be characterized with a tensor reflection coefficient.
- To verify, with simulations and experiments, that there is a radiation produced by a slow wave in a non-periodic antenna, to apply it to the proposed slot-ALTSA antenna. In addition, to interpret the radiation pattern of a periodic leakage wave antenna (PLWA) with its fundamental mode even if the fundamental mode is a slow wave, and to clarify that whether a mode in a periodic structure produces radiates or not, it can’t be identified based on only its longitudinal wavenumbers. As a result of this study, it might no longer be an unacceptable opinion that it is the fundamental mode in a PLWA that produces radiation even if the fundamental mode is a slow wave. The work will also help to understand the radiation phenomena in a periodic transmission line such as SIW, composite right and left hands transmission line (CRLH) and spoof surface plasmon polariton (SSPP).

The work of the thesis would provide a solid conceptual foundation and a comprehensive method for the researches and applications relative to periodic structures, and expand SIW-based antennas to diverse end-fire planar composite antennas.

TABLE OF CONTENTS

LIST OF TABLES

LIST OF FIGURES

LIST OF SYMBOLS AND ABBREVIATIONS

1-D	One-dimensional
2-D	Two-dimensional
3D	Three-dimensional
ALTSA	Antipodal linearly tapered slot antenna
AR	Axial ratio
CP	Circular polarized
CPW	Coplanar waveguide
CRLH	Composite right and left hands transmission line
DFW	Dielectric filled waveguide
EIRP	Equivalent isotropically radiated power
FTBR	Front-to-back ratio
FFT	Fast Fourier transform
FPPS	Formulas of characteristic parameters in a periodic structure
HP	Horizontally polarized
NRD	Non-radiative dielectric waveguide
PCB	Printed circuit borad
PLWA	Periodic leakage wave antenna
SIW	Substrate integrated waveguide
SSPP	Spoof surface plasmon polariton
SIC	Substrate integrated circuit
TE	Transverse electric
TEM	Transverse electromagnetic
TM	Transverse magnetic

UDR	Unidirectional dielectric radiator
VP	Vertically polarized
VSWR	Voltage standing wave ratio

CHAPTER 1 INTRODUCTION

1.1 Motivation

Substrate integrated waveguide (SIW) is a solution to the planar integration of the bulky and heavy three-dimensional metallic waveguide [1]-[5]. SIWs inherit the merits of the metallic waveguide, such as low loss, and have also advantages of planar circuits, such as low cost and easy integration with an RF and microwave component. These merits and advantages match well with the rising requirements for modern wireless application systems, such as multifunction, all-integration, miniaturization, low cost, high speed, and wide bandwidth. After nearly two decades of developments, SIW technologies have widely been applied to diverse wireless related fields, including antennas, passive components, active devices, functional module and all-functional systems [6]-[21]. For future diverse applications of SIW technologies, however, certain explorements of radiation properties and antenna developments through periodic and end-fire composite structures are still required.

Diverse fully planar high-gain end-fire circularly polarized (CP) antennas, especially easily-integrated with RF circuits, are highly desired in wireless systems due to the requirements of miniaturization and low cost. CP antennas are well known for their usefulness in satellite and mobile communications, indoor positioning and sensing systems, and they have certain obvious advantages over linearly polarized (LP) antennas, such as being less sensitive to antenna axial rotation and multipath, and having a less delay spread. For broadside radiation, when a substrate is regarded as the reference plane, a planar antenna has a large area to accommodate various radiators with enough equivalent radiation areas. Therefore, the main beam for most of planar CP antennas presented to date is broadside, and this could be an obstacle in the implementation of substrate-integrated circuits (SICs) and interstellar telecommunications that generally require end-fire antennas (Figure 1.1).

Compared to LP antenna, a planar end-fire CP antenna, when its substrate is regarded as a reference plane, is much more difficult to realize. A CP radiation must include two orthogonally polarized radiation components, namely horizontally polarized (HP) and vertically polarized (VP) (perpendicular to substrate) radiation components. Because there is not enough space to arrange two metal plates with a large spacing in its vertical dimension of a planar antenna when the substrate is thin, it is more difficult to produce VP radiation than HP one. To have a reasonable VP radiation, a planar end-fire CP antenna usually uses a dielectric resonator fed by a cable probe mounted vertically on a substrate, or a thick substrate. The former is not a fully planar structure and would bring certain difficulties for integration with RF circuits. The latter would also bring certain difficulties for integration.

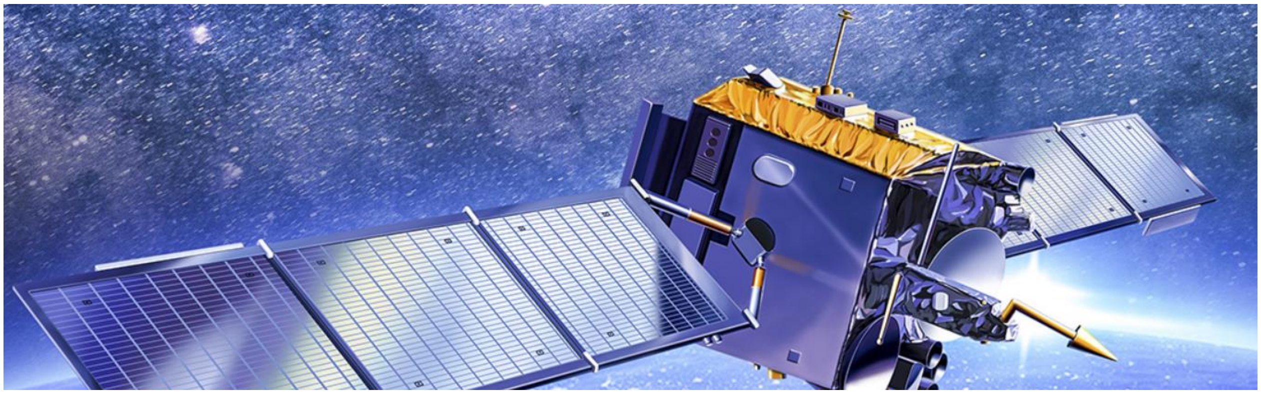

Figure 1.1: End-fire planar CP antennas in satellite could be attached on its side faces to avoid conflicts with other antennas

(Picture from China Aerospace Science and Technology Corporation)

To be integrated with a mingled multilayer RF circuit easily, a planar antenna should be fabricated on a thin single-layer substrate, or on a multilayer substrate with a thin feeding layer. To suppress high-order modes and surface wave modes in RF circuits, the RF layer of a multilayer substrate must be thin compared to operating wavelength. The thickness of the RF layer usually should be less than $0.05\lambda_0$ in millimeter wave, which is roughly 0.508 mm at 30 GHz, and 0.254 mm or 0.127 mm at 77 GHz. Consequently, to integrate a planar multilayer substrate antenna with an RF circuit, the feeding layer of the antenna should be also as thin as the RF layer of a multilayer substrate. Besides, when the feeding layer is thick compared to wavelength, the transition from an antenna to an RF circuit is easy to cause a parasitic radiation, which would degrade the performances of the antenna. Therefore, a fully planar mingled multilayer antenna with a thin feeding substrate is highly desired in diverse wireless systems.

A heterogeneous composite array is an effective solution to a high gain CP antenna. A planar composite antenna, which combines various antenna elements or radiators into one antenna, could be highly expected to meet the diverse requirements, such as CP radiation. Various SIW-based planar antennas and arrays have also been developed, and almost all the antennas imitate conventional rectangle waveguides [9], [19], [21]-[32]. When diverse requirements of antennas are appearing, and the developments of SIW technology would be beyond simple duplications of the classic three-dimensional waveguide. Different from the antenna element in an array, the radiators in a composite antenna usually have different structures and radiation patterns. An end-fire CP radiation must be composed of two end-fire orthogonally polarized radiations, so that it is reasonable to use two orthogonally polarized radiators in a composite antenna.

An SIW is a good candidate structure for diverse planar end-fire composite antennas, but only the open aperture of an SIW has been used in current end-fire CP planar composite antennas. An SIW includes two broad walls, two side walls, one input aperture and one open aperture. A classic solution for CP planar antenna uses the open aperture of an SIW [30]-[32]. On the other hand, in these SIW-based antennas, the broad walls of the SIW have not been used to form radiators. In traditional designs, a slotted SIW and an SIW horn are regarded as two different antennas, and will not be integrated into one antenna. A slotted SIW has slots on its broad walls, and produces a broadside or scanning beam. An SIW horn has an end-fire beam [33]-[36]. One would wonder if the slots on broad walls and the open aperture of SIW could be deployed to form an SIW-based end-fire composite antenna.

Radiation characteristics produced by a slow wave in a slotted width-tapered SIW have been not fully investigated. When an SIW is filled with a dielectric, it can support either a fast or slow wave, depending on operating frequency. People tends to believe that a slow wave in slotted SIW does not produce radiation. For example, a periodic SIW leaky wave antenna can support the existence of a fundamental mode and many space harmonic modes simultaneously. The modes related to fast waves can radiate leaky waves, but the fundamental mode cannot radiate if it is a slow wave [36]-[37]. A width-tapered slotted SIW, however, is not a periodic structure so that there is no any space harmonics in it. Consequently, if the width-tapered slotted SIW produces radiations, it must work with its fundamental mode. In this case, due to a well-known thought that a slow wave does not produce radiations [36]-[38], whether the fundamental mode in the width-tapered slotted SIW must be a fast wave or not? What will happen in a width-tapered slotted SIW when the fundamental mode is a slow wave? The answer to the above questions is crucial to understand the radiation mechanism of an SIW-based CP composite antenna with slots on the SIW.

Furthermore, the radiation from a slow wave should be fully investigated in a broader view. If a slow wave in a width-tapered slotted SIW can produce leaky wave radiation, why a slow wave in a width-uniform slotted SIW cannot produce leaky wave radiation? A width-uniform slotted SIW is periodic rather tha uniform. The propagation constant of a mode in a periodic structure is a parameter characterized only in an average sense [39]. The propagation constant can be used to determine whether a mode is a slow wave or not. However, it cannot be used to determine all the propagation characteristics. Accordingly, it is not rigorous to identify the possibility of slow wave radiation stemmed from a periodic structure only based on its propagation constant, and a full investigation on slow wave radiation is interesting and necessary.

Moreover, the effects of periodicity in SIW-based antennas or associated SIW transmission lines should be explored when operating frequency is high, let's say, with referece to electrical length. When the periodicity length in an SIW is much smaller than the wavelength in the SIW, the effects of periodicity can be ignored [5], the SIW can be totally equivalent to a dielectric-filled waveguide (DFW). When the diameter of a via is less than 0.3 mm, its metallization is difficult, and a 0.2 mm minimum spacing between two vias is generally required in practice for a conventional print circuit board (PCB). Therefore, the available minimum periodicity of via arrays in an SIW made with PCB technology is roughly 0.5 mm. If an SIW is fabricated on a substrate with a relative permittivity of 4, when operating frequency is 75 GHz, the guided wavelength in the SIW can be close to 2.5 mm. The periodicity length in the SIW is comparable to the operating wavelength, and the effects of periodicity must be taken into account.

Both the propagation constant and the wave impedance in a periodic transmission line have certain characteristics different from that in a uniform transmission line, and these characteristics are important to understand the physics of a periodic transmission line.

Methods to calculate the characteristic parameters of a periodic transmission line should be also developed, to explore what happens in a practical transmission line. Conventional simulation tool packages, such as CST STUDIO and Ansoft HFSS, are powerful but not omnipotent. When a periodic transmission line is lossless, its propagation constant can be calculated by an Eigenmode

Solver in CST or HFSS. However, these Eigenmode Solvers are not applicable to a periodic structure involving radiation, such as slotted SIW antenna. Moreover, both the eigenmode solver methods and the equivalent network methods [39]-[40] involve only a unit cell in a periodic structure and are independent of exciting signals. These methods cannot obtain the number and amplitudes of the Bloch/Floquet modes, and cannot be applied to the calculation of wave reflections in a practical finitely-numbered periodic structure. Usually, both the forward waves and backward waves exist in such a practical periodic structure simultaneously, and the total wave at an arbitrary point inside the periodic structure is the sum or superposition of the forward waves and the backward waves. To extract the forward waves or backward waves from the total wave is critical for calculating the reflection coefficients or space harmonics in a practical periodic structure. Conventional electromagnetic full-wave simulation tools, such as CTS or HFSS, also don’t have such a capability of separating the forward waves and backward waves.

Accordingly, the research work of this thesis is concentrated on following aspects.

1) To devise SIW-based fully planar composite antennas to achieve diverse performances, addressing end-fire CP radiation problems with high gain. The composite antenna is made of various radiators integrated with an SIW, and should be a kind of fully planar structures, including its feeding structure. They should be fabricated on a single-layer substrate, or on a mingled multilayer substrate with a very thin feeding layer. The composite antenna had better could work with a slow wave mode so that operating frequency would be as wide as possible. It should actually provide a general solution of SIW-based planar composite antenna, applicable to a large array, to well satisfy various requirements of antennas and antenna applications.
2) To find a comprehensive calculation method of characteristic parameters in a practical periodic structure, such as an SIW, with excited signals. The method should be used to calculate the propagation constants and amplitudes of the Bloch/Floquet modes in a practical periodic structure, to separate the forward waves and backward waves from the total wave at any point in the structure and to calculate the reflection coefficients and characteristic wave impedances. The method should be applicable to uniform and periodic, transmission and radiation structures.
3) To explore propagation, radiation, impedance and reflection characteristics in a periodic structure such as an SIW. Whether the wave impedance of a mode in a periodic transmission

line is still real or complex? Is the wave impedance still uniform or inhomogeneous? Is the reflection coefficient at an inner point inside a periodic structure equal to the port reflection coefficient? Is it homogeneous and independent of polarization? Does a slow wave in non-periodic antenna produce a radiation? Is it reasonable to interpret the radiation in a periodic leaky wave antenna (PLWA) with its fundamental mode when the mode is a slow wave? Is it possible to judge whether a mode in a periodic structure produces radiation only based on the longitudinal propagation constant of the mode?

1.2 State-of-the-Art and Present Trend

1.2.1 Planar End-fire CP Composite Antennas

An end-fire planar antenna has both planar structure and end-fire radiation pattern. In this thesis, the term “planar antenna” is referred as to not only its structure shape but also the process through which the antenna is manufactured. Therefore, a planar antenna should be manufactured on substrates through planar manufacturing processes such as printed circuit board (PCB) processes and LTCC techniques. A planar antenna was also defined as one structure manufactured on a thin substrate, and the thickness of this substrate should be less than one-tenth wavelength. On the other hand, such thin-structured antennas are often called as low profile antennas. To avoid potential confusions, we would identify whether an antenna is planar or not based on only its manufacturing processes rather than its thickness of substrate.

The planar end-fire CP antennas in literatures are relatively limited in number, especially the fully planar end-fire CP antennas with high gains. A CP antenna should generate two orthogonally polarized radiations, and they should feature the fundamental characteristics of equal-amplitude and quadrature-phase. To produce such CP radiation, a CP antenna makes use of one radiator or more. A helical antenna has a radiator which becomes an end-fire CP antenna when the circumference of the helix is approximately equal to one guided wavelength [41].

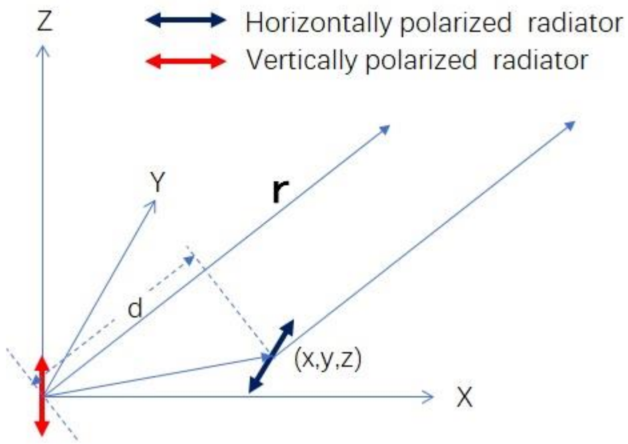

Figure 1.2: Modal of a CP antenna

A simple model, as shown in Figure 1.2, can be used to demonstrate how the configuration of a CP antenna influences the performance of its axial ratio (AR). In the model, the CP antenna consists of a VP radiator and a HP radiator, which produce two corresponding radiations in space. Without loss of generality, the phase center of the VP radiator is placed at the origin, and the phase center of the HP radiator is at (*x*,*y*,*z*). In the far zone, the phase difference between the two orthogonally polarized electric fields is as follows

$$\Delta\varphi = k_0 d + \varphi_0 \tag{1.1}$$

$$d = x\sin\theta\cos\phi + y\sin\theta\sin\phi + z\cos\theta \tag{1.2}$$

where k_0 is wave-number in the free space, $k_0 d$ is space phase delay, and φ_0 is feeding phase delay of the two orthogonally polarized radiators. Substituting (1.2) into (1.1), one has

$$\Delta\varphi = k_0(x\sin\theta\cos\phi + y\sin\theta\sin\phi + z\cos\theta) + \varphi_0 \tag{1.3}$$

Realizing CP radiation, it should have

$$\Delta\varphi = n\cdot\pi + \frac{\pi}{2}, (n = 0, \pm1, \pm2, \cdots) \tag{1.4}$$

When the phase centers of the two orthogonally polarized radiators coincides with each other, the $d = 0$, and $\Delta\varphi$ becomes independent of space angles. In this case, the CP antenna is expected to have a wide AR beamwidth. If its feeding phase delay φ_0 is not sensitive to frequency, the CP antenna is also expected to have a wide AR bandwidth in all the space angles. Therefore, when a CP antenna utilizes a radiator to produce two orthogonally polarized radiations simultaneously, it means that $d = 0$ so that the antenna has a wide AR beam width and bandwidth.

When a CP antenna is composed of two orthogonally polarized radiators with two separate phase centers, $d>0$, and $\Delta\varphi$ depends on both the space angles and operating frequency. As a result, it would narrow down both the AR beamwidth and AR bandwidth. The farther the distance between the two phase centers is, the narrower the AR beamwidth and the AR bandwidth of the CP antenna become.

On the other hand, when frequency changes, the phase center of a radiator is usually located over a region rather than at a fixed point. Besides, the phase center of a radiator also depends on its radiation direction. A stable phase center would be beneficial for the CP performance of a CP antenna.

In most of CP antennas, feeding phase delay φ_0 also depends on operating frequency. When the feeding phase delay φ_0 can offset the space phase delay k_0d, the CP antenna is expected to have a wide AR bandwidth. However, it is a challenging task.

For achieving good radiation performances, the two orthogonally polarized radiation of an end-fire CP antenna should be of end-fire and have the same beam width. As a result, the AR beam width of the end-fire CP antenna could be almost the same as its beam width, and the feature would certainly benefit its applications.

To have a high gain or a complex radiation pattern, an array architecture would be a preferred option. Therefore, one could also evaluate the structure of an end-fire CP antenna based on the array viewpoint.

From the historical perspectives, it has taken a long time for a three-dimensional non-planar end-fire CP antenna to evolve into its planar form. Among end-fire CP antennas, a helical antenna is the earliest one that was proposed in 1948. As late as 2015, however, an end-fire CP planar helical antenna was proposed in [42]. Since then, diversified end-fire CP planar antennas have been proposed and studied [30] [43]-[46].

Most of end-fire CP planar antennas are of composite antennas with multiple radiators, and could be categorized based on different criteria. With reference to the number of radiators, they can be classified into single-radiator or multi-radiator. Based on the mechanism of radiators, they can be divided into resonate or traveling-wave types. Based on the feeding structures, they may be organized into planar feeding or nonplanar types. Bnased on the structure of radiators, they can be arranged into helical antennas, dielectric resonator antennas, SIW horns, antipodal linearly tapered slot antennas (ALTSA), dipole antennas, or loop antennas. For an easy presentation in the thesis, end-fire CP planar antennas are classified into four groups, namely end-fire CP planar helical antennas, end-fire CP planar composite antennas fed by microstrip line, planar electric and magnetic dipole-based end-fire CP composite antenna, and SIW horn-based planar end-fire CP composite antenna.

1.2.2.1 End-fire CP Planar Helical Antenna

The helical antenna is the oldest end-fire CP antenna [41], and has wide impedance and AR bandwidths. Yet, no planar end-fire CP helical antenna was proposed until 2015 [42]. A helical CP antenna has only a radiator. When the circumference of a helix is approximately equal to one guided wavelength, which is necessary for end-fire radiation, the VP radiation is much weaker than its horizontal counterpart due to the thin substrate. Therefore, it is rather challenging to devise a planar end-fire CP helical antenna in a relatively low frequency band. For example, a 2.54-mm thick substrate is still regarded as a thin substrate at 10 GHz because it is less than $0.1\lambda_0$.

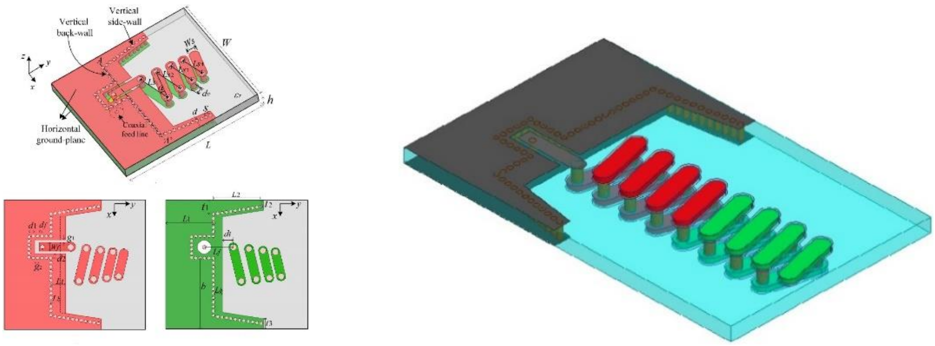

(a) (b)

Figure 1.3: (a) Planar helical antenna [42] and (b) planar plasma helical antenna with reconfigurable bandwidth [47]

The end-fire CP planar helical antenna in [42] is composed of strips and metallic vias as shown in Figure 1.3 (a). The strips are formed on the two plates of the substrate and are connected through the metallic vias to form an axial helix. The strips contribute to HP radiation, whereas the vias contribute to VP radiation. The ground plane is supposed to help maintain the equality of the VP and HP radiation. An SMA connector mounted vertically on the substrate connects to a grounded coplanar waveguide, and this coplanar waveguide then feeds the helix. The open aperture of the grounded coplanar waveguide could also contribute to the VP radiation. Consequently, the CP antenna can achieve an 8-dBi gain at the center frequency on a thin substrate of only $0.11\lambda_0$.

The structure of an end-fire CP planar plasma helical antenna with a reconfigurable bandwidth reported in [47] is similar to that described in [42], and its gain is 8.5 dBi. In the antenna, as shown in Figure 1.3 (b), a set of tubes containing ionized noble gases (such as argon, neon, or xenon) are used to replace conventional copper to form a multi-turn plasma helical (red in Figure 1.3 (b)), which make its bandwidth reconfigurable.

1.2.2.2 End-fire CP planar composite antenna fed by microstrip

When an end-fire CP planar antenna is fed by a microstrip line, producing VP radiation is a critical for the generation of CP radiation. In [46], an end-fire CP planar loop antenna fed by a microstrip line is proposed, as shown in Figure 1.4 (a). The antenna uses a printed quadrangle loop which is composed of four strips on the top and bottom layer of a substrate and connected by three metallic via holes. To improve bandwidth, two stubs are loaded onto two strips, and the edge of the ground is modified with sawtooths. The antenna shows very good performances, however, certain important parameters, such as thickness, are missing in [46].

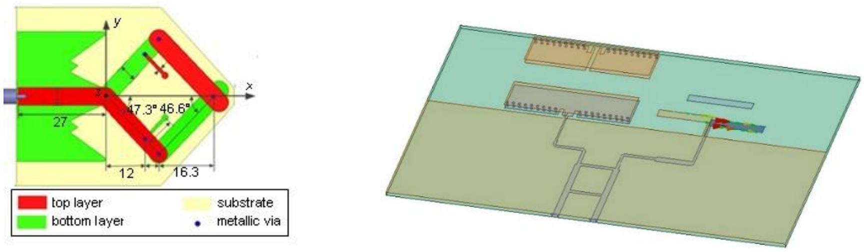

(a) (b)

Figure 1.4: (a) Planar loop antenna fed by a microstrip line [46] and (b) dual CP planar antenna [51]

A Yagi array [48] and its planar forms [49] [50] are classical end-fire antennas. They are used as HP radiators to achieve CP antennas. In [51] a Yagi end-fire dual CP planar antenna uses a magnetic dipole Yagi element and an electric dipole Yagi element on a substrate with a thickness of $0.02\lambda_0$, as shown in Figure 1.4 (b). The magnetic dipole Yagi element is composed of two one-edge-shorted rectangular patches separated by a spacing. The electric dipole Yagi element is a strip half-wave dipole and a strip director. The antenna is fed by a hybrid network composed of microstrip lines and parallel strip lines to achieve dual CP radiation with a 5.3 dBi gain.

1.2.2.3 Planar electric and magnetic dipole-based end-fire CP composite antenna

Q. X. Chu and W. J. Lu et al devised a type of low-profile end-fire CP planar antennas [30][53]-[71]. The conceptual three-dimensional prototype of these antennas can be found in [72]-[73]. Figure 1.5 describes the conceptual configuration of a planar electric and magnetic dipole-based end-fire CP composite antenna [60]. In the antenna, a planar magnetic dipole produces VP radiation, and a planar electric dipole produces HP radiation. Therefore, the type of antennas is referred to as electric and magnetic dipole-based end-fire CP antennas. The magnetic dipole associated with VP radiation also feeds the HP radiator, either directly [58]-[59] [62][64][69] or by a phase shift line of a quarter [30] [54]-[57] [61] [63][65]-[68] [70]-[71] or three eighth wavelength[53], which are used to achieve a quadrature-phase of the two orthogonal modes for the CP generation. A practical complete electric and magnetic dipole-based end-fire CP antenna usually includes four functional parts: VP radiator, HP radiator, phase-shifting component and feeding connector. W. J. Lu et al have given a detailed review of this type of end-fire CP planar antennas in [60].

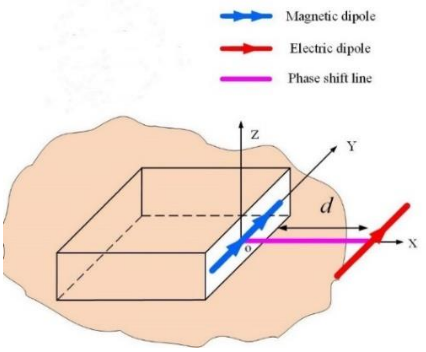

Figure 1.5: Conceptual configuration of planar electric and magnetic dipoles based end-fire CP composite antenna [60]

A low-profile planar magnetic dipole can produce a large VP radiation, and it is a significant benefit, especially for low frequency CP antenna. The planar magnetic dipole in these antennas is actually a dielectric resonator antenna (DRA) rather than a horn antenna or another traveling-wave radiator because it works in a resonant mode rather than in a propagating mode. The planar magnetic dipoles include two types of structures: a rectangle dielectric resonator radiator as shown in Figure 1.6 (a) and (b), and a semicircular dielectric resonator radiator, as shown in Figure 1.6 (c). Both rectangle and semicircular dielectric resonator radiators are covered with conducting layers on their top and bottom surfaces.

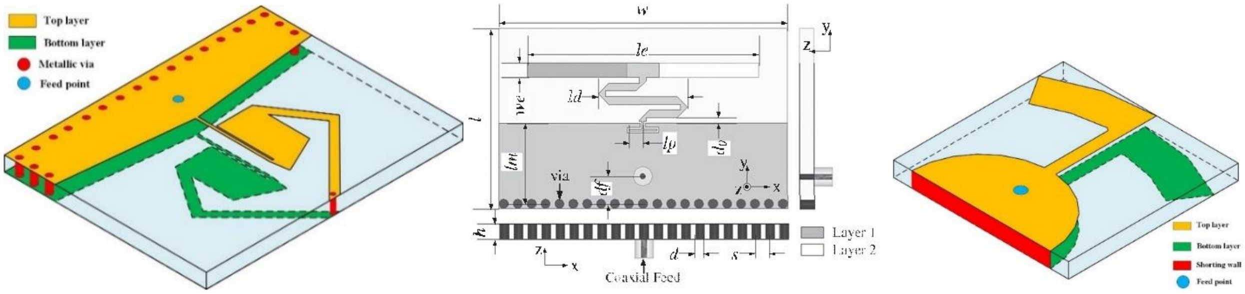

(a) (b) (c)

Figure 1.6: The planar magnetic dipoles

(a) Rectangle dielectric resonator radiator with three shorting edges [60], (b) rectangle dielectric resonator radiator with one shorting edge [70], and (b) semicircular dielectric resonator radiator [60]

The one (Figure 1.6 (b)) or three (Figure 1.6 (a)) of four rectangle dielectric edges are shorted by metallic via arrays or walls, and at least one edge is an open aperture for radiation [30] [53] [56] [58] [61]-[62] [66]-[71] [74]. These CP antennas usually have unidirectional end-fire patterns on the plane of the substrate. Similarly, the straight edge of the semicircular dielectric is shorted by metallic via arrays or walls, as shown in Figure 1.6 (c), and its circular edge is open [54]-[55] [57] [59].

Due to theirs feature, these magnetic dipole structure could be treated as various dielectric resonators, and operating frequencies and the field distributions can then be determined and studied using the theory on DRA.

In aforementioned antennas, the basic structures in the diverse types of the HP radiators, which are also called electric dipoles, are generally dipoles and loops. Figure 1.7 displays various shapes of dipoles, which each have diverse characteristics. The single straight dipoles in Figure 1.7 (a) (m) (n) have an omnidirectional pattern on the pitch plane and a low gain, and such as the end-fire CP antennas also exhibit a relatively low gain about 3 dB [53] [69]-[70]. The various annular dipoles in Figure 1.7 (b) (c) and (f) can provide a wide beam of HP radiation on the azimuth plane to achieve a wide AR beam width on the azimuth plane [54]-[55] [59]. The inverted V-shape dipoles, as shown in Figure 1.7 (d), have a similar shape and AR radiation pattern to annular dipoles [56]-[57]. Because the straight, annular and inverted V-shape dipoles have not end-fire radiation patterns, the gains of the end-fire CP antennas associated with these dipoles are also relatively low. Compared to straight diploes, the V-shape dipoles in Figure 1.7 (e) (h) (l) have an end-fire pattern and a relatively high gain, and are applied to high gain end-fire CP antennas [58] [62] [68]. When a higher gain is desired, magnetic and electric diploe arrays are preferred. Figure 1.7 (e) (g) (h) (j) (k) (l) (o) (p) show diverse end-fire CP antenna array [58] [61]-[62] [65]-[66] [68] [71] [74].

A meandered dipole shown in Figure 1.7 (i) is used to facilitate the assembly of p-i-n diodes, reduce the lateral dimension, and enable switchable polarized radiation between left-hand circular polarization and right-hand circular polarization [64]. Stubs in Figure 1.7 (c) is loaded to dipoles to achieve a wide bandwidth [55].

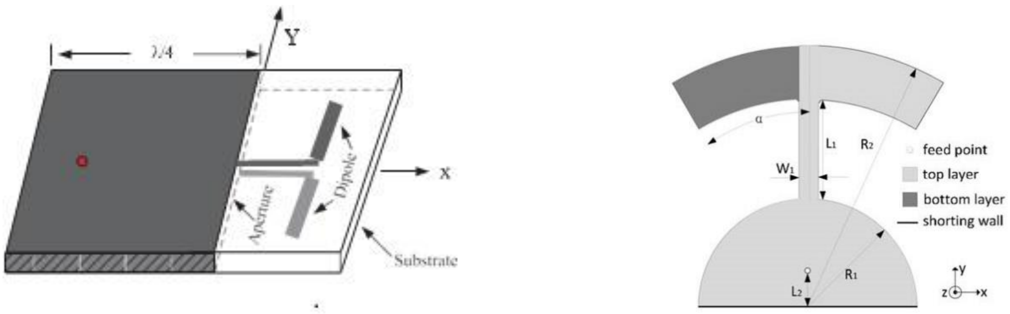

(a) (b)

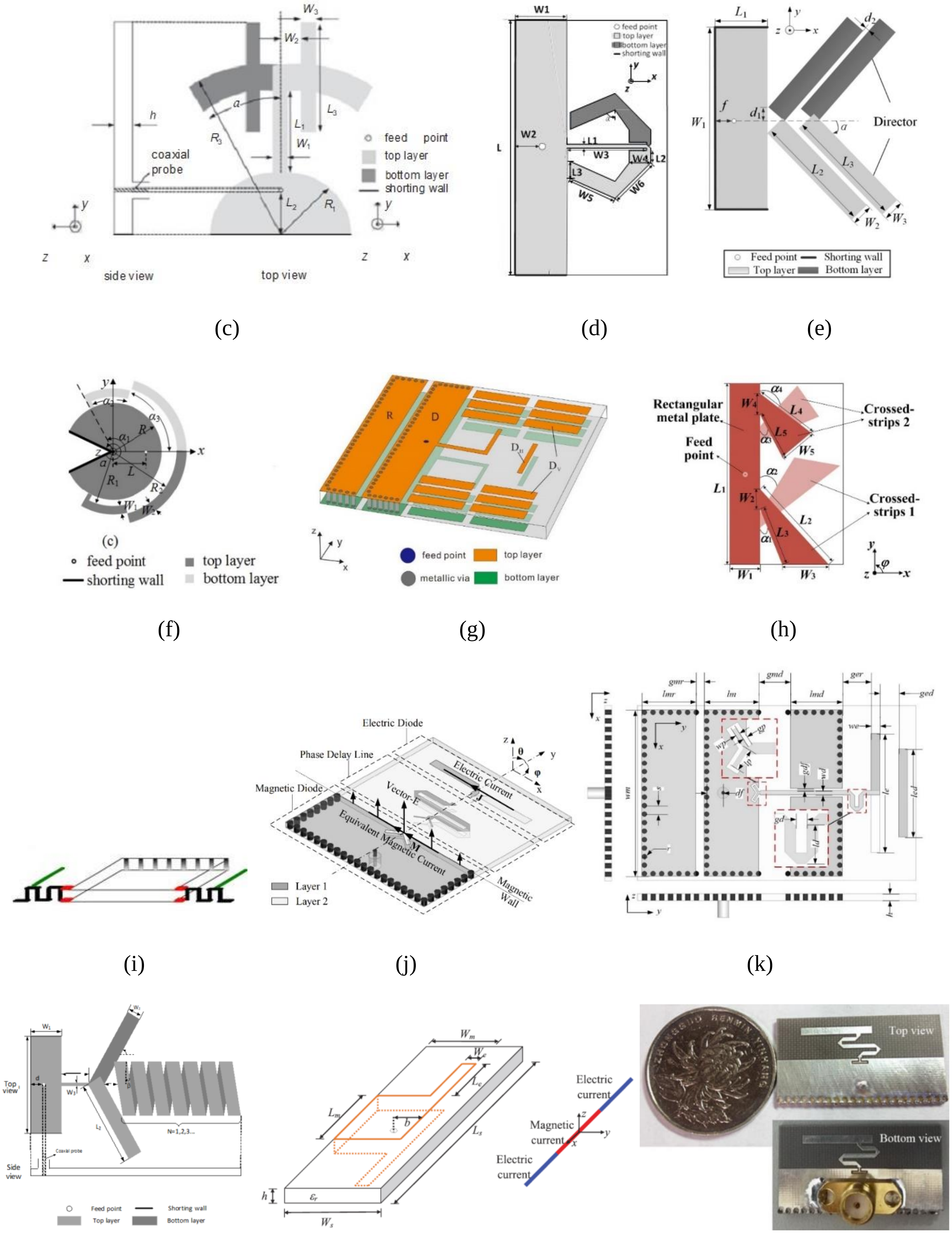

(c) (d) (e)

(f) (g) (h)

(i) (j) (k)

(l) (m) (n)

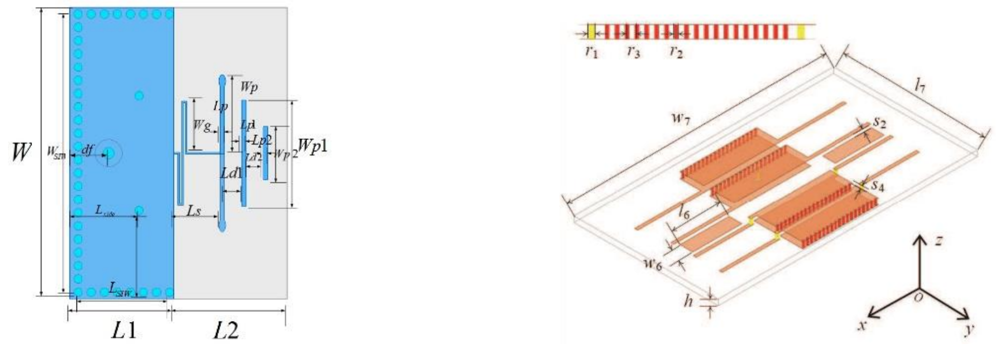

(o) (p)

Figure 1.7: Various shapes of dipoles

(a) dipole [53], (b) annular dipole [54], (c) stub loaded annular dipole [55], (d) V-shape dipole [56], (e) V-shape dipole Yagi array [58], (f) annular dipole loaded with parasitic annular strip [59], (g) Yagi array of dipoles with parasitic strips [61], (h) two different V-shape dipoles [62], (i) meandered monopole array[64], (j) dipole Yagi array [65], (k) dipole-cavity Yagi array [66] (l) V-shape dipole loaded with parasitic helix [68], (m) monopole array [69] (n) dipole with slot coupling [70], (o) dipole Yagi array [71], and (p) extended strip Yagi array on top or bottom layer with two coupling patches [74]

Compared to the aforementioned dipoles which produce HP radiation with an omnidirectional pattern on the pitch plane, the squared loop in [30], as shown in Figure 1.8 (a), and square loop fed by a coupling dipole in [63], as shown in Figure 1.8 (b), are also magnetic dipoles which produce HP radiation but have omnidirectional pattern on the azimuth plane.

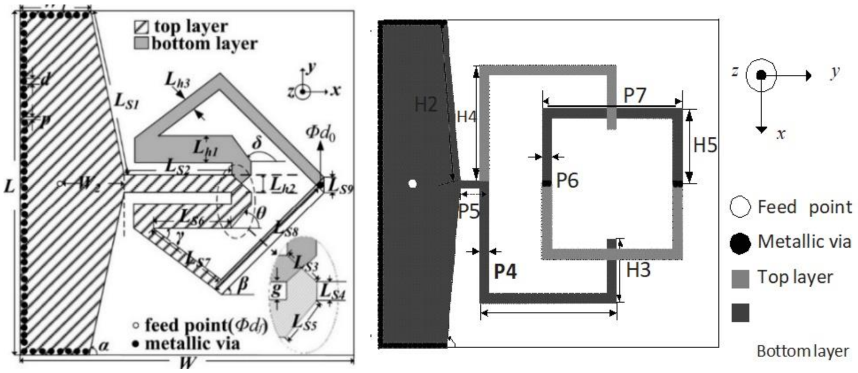

(a) (b)

Figure 1.8: The squared loop

(a) Square loop [30], and (b) square loop fed by a coupling dipole [63]

Beside unidirectional operation, an end-fire CP planar antenna can be designed to generate bidirectional or omnidirectional patterns. Figure 1.9 (a) presents a single-layer single-fed bidirectional end-fire CP planar antenna [45], which could be viewed as a combination of two back-to-back unidirectional end-fire CP planar antennas sharing a common port. The two back-to-back dielectric resonating radiators produce VP radiation and two strip dipoles produce HP radiation. The two back-to-back dielectric resonating radiators share a common metallic via array with a window where an SMA connector is located with its inner conductor attached to the upper layer and its outer conductor soldered to the lower layer. The dielectric resonating radiators feed the electric dipoles using double-sided slot-coupled lines and meandered double-sided parallel strip lines. The double-sided parallel strip lines provide a phase compensation for CP radiation. The length of the double-sided parallel strip line and the distance from the dielectric resonating radiator to the dipole have a strong effect on the phase difference between the VP and HP radiation. Figure 1.9 (b) describes a bidirectional end-fire CP surface wave antenna fed by an SMA connector [75]. The planar antenna is composed of a microstrip radiator for the VP radiation and two hook-shaped strips on the ground plane for HP radiation. The two bidirectional end-fire CP planar antennas have a very low profile of 0.029λ0, which is important to the application in the band of 5.8-GHz ISM or lower frequency.

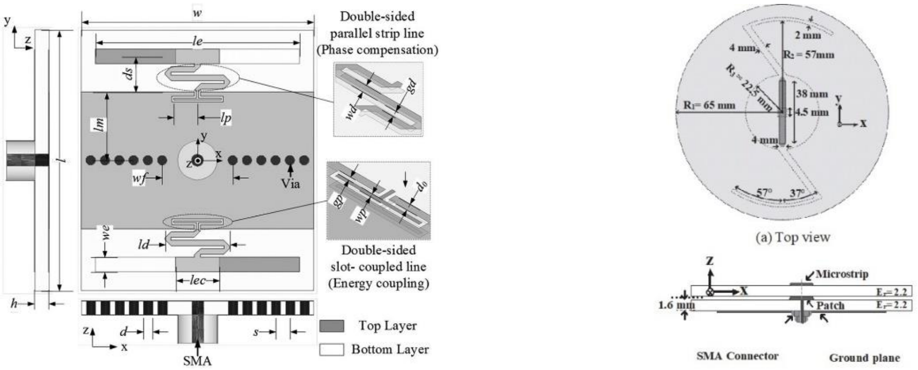

(a) (b)

Figure 1.9: End-fire CP planar antenna

(a) Single-fed bidirectional end-fire CP planar antenna [45], and (b) CP surface wave antenna composed of a microstrip radiator and two hook-shaped strips [75]

These planar end-fire CP antennas are all the composite antennas composed of vertically and HP radiators. The two orthogonally polarized radiations should exhibit a quadrature-phase, and strip lines between the two radiators are used to achieve this required quadrature-phase. On the other hand, the phase centers of the VP and the HP radiators in these antennas do not coincide with each other. Therefore, the strip lines might be meandered ones, as shown in Figure 1.7 (j) (k) and (n). The connection between the strip lines and the VP radiator and the HP radiator could be a direct connection or be achieved by the coupling of slots or strips. The coupling of slots or strips would introduce a phase shift, and thus the quadrature-phase can be achieved without an extra strip line [62] [64], as shown in Figure 1.7 (h) and (i).

Table 1.1 is a brief comparison of the key performances of these planar electric and magnetic dipole-based end-fire CP composite antennas.

Table 1.1: Comparison of electric and magnetic dipole-based end-fire cp composite antennas

References	**Bandwidth (%)**	**AR Band-width(%)**	**AR Beam width Pitch/Azimuth**	**Gain (dBi)**	**Size/λ₀**	**Fre. (GHz)**	**HP radiator**
[30]	2.4	9.2	104/92	2.6	0.6*0.71*0.04	5.8	Loop
[53]	1.9	14.5	110/80	2.3	0.65*0.73*0.04	5.8	Dipole
[54]	6.5	14.4	92/67	4.9	0.83*0.59*0.033	2.45	Dipole
[55]	25	19	N.A.	3.0	0.88*0.59*0.033	2.45	Dipole
[56]	22	8	250/240	1.5	0.53*0.74*0.04	2.45	Dipole
[57]	11	11	180/115	2.5	0.61*0.64*0.05	2.45	Dipole

[58]	5	25	92/29	6.1	1.17*1.48*0.034	2.5	Yagi array
[59]	13.7	2	50/65	0.41	0.54*0.66*0.04	2.5	Dipoles
[61]	13.1	10.5	N.A.	8	1.09*1.14*0.05	5.0	Yagi array
[62]	55.4	48.2	N.A.	7.28	0.72*1.15*0.07	2.4	Dipole array
[63]*	5	14	N.A.	3	0.44*0.73*0.04	5.8	Loop
[64]	2.1	9	N.A.	1.58	0.16*1.19*0.026	2.4	Monopole array
[65]*	2.1	4.3	179/164	4.1	0.35*0.6*0.029	5.8	Yagi array
[66]*	1	1.5	N.A.	7.23	1.05*0.65*0.026	10	Yagi array
[67]*	2	8.2	N.A.	NA	? *? *0.016	2.45	Dipole
[68]*	3.82	13	N.A.	7.1	2.64*1.29*0.034	2.45	Yagi array
[69]	4.3	4.3	360/36	3.3	0.31*1.32*0.039	5.8	Monopole array
[70]	3.5	4.3	168/85	4	0.32*0.60*0.029	5.8	Dipole
[71]*	3.0	12	N.A.	4.18	0.6*0.77*0.047	7	Yagi array
[74]	5.2	5	N.A.	7.8	0.97*1.74*0.04	5.8	Yagi array
*: Only simulated results available.							

The electric and magnetic dipoles-based end-fire CP antennas in Table 1.1 are generally working at low frequencies. Because the gain of a single straight electric dipole for HP radiation is low compared to magnetic dipoles, the gains of the planar electric and magnetic dipole-based end-fire CP composite antennas are relatively low, about 2 dBi. To achieve a high gain, a Yagi architecture is preferred [58] [61] [66] [68] [71] [74]. Directors in [58] [68] [71] are used to enhance the gains of electric dipoles. In [61] [66] [74], both reflectors and directors are used. The former is to enhance the gain of VP radiation, and the latter is to enhance the gain of HP radiation. In [62] [64], transverse two-element dipole arrays are used to enhance the gain of HP radiation.

Because the HP radiator is fed by the VP radiator in aforementioned CP antennas, a reflector can be added to the VP radiator to increase its gain. It is difficult to add directors to the VP radiator. Therefore, the gain of the VP radiator and in turn the gain of a single electric and magnetic dipoles-based end-fire CP antenna would not be very high, e.g. over 8 dBi.

The structure of a dielectric resonating radiator can produce strong enough VP radiation for a CP antenna with very thin substrates, but it is difficult to feed a dielectric resonating radiator with a planar structure. All the antennas in Table 1.1 are fed with SMA connectors perpendicularly mounted on the bottom face of substrate. Therefore, this type of feeding structure is not fully planar. It would bring up difficulties when forming an end-fire CP antenna array， which is necessary in most cases to achieve a high gain beam or a scanning beam.

1.2.2.4 SIW horn-based planar end-fire CP composite antenna

To the knowledge of the author, the oldest end-fire CP planar antenna based on SIW technology was derived from the ALTSA fed by an SIW in 2007 [43]. As shown in Figure 1.10, the two flaring wings of the ALTSA have not overlapping at the SIW aperture. The open aperture of the SIW produces VP radiation. Its source is the transverse electric field of the TE10 mode in the SIW. The ALTSA produces HP radiation, and its source is mainly from the longitudinally magnetic field of the TE10 mode in the SIW. The transverse electric field and the longitudinally magnetic field of the TE10 mode in an SIW are quadrature-phase in natrue. The phase centers of the VP and the HP radiations, however, do not coincide with each other. As such, the quadrature-phase of the transverse electric field and the longitudinally magnetic field do not naturally ensure the phase condition of CP radiation. To resolve this issue, a polystyrene rod, which is supposed to be in favor of the quadrature-phase, surrounded by the edge of the flaring wings is used to increase the AR bandwidth.

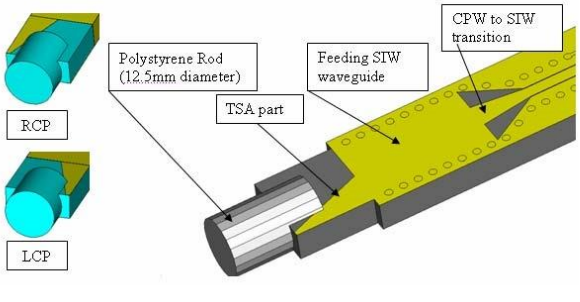

Figure 1.10: Earliest ALTSAn end-fire CP planar antenna fed by an SIW in 2007 [43]

Although the ALTSA in [43] is not a totally planar antenna due to the loading dielectric rod, it has paved the way for a totally planar antenna. Still, it was a long time before an end-fire CP planar ALTSA fed by an SIW, as shown in Figure 1.11 (a), wss proposed in 2017 [76]. The ALTSA without a loading dielectric rod has a wide AR bandwidth, and its flaring wings are overlapped at the open aperture of the SIW. Since the two flaring wings are over different faces of the substrate, the ALTSA does also produces a little of VP radiation. [77] made use of two antipodal notches etched at the edges of the two broad walls of an open-ended SIW, as shown in Figure 1.11 (b), to produce CP radiation. To further increase the gain and front-to-back ratio (FTBR) of the antenna, a thick tapered three-layer dielectric rod is placed in front of the antenna. The substrate of the CP antenna in [43][76]-[77] must also be thick enough to ensure the equally-amplitude of two orthogonally polarized radiations.

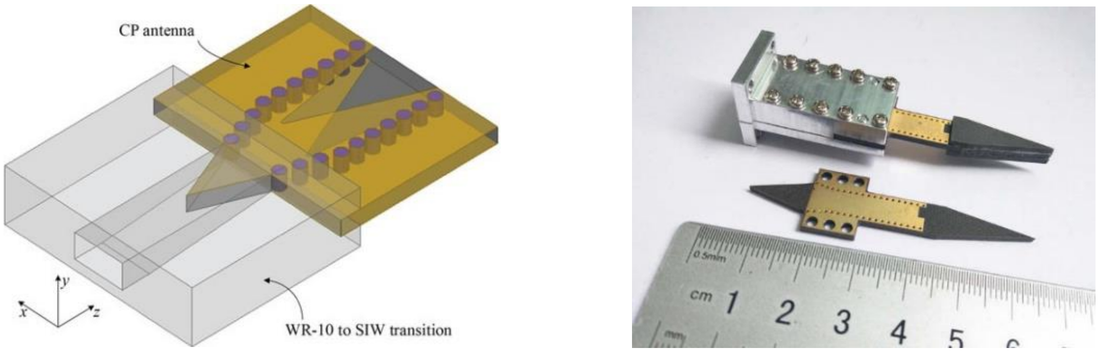

(a) (b)

Figure 1.11: Planar ALTSA fed by SIW

(a) without loaded dielectric [76] and (b) with loaded dielectrics [77]

Y. Cai and Z. Qian proposed a septum polarizer based SIW end-fire dual CP antenna, as shown in Figure 1.12 (a), in 2016 [44]. It is entirely an SIW horn without any other radiator. The antenna uses two layer of thick substrates and has two input/output SIWs for LHCP and RHCP. In its transition section, a sloping open slot etched on the common broad wall between the two SIWs, is tasked to transform the TE10 mode into two orthogonal modes, namely TE10 and TE01, at the common open ends of the two SIWs. In the flaring section, the two SIW parts also form a common rectangle horn with different widths to achieve the quadrature-phase for CP radiation. To radiate two orthogonal modes in a common horn, the antenna must use two thick substrates. The total thickness is about $0.6\lambda_0$. The antenna is fed by a WR-42 waveguide due to the thick substrates.

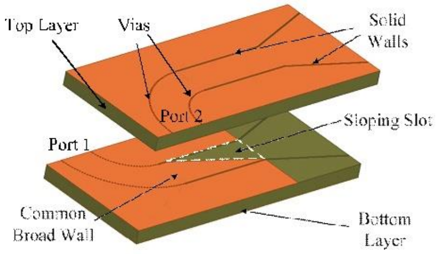

,

Figure 1.12: Septum polarizer based End-fire dual CP SIW horn antenna [44]

Before the reporting of such an end-fire CP antenna in [76], Sara S. Hesari and J. Bornemann proposed an SIW end-fire dual CP antenna, as shown in Figure 1.13. It consists of an antipodal Vivaldi antenna and an SIW H-plane horn [79]. Both the antipodal Vivaldi antenna and the SIW horn are fed by an SIW 3-dB coupler to achieve the equally-amplitude and quadrature-phase. The phase centers of the two radiators are obviously separated.

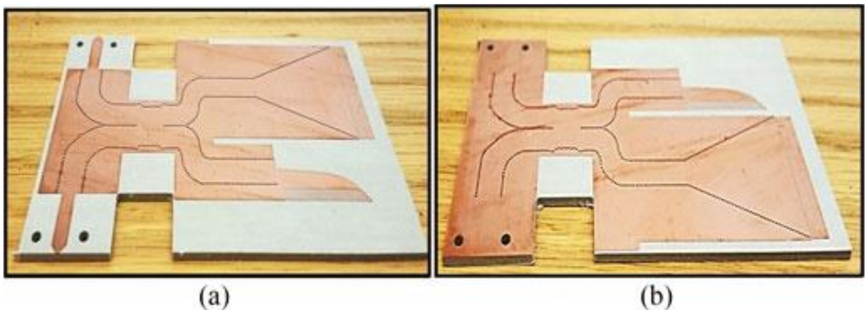
(a) (b)

Figure 1.13: SIW end-fire dual CP antenna [79]

Table 1.2 presents a performance comparison among the SIW horn-based end-fire CP composite antennas. Different from the electric and magnetic dipole-based CP planar antennas, the SIW horn-based end-fire CP planar composite antennas are traveling-wave type of antennas. These antennas feature fully planar feeding structures, and the feature makes the SIW-based end-fire CP easily to be integrated with its associated RF circuit. Consequently, the structure of the SIW-based planar end-fire CP antennas is competitive in the development of systems at millimeter-wave frequencies or above.

Table 1.2: Comparison of siw horn-based end-fire cp planar composite antennas

Reference	**Bandwidth(%)**	**AR band-width(%)**	**Gain (dBi)**	**Size/λ₀**	**Fre. (GHz)**	**Structure features /Connector**
[43](NP)	29	14	5.5	?*?*0.106	10	Non-planar/WR
[44]	25.6	11.8	9	4.6*2.3*0.58	20	Two-layers/ WR
[76]	31.5	34.7	7.9	3.5*1.5*0.25	95	Single Layer /WR
[77]*	52.9	41	12.9	5.88*0.71*0.15/0.45	30	Three-layer/WR
[79]	16	9.0	8.4	7.2*5.4*0.13	25	Single Layer/MS
[32]	5	5	6.2	2.22*3.23*0.13	12	Single Layer/CPW

1.2.2.5 End-fire CP planar antenna array

To achieve flexible and diverse performances with potential reconfigurable and tunable features, researchers and engineers have significantly focused on the development of antenna arrays. Based on the structures and topologies of building elements, these end-fire CP planar antenna arrays can be divided into two groups, namely, dipole-based element antennas [52] [80]-[81] and septum polarizer element antennas [78] [82]-[84].

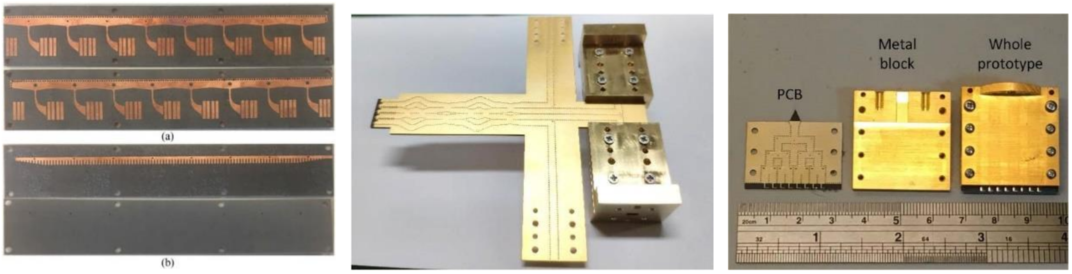

(a) (b) (c)

Figure 1.14: (a) Beam-scanning end-fire CP planar antenna array [52], (b) multi-beam [80], and (c) fixed-beam [81]

Figure 1.14(a) presents a beam-scanning planar end-fire CP antenna array, which was reported in [52]. The antenna consists of 8 tapered dipoles that produces a HP radiation, and each dipole is loaded with parasite strips. The array is fed by a leaky wave antenna made of periodic microstrip line, which produces a VP radiation. The antenna has a main beam scanning from –5° to +37° in a lateral plane, and demonstrates a wide bandwidth due to leaky wave radiation mechanism. The V-band end-fire CP antenna array, as shown in Figure 1.14(b), uses notched dipoles as constituent element CP antennas [80]. These dipoles are fed by an SIW Butler matrix, and a multi-beam with wide beam coverage is achieved. The antenna in Figure 1.14(c) describes an 8-element complementary dipoles array. The antenna array uses two metal blacks as reflector, and it demonstrates a high peak gain of 15.3 dBic.

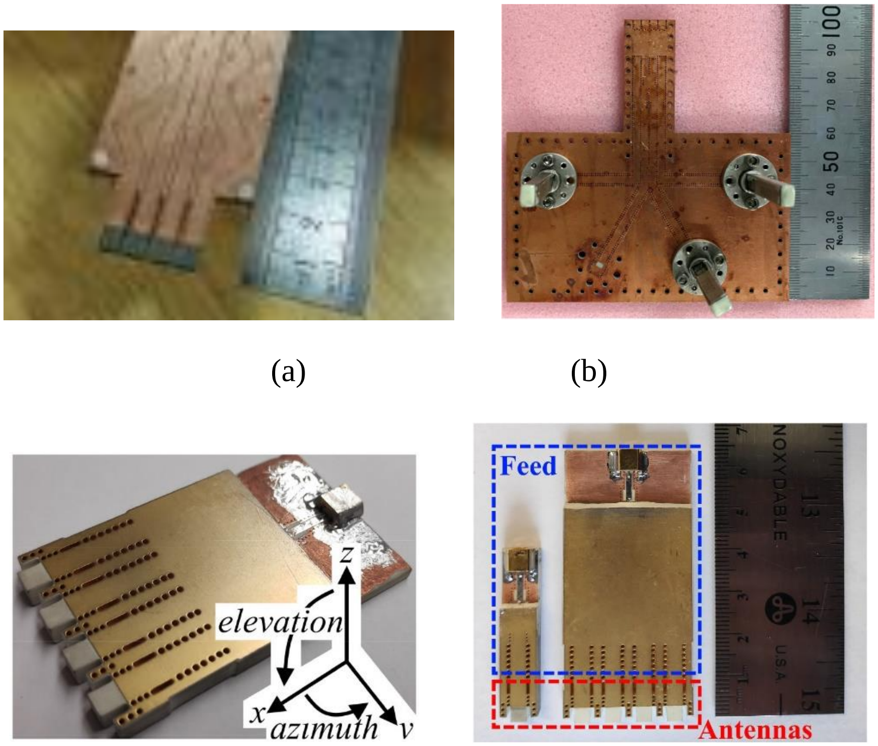

(a) (b)

(c) (d)

Figure 1.15: Septum polarized-based end-fire CP antenna arrays

(a) multi-beam array with loaded dielectrics [78], (b) multi-beam array [82], (c) fixed-beam with loaded dielectrics [83], and (d) fixed-beam [84]

Q. Wu and H. Wang *et al*. developed and extended an end-fire dual CP SIW horn [6] into a multi-beam array, as shown in Figure 1.15(a) for 5G millimeter-wave applications [78]. The antenna in [78] also uses two thick substrates of $0.75\lambda_0$, in which four dielectrics are loaded in front of the open apertures of SIWs to enhance a peak gain of 12.9 dBic. X. Cheng and X. Chen *et al*. studied and developed a compact end-fire CP septum antenna array, as shown in Figure 1.15(b), and it also use an SIW-based Butler matrix to achieve a multi-beam with peak gain of 11.0 dBic [84]. K. Al-Amoodi et al. also devised and demonstrated end-fire CP septum-based antennas array, as shown in Figure 1.15(c) and (d). The array in [81] has a fixed-beam with peak gain of 10.5 dBic, and the array in [83] can achieve a steering beam through different parameters of passive shifters in its feeding network.

Table 1.3 presents a comparison of various planar end-fire CP antenna arrays in terms of performance, size and structures of element antennas.

Table 1.3: Comparison of Different Planar End-Fire CP Antenna Arrays

References	**IM BW(%)**	**AR BW(%)**	**Peak Gain (dBic)**	**Size/λ0**	**Fre. (GHz)**	**Element Antenna**
[52]	31	15	9.5	0.8*(0.68*8)*0.13	15	Complementary Dipole
[80]	24.6	28.5	10.4	?*(0.53*4)*0.20	60	Complementary Dipole
[81]	26	23.8	15.3	?*(0.53*8)*1.45	64	Complementary Dipole
[78]	29	23	12.8	20*(0.75*4)*0.38	38	Septum Polarizer
[82]	7.8	?	11	?*(0.66*4)*0.72	60	Septum Polarizer
[83]	7.9	4.5	10	?*(0.53*4)*0.35	29	Septum Polarizer
[84]	11.4	3.7	10.5	2.9*(0.7*4)*0.36	28	Septum Polarizer
?: no available information						

Feeding networks in the aforementioned end-fire CP antenna arrays feature large sizes and their losses are also generally high, which limit the usefulness in a number of millimeter-wave applications. Moreover, although the beam-width on elevation plane in the array becomes narrow, the beam-width on azimuth plane is still wide, since the element antennas in an array are transversely stretched over the plane of substrate. In 5G and B5G applications, the beam-width on azimuth plane should be also narrowed down for high energy efficiency.

1.2.2.6 Short summary

Although diverse end-fire CP planar antennas have been proposed and demonstrated, fully planar high gain end-fire CP antennas are highly desired.

The radiating structures of these electric and magnetic dipole-based end-fire CP antennas are planar and can use very thin substrates. It is a significant benefit to applications. These antennas, however, are usually fed with cable probes perpendicularly mounted on the bottom face of the substrate. Therefore, this type of feeding is not supposed to be fully planar structure. It would bring difficulties to form an end-fire CP antenna array, which is necessary to achieve a high gain beam or a scanning beam. Moreover, most of these antennas have low gains. Helical based end-fire CP planar antennas [42] [47], and Yagi-like end-fire CP planar antennas [61] [66] [74] could have high gains, but they are also fed by vertically mounted probes, so that are supposed not to be fully planar structures.

The high gain VP radiator is crucial to a fully planar high gain end-fire CP antenna, especially to the antenna on thin substrates. To be CP radiation, the equivalent isotropically radiated powers (EIRPs) of the HP and VP radiators should be equal. When the powers distributed to the HP radiator and VP radiator are equal, the gains of the two radiators should also be equal. When a high gain, for example above 8.0 dBi, fully planar end-fire CP antenna is desired, both the VP and HP radiators should have high gains.

An SIW-based end-fire CP antenna could be a fully planar structure and have high gain [44]. There are some end-fire CP planar antennas fed by waveguides [76]-[78], which could be replaced with SIWs. These antennas, hovever, use thick substrates compared to wavelength.

The ways to enhance the VP gain in a CP antenna include using thick substrates or forming arrays. In [44][79] SIW schemes use two thick substrates of more than $0.58\lambda_0$ to ensure high VP gains. In [76], an ALTSA fed by a waveguide also uses a thick substrate of $0.25\lambda_0$. In [77], an ALTSA, also fed by a waveguide, on a substrate of $0.152\lambda_0$ is used, and a piece of dielectric with a thickness of $0.456\lambda_0$ is placed in front of the ALTSA to enhance the whole CP gain rather than only VP gain.

An ALTSA or antipodal Vivaldi antenna is often used as a HP radiator in a high gain end-fire CP planar antenna due to its high gain [76][77][79]. In fact, an ALTSA fed by an SIW can produce both HP and VP radiation. When only a thin substrate is available in a high gain ALTSA, however, the VP radiation of the ALTSA is much weaker than HP radiation. To match the high HP gain of the ALTSA, it is necessary to introduce extra VP radiators to form a high gain VP array.

The end-fire dual CP antenna fed by an SIW 3-dB coupler in [79] consists of an antipodal Vivaldi antenna and an SIW H-plane horn, and the latter is used to produce VP radiation. The configuration in [79] leads to a large spacing between the two phase centers of HP and HP radiators, which would degrade the AR beamwidth.

1.2.2 Characteristics of Periodic Structure and Its Calculation Method

SIWs can be used as part of either transmission lines or antennas. Transmission lines could be divided into two types: uniform and non-uniform transmission lines. A periodic transmission line, such as an SIW, is one kind of the non-uniform transmission lines. An SIW planar horn antenna actually is a width-tapered SIW transmission line with an open end, and so that it is a non-uniform transmission line but not a periodic transmission line.

The theory and analytical method of uniform transmission lines are well known [39], [38]. In a uniform transmission line, both the propagation constant and the wave impedance of an eigenmode only depend on the geometer of its cross section and medium with which the transmission line is filled. As a result, the field and associated characteristic parameters of an eigenmode in a uniform transmission line can be obtained by solving a two-dimensional wave equation on its arbitrary cross section. Again, both the propagation constant and the wave impedance of an eigenmode are uniform and independent of positions.

The theory and analytical method of periodic transmission lines [38], [85]-[97] are also well-developed, but the characteristics of fundamental mode or space harmonics in a periodic transmission line are not well known compared to eigenmodes in a uniform transmission line. Periodic transmission lines were originally used in vacuum tubes, filters, accelerators, and then in antennas in 1953 [98]. A well known difference between uniform and periodic transmission lines is that there are fundamental mode and space harmonics in a periodic transmission line. A space harmonic is also called as a Floquet mode. Different from a uniform transmission line, the fundamental mode and associated characteristic parameters in a periodic transmission line are obtained by solving a three-dimensional wave equation for a unit cell. The wave equation can be written as a set of differential equations having non-constant coefficients because the shape of transverse section of the periodic transmission line varies along the line. Besides, any individual space harmonics do not satisfy the boundary conditions of a periodic transmission line individually, and cannot exist alone, which will make it actually is impossible to have a relationship, as simple as the Pythagorean theorem, among the propagation constants and transverse wave-numbers of a Floquet mode or the fundamental mode. The fundamental mode or a Floquet mode, however, might be treated wrongly as a type of fields in a uniform transmission line, and then it is in turn expanded wrongly with eigenmodes. This is the fundamental concept of partial waves.

On the other hand, the investigation on the radiation of a slow wave in a non-uniform structure is quite limited, mostly due to a well-known but exorbitantly simplified concept or speculation in that a slow wave does not produce radiation. As a matter of fact, in reference [99], there are certain results that have implied the existence of radiation produced by a slow wave in a non-uniform slotted leaky wave antenna. The antenna in [99] is not a periodic structure, however, the authors still suggested that the radiation be produced by space harmonics in the structure. In fact, there are no space harmonics due to the non-uniform slots in the structure. The radiation from slow waves also happens in certain so-called doubly-periodic leaky wave antennas [100], in which there are usually a long spatial periodicity and a short spatial periodicity. The periodicity of a doubly-periodic structure is the least common multiple of the long periodicity and the short periodicity. Consequently, there are no any space harmonics associated with the short periodicity, and therefore it is unreasonable to explain the radiation with the space harmonics of the short periodicity. If possible, it is certainly more reasonable to explain the radiation with the fundamental mode, even the fundamental mode is a slow wave.

So far, we have not found a rigorous proof that a slow wave in non-uniform structure does not produce radiation. On the other hand, no matter its fundamental mode is a fast or slow wave, the radiation characteristics of a PLWA can well be interpreted based on its fundamental mode as well as its space harmonics. The feeding phase delay of the fundamental mode between adjacent elements is different from that of a space harmonic. However, the difference of the two phase delays is $2n\pi$. Based on an antenna array theory [101], when the feeding phase delay between two radiating elements is changed from its initial phase delay by $2n\pi$, it does not bring any effect on its radiation pattern. It means one cannot find an evidence based on the antenna array theory to support the concept that a slow wave in periodic structure does not produce radiation. Accordingly, it is necessary to fully investigate the radiation by a slow wave, in order to understand the physics of radiation.

To explore propagation, radiation, reflection and impedance characteristics of a periodic structure, a comprehensive calculation method is necessary. Both the eigenmode solver method and the equivalent network method can be used to calculate phase constants in a periodic structure. The eigenmode solver method is convenient to calculate the phase constants. Although the eigenmode solver method can account for the loss from dielectric, it cannot calculate attenuation constants. When there exists conductor loss or radiation loss, the eigenmode solver method is no longer available. An equivalent network method in [39] is only suitable for a periodic transmission line whose unit cells have lumped or weak discontinuities. A multi-mode equivalent network method in [40] overcomes the above issues. The equivalent network methods use full-wave simulation tools to calculate scattering parameters and the associated transmission matrix parameters of a unit cell and find the complex roots of an eigenvalue equation by using numerical methods. The equivalent network method is applicable to the calculation of characteristic parameters, including propagation constants and normalized impedances [39]-[40], [88], [90]. The method has widely been used in recent research and developments of leakage wave antennas and microwave wave components associated with spoof surface plasmon polariton (SSPP). These methods suffer from certain challenges in the following cases:

1) Both the eigenmode solver method and the equivalent network method cannot be applied to the modeling of dielectric transmission lines such as dielectric waveguide.
2) When the loss, especially the radiation loss, in a unit cell is large, the method becomes inaccurate. By the way, the eigenmode solvers in most of electromagnetic field simulation tools, such as CST and HFSS, are not able to deal with a unit cell of an open and radiative structure.
3) The impedance in the equivalent network method is a kind of normalized impedance at one port, also called as Bloch impedance. To determine an actual impedance from its normalized value, one must know the value of a standard impedance. Because the wave impedance of a periodic transmission line is no longer uniform on its transverse cross section, how to define an applicable standard impedance is still unknown.
4) The above-mentioned methods cannot separate the backward and forward waves in a practical periodic structure, and they cannot be used to calculate reflections and wave impedances inside the structure.

To acquire the information about reflection, an approach is to approximate the total fields with the forward and backward modes, and then to determine the weighting coefficients of these modes with an arduous optimization process [33]. It is not an easy task, especially in a practical periodic structure because usually there are no available known mode functions to express the fields in the periodic structure. Moreover, if the reflections in the periodic structure are inhomogeneous, it is much more complex to extract the forward and backward waves by using a numerical method with an exponential approximation as in [33]. More importantly, an exponential approximation is a nonlinear mathematic problem and there is no robust high-efficient calculation method. Consequently, an appropriatemethod is not always available in reality. A robust direct method to determine the characteristic parameters associated with the modes in a transmission line is highly desired.

1.3 Outline of Thesis

This thesis presents three types of end-fire CP antennas, two LP antennas, and the characteristics and calculation formulas of periodic structures. The thesis is organized as follows.

Chapter 2 proposes two types of fully planar SIW-based high-gain end-fire CP composite antennas on single-layer substrates and a slot-horn composite antenna with omnidirectional pattern on E-plane. Section 2.1 is brief introductions to SIW horn and ALTSA which have been used in following composite antennas. Section 2.2 demonstrates an SIW horn-ALTSA end-fire CP antenna [102], which has a multiple sub-horns VP radiator array and a feeding network embedded the SIW horn. The antenna is actually a heterogeneous linear array transversely stretching on the substrate. Section 2.3 demonstrates an SIW slot-ALTSA end-fire CP antenna. The antenna uses a slot array etched on the broad walls of the SIW to form an extra VP radiator, and the mode in the SIW could be a slow wave and would produce VP radiation to enhance VP gain. The antenna is actually a heterogeneous linear array longitudinally stretching on the substrate. Section 2.4 explores a slot-horn composite antenna.

Chapter 3 demonstrates two types of SIW composite antennas relative to unidirectional dielectric radiators (UDR) with simulations and experiments. These UDR antennas are fed by an SIW on very thin feeding substrates of $0.05\lambda_0$, and could be fabricated with mingled multilayer PCB technology. Section 3.1 explores and investigates a UDR-SIW VP antenna fed by slots on a shorting SIW. The UDR-SIW has an end-fire pattern along the SIW, and a polarization normal to the broad walls of the SIW. These features of the UDR-SIW will certainly benefit its applications to planar high gain end-fire antennas. Section 3.2 explores and investigates a fully planar high gain UDR-ALTSA end-fire CP antenna. The UDR-ALTSA uses a UDR to enhance the VP gain, and the UDR is placed normal to the substrate of the ALTSA and the SIW. Accordingly, the UDR-ALTSA is actually a heterogeneous linear array stretching along the direction normal to the substrate.

Chapter 4 concentrates on the characteristic parameters and calculation methods related to periodic structures such as SIWs. First in Section 4.1 and Section 4.2, the propagation and impedance characteristics of SIW are introduced. The periodic characteristics of SIW lead to the differences between SIW and the uniform transmission. Then, Section 4.3 demonstrates that wave impedances in an SIW is not uniform. Section 4.4 proposes comprehensive closed-form formulas of characteristic parameters in a periodic structure (FPPS), and examines its performances in diverse structures. The FPPS has been used not only to explore the reflection characteristics inside a periodic structure, but also to verify the mechanism of the UDR-SIW antenna.

Chapter 5 examines the radiations produced by diverse slots, addressing that a slow wave could produce radiation, in both non-periodic and periodic structures. In the thesis, diverse slots have been used to enhance VP radiation, or modify radiation patterns. Section 5.1 examines the radiation characteristics of a slot on the wide side of an SIW, addressing that the radiation is produced by a slow wave. Section 5.2 examines the radiation characteristics of two slots on the wide side of a width-uniform and a width-tapered SIW, addressing radiation from a slow wave. Section 5.3 clarifies that the radiation pattern of a PLWA can be interpreted well with its fundamental mode even if the mode is a slow wave, and demonstrate that the interpretation does not contradict physical and mathematical rules.

The contents and the correlation among them in the thesis is shown in Figure 1.16.

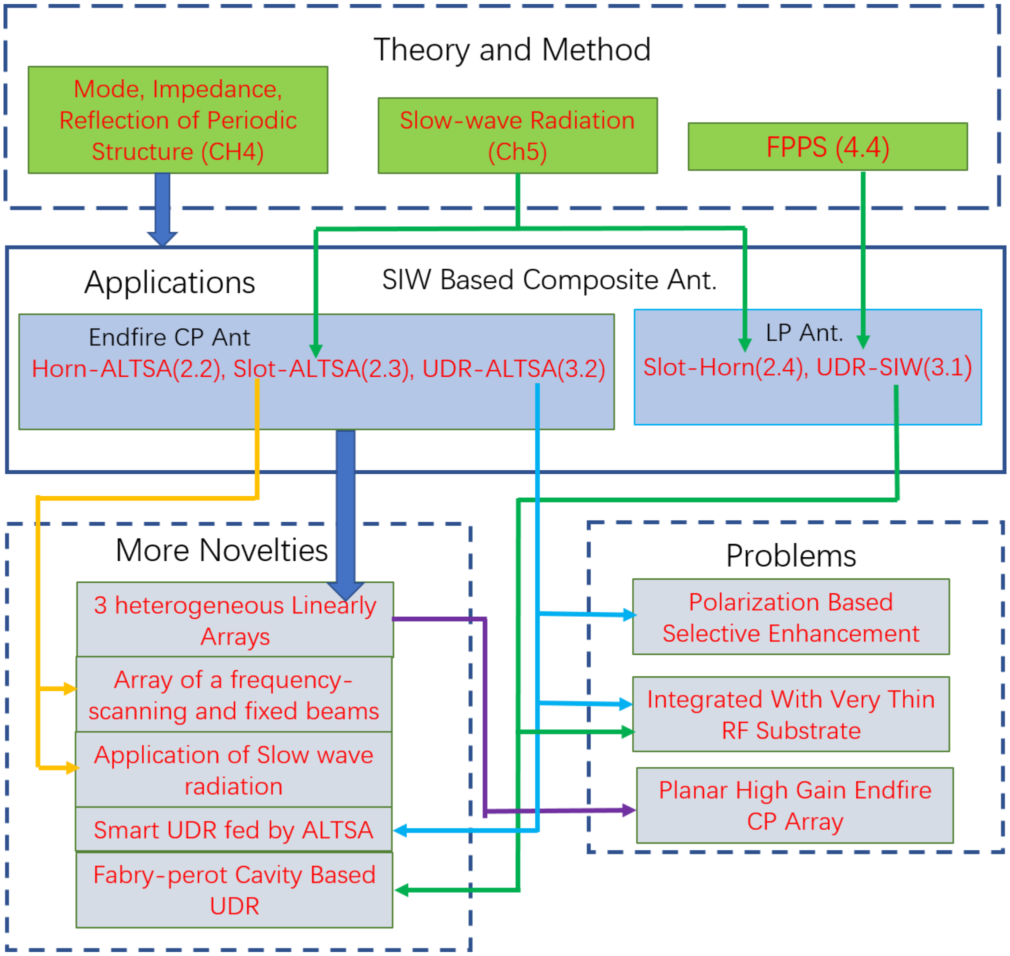

Figure 1.16: Contents and their correlation

CHAPTER 2 PLANAR SINGLE-LAYER SUBSTRATE SIW-BASED END-FIRE CP COMPOSITE ANTENNAS

A high gain VP radiator is crucial to a high gain end-fire CP antenna. Dipole-like antennas are used as HP radiators in a low gain CP antenna [30]-[32][53]-[57][103], and the gains of the HP radiators are relatively low, about 2 dB. The gains of VP radiators are also low, and the open aperture of an SIW horn is available to such low gain. To achieve a high gain CP antenna, a high gain HP radiator, such as ALTSA, is usually used. Consequently, the high gain fully planar end-fire VP radiator is highly desired.

Among SIW-based end-fire CP planar composite antenna, the open aperture or horn of an SIW is usually used as a VP radiator. To be a high gain, the SIW usually uses a thick substrate. A thick SIW is not always available due to high cost, low efficiency, or high-order mode. Is there any other way to enhance gain of a VP radiator?

Using an array of multiple VP radiators would be an effective way to enhance VP gain in a high gain CP planar antenna. The multiple VP radiators could be the same or different types. This Chapter will use two types of VP radiator array on single-layer substrates. The first is a homogeneous array of SIW horns, and the second is a heterogeneous array of SIW horn and slots etched on the broad walls of the SIW.

The radiation characteristics of an SIW horn and a ALTSA are crucial to the implemental of the composite antennas in this thesis, and will be examined briefly in Section 2.1, Section 2.2 proposes and demonstrates an SIW horn-ALTSA end-fire CP composite antenna, which has a multiple sub-horn VP radiator array and a feeding network embedded the SIW horn. The antenna is actually a homogeneous linear array transversely stretching on the substrate. Section 2.3 proposes and demonstrates a slot-ALTSA end-fire CP composite antenna. The antenna uses a slot array etched on the broad walls of the SIW to form an extra VP radiator to enhance VP gain, which is actually a heterogeneous linear array longitudinally stretching on the substrate. The heterogeneous array achieves an end-fire beam synthesis of a scanning beam and an end-fire beam. Moreover, the slot-ALTSA composite antenna can still work when it is fed with a slow wave mode, which was regarded as impossible.

The radiation of a slot array on the broad walls could be also synthesized with the radiation of a horn to generate diverse radiation patterns. Section 2.4 proposes and investigates a single-layer substrate slotted SIW horn, namely slot-horn composite antenna, consisting of an SIW horn and a slot array etched on the broad walls of the SIW. The slot-horn composite antenna could exhibit an omnidirectional pattern and a filtering response simultaneously.

2.1 SIW H-plane Horn and Antipodal Linearly Tapered Slot Antenna Fed by SIW

2.1.1 SIW H-plane Antenna

Horn or open waveguide is one of the oldest wave radiating structures, in not only electromagnetic but also acoustics spectrum. Horn antennas or open waveguides can be used not only as end-fire radiators but also as feeding structures to feed other antennas or array [101]. Horns have different flare angles in the E-field and H-field directions, leading to pyramidal horns, E-plane horns, and the H-plane horns. Among the above three types of horn antenna, H-plane configuration has a low profile structure and is widely used in combination with the planar circuits. An SIW technology [1] offers a promising approach to realize planar H-plane horn antennas by using the PCB process or other fabrication techniques that can provide the possibility of designing and implementing large-scale SICs in planar form [104]-[105]. The most common and well-demonstrated SIW antenna solutions for these SICs-related applications are to use H-plane SIW horns [24]-[28], [106]-[111].

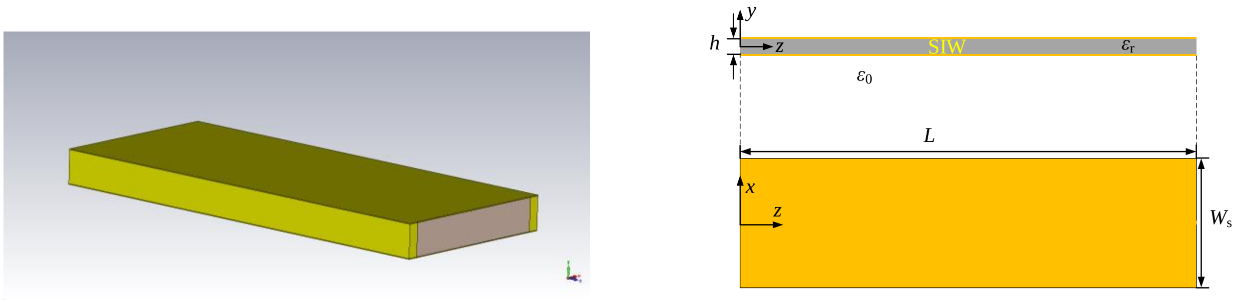

Figure 2.1: Open-end SIW

(h=0.508 mm, L=22 mm, W_s=6 mm, ε_r=2.2)

An open-end SIW open aperture, as shown Figure 2.1, has a radiation pattern similar to an SIW horn, and its radiation performance is crucial to end-fire CP composite antennas. In a composite antenna, when an SIW is used to feed radiators, and its open aperture would also produce a VP radiation. The VP radiation performances and impedance bandwidth of both the SIW horns and open-end SIW is highly related to the thickness of the substrate. When a parameter changes during following simulations, the other parameters will keep the same as in the caption of Figure 2.1.

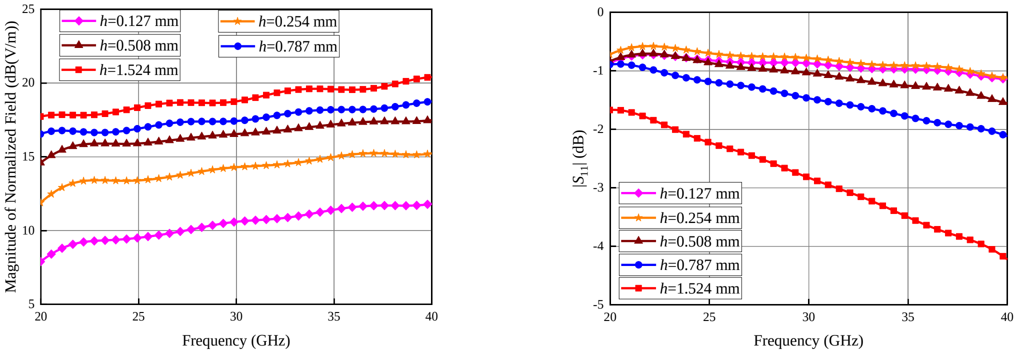

(a)

(b)

Figure 2.2: (a) Normalized VP radiation and (b) reflection coefficient of open-end SIW

Figure 2.2 (a) is the simulated normalized VP radiation of an open-end SIW at a monitoring point with different thicknesses. The monitoring point in the far zone is 200 mm away from the SIW. To remove reflection effect, the VP electric field is normalized by a factor of $(1-|S_{11}|^2)$. Figure 2.2 (a) shows that the thinner the substrate is, the weaker the VP radiation of the open-end SIW is. Moreover, the degrading rate becomes fast when the substrate becomes thinner.

Weak radiation means a small radiating resistor and a high factor of quality, and it will lead to a poor matching. Figure 2.2 (b) is the simulated reflection coefficients of an open-end SIW. As the substrate becomes thinner, the reflection becomes larger.

Consequently, when SIW horn or open-end SIW is used as a VP radiator in an end-fire CP composite antenna, it is much more difficult to design a high gain CP antenna with thin substrates.

Figure 2.3 is the reflection coefficients of open-end SIWs with different dielectrics, and it shows that the larger the permittivity of the filled dielectric is, the strong the reflection of the SIW is. When the permittivity is very large, the open-end SIW actually acts as a resonator with a high Q.

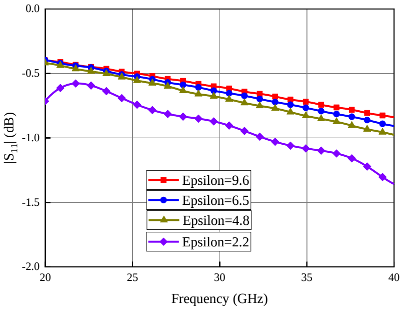

Figure 2.3: Reflection of open-end SIW with different dielectrics

2.1.2 Antipodal Linearly Tapered Slot Antenna

An ALTSA, evolving from a tapered slot antenna (TSA), is often used as a HP radiator in a high gain end-fire CP composite antenna.

A TSA is well known for the features of planar structure, low weight, easy to fabricate, broadband, and suitable for microwave integrated circuits. Different tapered profiles, such as the initially proposed exponential [112] and linear [113]-[115] profiles combined with the subsequently emerged Fermi [103], hyperbolic [116], elliptic [117], and Gaussian [118] profiles, have been utilized to design TSAs. Among these tapered profiles, due to the simplicity along with attractive features such as narrow beam width, wide bandwidth and small element space in antenna arrays [113]-[114][119]-[121], the linearly tapered slot antenna (LTSA) has been applied widely.

Because of the high impedance of a slotline, the TSAs suffer from a mismatching problem and operating bandwidth is degraded due to the feeding structure. Therefore, antipodal linearly tapered slot antenna (ALTSA) is proposed with an improved bandwidth [113], and an ALTSA fed by SIW is developed [114]. Compared with other feeding technologies, SIW-based feeding structure is able to avoid the radiation from the feedline [114]. The ALTSA, however, is much wider than the SIW in previous ALTSA fed by SIW [114], and its structure is not suit for certain application, such as the following horn-ALTSA and slot-ALTSA composite antennas.

Figure 2.4 shows the configuration of an ALTSA with metallic side walls, which is fed by an SIW. The ALTSA consists of two linearly flaring conductor claddings on opposite sides of a dielectric substrate. The open aperture of the flaring SIW is as wide as the ALTSA. For a HP radiated field, a linear tapered section is utilized to vary the polarization of the electric field as well as the radiator.

Different from the conventional ALTSA, two metalized side walls are also implemented at two side surfaces of the flaring wings in the radiation section.

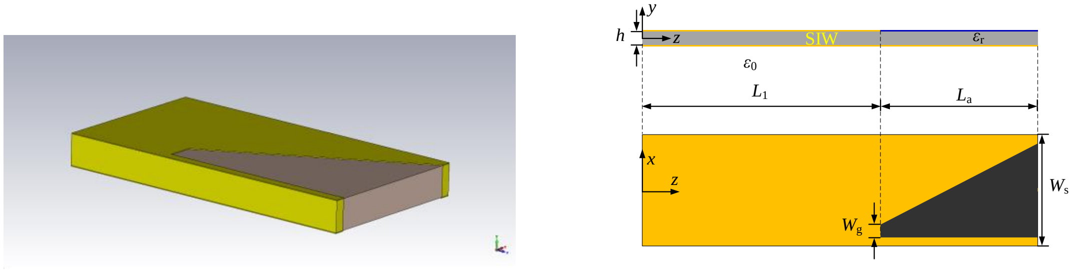

Figure 2.4: Structure of ALTSA
(L1=5.72 mm, La=10.1 mm, WS=7.4 mm, Wg=1.3 mm, h=0.508 mm, εr=2.2)

Since there are not explicit formulas of radiation pattern and gain for an ALTSA, a full wave simulation software would be adopted to investigate the performance of an ALTSA. The simulation tool is CST Microwave Studio 2015. When a parameter changes, the other parameters will keep the same as in the caption of Figure 2.4.

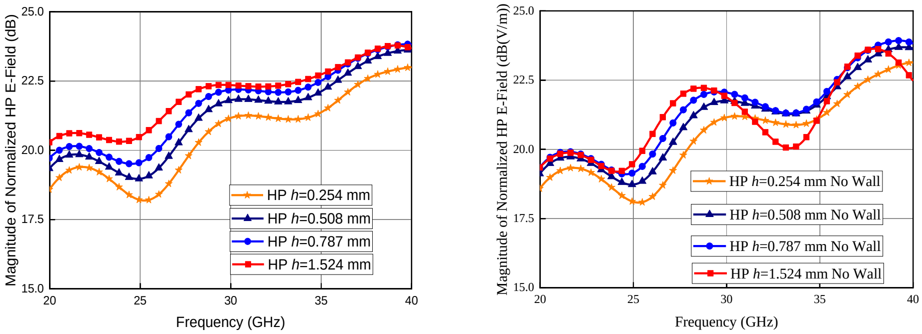

(a) (b)

Figure 2.5: Normalized HP radiation of ALTSA

(a) with metalized side walls and (b) without metalized side walls

Figure 2.5 is the normalized HP radiation of an ALTSA fed by an SIW at the monitoring point with different thicknesses. The SIW is the same as that in Section 2.1.1. Figure 2.5 shows that the HP radiation of the ALTSA is strong, and much stronger than VP radiation in Figure 2.2 (a). The HP radiation differences among ALTSAs with different thick substrates are also smaller than that of the open-end SIWs. It means that the thickness is not crucial to HP radiation of an ALTSA. Figure

2.5 also shows that the HP radiation of an ALTSA with metalized side walls is smoother than without metalized side walls. Therefore, one would prefer to an ALTSA with metalized side walls for a wide bandwidth.

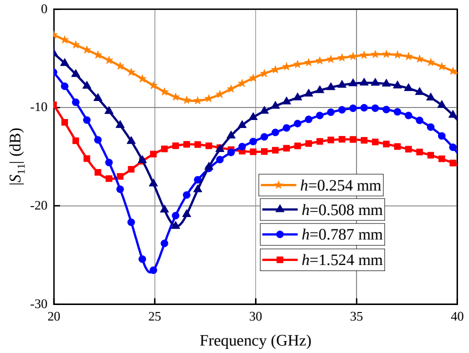

Figure 2.6: Reflection of ALTSA

Because of a strong HP radiation, An ALTSA fed by an SIW is easy to match even using thin substrates, and has a wide impedance bandwidth, as shown in Figure 2.6.

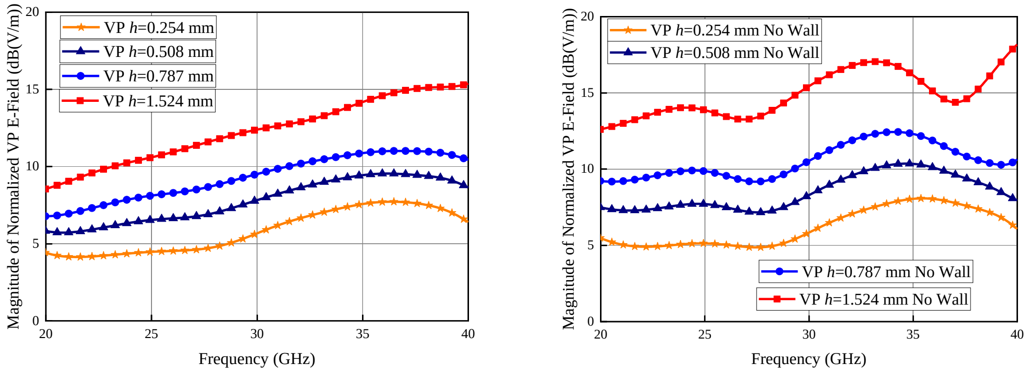

(a) (b)

Figure 2.7: Normalize VP radiation of ALTSA

(a) with metalized side walls and (b) without metalized side walls

Because of both the open aperture of the feeding SIW and the two flaring wing plate on the two opposite surfaces of a substrate, an ALTSA will also produces both HP and VP radiations simultaneously. Figure 2.7 is the normalized VP radiation of an ALTSA at the monitoring point, and it shows that the VP radiation of an ALTSA is smaller by about 8 dB than that of its associated SIW, as shown in Figure 2.2 (a). Therefore, an ALTSA would weaken the original VP radiation of its feeding SIW. The weakening degree will decrease when the substrate becomes thick. Figure 2.7 also shows that the VP radiation of an ALTSA with metalized side walls is smoother than without metalized side walls.

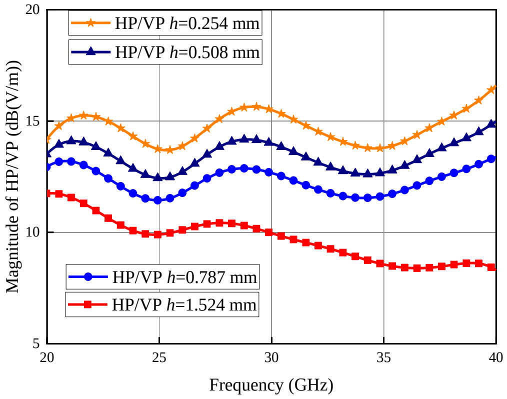

Figure 2.8: Magnitude ratio of HP to VP radiations vs frequency

A single ALTSA fed by an SIW would not be a CP antenna unless it uses a very thick substrate. Although an ALTSA will produces both HP and VP radiations, its VP radiation is usually smaller than HP. Figure 2.8 shows that the ratio of HP to VP radiation is over 10 dB. On the other hand, an ALTSA could have a high gain, compact size, wide bandwidth, and be fed by an SIW easily. Consequently, an ALTSA is usually used as a HP radiator in a high gain end-fire CP antenna, but an enhanced VP radiation is still crucial to a CP radiation.

The main parameters affecting the performances of an ALTSA are the open width of the ALTSA, the length and staring width of its two wings. The open width of the ALTSA is actually the width of the feeding SIW. The open of ALTSA should be at least half a wavelength to ensure a sufficient radiation, and it usually is determined based on operating band. Usually the wing length should be larger than two wavelengths to ensure a good unidirectional radiation, and the starting width should be a little wider than half a width of the open aperture of the SIW to ensure a good matching. To investigate how the shape and size of the two wings affect the directivity of an ALTSA, we simulate the directivity with different open widths and lengths of two wings

To providing a general impression of the radiation characteristics, the 3D radiation pattern of an ALTSA at 28 GHz is also presented, and is showing in Figure 2.9.

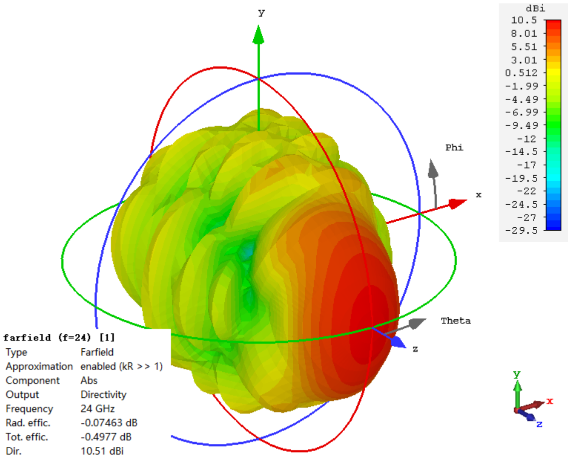

farfield (f=24) [1]

Type	Farfield
Approximation	enabled (kR >> 1)
Component	Abs
Output	Directivity
Frequency	24 GHz
Rad. effic.	-0.07463 dB
Tot. effic.	-0.4977 dB
Dir.	10.51 dBi

(a) With the side wall

Figure 2.9: 3D radiation pattern of an ALTSA at 28 GHz

The structure, gain, and radiation pattern of the ALTSA are all proper for being used as a radiator of the ALTSA-horn CP composite antenna.

2.2 Single-Layered SIW-based End-fire CP Horn-ALTSA Composite Antenna

2.2.1 Mechanism of CP Radiation

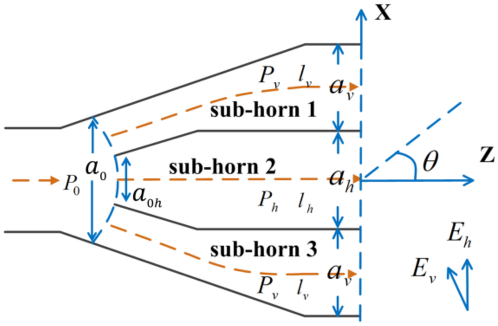

Figure 2.10: Schematic view of the proposed CP SIW horn antenna

The SIW horn-ALTSA end-fire CP planar composite antenna uses a single-layered substrate, and is composed of an SIW horn and a number of modified ALTSA units connected to it. The SIW horn is divided into several sub horn units, as shown in Figure 2.10, with arrays of metallic vias inside the horn. Two of these sub horns radiate VP waves while the polarization of the other sub horn is horizontal. The amplitude and phase of the VP and HP waves can be controlled by the metallic via arrays so that a CP wave is generated.

A schematic view of the proposed SIW horn-ALTSA composite CP antenna to explain its mechanism is depicted in Figure 2.10. Metallic walls/vias in the substrate are used to form a microstrip-fed SIW horn antenna. At the same time, these metallic walls divide the horn into three sub-horns. The sub-horn in the middle of the main horn feeds an ALTSA that radiates HP waves while the other two sub-horns exhibit a VP radiation. The final radiated wave is in fact a sum or superposition of three different waves from the three sub-horns that effectively involves both HP and VP radiation. This is in fact a geometrical wave synthesis through a number of wavelets in space.

The only mode that exists in the aforementioned sub-horns is the quasi-TE_{m0} mode with a propagation constant that depends mainly on the width of the sub-horn. Accordingly, it is possible to design the propagation constants of sub-horns by choosing a proper position of the metallic walls/vias placed inside the SIW horn. The flexible technique was introduced in [28] to control the phase distribution on the aperture of the horn, so that to improve the design of the horn feed and also enhance the gain. The technique is also used in the design of the CP SIW horn antenna, to feed two orthogonally polarized radiating elements with a quadrature phase. In addition, the position of metallic walls/vias inside the horn is related to the power ratio of the central to lateral sub-horns. The wider the mouth of a sub-horn is, the higher power it receives and radiates. In general, the amplitude and phase of the vertical and horizontal waves can be controlled by these metallic walls so that a CP wave generation is expected.

When the main horn is fed, the corresponding electromagnetic wave will be divided into three parts and each part goes into one of the three sub-horns. The central sub-horn 2 has HP radiation whereas the lateral sub-horns 1 and 3 are seen with VP radiation. In fact, two VP sub horns forms a two-horn array to enhance the gain of VP radiation, and the metallic via arrays can adjust the power ratio of VP radiated to HP radiated. Therefore, EIRP of VP could be reasonable for a CP radiation even if the substrate is relatively thin. It is important to mention that this work also provides a solution to an end-fire CP SIW antenna array in a substrate with multiple elements.

One can devise a relationship between the input power of the sub-horn 2 and the other sub-horns 1 and 3. For a dominant mode TE_{10}, the receiving power P_0 of an SIW is expressed as

$$P_0 = \frac{E_0^2 h a_0}{4Z} \tag{2.1}$$

where h and a_0 are the height and width of the SIW at the begin of horn, E_0 is the maximum value of electric field, and Z is the wave impedance which is defined in (4.30). When the SIW is divided into the central sub-horn 2 and two symmetrical lateral sub-horns 1 and 3, the input power P_h of the central sub-horn 2 is as follow

$$P_h = \frac{E_0^2 h a_0}{4Z\pi}[\frac{\pi a_{0h}}{a_0} + \sin\frac{\pi a_{0h}}{a_0}] \tag{2.2}$$

where a_{0h} is the entrance width of the central sub-horn 2. The input power P_v of the lateral sub-horn 1 is

$$P_v = \frac{P_0 - P_h}{2} \tag{2.3}$$

and from (2.1) and (2.2), one has

$$P_v = \frac{E_0^2 h a_0}{4Z\pi}[\frac{\pi}{2a_0}(a_0 - a_{0h}) - \frac{1}{2}\sin\frac{\pi a_{0h}}{a_0}] \tag{2.4}$$

Let S_h to be the density of power flux for the HP radiated wave in the far-field zone from the sub-horn 2, and S_h is expressed as follow

$$S_h = \frac{P_h G_h}{4\pi r^2} f_h(\theta) \tag{2.5}$$

where G_h is the power gain of the horizontally radiating antenna, $f_h(\theta)$ is the normalized directivity of the antenna, and θ is spatial angle. The sub-horn 1 and 3 radiate VP wave and can be simply regarded as a two-element antenna array. Let S_v to be the density of power flux for the VP radiated wave in the far-field zone, and S_v is deduced as follows [101]

$$S_v = \frac{2P_v G_v}{4\pi r^2} 2\cos^2(0.5k(a_h + a_v)\sin\theta) f_v(\theta) \tag{2.6}$$

where G_v is the power gain of the sub-horn 1 antenna, $f_v(\theta)$ is the normalized directivity of the antenna element, k is wave number in free space, ah is the aperture width of the sub-horn 2, and a_v is the aperture width of the lateral sub-horn 1 and 3.

Because both the central and the lateral sub-horns reach the maximum radiation in end-fire direction, both the $f_h(\theta)$ and the $f_v(\theta)$ are 1 when $\theta = 0$. To achieve a CP wave, S_h and S_v should be the same when $\theta = 0$, and it gives

$$P_h G_h = 4 P_v G_v \tag{2.7}$$,

Combining (2.2) and (2.4) into (2.7), we obtain

$$[\frac{\pi a_{0h}}{a_0} + \sin\frac{\pi a_{0h}}{a_0}]G_h = 2[\pi(1-\frac{a_{0h}}{a_0}) - \sin\frac{\pi a_{0h}}{a_0}]G_v \tag{2.8}$$

Equation（2.8）shows a constraint among the gains and the entrance width of the central sub-horn 2. When the gain of the VP radiating element becomes higher, the entrance width must be narrower, namely the power into sub-horn 2 must decreases. Therefore, we can adjust the entrance width to achieve a better AR.

In order to achieve a CP wave over a wide range of spatial angle θ, S_h and S_v should be kept as same as possible for different θ value in a main lobe. Accordingly, an objective function is defined for the design of the CP horn antenna, which is $Min|S_h\text{-}S_v|$. From equations (2.5) to (2.7), the objective function can be expressed as

$$Min\left| f_h(\theta) - \cos^2(0.5k(a_h + a_v)\sin\theta)\, f_v(\theta) \right| \tag{2.9}$$

The above objective function concerns the span of the spatial angles on both XZ and YZ planes. Both sub-horns 1 and 3 have wider beams on the YZ plane compared to the XZ plane, and they effectively form a two-element array to narrow the beam on the XZ plane. The phase centers of the central sub-horn and the array of two sub-horns have the same x-coordinate, which would bring benefit to a wide AR beamwidth.

In addition to the equality for the amplitude of the VP and VP components, a phase difference of 90-degree should be considered and achieved over the operating frequency range. The difference of phase delay along the length of sub-horns 1 and 2 can be written as follows

$$\varphi = \beta_v l_v - \beta_h l_h \tag{2.10}$$

where l_v and l_h are the lengths that the wave travels through along the sub-horns 1 and 2 with the propagation constants of β_v and β_h respectively. For a CP wave, the phase difference between the VP and HP components should be 90°, and it means

$$\beta_v l_v - \beta_h l_h = n\pi \pm \frac{\pi}{2} \tag{2.11}$$

On the other hand, for a wide AR bandwidth, the variation speed of the phase difference should keep as small as possible while the operating frequency changes. Since there are expressions

$$\beta_v = \frac{2\pi}{\lambda}\sqrt{1-\left(\frac{\lambda}{2a_v}\right)^2} \tag{2.12}$$

and

$$\beta_h = \frac{2\pi}{\lambda}\sqrt{1-\left(\frac{\lambda}{2a_h}\right)^2} \tag{2.13}$$

One can formulate

$$\frac{d\varphi}{d\lambda} = -\frac{2\pi}{\lambda^2} l_v \sqrt{1-\left(\frac{\lambda}{2a_v}\right)^2} - \frac{2\pi}{\lambda} l_v \frac{1}{\sqrt{1-\left(\frac{\lambda}{2a_v}\right)^2}} \frac{\lambda}{4a_v^2} + \frac{2\pi}{\lambda^2} l_h \sqrt{1-\left(\frac{\lambda}{2a_h}\right)^2} + \frac{2\pi}{\lambda} l_h \frac{1}{\sqrt{1-\left(\frac{\lambda}{2a_h}\right)^2}} \frac{\lambda}{4a_h^2} \tag{2.14}$$

From (2.11) and (2.14), we can write

$$\lambda \frac{d\varphi}{d\lambda} = \left(n \pm \frac{1}{2}\right)\pi + \frac{\pi}{2}\left(\frac{l_v \lambda_{gv}}{a_v^2} - \frac{l_h \lambda_{gh}}{a_h^2}\right) \tag{2.15}$$

Because the widths of these sub-horns are non-uniform, in equation (2.15) λ_{gv} and λ_{gh} should be the average guided wavelength, and a_h and a_v should be the average aperture width in the sub-horns 1 and 2 respectively. In practice, the second term on the right side of equation (2.15) is smaller than the first term if n is large. Therefore, it can be deduced that n should be as small as possible in order to keep the variation speed of the phase difference slow enough and also preserve the 90-degree phase difference to meet the requirement of CP radiation. When n=0, (2.15) changes into

$$\lambda \frac{d\varphi}{d\lambda} = \pm\frac{1}{2}\pi + \frac{\pi}{2}\left(\frac{l_v \lambda_{gv}}{a_v^2} - \frac{l_h \lambda_{gh}}{a_h^2}\right) \tag{2.16}$$

The parameters, l_v , l_h λ_{gv} and λ_{gh} , are all relative to the positions of the metallic via arrays in the horn, so that the positions of metallic walls/via arrays are crucial to the performances of CP radiation.

2.2.2 Design Rules

Because there are not explicit formulas of G_h and $f_h(\theta)$ for an ALTSA, it is difficult to conclude a set of closed-form, approximate formulas that can be used to directly determine all the physical parameters of the antenna as explained in [114]. However, based on equations (2.8), (2.9) and (2.15), one can design the CP SIW horn antenna using commercial fully-wave simulation software packages, such as CST or HFSS, in a step-by-step guide as follows:

(1) SIW horn antenna. The SIW horn antenna consists of four sections: the feed section, the input section, the flaring section and finally the output section. The feed section usually is a short microstrip line connected with a connector, such as SMA. If the feed structure is a probe fed vertically into the SIW from its broad wall, the non-planar feed section could be merged with the input section.

The input section is an SIW straight structure, and its width should be large enough to support the transmission of a single TE_{10} mode. The open aperture width of the horn antenna should be large enough to accommodate several sub-horns, and the aperture width of each sub-horn should larger than 0.5λ. The metallic walls or via arrays that help to form the sub-horns are stretched from the flaring section to the output section.

As already mentioned, a 90^o phase difference between the lateral and central sub-horns is required for a CP radiation. The metallic walls or via arrays can be used to tune the phase difference based on both the aperture efficiency and the requirement of CP radiation. The output section is used to keep transmission wave in-phase at the output aperture of sub-horn and also to accommodate an ALTSA.

(2) Number of sub-horns and layout. The proposed solution to SIW CP antennas is in fact an array solution, and each sub-horn is an element antenna of the array. If a higher gain is desired, the element number should be large. In the array, there are two different sorts of elements/sub-horns encountered in our design: The ones that have VP radiations and the other with HP radiations. In order to radiate a CP wave, the phase centers of these two should be concerned. To achieve this, the total element number should be odd and the sub-horns for vertical and horizontal waves should be placed alternately. Thus, the difference between the element numbers of the sub-horns for vertical and horizontal waves should be one.

The proposed antenna has three sub-horns: one is the central sub-horn responsible for the HP radiation and two lateral sub-horns for the VP radiation. Their radiation patterns should be as same as possible, especially in their main lobes.

(3) Position of Metallic Walls or Via Arrays. . he metallic walls or via arrays inside the main horn correspond to the shape of the sub-horns, and also they are related to the phase and amplitude of the horizontal and vertical wave components. The exact shape and position of these walls should be determined to keep the radiation pattern of the central and lateral sub-horns as similar as possible. This can be done by using a commercial or a customized software package. In this work, CST Microwave Studio optimization tool based on the equations (2.8), (2.9) and (2.15) is deployed to conduct this task.

When the aperture widths of both central and lateral sub-horns are initially defined, designers can calculate the gains and radiation patterns of the two sub-horns by CST independently, and then calculate the objective function at certain spatial angles in the range of main lobe based on formula (2.9). In this way, designers can tune or optimize the widths of the two sub-horns to achieve a wide CP beamwidth. After the widths and gains of the two sub-horns have been determined, designers can use equation (2.8) to calculate the ratio of a0h and a0.

(4) Polarization Rotation Direction. The sense of the circular polarization can be changed by exchanging the positions where the two flaring wines of the linearly tapered slot are connected to the central sub horn.

2.2.3 Prototype and Measurement

To verify the design rules and simulated results, a prototype of the SIW end-fire CP horn-ALTSA has been fabricated as shown in Figure 2.11. This antenna is fabricated by using a low-cost standard PCB technology on a single-layer substrate with a thickness of $0.122\lambda_0$ at the center frequency for 24 GHz applications. The presented structure is comprised of two SIW sub-horn antennas and an ALTSA fed by a center sub-horn, with a fully integrated phase control and power divider structure inside the whole horn antenna.

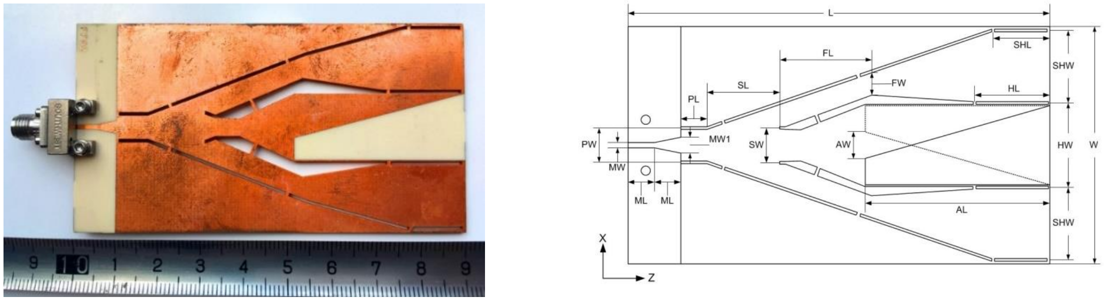

(a) (b)

Figure 2.11: (a) Fabricated prototype of horn-ALTSA and (b) structure diagram

(L=93, W=50, ML=5, PL=7.4, SL=14.8, FL=22.8, AL=40.6, HL=19, SHL=13.8, MW=1, MW1=3, PW=6.4, SW=6, AW=5, FW=5.4, HW=17, SHW=15.4 unit: mm.)

The reflection coefficient of the antenna is measured through an Agilent N5247A Network Analyzer using a 2.92mm type end-launch connector and the experimental results are plotted in Figure 2.12. According to the results, there is a good matching over the frequency range from 23.7GHz to 24.9 GHz with a bandwidth for which the AR is below 3dB and VSWR is below 2.

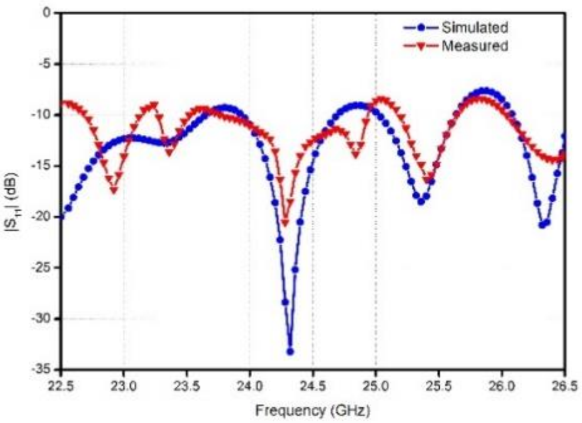

Figure 2.12: Simulated and measured reflection coefficients of the prototyped antenna over the frequency range of interest

To better investigate the phase and polarization characteristics of the sub-horns, the wave propagation in the antenna at different frequencies are simulated. Figure 2.13 depicts the wave propagation in the whole structure at 24.5GHz.

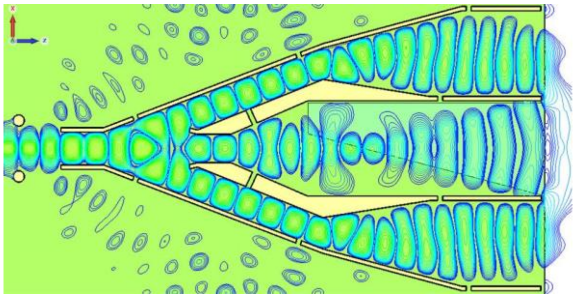

Figure 2.13: Wave propagation in the antenna structure

According to this figure, we can only see the dominant TE_{10} mode in the input section. Within each sub-horn, there is only the dominant mode that is necessary to radiate efficiently. As shown in Figure 2.13, there are sixteen and a half ellipses in the lateral sub-horns and fifteen ellipses in the central sub-horn. Each ellipse in Figure 2.13 stands for half a wavelength, or in other words a 180^o phase shift. Therefore, it can be concluded that the VP and HP components from the sub-horns 1 and 2 are in quadrature phase, which coincides with equation (2.11) and parameter n in the proposed antenna is one. Figure 2.13 also shows the energy leakage in the feed section that would affect the antenna gain in an undesired way. The reason for this loss is that there should be a number of slots between the metal walls to keep the whole structure mechanically connected and robust.

The antenna gain is determined by using a comparative method that involves measuring the signals received from the reference antenna and the antenna under test, and then calculating the relative difference. The loss of the 2.92 mm end-launch connector is extracted from the connector datasheet and it is included in the measured reflection coefficient. This loss was also taken into account in the gain measurement. The antenna gain versus frequency is plotted in Figure 2.14.

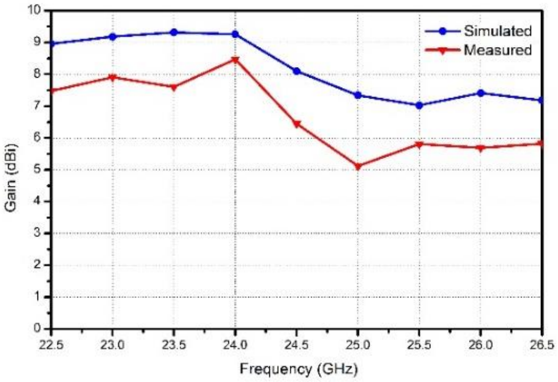

Figure 2.14: Simulated and measured gains of the antenna

As seen in Figure 2.14, the antenna simulated gain is almost flat and around 9 dBi up to 24 GHz. However, due to the input matching issues and energy leakage, it decreases to 7.5 dBi at 25 GHz. The discrepancies between the measurement and simulation can be easily attributed to our fabrication inaccuracies and tolerances.

The prototype antenna radiates LHCP wave, its measured and simulated normalized radiation patterns at 24.5GHz in both YZ and XZ planes are plotted in Figure 2.15.

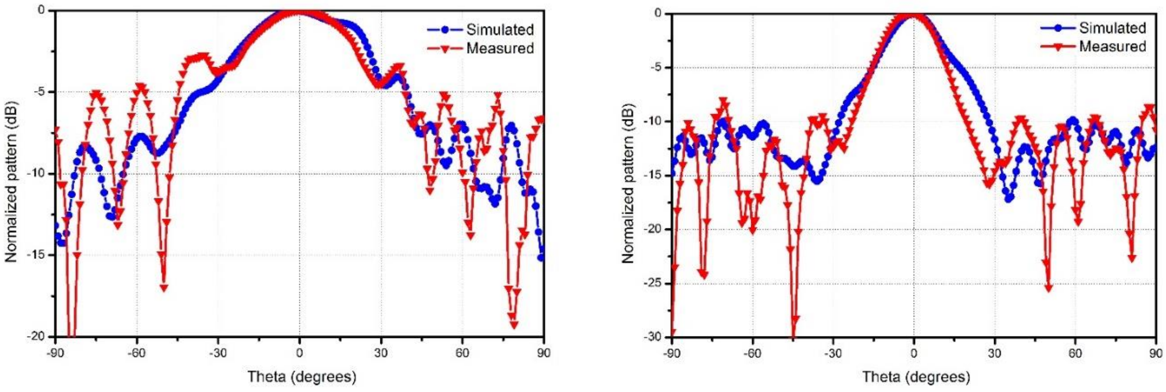

(a) (b)

Figure 2.15: Normalized simulated and measured radiation patterns at 24.5GHz

(a) *y*-*z* plane. (b) *x*-*z* plane

It is difficult to measure a radiation pattern of cross-polarization for the prototype antenna in our laboratory. However, the cross-polarization of a CP antenna can be evaluated by using co-polarization and axial AR as explained in reference [122]. The method is based on the formula (2.17) as follow,

$$AR = 20\log_{10}\left(\frac{1-e}{1+e}\right) \tag{2.17}$$

where $e = 10^{-P(dB)/20}$ and $P(dB)$ is the ratio of cross-polarization power.

The antenna AR versus frequency, pitch angle and azimuth angle are plotted in Figure 2.16.

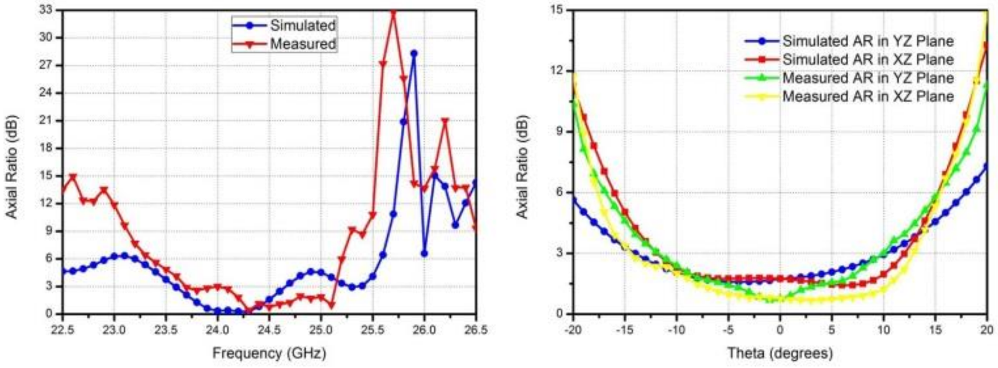

(a) (b)

Figure 2.16: Simulated and measured AR of the antenna

(a) vs frequency and (b) vs pitch and azimuth angles

According to the results in Figure 2.16, the measured AR of the proposed antenna is under 3 dB between -10° to 10° in both pitch and azimuth angles, it also reveals the cross-polarization pattern is quite small in the same spatial angles. The proposed antenna shows a good circular polarization in the frequency range of 23.7 GHz to 25.15 GHz. Comparing this result to the results of Figure 2.12, one can observe that over the same frequency range the reflection coefficient is almost below -10 dB and therefore the antenna is well matched.

2.3 Single-Layered End-fire CP Slot-ALTSA fed by Slotted Width-tapered SIW

In Section 2.2 the horn-ALTSA uses same type of multiple sub-horns to compose a homogeneous VP array to match the gain of the ALTSA, and achieves a fully planar high gain end-fire CP antenna.

The sub-horns stretch transversely on the plane of a substrate, so that the area of the substrate is large. On the other hand, the beam width on azimuth plane is much narrower than on pitch plane when the number of sub-horns is large. When a pencil-shape pattern, or a narrower pitch pattern is preferable, VP radiators with a narrower pitch pattern is desired.

The SIW in the previously developed ALTSA schemes usually acts as only a feeder instead of a radiator. In fact, when an SIW feeds an ALTSA, there is certain VP radiation, though relatively small and generally ignored in the analysis. The VP radiation originates from the open aperture of the SIW rather than the ALTSA, whereas it is weakened by the ALTSA. Its source is the transverse electric field in the SIW. On the other hand, the radiation from the ALTSA is HP, and its source is mainly from the longitudinally magnetic field in the SIW. The transverse electric field and the longitudinally magnetic field are phase quadrature, which naturally satisfies the phase condition of CP radiation. When the substrate is thin, the VP radiation is usually much smaller than HP radiation. Therefore, to create a high gain CP antenna, an ALTSA fed by an SIW should have an enhanced VP radiation.

The broad walls of the SIW in such ALTSA structuree, however, are still spare and have not been utilized. Transverse slots on the broad walls of the SIW would able to produce VP radiation. If the radiation from the slots has an end-fire pattern, it can be used to enhance the VP radiation of the ALTSA. The antenna is a kind of CP ALTSA fed by a slotted SIW, and is also called as slot-ALTSA.

In this Section, an innovative single-layered end-fire CP slot-ALTSA composite antenna, consisting of a slotted width-tapered SIW and an ALTSA fed by the slotted SIW is proposed and investigated by simulations and experiments. The width-tapered slotted SIW has also an end-fire radiation pattern which would enhance VP radiation of the slot-ALTSA. Compared to the existing planar SIW antennas, the proposed CP composite antenna has three novel features as follows:

(1) A slotted width-tapered SIW and an ALTSA are integrated into a slot-ALTSA antenna to produce CP radiation. The slots etched on the two broad walls of the slotted SIW act as a slot array radiator, and the open aperture of the slotted SIW serves as both a feeder to excite the ALTSA and a horn to produce the VP radiation. The proposed antenna is in fact an organic combination of a leaky-

wave antenna and an ALTSA. This kind of combination is novel and is supposed to be difficult to design because of a potential frequency-scanning beam of the leaky-wave antenna.

(2) A novel way to enhance VP radiation is introduced. The slot array uses the spare space of a feeding SIW, and form an array, longitudinally stretching, to narrow beam on pitch plane. The slot radiators could have diverse configurations to achieve various radiation patterns.

(3) The novel slotted width-tapered SIW is not a periodic leaky-wave antenna even if the slots have uniform spacing, and there are no space harmonics occurring in the SIW structure. When the operating frequency is high, the driving mode TE10 in the width-tapered SIW would be a slow wave; thus, its radiation must be excited by a slow wave. The slow wave radiation mechanism is not reported on as much, and its application is interesting to explore.

2.3.1 Mechanism of CP Radiation and Design Proceeding

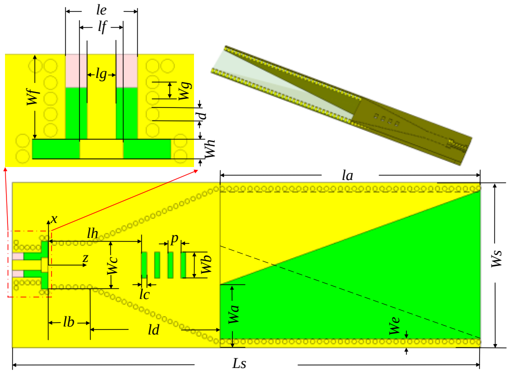

Figure 2.17: Structure of the propose composite antenna

(*Ls*=40.8, *Ws*=14.4, *la*=22.8, *lb*=3.57, *Wa*=4.8, *We*=0.684, *Wd*=0.684, *Lc*=0.46, *Ld*=11.4, *Wb*=2.28, *Wc*=3.5, *p*=1.14, *le*=2.16, *lf*=1.315, *lg*=0.866, *lh=8.13*, *Wg*=0.6, *Wf*=2.5, *d*=0.3. unit: mm)

The proposed composite antenna, as shown in Figure 2.17, use RO4003 substrates with the relative permittivity of 3.55 and loss tangent of 0.0012, and the substrate is 1.524 mm thick. The proposed composite antenna consists of a slotted width-tapered SIW and an ALTSA fed by the SIW. Eight transverse slots are symmetrically etched on the two broad walls of the SIW to form a slotted width-tapered SIW, and act as a slot array to produce an end-fire VP radiation. The open aperture of slotted SIW also produces an end-fire VP radiation and feeds the ALTSA to produce an end-fire HP radiation. When CP radiation is required, the EIRPs of the two orthogonally-polarized radiations should be equal in the far zone, which can be written as follow.

$$P_{sv}G_{sv}+P_{av}G_{av}=P_hG_h \tag{2.18}$$

where P_{sv} and P_{av} are the VP radiated powers from the slot array and the aperture of the SIW respectively, and G_{sv} and G_{av} are their respective gains. The P_h is HP radiated power from the ALTSA, and G_h is its gain. Because the ALTSA are fed by the open aperture of the SIW and the slot array is on the broad walls of the SIW, the slot array and the ALTSA are in a series connection; the slot array is closer to the input port of the composite antenna. The input power is fed first to the slotted array then to the ALTSA, the more power is radiated by the slotted array, the less power is radiated by the ALTSA. In this way, the condition in (2.18) could be satisfied.

With an appropriate design, the orthogonally-polarized radiation can be made with a difference of quadrature phase. Since the whole open aperture of the SIW is used to feed the ALTSA, the phase difference of the VP radiation from the open aperture and the HP radiation from the ALTSA depend on the thickness of the substrate, and on the shape and size of the ALTSA. On the other hand, the phase difference of the radiations from the slot array and ALTSA depends on the distance between the two phase centers of the slot array and the ALTSA

To investigate the phase center, the slots could be treated as a linear array with uniform spacing. When the slot array has an end-fire beam, its phase center is located among the slots, and the phase center, z_{pv}, can be written as

$$z_{pv}=lh+0.5(N-1)p(K-1). \tag{2.19}$$

$$K=\frac{\overline{\beta}_s}{k_0} \tag{2.20}$$

where N is the number of the slots, p is the spacing of the slot array, $\overline{\beta}_s$ is the average phase constant in the slot region of the SIW, and k_0 is the wave number in the free space.

The droving mode in the SWI is TE_{10}. As the SIW has a tapered width, one can deduce its average phase constant in the slot region through

$$\bar{\beta}_s = \frac{1}{(N-1)p}\int_{lh}^{lh+(N-1)p}\left[\frac{2\pi}{\lambda_0}\sqrt{\varepsilon_r - \left(\frac{\lambda_0}{2W(z)}\right)^2}\right]dz \tag{2.21}$$

The average phase constant depends mainly on the width of the SIW in the slot region, the permittivity of the substrate and the operating frequency. Based on the formulas (2.19)-(2.21), when the operating frequency increases and/or the width increases, the average phase constant and K would increase, and the phase center of the slot array would move toward the open aperture of the SIW. As such z_{pv} would increase. One can also use CST to locate the phase centers of the slot array and compare its result to that by formula (2.21). We use parameters list in the caption of Figure 2.17 to calculate the results, which are shown in Figure 2.18.

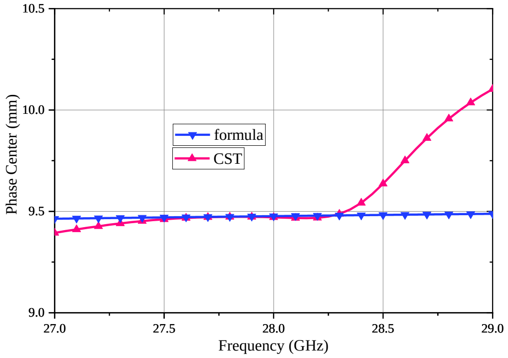

Figure 2.18: Phase centers of the slot array of the SIW vs frequency

Figure 2.18 shows that results obtained by CST and formula (2.19) agree very well with each other from 27.0 GHz to 28.4 GHz. When frequency increases from 28.4 GHz, the results calculated by CST shows that the phase center moves toward the open aperture of the SIW. The deviation between the CST and formula (2.19) beyond 28.4 GHz, however, is still relatively small. This deviation could be explained by the limitations of the formula (2.19) as it is only based on the end-fire radiation pattern of an array and does not take into account the radiation of the slot element. When frequency exceeds 28.4 GHz, the whole radiation pattern is no longer a simple end-fire beam, which would make the results calculated by the CST larger. In any case, the results generated in both suggest that the phase center of the slot array is stable from 27 GHz to 28.5 GHz.

There is no available analytical formula for the phase center of an ALTSA. So, we must use a simulation tool to locate the phase centers and investigate its frequency stability.

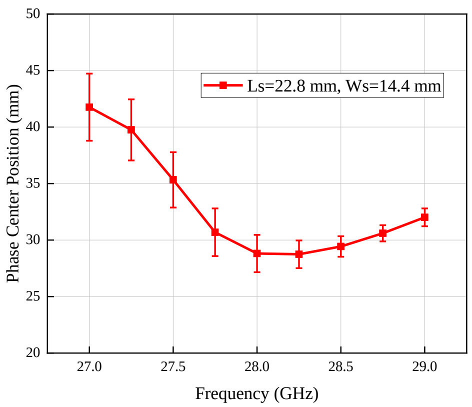

Figure 2.19: Phase centers of ALTSA fed by SIW vs frequency

Based on the parameters list in the caption of Figure 2.17, we use CST to calculate the phase center of the ALTSA fed by the SIW free of any slots on it when operating frequency scans from 27 GHz to 29 GHz. The results are presented in Figure 2.19, which shows that the phase center of the ALTSA is not related to a particular point but to a region even though the frequency is fixed. The span length of the region indicates the magnitude of the uncertainty of the phase center. In this case, this uncertainty can be explained by the open aperture of the SIW in the ALTSA which also produces VP radiation. On the other hand, when frequency increases, the phase center first moves toward its feeding aperture, which is opposite to movement direction of the phase center of the slot array. When the frequency exceeds to around 28 GHz, however, the phase center of the ALTSA becomes relatively stable.

The phase difference between the VP radiation from the slot array and HP radiation of ALTSA is expressed by

$$\varphi \approx (\overline{\beta} - k_0)(z_{ph} - z_{pv}). \tag{2.22}$$

where z_{ph} is the position of the phase center of HP radiation of ALTSA. Therefore, $\overline{\beta}$ is the average phase constant of the width-tapered SIW in the region from the phase center of the slot array to the phase center of HP radiation of ALTSA, which is

$$\overline{\beta} = \frac{1}{z_{ph} - z_{pv}} \int_{z_{pv}}^{z_{ph}} [\frac{2\pi}{\lambda_0} \sqrt{\varepsilon_r - \left(\frac{\lambda_0}{2W(z)}\right)^2}]dz \tag{2.23}$$

When operating frequency increases or the width increases, the $\bar{\beta}$ would increase, and it could compensate the increase of z_{pv} and the decrease of z_{ph} in the same cases. This feature would be useful in the design of a wide bandwidth of the AR in a composite CP antenna.

To create CP radiation, the phase difference, $\Delta\varphi$, between the VP radiation and HP radiation should be

$$\Delta\varphi=\frac{\pi}{2}+n\pi, (n=0,1,2\cdots) \tag{2.24}$$

It can be designed based on formulas (2.19) to (2.23).

We can move the slot array on the broad wall of the SIW to achieve the condition (2.24). To check and validate it, when the slot array moves toward the open aperture of the SIW, we use CST to simulation the phase difference of the two orthogonally polarized radiations at 28 GHz at the point z=200 mm where is in the far zone. We also calculate the z_{pv} and z_{ph} in the same case. These results are plotted in Figure 2.20.

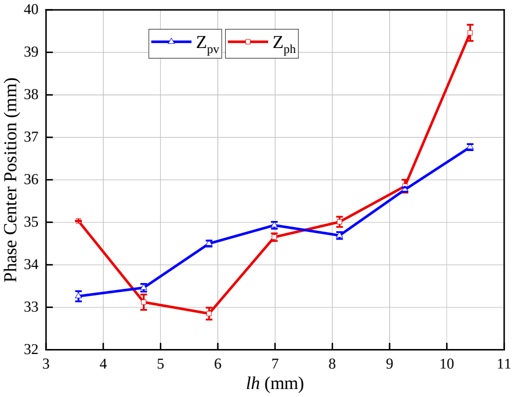

Figure 2.20: Phase centers of the slot array and ALTSA vs the position of the slot array

The results in Figure 2.20 show that the phase center of the slot array move as the slot array moves, which consists with the expectation. As the slot array moves, however, the phase center of the ALTSA changes significantly, which makes the design more complicated.

Based on the structure of the proposed composite antenna and its CP radiation mechanism, a general simulation tool-based design procedure can be summarized as follows:

Step 1: To choose a substrate with a proper thickness. A small permittivity, e.g. $\varepsilon_r = 2.2$, would benefit radiation but is adverse to the transition from a connector to the SIW. The thickness should exceed one tenth of the wavelength in free space because the antenna performance usually degrades when the substrate thickness becomes much smaller than the wavelength. On the other hand, this thickness cannot be increased beyond than a certain limit because the metallization of the vias may be difficult to implement with a larger thickness. A thick substrate would also trigger a large radiation loss over the transition.

Step 2: To design an end-fire transverse slotted width-tapered SIW leaky-wave antenna with the open aperture loaded with a matching port. The slotted width-tapered SIW is closer to input port of the composite antenna than ALTSA. After the radiation by the slot array, the rest of the input power will go through the aperture and be fed into ALTSA to radiate away.

Step 3: To design an ALTSA fed by the width-tapered SIW without slots. The ALTSA should have nearly 100% radiation efficiency.

Step 4: To combine the slotted width-tapered SIW and the ALTAS into a composite antenna. Based on formulas from (2.19) to (2.24), one can determine the distance from the slotted array to the aperture of the SIW to achieve a quadrature phase of the two orthogonally polarized radiations.

Step 5: To optimize structure parameters to achieve a good performance. When the slotted width-tapered SIW and the ALTAS are combined to form a composite antenna, the performances of both the two radiators are certainly different from when the two radiators exist individually. The position of the slot array is also different from that in step 2. Therefore, one must optimize structure parameters, marked in Figure 2.15, with the help of a simulation tool. During the optimization, we would set a field probe in the simulation tool at a point in the far zone in the end-fire direction. We would check the amplitudes and phases of the two orthogonally polarized components of the E-field, and it should have the same amplitudes and a quadrature phase difference. Consequently, the field probe can guide the optimization process.

The orientation of the circular polarization is affected by the phase difference of the two orthogonally polarized radiation, namely by the n in formula (2.24). It can also be altered by exchanging the positions where the two flaring wings of the slot-ALTSA are connected to the slotted width-tapered SIW.

2.3.2 Radiation Pattern of Transverse Slotted Width-tapered SIW

This section will introduce the design of the transverse slotted width-tapered SIW in step 2 in Section 2.3.1 in detail. First, we will determine the array parameters, namely the number and spacing of the slots. Second, we will introduce the equivalent circuit of a transverse slot on the broad wall of a width-tapered SIW, and address the difference from the width-uniform SIW. Finally, we will investigate the effect of the size of the slots on its radiation efficiency of these solts.

The slotted width-tapered SIW is a VP leaky-wave antenna, and it has a frequency-scanning beam. As one of the two orthogonally polarized radiators of a CP composite antenna, the slotted width-tapered SIW is desired to have an end-fire radiation pattern with a wide bandwidth. Since both top and bottom broad walls have the same slots, the radiation pattern of the slotted width-tapered SIW is the superposition of the two beams attributed to the top and the bottom slots. The pattern of the slot on the top wall has a main lobe over the broadside, and its radiation is relatively weak at the end-fire and very weak below the top wall. The top slots act like a linear array with uniform spacing. If the array has an end-fire pattern, the radiation of the top slot array occurs mainly above the top wall, generally exhibiting a frequency-scanning forward main lobe. Similarly, the radiation of the bottom slot array happens mainly below the bottom wall, and also presents a frequency-scanning forward main lobe. Consequently, the total radiation pattern of the slotted width-tapered SIW could have an end-fire main lobe.

Both the top and the bottom slots act like a linearly array with uniform spacing of *p*, and the array pattern is

$$F = \frac{\sin(0.5Nu)}{\sin(0.5u)} \tag{2.25}$$

Where $u = pk_0(K - \cos\theta)$ and θ is the angle with reference to the end-fire direction. The droving mode TE_{10} along the width-tapered SIW is a slow wave because the operating wavelength satisfies the following condition

$$\lambda_0 \le 2W_{\min}\sqrt{\varepsilon_r - 1} \tag{2.26}$$

where $W_{\min}$ is the smallest width. Therefore, $K>1$ holds in this case. The array has a frequency-scanning pattern. To enable the array to exhibit an end-fire pattern over a wide bandwidth, there will be a constraint on the number and spacing of the array slots. When $0.5Nu=\pi$, the array pattern reaches its first null point. Therefore, if $K>1$ and

$$pk_0K < 2\pi / N \tag{2.27}$$

there is only one lobe in whole forward direction of $\theta<0.5\pi$, and the main lobe of the array is at end-fire direction even if the operating frequency changes. It should be noted that the equation (2.27) is a sufficient condition for the end-fire but not a necessary condition. When $pk_0K=2\pi / N$, the backward lobe might not be null or even large, and we should decrease the spacing further in this case. The backward lobe can be null when

$$pk_0(K+1)=2\pi/N \tag{2.28}$$

Once the condition (2.28) is satisfied, the forward end-fire lobe is larger than when $pk_0K=2\pi / N$, so we can use the condition (2.28) to determine the number and the spacing of the slot array. Based on formula (2.21), we have

$$K=\sqrt{\varepsilon_r-\left(\frac{\lambda_0}{2\bar{W}}\right)^2} \approx \sqrt{\varepsilon_r} \tag{2.29}$$

where $\bar{W}$ is the average width of the SIW in the slot region. When (2.29) is substituted into (2.28), one has

$$p \approx \frac{\lambda_0}{(\sqrt{\varepsilon_r}+1)N} \tag{2.30}$$

With the help of formula (2.30), one can expect that a large N or a substrate of high permittivity would lead to a very small spacing of slots, which in turn would degrade the radiation efficiency. For example, when we use the RO4003 substrate with a relative permittivity of 3.55 and set N=4, the spacing of the slots should satisfy the following condition

$$p \approx 0.09\lambda_0 \tag{2.31}$$

Formula (2.28) ensures an end-fire beam and null backward radiation. Nevertheless, it is not a necessary condition for realizing an end-fire beam. The spacing of the slots also has influences on the gain and matching conditions of the slotted width-tapered SIW so we would modify *p* during subsequent simulations.

In this example, we attempt to simulate the radiation patterns of the above-described slot array with different spacing at 28 GHz. The rest of the parameters of the slotted width-tapered SIW are all listed in the Figure 2.17 caption. Figure 2.21 shows the simulated E-plane patterns.

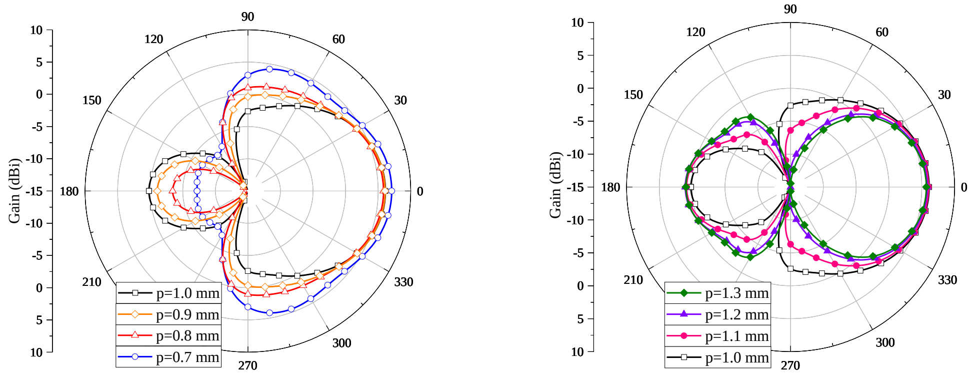

Figure 2.21: E-plane pattern of slot array of width-tapered SWI vs the spacing of the slots

When frequency is set at 28 GHz, λ_0=10.7 mm and *p*=1 mm. The results in Figure 2.19 show that the backward radiation still exists even though condition (2.18) is satisfied. This condition is based on the consideration of an array in which every element has the same radiation pattern and feeding amplitude. The slot array is fed by a traveling wave; the number of the slots in the array is small; and each slot is fed with different amplitude. Moreover， the spacing is much smaller than the wavelength of interest, and the coupling between adjacent slots is so strong that the radiation patterns of every single slot are different from one another. Therefore, the simulated patterns do not agree well with the prediction of the well-conditioned array theory. Nonetheless, the slot array preserves the end-fire patterns when the spacing *p* changes from 0.7 mm to 1.3 mm. This outcome also means that if *p*=1 mm, the slot array would keep the end-fire patterns in a bandwidth of about 60%. If the operating frequency changes from 27 GHz to 29 GHz, the slot array would still keep the end-fire patterns when the spacing is selected between 0.75 mm to 1.25 mm. It is a constraint on the spacing of the slots when we attempt to optimize the performances of this composite antenna.

Although the backward radiation is weak, the forward lobe is very wide, over 180^{o}, which does not match the pattern of the ALTSA when the spacing is less than 1 mm. Therefore, we would use slightly larger spacing than in formula (2.31), e.g. 1.14 mm.

Since the SIW width in the composite antenna is not uniform, a transverse slot on the broad wall of this width-tapered SIW does not act totally in the same way as in a width-uniform SIW. A transverse slot on the width-tapered SIW actually has the equivalent effects of both transverse slot and longitudinal slot on a width-uniform SIW. Therefore, it acts as a compound slot in a width-uniform SIW [123]. A transverse slot on the broad wall of a width-uniform SIW makes the longitudinal currents on the broad wall go around the slot which introduces a longitudinal electric field across the slot and forms a jumping voltage across the slot. Therefore, the transverse slot acts as a series impedance [124], including both reactance and resistance, in the equivalent circuit of an SIW. A longitudinal slot on the broad wall of a width-uniform SIW makes the transverse currents on the broad wall go around the slot which would alter the longitudinal currents. Therefore, the longitudinal slot acts as a shunt admittance [125], including both susceptance and conductance, in the equivalent circuit of an SIW. Consequently, the equivalent circuit of a transverse slot on the broad wall of a width-tapered SIW is described in Figure 2.22.

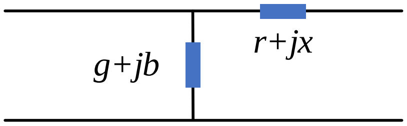

Figure 2.22: Equivalent circuit of a transverse slot on the broad wall of a width-tapered SIW

The resistance and conductance represent the contributions of a radiated energy by the slot, and the reactance are related to the stored energy of the high-order modes due to the slot. The resonant length of the slot is much shorter than half a wavelength in free space, which is the case in an air waveguide [126]. When the slot is at resonance, both reactance and susceptance would vanish [123]-[125], and only the resistance and the conductance are left in the equivalent circuit. If there is only a series resistance without a shunt conductance as in the case of a transverse resonant slot in a width-uniform SIW, the total normalized resistance is always larger than 1 when the SIW has a matching load. As such, the reflection from the transverse resonant slot is inevitable along a width-uniform SIW.

In the width-tapered SIW, however, there is a shunt admittance due to the non-uniform width of the SIW. The shunt admittance would be in parallel with the matching load and thus form an equivalent resistance whose normalized value is smaller than 1. The total normalized resistance of the equivalent and series resistance could be 1, so that a transverse resonant slot with a perfect matching could be available in a slotted width-tapered SIW.

We have discussed and given the design rules of the number and spacing of the slots. The area of a slot on the broad wall is in relation to its radiation strength; the area has a relatively strong effect on its radiation strength [124]. The larger the slot area is, the stronger the radiation of the slot becomes, and the higher the radiation efficiency of the slot is. Therefore, the radiation efficiency of the transverse slotted SIW depends on both the slot size and the number of the slots.

We could use a simple model of only two transverse slots on the top and bottom broad walls of a lossless width-tapered SIW to investigate the effect of the length and width of the slots on radiation efficiency. The radiation efficiency of a lossless slotted SIW is $((1-|S_{11}|^2-|S_{21}|^2)/(1-|S_{11}|^2))$, which can be used to navigate design of the slot.

The reflection and radiation efficiency of two slots is simulated with different lengths and widths, which are listed in Table 2.1, and the parameter of the width-tapered SIW is listed in the Figure 2.17 caption. These results are shown in Figure 2.23.

Table 2.1: Widths and lengths of slots in width-tapered SIW

Slot Number	**1**	**2**	**3**	**4**	**5**	**6**	**7**	**8**	**9**
Wb (mm)	2.00	2.00	2.00	2.28	2.28	2.28	2.56	2.56	2.56
Lc (mm)	0.36	0.46	0.56	0.36	0.46	0.56	0.36	0.46	0.56

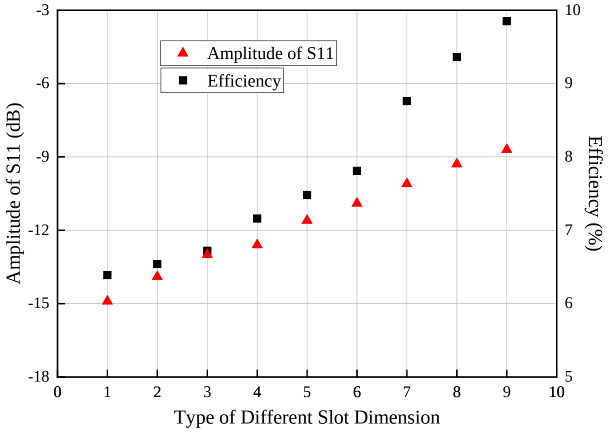

Figure 2.23: Reflection and radiation efficiency of two transverse slots on the broad walls of a width-tapered SIW

Based on the results in Figure 2.23, we can determine the length and width of the two slots under the conditions of a specific radiation efficiency and lowest reflection. The results suggest that the larger the size of the slots is, the stronger the radiation of the slots is.

The above formulas provide the design rules of the slot array on the slotted width-tapered SIW. The rest of the parameters are actually concerned with an SIW horn. They can be designed based on a guide found in reference [28].

So far, all the parameters of a slot array have been determined. Since the spacing of the slot array is much smaller than in conventional arrays, the coupling between adjacent slots is strong, which in turn has an effect on the performance of the slot array. Therefore, we can use a simulation tool to modify these parameters. All the parameters of a prototype of the slotted width-tapered SIW is listed in the caption of Figure 2.17. Figure 2.24 is a simulated pattern of the vertically polarized radiation at 28 GHz. The simulation tool used in this work is CST Studio Suite. During the simulation, the two ends of the SIW are set to be wave ports so that the radiation in Fig. 8 is produced only by the slots on the SIW.

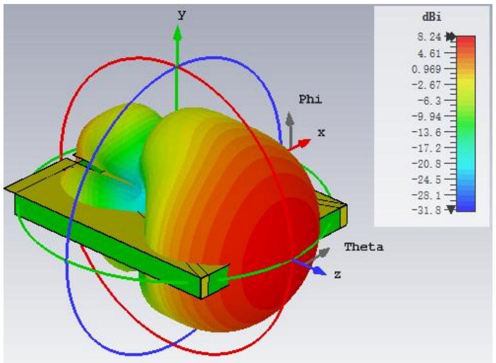

Figure 2.24: Simulated VP radiation pattern of slotted width-tapered SIW

The result in Figure 2.24 shows that the slotted width-tapered SIW has an end-fire VP radiation with a directivity of 8.24 dBi.

It has been believed that a slow wave in a periodic leaky wave antenna does not produce radiation. When the fundamental mode is a slow wave along the periodic leaky wave antenna, the radiation is produced only by space harmonics related to fast waves. In the slotted width-tapered SIW, however, there are no space harmonics. It is an only the slow wave responsible for the generation of radiation as shown in Figure 2.22. The slow wave radiation is an interesting phenomenon, and little is known or documented at this time.

2.3.3 Design of ALTSA Fed by Width-tapered SIW

The ALTSA in the composite antenna is fed by a flaring open aperture of the slotted width-tapered SIW. Different from the conventional ALTSA, the two metalized walls in this case are implemented at the two side surfaces of the flaring wings, as such the variation for the gain of the ALTSA is relatively small during operating frequency changing, and it is favorable for the circular polarization design.

There are no explicit formulas of radiation pattern and gain for the ALTSA, and a full wave simulation software becomes necessary for its design. The main parameters affecting the performance of an ALTSA are its open width and the length and staring width of its two wings. The open width is actually the width of the SIW open aperture. The opening of the ALTSA should be at least half a wavelength to ensure sufficient radiation. Usually, the wing length should be larger than two wavelengths to ensure good unidirectional radiation, and the starting width should be slightly wider than half the width of the open aperture of the SIW to ensure a good matching. To investigate how the shape and size of the two wings affect the directivity of the ALTSA, we simulate the directivity with different open widths and lengths of the two wings, which are listed in Table 2.2. The other parameters are listed in the Figure 2.17 caption.

Table 2.2: Sizes of ALTSAs fed by SIW

ALTSA Number	1	2	3	4	5
Ws (mm)	14.4	14.4	14.4	10.5	20.0
La (mm)	16.0	22.28	32.6	22.8	22.8

The ALTSA 1 and 5, and ALTSA 4 and 3 have the same geometry but different size. Figure 2.25 is the simulated directivity when frequency changes from 27 GHz to 29 GHz. Once the geometry of the ALTSA remains the same, the larger the ALTSA is and the higher its directivity is. On the other hand, when the length of the wing remains unchanged, the wider the opening of the ALTSA is and the higher its directivity is.

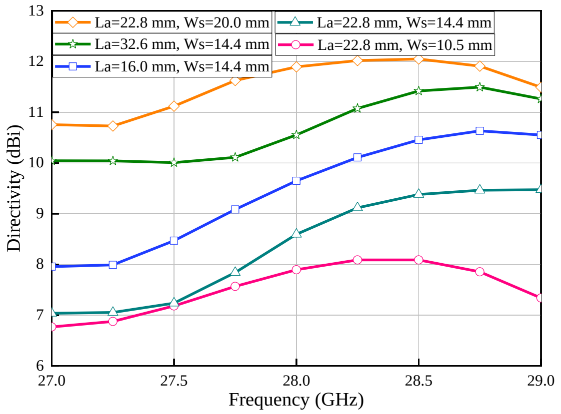

Figure 2.25: Directivity of ALTSA as widths and lengths of two wings

With the use of CST Microwave Studio, we designed an experimental prototype of an ALTSA fed by the prototype of a slotted width-tapered SIW. Its parameters are also listed in the Figure 2.17 caption. The SIW structure is the same as described in Figure 2.17 though without any slot. Figure 2.26 presents the simulated radiation pattern, which shows that the ALTSA produces both end-fire and horizontally polarized radiation and has a gain of 8.32 dBi, which is nearly equal to the 8.24-dBi directivity of the slotted width-tapered SIW of Figure 2.24.

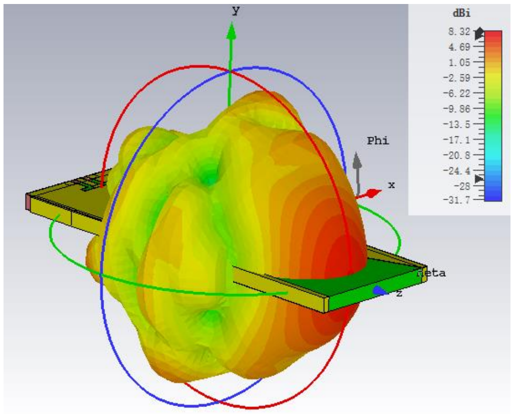

Figure 2.26: Simulated HP radiation pattern of ALTSA

2.3.4 Simulation and Measurement Results

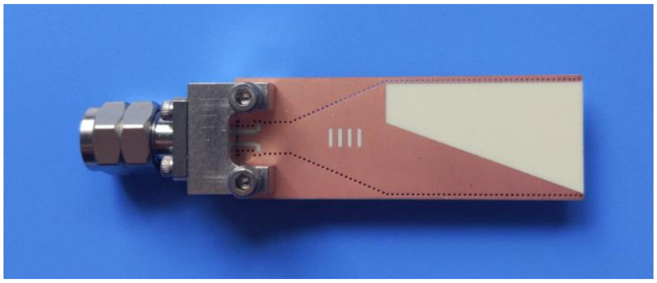

Figure 2.27: View of the fabricated slot-ALTSA composite antenna

The experimental prototypes of the proposed single-layered end-fire CP slot-ALTSA composite antenna, as shown in Figure 2.27, are fabricated and measured for verification of the above-described design procedure. All the size parameters are list in caption of Figure 2.17.

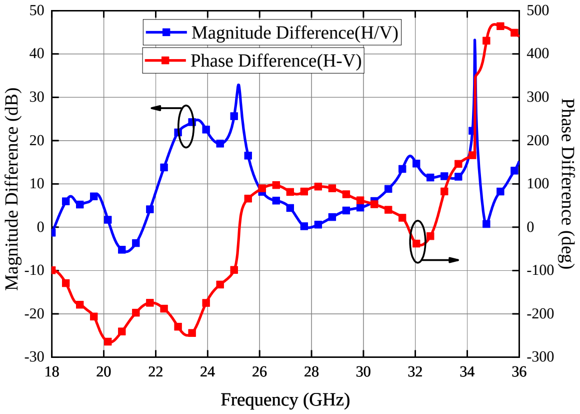

Figure 2.28: Amplitude and phase differences vs frequency

To make up a CP wave, the two orthogonally polarized E-field components of the composite antenna should have the same amplitudes and 90-degree phase difference in the far zone. To check how well it is satisfied, we set up an E-field probe in the simulation tool at the point of z=200 mm where the far zone is considered to be and simulate the two orthogonally polarized components of the radiating E-field. Figure 2.28 plots the simulated amplitude and phase difference between the vertically and horizontally polarized radiations as the operating frequency changes. The results in Figure 2.28 show that the two orthogonally polarized radiations have about a 90-degree phase difference from 25.6 GHz to 29.4 GHz, and the amplitude equality of the two orthogonally polarized radiations is only well pronounced in a narrow band around 28 GHz. Therefore, the AR bandwidth of the CP composite antenna degrades mainly due to the amplitude inequality of the two orthogonally polarized radiations. The information of the E-field probe in the far zone could also be used to guide the design of the proposed antenna. If it shows the vertically polarized E-field as stronger than the horizontally polarized E-field, we should decrease the directivity or the radiation efficiency of the slotted SIW or increase the gain of the ALTSA. If the phase difference of the two orthogonally polarized E-fields deviates off 90 degrees, we should move the slot array along the z-axis and modify the shape of the ALTSA wings to restore the desired orthogonal phase difference.

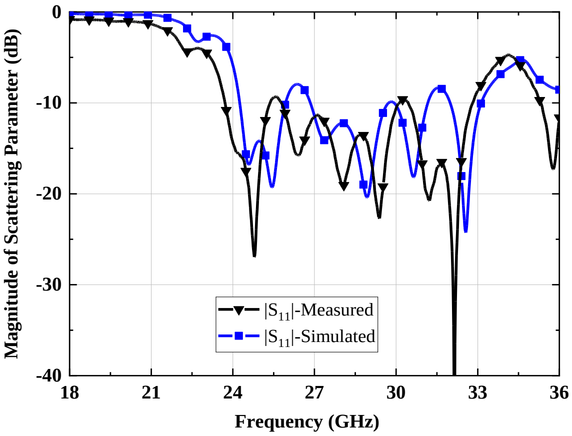

Figure 2.29: Simulated and measured reflection coefficients

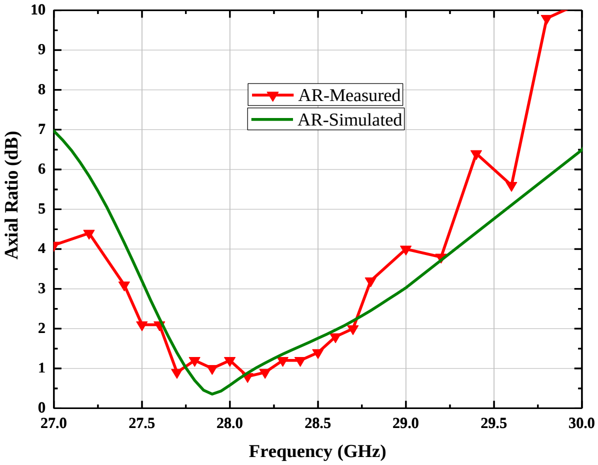

Figure 2.30: Simulated and measured AR vs frequency

Figure 2.29 presents the measured and simulated reflection coefficients showing that the bandwidth of VSWR <2 is about 9 GHz. The bandwidth is limited mainly by the slot array in the width-tapered

SIW. The slot array should exhibit an end-fire radiation which enforces a strong constraint on the number of slots and their spacing. There are few parameters under consideration for matching.

Figure 2.30 provides the measured and simulated axial ratios of the main lobe at different frequencies, displaying an axial ratio bandwidth of about 1.4 GHz from 27.35 GHz to 28.75 GHz.

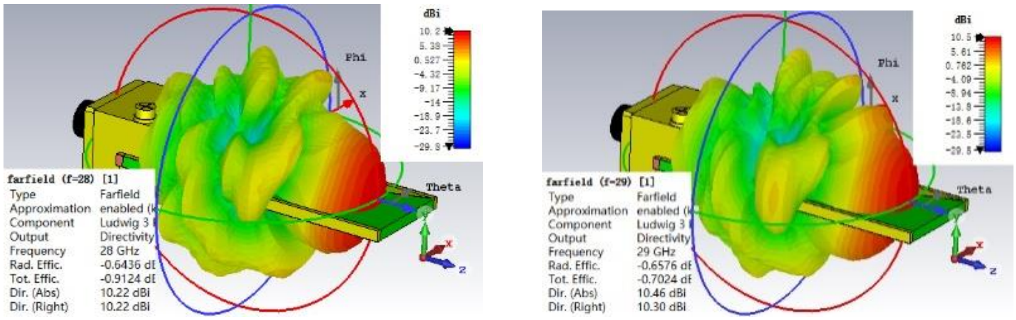

farfield (f=28) [1]
Type Farfield
Approximation enabled (k
Component Ludwig 3
Output Directivity
Frequency 28 GHz
Rad. Effic. -0.6436 d
Tot. Effic. -0.9124 d
Dir. (Abs) 10.22 dBi
Dir. (Right) 10.22 dBi

farfield (f=29) [1]
Type Farfield
Approximation enabled (k
Component Ludwig 3
Output Directivity
Frequency 29 GHz
Rad. Effic. -0.6576 d
Tot. Effic. -0.7024 d
Dir. (Abs) 10.46 dBi
Dir. (Right) 10.30 dBi

(a) (b)

Figure 2.31: Simulated 3-D radiation pattern (a) 28 GHz and (b) 29 GHz

Figure 2.31 illustrates the simulated 3-D radiation pattern at 28 GHz and 29 GHz, clearly demonstrating that the proposed CP composite antenna produces the end-fire radiation patterns.

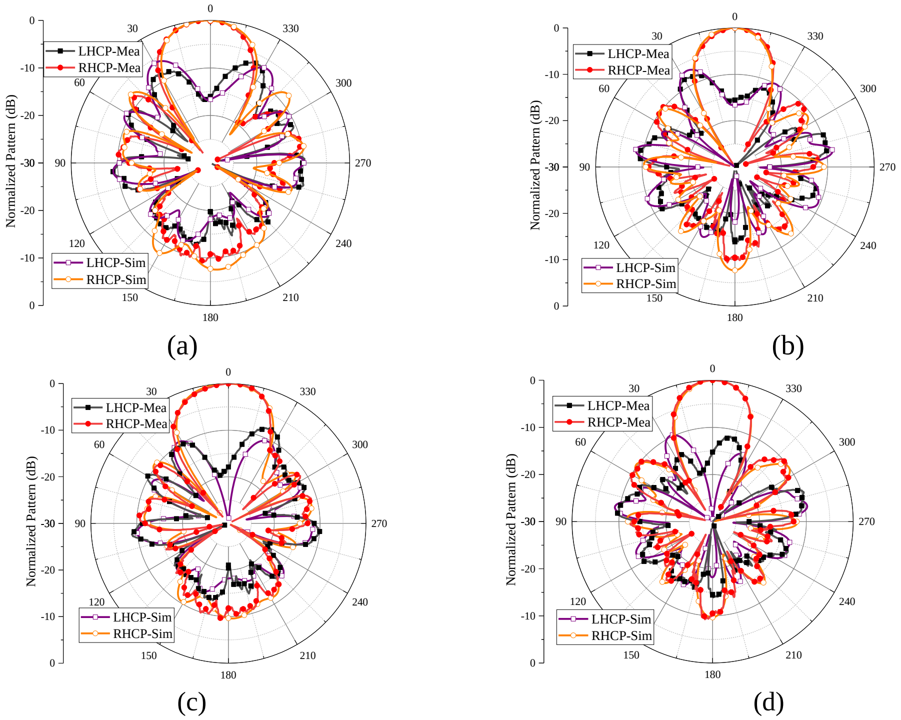

(a) (b)

(c) (d)

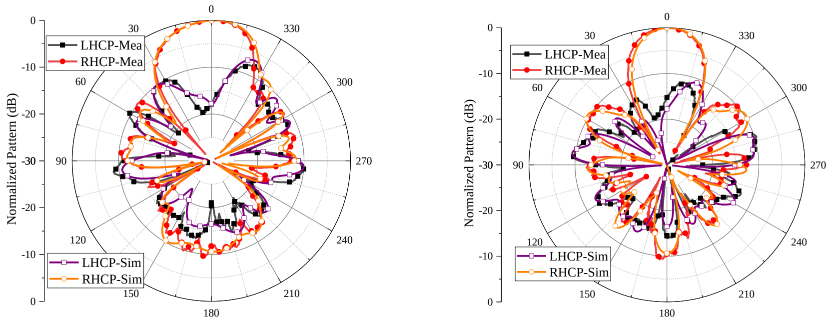

(e) (f)

Figure 2.32: Simulated and measured radiation pattern

(a) yoz plane at 27.5 GHz, (b) xoz plane at 27.5 Ghz, (c) yoz plane at 28 GHz, (d) xoz plane at 28 Ghz, (e) yoz plane at 28.8 GHz and (f) xoz plane at 28.8 GHz

Figure 2.32 presents a series of comparisons between the simulated and measured radiation patterns on the *yoz* and *xoz* planes at 27.5 GHz, 28 GHz and 28.8 GHz, and they show a good agreement between the simulated and measured results.

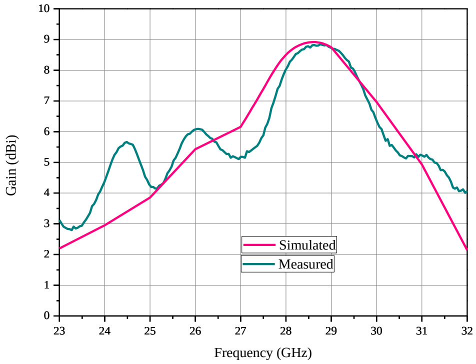

Figure 2.33: Simulated and measured gain

Figure 2.33 gives the measured and simulated gains at different frequencies; it shows a gain of 8.7 dBi at 28.8 GHz, and from 25.5 GHz to 31.3 GHz the gain is higher than 5 dBi. These figures show an obvious agreement between the measured and simulated results. Figure 2.34 is the simulated and measured AR on the *yoz* plane and *xoz* plane at 28 GHz. The proposed antenna yields measured 26^{o} and 21^{o} 3 dB AR beamwidths on the yoz and xoz planes, respectively.

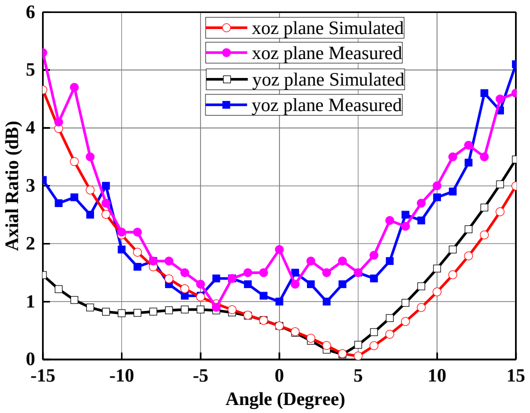

Figure 2.34: Simulated and measured AR of the antenna vs spatial angles

The proposed transverse slotted width-tapered SIW in the ALTSA is an extension of the conventional transverse slotted width-uniform SIW and is easier to match. This CP ALTSA is designed to utilizes slots on the spare broad walls of the SIW to form an extra radiator which enhances the VP radiation. This scheme avoids the drawback of low gain of the previous works. Furthermore, the solution offers flexibility in the choice of number and structure of slots. Even the gain and radiation pattern of the antenna can be adjusted to meet diverse requirements for practical applications.

2.4 SIW Slot-Horn Antenna

When an SIW H-plane horn has transverse slots on its broad wall, it becomes an SIW slot-horn composite antenna, as shown in Figure 2.35. The slot-horn antenna has two radiators: an SIW horn and a slot array on the broad walls of the SIW. The radiation wave from the SIW slot-horn antenna is a sum or superposition from the two radiators. The two radiators could be co- or cross-polarizations. The slot array acts as a leaky wave radiator on a width-tapered SIW, its radiation characteristics have been investigated in Section 2.3, and has been applied to enhance VP radiation of a CP antenna.

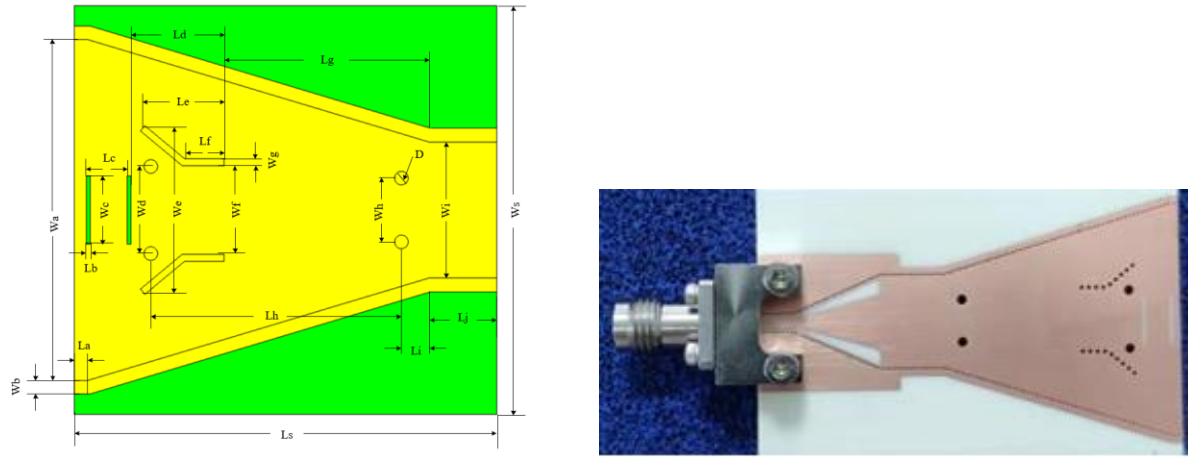

(a) (b)

Figure 2.35: (a) Structure and (b) prototype of SIW slot-horn composite antenna

(*D*=1, *La*=1, *Lb*=0.3, *Lc*=3, *Ld*=6.85, *Le=5.8*, *Lf*=3.1, *Lg*=15.1, *Lh*=18.4, *Li*=2.1, *Lj*=4.85, *Ls*=31, *Wa*=25, *Wb*=1, *Wc*=5.6, *Wd*=6.4, *We*=12.4, *Wf*=6.5, *Wh*=4.68, *Wi*=10, *Ws*=30, unit: mm)

In this Section, the attention will be paid to the radiation characteristics of SIW slot-horn composite antennas. Again when simulating, an SIW is replaced with its equivalent DFW.

As aforementioned the distance between the slot array and the aperture of the horn has an effect on the radiation pattern of the slot array. The spacing of the two adjacent slots and the width of the SIW where the slot array locates have also effects on the radiation pattern. Again the distance and the phase velocity inside the horn determine the feeding phase delay between the two radiators. Therefore, the distance, the spacing and the width are three key factors to shape the radiation pattern of the slot-horn antenna.

To facilitate the control of power radiated by the slot array, two metallic via array are be put inside the horn. Because the reflection from the slot is remarkable even the slot is under resonance, a pair of symmetrical tuning metallic vias are placed at between via array and the slot array, and another pair of symmetrical tuning metallic vias are placed near input waveguide.

Both the horn and the slot of the SIW are not omnidirectional radiation patterns, however, an SIW slot-horn composite antenna can have an omnidirectional pattern on E-plane. For measurement, a connector is necessary. The connector, however, has a strong effect on the radiation pattern of the antenna, especially on its backward radiation on the E-plane, which will degrade its omnidirectional performance. Figure 2.36 displays the simulated radiation patterns of the slot-horn antenna free of the connector, which shows an omnidirectional pattern on the E-plane. We have not solved the issue.

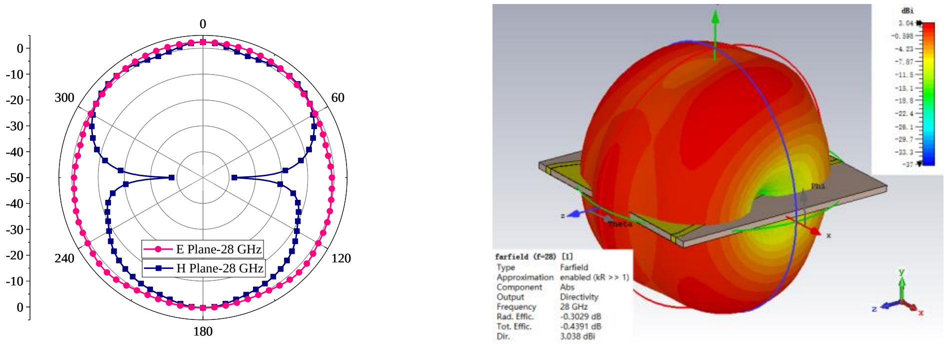

farfield (f=28) [1]
Type Farfield
Approximation enabled (kR >> 1)
Component Abs
Output Directivity
Frequency 28 GHz
Rad. Effic. -0.3029 dB
Tot. Effic. -0.4391 dB
Dir. 3.038 dBi

(a) (b)

Figure 2.36: Radiation pattern of the slot-horn composite antenna

(a) on E-plane and H-plane, and (b) 3D-pattern

An experiment prototype of the proposed slot-horn antenna, as shown in Figure 2.35 (b), is designed and fabricaied, and its size is listed in Figure 2.35 caption. Figure 2.37 (a) exhibits the simulated and measured reflection coefficient of the prototyped slot-horn antenna. The agreement between the simulated and measured results are not well due to a mistake. During design, the recommended value of the permittivity of the substrate rather than the measured value on datasheet should be used.

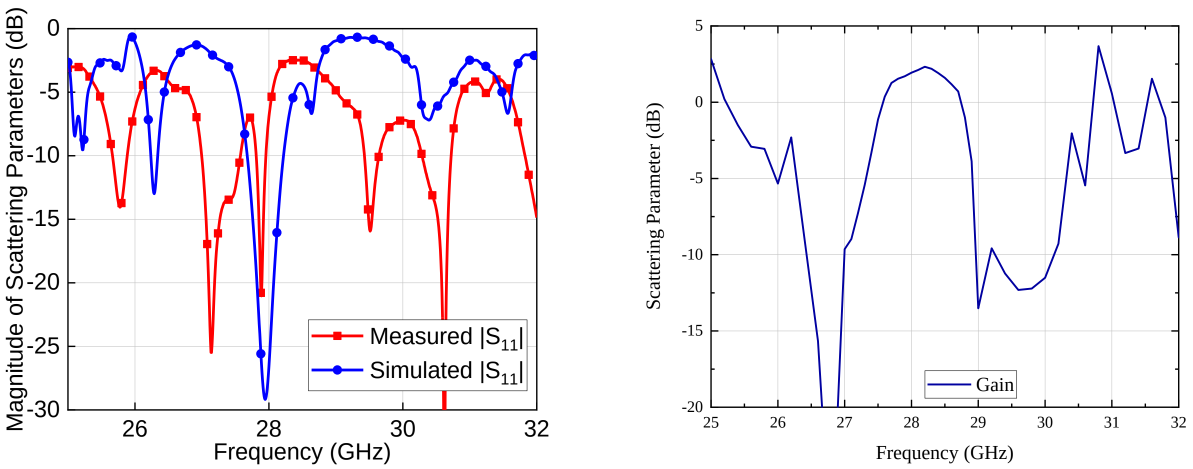

(a)

(b)

Figure 2.37: Reflection coefficient and gain of a slot-horn composite antenna with omnidirectional pattern

(a) reflection coefficient and (b) gain

Figure 2.37 (b) displays the simulated gain of the composite slot-horn antenna. The gain transitions between in-band and out-band are very sharp, which exhibits a good filter performance. Therefore, the slot-horn composite antenna is also a filter antenna.

CHAPTER 3 UNIDIRECTIONAL DIELECTRIC RADIATOR ANTENNAS FED BY THIN SIW

An RF subsystem is usually manufactured with a mingled multilayer substrate on PCB technology or similar planar platforms, and the RF layer of such multilayer substrates must be thin enough to suppress high-order modes and surface wave modes in RF circuits. The thickness of the RF layer should usually be less than $0.05\lambda_0$, which is roughly 0.508 mm at 30 GHz, for example. When the substrate is thick, the loss of a planar transition between an antenna and a connector could be large due to radiation and surface wave when operating at millimeter-wave frequencies or above. Consequently, planar end-fire VP and CP antennas with relatively thin feeding substrates are highly desired.

As one type of dielectric antennas, a UDR has an end-fire radiation pattern. Consequently, it is desired to feed a URD with a thin SIW to form a VP antenna. Moreover, it is also expected to use a UDR as the VP radiator in a fully planar high gain end-fire CP antenna.

This Chapter demonstrates two types of planar mingled multilayer UDR end-fire antennas: UDR-SIW and UDR-ALTSA. In Section 3.1, a UDR-SIW fed by slots on the broad walls of a thin SIW is proposed, and demonstrated with simulations and experiments. The UDR-SIW has a polarization normal to the broad walls of the SIW, a circular symmetric end-fire pattern along the SIW with high, and the front-to-back ratio of the pattern is high. These features of the UDR-SIW make it to be an update to a conventional SIW H-plane horn, and will certainly benefit its applications to planar high gain antennas and arrays. In Section 3.2, a fully planar high gain UDR-ALTSA end-fire CP antenna fed by a thin SIW is devised, and demonstrated with simulations and experiments. The UDR-ALTSA uses a UDR to enhance the VP gain, and the UDR is placed normal to the substrate on which the ALTSA and the feeding SIW are fabricated. The UDR-ALTSA is actually a heterogeneous linear array stretching along the direction normal to the substrate. Therefore, the UDR-ALTSA not only has wide impedance and AR bandwidths, but also is very compact, which make it easy to be element antennas of a big array.

3.1 Unidirectional Dielectric Radiator Antenna Fed by Slots on a very thin SIW

3.1.1 Introduction

Both the dielectric resonator antennas and the dielectric rod antennas are two conventional types of dielectric antennas [127]-[134]. The radiation pattern and structures of a dielectric resonator antenna and a dielectric rod antenna are distinctly different. A dielectric resonator antenna has a broadside radiation pattern, and the dielectric resonator is on a conducting plate or a substrate with a conducting plate. A dielectric rod antenna consists of only a dielectric rod without conducting plates [131]-[134]. A dielectric rod antenna has an end-fire radiation pattern along the dielectric rod, and it is usually excited at its one end by a horn, an open waveguide, or other end-fire feeding antennas.

A conventional UDR antenna, as shown in Figure 3.1 (a)， is different from both the dielectric resonator antenna and the dielectric rod antenna shown [135]-[138], and could be regarded as a mixture of the two dielectric antennas. The structure and feeding of a UDR are similar to a dielectric resonator antenna, and they all have conducting plates. A UDR works usually with a resonant mode, and it is also a resonant antenna. On the other hand, a UDR has an end-fire pattern that is similar to a dielectric rod antenna.

The structure of a conventional UDR is slightly complex, and its unidirectional radiation pattern is basically achieved thanks to a non-radiative dielectric (NRD) waveguide [139]-[140]. The UDR consists of a dielectric resonator sandwiched between two parallel metallic plates. The dielectric resonator is within close proximity to one of the plate edge aperture so that an end-fire radiation is achieved in one direction while the other directions are set in non-radiative conditions. A conventional UDR antenna is usually fed by a slot on its conducting plane or a vertically mounted probe. The conventional UDR, however, is a HP radiation antenna due to its usually selected operating mode.

This thesis devises a planar end-fire VP Fabry-Perot UDR-SIW antenna fed by a rather thin SIW. Without two covered parallel metallic plates, a UDR-SIW, as sshown in Figure 3.1 (c), consists of two identical dielectric substrates and one embedded feeding slotted SIW between the two dielectric substrates. The UDR-SIW is fed by two transverse slots on the top and bottom broad walls of the embedded feeding SIW. And the feeding SIW has a shorting end so that the slotted SIW could be regarded as a resonant antenna.

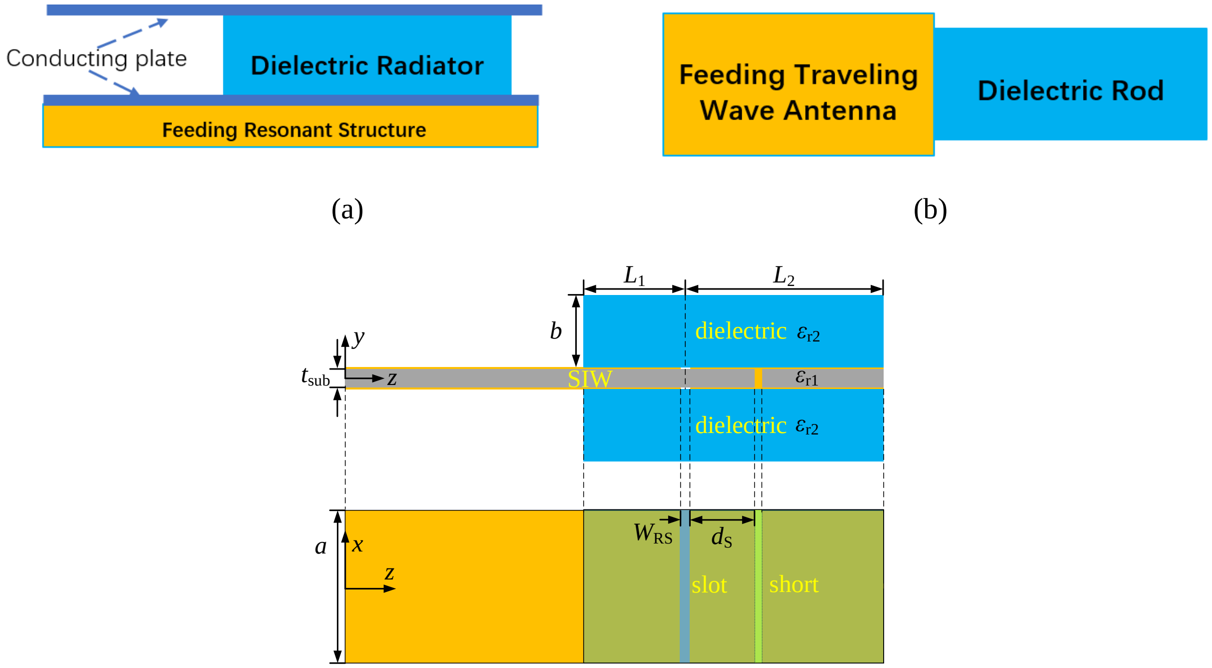

(a) (b)

(c)

Figure 3.1: Configuration of dielectric antennas

(a) conventional UDR , (b) dielectric rod antenna, and (c) UDR-SIW. (h=0.508 mm, b=1.524 mm, L_1=1.9 mm, L_2=9.1 mm, a=6 mm, W_{RS}=0.4 mm, d_s=1.4 mm, ε_{r1}=2.2, ε_{r2}=3.55)

The UDR-SIW presents certain interesting features as follows.

(1) The VP UDR mechanism is based on a generalized Fabry-Perot cavity.

(2) The SIW-based VP UDR antenna has a very thin substrate, and its polarization is orthogonal to a conventional UDR.

(3) It is easily integrated with an RF subsystem with a mingled multilayer PCB technology due to the very thin feeding substrate.

(4) It has a symmetrical pattern and improved front to back ratio (FTBR).

(5) The attractive UDR is integrated with its embedded feeding SIW, which makes the UDR-SIW compact and efficiently excited.

(6) Finally, it has a travelling-wave antenna excited by resonant slots.

The proposed UDR-SIW could also be regarded as the combination of a dielectric rod antenna and a conventional UDR but with orthogonal polarization, and this combined topology takes advantage of the two antennas. Figure 3.1 (b) shows the schematic of a dielectric rod antenna. A dielectric rod antenna is usually fed longitudinally by a travelling-wave antenna, leading to a long longitudinal size. Besides, the equivalent radiating aperture of the feeding travelling-wave antenna should be comparable to the cross-section of the dielectric rod for an effective excitation. A conventional UDR, which is usually fed by a resonant structure under one of its two conducting plates, and the longitudinal size could be made short. The conducting plates, however, must be large enough to ensure a unidirectional radiation so that a conventional UDR is arduously made compact. Compared to the dielectric rod antenna, the proposed UDR-SIW is fed by one embedded resonant structure between two dielectric substrates, which would ensure an effective excitation as well as a compact size. A diligent feeding structure design could not only decrease its longitudinal size but also use a very thin feeding substrate. Compared to a conventional UDR, the broad walls of a UDR-SIW act as the conducting plates in a conventional UDR to double the equivalent thickness of dielectric substrates. The size of broad walls, however, is much smaller than the conducting plates of a conventional UDR because the UDR-SIW does not need extra-large plates to achieve unidirectional radiation.

The UDR-SIW can be fabricated with a conventional mingled multilayer PCB technology, is fed with an SIW on a very thin substrate less than $0.05\lambda_0$, and these features will certainly make it to be available to various applications.

3.1.2 Mechanism of UDR-SIW End-fire VP Radiation

3.1.2.1 Modes in Rectangle Dielectric

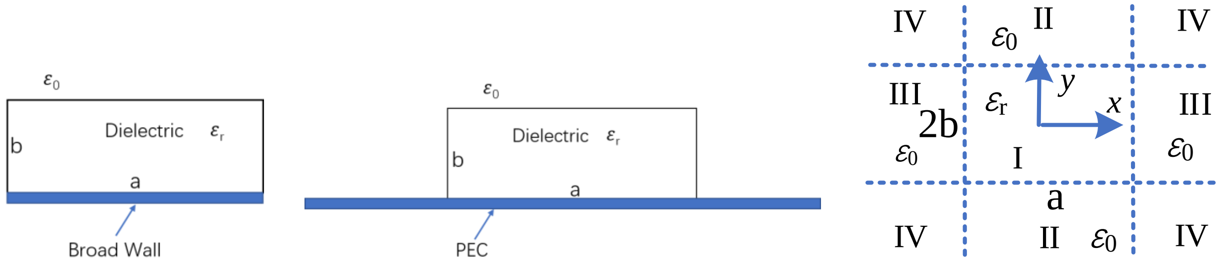

(a) (b) (c)

Figure 3.2: (a) Rectangular dielectric substrate on SIW, (b) rectangular dielectric substrate on infinite PEC and (c) its equivalent dielectric rod in free space

To understand how a UDR in the proposed UDR-SIW produces unidirectional radiation, one should examine modal behaviors in the dielectric substrates and how these modes propagate in the dielectric substrates.

The SIW broad wall shown in Figure 3.2(a) could be practically treated as an infinite PEC, as shown in Figure 3.2(b); then, the rectangular dielectric substrate in Figure 3.2(b) would be equivalent to an enlarged rectangular dielectric rod in free space, as shown in Figure 3.2(c). Although both the TM_{mn}^{y} and TM_{mn}^{x} modes could exist in a rectangular dielectric rod, only the TM_{mn}^{y} mode is available because the rectangular dielectric substrate is excited by a transverse slot with a transverse magnetic current. The main field components of TM_{mn}^{y} are E_y and H_x, and H_y equals zero Therefore, a TM_{mn}^{y} is associated with a VP field in the UDR-SIW antenna.

In the rectangle dielectric rod TM_{mn}^{y} and TM_{mn}^{x} can exist.

For TM_{mn}^{y}, there is $H_y = 0$, and E_y and H_x are main field components of propagating modes. The other field components of TM_{mn}^{y} can be expressed with H_x as follows

$$E_x = -\frac{1}{\omega\varepsilon\beta}\frac{\partial^2 H_x}{\partial x \partial y} \tag{3.1}$$

$$E_y = -\frac{\omega\mu}{\beta} H_x - \frac{1}{\omega\varepsilon\beta}\frac{\partial^2 H_x}{\partial y^2} \tag{3.2}$$

$$E_z = \frac{j}{\omega\varepsilon}\frac{\partial H_x}{\partial y} \tag{3.3}$$

$$H_z = -\frac{j}{\beta}\frac{\partial H_x}{\partial x} \tag{3.4}$$

$$H_y = 0 \tag{3.5}$$

As an approximation, one could ignore the fields of TM_{mn}^{y} in region IV, and the fields in other regions would be expressed as follows

$$H_x = H_0 \cos(k_x x)\cos(k_y y)e^{-j\beta z}, \quad (|x| < 0.5a, y < b) \quad \text{in region I} \tag{3.6}$$

$$H_x = H_1 \cos(k_x x)e^{-\alpha_y y}e^{-j\beta z}, \quad (y \ge b) \quad \text{in region II} \tag{3.7}$$

$$H_x = H_2 \cos(k_y y)e^{-\alpha_x |x|}e^{-j\beta z}, \quad (|x| \ge 0.5a) \quad \text{in region III} \tag{3.8}$$

where H_0 is the excited magnitude of TM_{mn}^{y}. The wavenumber in each region observe the following equations.

$$k_x^2 + k_y^2 + \beta^2 = \varepsilon_r k_0^2 \tag{3.9}$$

$$k_x^2 - \alpha_y^2 + \beta^2 = k_0^2 \tag{3.10}$$

$$-\alpha_x^2 + k_y^2 + \beta^2 = k_0^2 \tag{3.11}$$

When enforcing boundary conditions on interfaces between these regions and using an effective refractive index method [141]-[142], one can calculate the propagation constants of TM_{mn}^{y}. Then the application of boundary conditions over planes $x=\pm 0.5a$ allows to deduce the following equations

$$k_x a = m\pi - 2\arctan(\frac{k_x}{\alpha_x}),(m = 1, 2, 3, \cdots) \tag{3.12}$$

Subtracting (3.11) from (3.09), one has

$$\alpha_x = \sqrt{k_0^2(\varepsilon_r - 1) - k_x^2} \tag{3.13}$$

When equations (3.12) and (3.13) are solved, k_x is obtained. And then the effective refractive index is defined as follows:

$$N^2 = \varepsilon_r - \left(\frac{k_x}{k_0}\right)^2 \tag{3.14}$$

To enforce the boundary conditions over planes $y=\pm b$, one can have

$$\alpha'_y = \sqrt{k_0^2(\varepsilon_r - 1) - k_x^2 - k_y^2} \tag{3.15}$$

$$2k_y b = n\pi - 2\arctan(\frac{k_y}{N^2\alpha'_y}),(n = 1,2,3\cdots) \tag{3.16}$$

When solving equations (3.14), (3.15) and (3.16), one can also obtain k_y and then calculate the propagation constants of TM_{mn}^y as follows:

$$\beta = \sqrt{k_0^2\varepsilon_r - k_x^2 - k_y^2} \tag{3.17}$$

The propagation constant of modes is known to be an important design parameter. The aforementioned calculation method for yielding the propagation constant is accurate but not easy to use because the expression for the propagation constant is not explicit. From the design viewpoint, an explicit or closed-form approximate expression of propagation constant is indeed desired.

When the permittivity of a dielectric is high, the interface between dielectric substrate and air could be approximately treated as a perfect magnetic wall, and the field would be totally confined in region I. This is actually the case when α_x and α'_y become infinite. In this case, formulas (3.12) and (3.16) become

$$k_x a = m\pi \tag{3.18}$$

and

$$k_y 2b = n\pi \tag{3.19}$$

When the permittivity is not high, the field will expand into regions II and III, and it is equivalent to have a set of larger *a* and *b*. As a result, one can use an explicit approximate expression of propagation constant as follows:

$$\beta = \sqrt{k_0^2\varepsilon_r - \left(\frac{m\pi}{\varsigma_a a}\right)^2 - \left(\frac{m\pi}{2\varsigma_b b}\right)^2} \tag{3.20}$$

The accuracy of ς_a and ς_b depends on the permittivity of the UDR. The larger the permittivity is, the smaller ς_a and ς_b are. In a primary design, one can set both ς_a and ς_b to be 1.3.

Based on formulas (3.1) to (3.6), the electric fields and magnetic fields of TM_{mn}^y in a rectangle dielectric rod, shown in Figure 3.2, are as follows

$$E_x = -\frac{H_0 k_x k_y}{\omega\varepsilon\beta}\sin(k_x x)\sin(k_y y)e^{-j\beta z} \tag{3.21}$$

$$E_y = H_0\cos(k_x x)\cos(k_y y)\left(\frac{k_y^2}{\omega\varepsilon\beta} - \frac{\omega\mu}{\beta}\right)e^{-j\beta z} \tag{3.22}$$

$$E_z = -\frac{jk_y H_0}{\omega\varepsilon}\cos(k_x x)\sin(k_y y)e^{-j\beta z} \tag{3.23}$$

$$H_x = H_0\cos(k_x x)\cos(k_y y)e^{-j\beta z} \tag{3.24}$$

$$H_z = \frac{jk_x H_0}{\beta}\sin(k_x x)\cos(k_y y)e^{-j\beta z} \tag{3.25}$$

$$H_y = 0 \tag{3.26}$$

Figure 3.3 is a sketch picture of the field configuration of TM_{11}^y mode on cross sections of a rectangle dielectric. Its magnetic field on ground plane is similar to that of TE_{10} in a metal rectangle waveguide. Therefore, it is effective to use an SIW to excite a TM_{11}^y in the UDR-SIW.

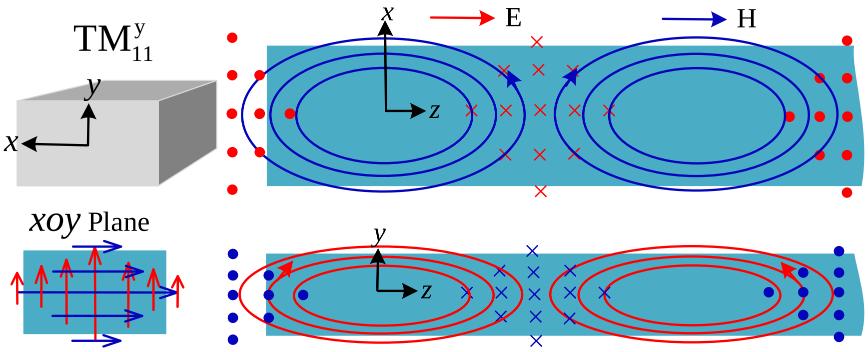

Figure 3.3: Field configuration of TM_{11}^{y} mode

By the means of a transverse slot, the TE10 mode inside the feeding SIW will excite the TM_{11}^{y} mode in the rectangular dielectric substrate. The equivalent transverse magnetic current along the slot is formulated by

$$J_m = \mathbf{e}_x J_0 \cos(\frac{\pi x}{W_{sl}}), \qquad W_{sl} < a \tag{3.27}$$

where W_{sl} is the length of the slots. The transverse magnetic field of TM_{11}^{y} on plane y=0 is given by

$$H_x = H_0 \cos(\frac{\pi x}{\varsigma_a a}), \qquad \varsigma_a > 1 \tag{3.28}$$

Consequently, the transverse magnetic current along the slot would excite the transverse magnetic field of TM_{11}^{y}. To fully excite TM_{11}^{y}, the slots should be as long as possible so that $W_{sl}=a$.

3.1.2.2 Generalized Fabry-Perot Based Mechanism of Unidirectional Radiation

To achieve unidirectional radiation, a UDR-SIW should be designed to utilize two different superposition effects at both the back-end and front-end. As it is similar to the Fabry-Perot principle, it is referred to as the generalized Fabry-Perot principle.

At the back-end, if the direct wave from the slot and the reflected wave from the front-end are out-of-phase, the backfire radiation would thus be undermined. At the front-end, if the direct wave from the slot and the reflected wave from the back-end are in phase, the end-fire radiation would be enhanced. Therefore, a UDR-SIW could effectively achieve a unidirectional radiation. An example shown in Figure 3.4 could be used to explain and verify the mechanism of unidirectional radiation achieved within the UDR-SIW structure.

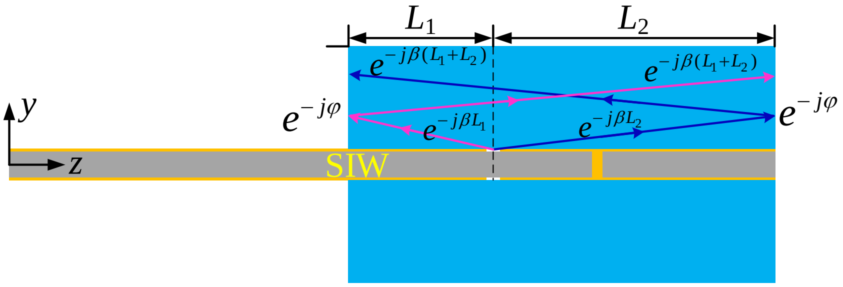

Figure 3.4: Schematic of generalized Fabry-Perot principle

The TM_{11}^{y} excited by the slot will trigger forward and backward propagations along the dielectric. When the phase difference between the reflected wave from the front-end and a direct propagating wave from the slot is out-of-phase at the back-end, namely

$$\beta L_2 + \varphi_r + \beta(L_1 + L_2) - \beta L_1 = (2m+1)\pi, \quad (m=1, 2, 3\cdots) \tag{3.29}$$

the backward radiation would be weakened. The φ_r in (3.29) is the reflection phase due to the reflection at the forward end. The formula (3.29) can be simplified into

$$2L_2\beta + \varphi_r = (2m+1)\pi, (m=1,2,3,\cdots) \tag{3.30}$$

The formula (3.30) is the condition for weak backfire radition.

Similarly, at the front-end, there is the superposition of a direct propagating wave from the slot and the reflected wave from the back-end. When the distance from the back-end to the slot satisfies the following condition,

$$\beta L_1 + \varphi_r + \beta(L_1 + L_2) - \beta L_2 = 2n\pi, \quad (n=1, 2, 3\cdots)$$

Namely,

$$2L_1\beta + \varphi_r = 2n\pi, (n=1,2,3,\cdots) \tag{3.31}$$

In this case, the direct propagating wave from the slot and the reflected wave from the back-end would be in-phase at the front-end. And the forward radiation would be enhanced. The formula (3.31) is the condition for realizing a strong end-fire radiation.

From (3.30) and (3.31), one can deduce that

$$\frac{(L_2 - L_1)\beta}{\pi} = m - n + 0.5 \tag{3.32}$$

Because of the slot, the phase constant in the UDR is not longitudinally uniform in the dielectric substrate, and (3.32) can be transformed as follows:

$$\frac{1}{\pi}\left(\int_0^{L_2} \beta dz - \int_0^{L_1} \beta dz\right) = m - n + 0.5 \tag{3.33}$$

When both the weak backfire radiation condition (3.30) and the strong end-fire radiation (3.31) are satisfied simultaneously, the FTBR would reach peak values, and (3.33) would hold true. To verify the unidirectional radiation mechanism of a UDR-SIW, the formula (3.33) will be examined with the following simulation.

The cut-off frequency of TM_{11}^{y} in the rectangle dielectric is about 18.6 GHz. The cut-off frequency of the feeding SIW is 16.9 GHz, and the band of 16.9-33.8 GHz accommodates the mono-mode propagation of the TE_{10} mode. When a parameter is changed in the following simulation, the other parameters will be kept the same as in Figure 3.1. Figure 3.5 is the simulated FTBR of the UDR-SIW of Figure 3.1, from 18 GHz to 35 GHz. It shows that the FTBR of the UDR-SIW reaches peak values at 19.7 GHz, 23.3 GHz, 26.2 GHz, 28.6 GHz, 31.1 GHz, and 33.6 GHz, which means that the formula (3.33) should hold true at these frequencies.

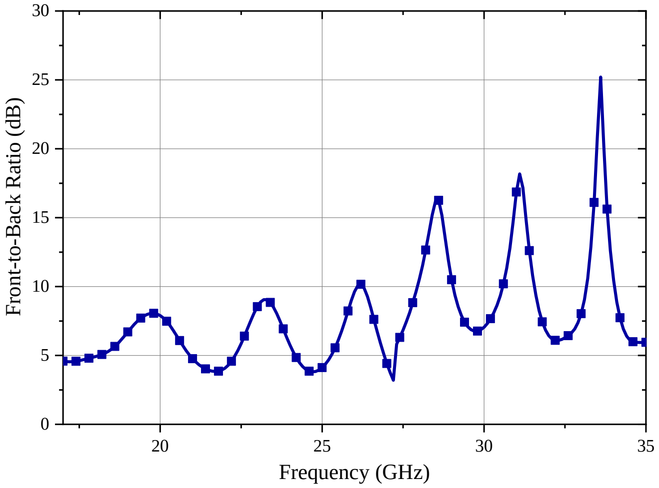

Figure 3.5: Simulated FTBR of a UDR-SIW vs frequency

Figure 3.6 is the simulated E-field in a UDR-SIW at 31.1 GHz. It shows that the phase constant in a UDR-SIW is not uniform due to the slot. To calculate the value on the left side of formula (3.33), one should know the phase constants at any points in the UDR-SIW.

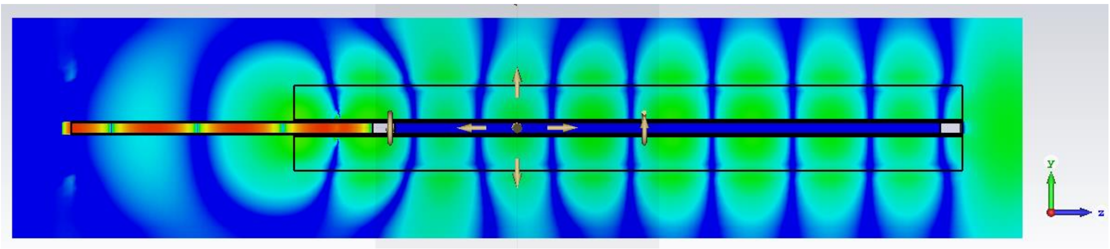

Figure 3.6: Simulated E-field of UDR at 28.6 GHz

The software package CST cannot be used to calculate the phase constant of a mode in the local region of a practical structure with reflection. Therefore, the FPPS is used to calculate the phase constants at any point inside the dielectric substrate at 19.7 GHz, 23.3 GHz, 26.2 GHz, 28.6 GHz, 31.1 GHz, and 33.6 GHz and then to calculate the values of the left end of formula (3.33) at these frequencies. Table 3.1 presents the calculated results.

Table 3.1: The left end of formula (3.33) calculated by FPPS

f (GHz)	19.7	23.3	26.2	28.6	31.1	33.6
Left end of (3.33)	3.41	4.63	5.66	6.55	7.56	8.51
$m-n+0.5$	3.5	4.5	5.5	6.5	7.5	8.5

The Table 3.1 shows that the formula (3.33) holds true in the UDR-SIW antenna at these frequencies where the FTBR reaches the peak values. It verifies the mechanism of unidirectional radiation in the UDR-SIW.

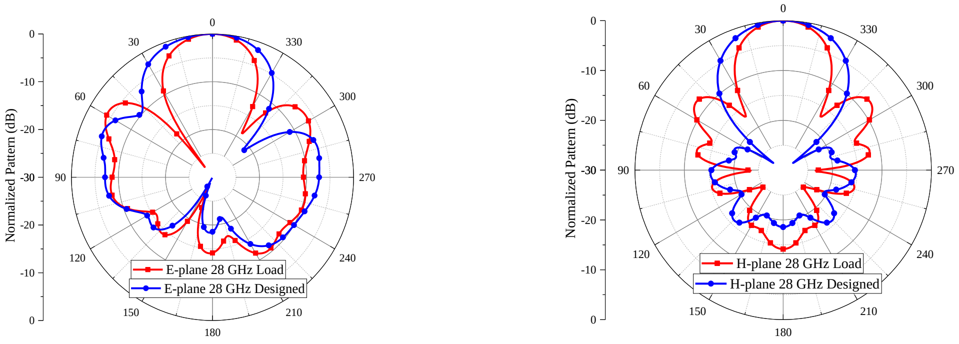

(a) (b)

Figure 3.7: Comparison of patterns between the UDR-SIWs with plane end and with a tapered end

(a) E-plane and (b) H-plane

A conventional dielectric rod antenna usually has an end of the tapered pyramid to enhance gain. It is also true for a UDR-SIW, as shown in Figure 3.7, which compares the simulated patterns of E-plane and H-plane at 28 GHz between a UDR-SIW with a plane end and another with a tapered end. Based on the mechanism of unidirectional radiation, however, a tapered end would decrease the FTBR of a UDR-SIW, which is also shown in Figure 3.7. Therefore, the results in Figure 3.7 also verify the generalized Fabry-Perot-based mechanism of unidirectional radiation in the UDR-SIW.

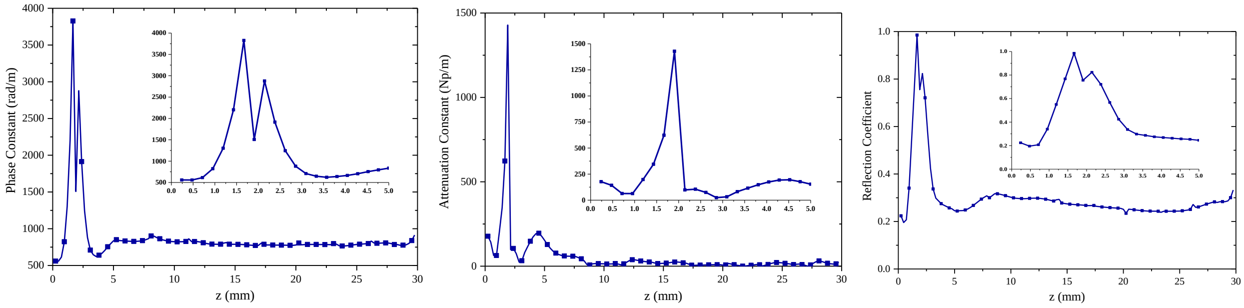

(a) (b) (c)

Figure 3.8: (a) Phase constants, (b) attenuation constants and (c) reflection at 28.6 GHz inside UDR

(slots are at z=1.9 mm)

Figure 3.8 shows the calculated phase constants, attenuation constants, and reflection coefficients at 28.6 GHz with the FPPS. It suggests that there is a reflection inside the dielectric substrate of the UDR-SIW. On the other hand, the phase constants are not uniform inside the dielectric substrate. Figure 3.8 (b) shows that the attenuation constants near the slot (z=1.9 mm) are large. This is due to the broadside radiation of the slot, which should be suppressed, and the slot should actually be narrow. On the other hand, if the slot is too narrow, the matching of the UDR-SIW would heavily deteriorate due to the machining error of the slot, so that a balance between the suppression of the broadside radiation and the machining tolerance is necessary.

Different from the reflections in a conventional Fabry-Perot cavity, the reflections on both the front-end and back-end in the UDR-SIW are not much stronger because the relative permittivity of the dielectric in Figure 3.1 is only 3.55. Consequently, at the back-end the reflected wave from the front-end is smaller than the direct wave from the slot, and as such the two waves could not be fully counterbalanced. Thus, the FTBR could not be very high. When the permittivity of a dielectric is high, e.g. over 16, the reflections on both the front-end and back-end are much stronger, and the FTBR would be also higher.

At the input port of the antenna, the transverse slots on the feeding SIW could be equivalent to a series impedance, consisting of a radiating resistor and a reactance. On the other hand, the shorting terminal in the feeding SIW could provide an opposite reactance to the slot reactance. It will benefit the matching of the UDR-SIW antenna.

3.1.2.3 Parametric study

Because the shorting end in the embedded feeding SIW can be used to tune the matching condition of the proposed UDR-SIW effectively, the parametric study could be concentrated on the parameters relative to the dielectric substrates. During the simulations, only a parameter is changed while the other parameters preserve the values listed in Figure 3.1 caption.

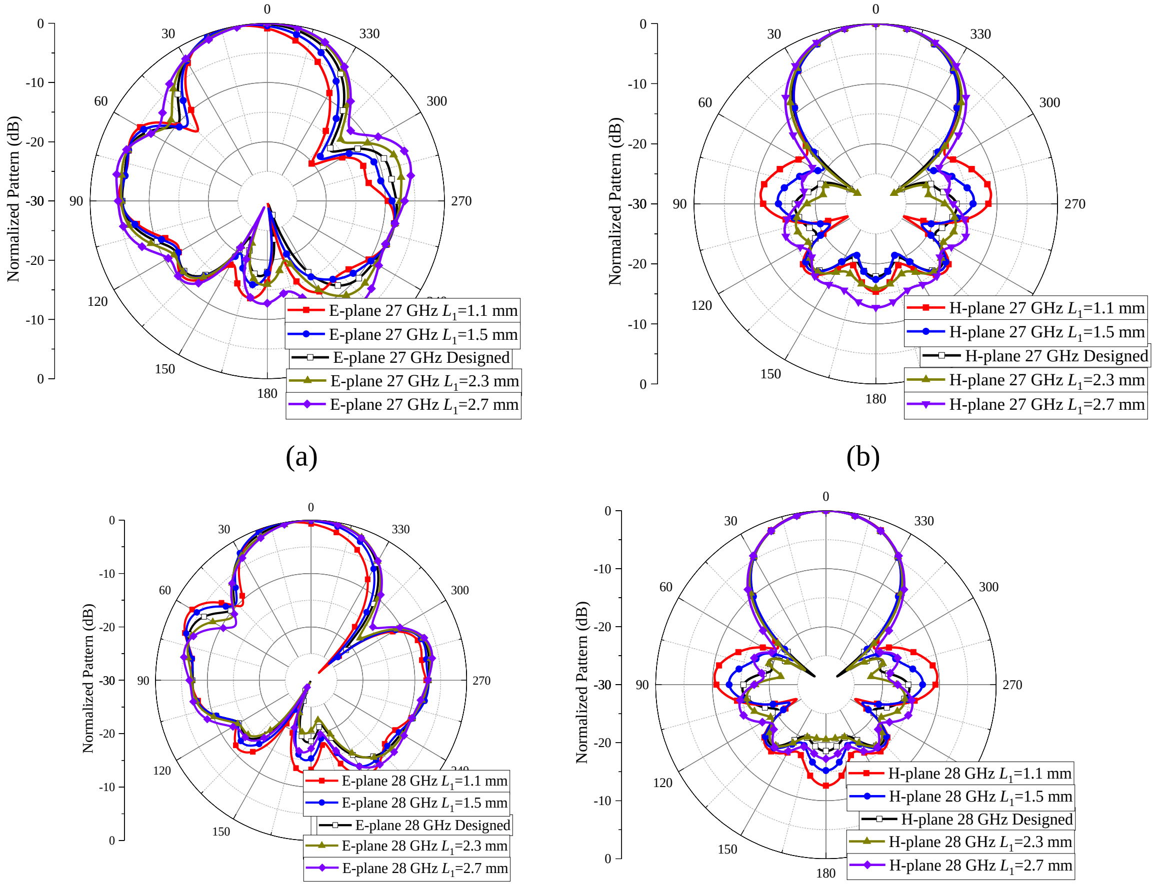

(a) (b)

(c) (d)

Figure 3.9: Radiation patterns of UDR-SIW with different distance from slot to backward end of dielectric substrate

(a) E-plane at 27 GHz, (b) H-plane at 27 GHz, (c) E-plane at 28 GHz and (d) H-plane at 28 GHz

Figure 3.9 shows the simulated patterns on the E-plane and H-plane at 27 GHz and 28 GHz with different distances from the feeding slots to the back-end of the dielectric substrates. The distance has a stronger effect on the main lobe of the E-plane than the H-plane. This phenomenon indicates that the dielectric substrates could be used to shape the E-plane radiation pattern. It is obvious that the distance has a strong effect on the FTBR of the proposed antenna, and thus a proper distance is important to the FTBR.

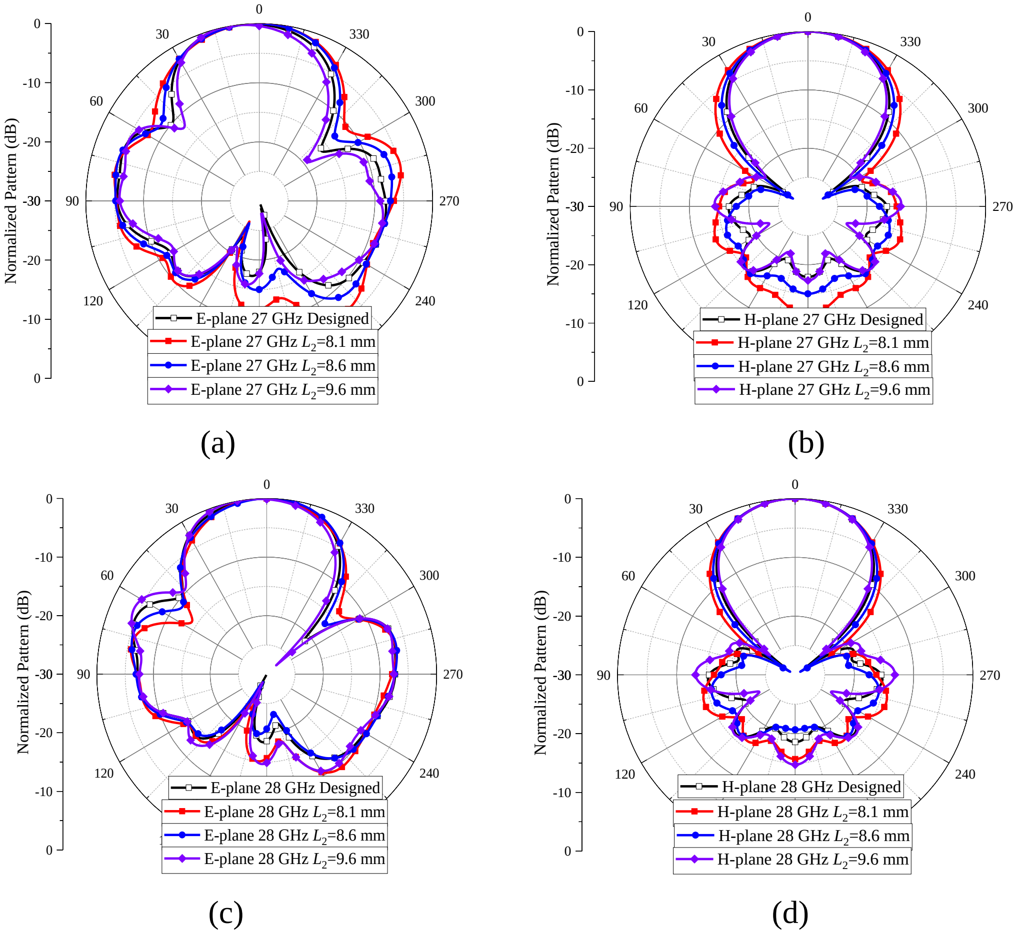

(a) (b)

(c) (d)

Figure 3.10: Radiation patterns of UDR-SIW with different distance from slot to forward end of dielectric substrate

(a) E-plane at 27 GHz, (b) H-plane at 27 GHz, (c) E-plane at 28 GHz and (d) H-plane at 28 GHz

Figure 3.10 presents the simulated patterns on the E-plane and the H-plane at 27 GHz and 28 GHz with different distance from the feeding slot to the front-end of the dielectric substrate. The distance also has a stronger effect on the main lobe of the E-plane than the H-plane. It is obvious that the distance also manifests a strong effect on the FTBR of the proposed antenna. Therefore, a proper distance is reiterated to be important to the FTBR.

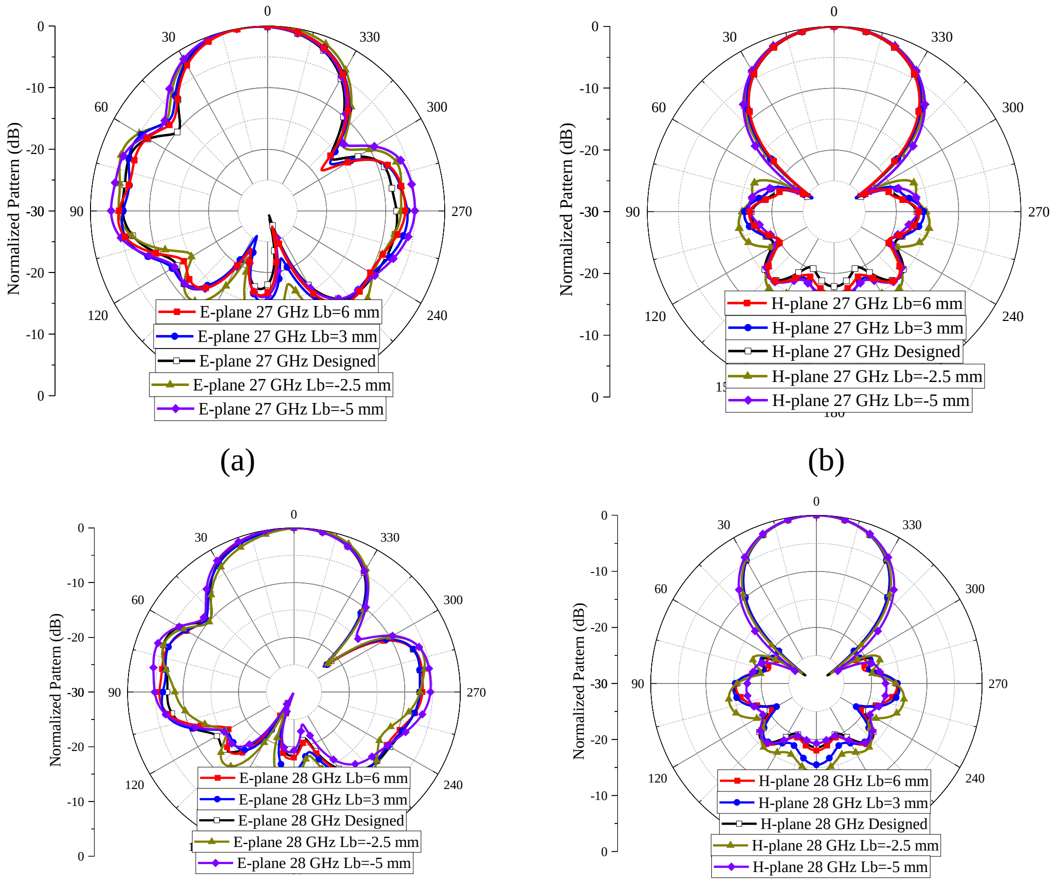

(a) (b)

(c) (d)

Figure 3.11: Radiation patterns of UDR-SIW with different lengths of feeding SIW

(a) E-plane at 27 GHz, (b) H-plane at 27 GHz, (c) E-plane at 28 GHz and (d) H-plane at 28 GHz

Figure 3.11 plots the simulated patterns on the E-plane and the H-plane at 27 GHz and 28 GHz with different lengths of the feeding SIW. When the length is negative, it represents a shorter distance from the slot to the end of the SIW than to the end of the dielectric substrate. In this case, the distance has little effect on the main lobe, and it mainly affects the FTBR. It is well understood because the feeding SIW also acts as the conducting plate of the UDR, and its length would affect the reflection at the front-end.

3.1.2.4 Design Guide

The following is a narrative description of the design guide for the proposed UDR-SIW antenna.

(1) To choose the dielectric substrate. The substrate should be thick enough to ensure the TM_{11}^{y} propagation in the dielectric substrate. An accurate relationship between dielectric sizes and its cut-off frequency is indirect and complex. In early design consideration for simplicity, an approximate formula (3.26) should be used to calculate the phase constant. In practical design, the thickness and permittivity of a dielectric substrate are usually specified. The width of the dielectric substrate could be used to tune the propagation constant of TM_{11}^{y} in the dielectric medium.

(2) To choose the SIW substrate. The substrate should be thin enough to ensure a reasonable performance and an easy integration with an RF subsystem. Usually its thickness should be $0.05\lambda_0$ in the millimeter-wave range.

(3) To determine the width of the SIW and dielectric. The choice of the width should ensure the TE_{10} propagation in the SIW. Usually the width is larger than the thickness of the dielectric so that the TM_{11}^{y} is also a propagating mode in the dielectric substrate.

(4) To determine the length of the dielectric. The L1 should be made as short as possible, and the value of n in (3.31) should be 1. The L2 is actually the main body of the antenna, which should be much larger than L1 for a desired gain.

(5) To determine the distance between the slot and the shorting terminal. The initial distance should be roughly a quarter-wavelength of TE_{10} for a large coupling between the SIW and the UDR. To ensure a good matching, the distance should be tuned at the last step of design.

(6) Finally, the aforementioned parameters should be optimized using a full wave simulation tool to ensure a good matching, a high FTBR, a desired pattern, and a desired gain, as well as a balance between performances and size.

3.1.3 Simulation and Measurement Results

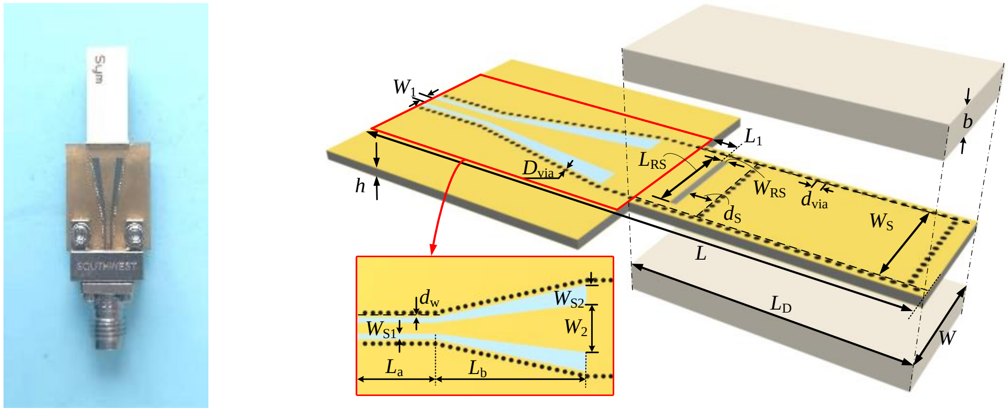

(a) (b)

Figure 3.12: (a) Prototype of UDR-SIW and (b) its structure diagram

(W_S=6, W_{S1}=0.33, W_{S2}=1.225, W_1=0.72, W_2=3.12, W_{RS}=0.4, W=7, D_{via}=, d_w=0.3, d_S=1.4, d_{via}=0.51, L=31.7, L_D=14.8, L_a=5, L_b=9.71, L_{RS}=5.05, L_1=1.7, h=0.508, b=1.524. unit: mm)

To verify the results of the simulation, an experimental prototype of the proposed UDR-SIW antenna has been designed, fabricated and measured. The size of the prototype has been optimized based on the UDR-SIW of Figure 3.1 to improve the radiation symmetry and gain. Fig. 12 shows the prototype and its geometric components. The feeding SIW substrate is Rogers5880 with εr=2.2, and the dielectric substrate is RO4003 of ε_r=3.55.

The UDR-SIW antenna has a compact planar structure suitable for mingled multilayer RF sub-systems and arrays. The UDR-SIW, including a transition of CPW-SIW, is $2.96\lambda_0*0.65\lambda_0*0.33\lambda_0$, and the feeding substrate is $0.047\lambda_0$ thick. When designed for a practical system, the UDR-SIW would be easily integrated with other components due to the thin feeding substrates; a transition would be unnecessary. The dimensions of a single URD-SIW area only $1.38\lambda_0*0.60\lambda_0*0.33\lambda_0$.

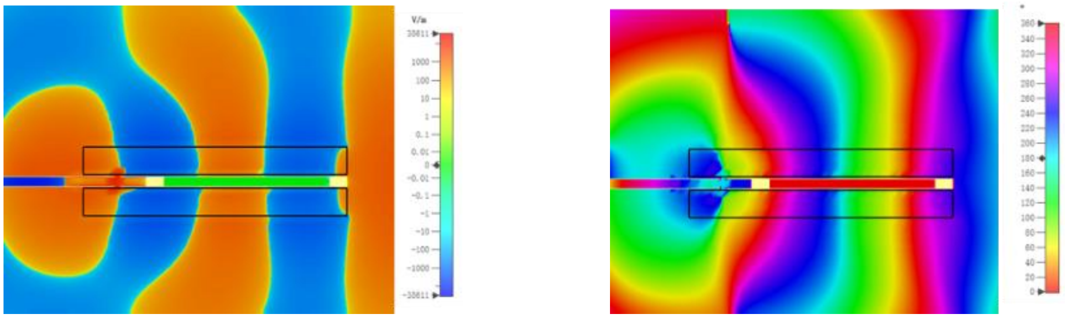

(a) (b)

Figure 3.13: Ey on x=0 plane at 28 GHz (a) magnitude and (b) phase

Fig. 3.13 presents the simulated Ey on plane *x*=0 at 28 GHz, and it shows that the equivalent radiating aperture is much larger than the cross-section of the dielectric substrate. Besides, the distribution of magnitude and phase are rather uniform on the equivalent radiating aperture of the prototype antenna.

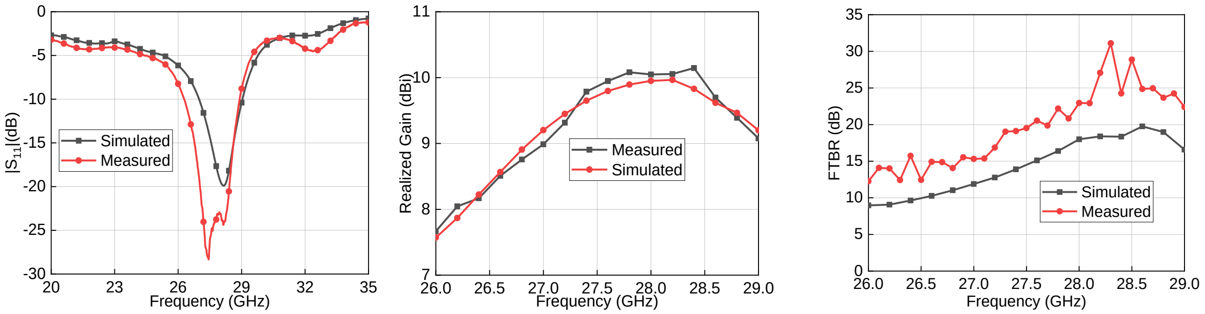

(a) (b) (c)

Figure 3.14: (a) Reflection coefficient, (b) gains of UDR-SIW and (c) FTBR

Figure 3.14 presents the simulated and measured reflection coefficients and gains. The UDR-SIW has a measured bandwidth of 9.4% from 26.3 GHz to 28.9 GHz. The measured gain ranges from 8.2 dBi to 10.3 dBi, and over 10 dBi from 27.7 GHz to 28.4 GHz. The simulated efficiency is 96%, and the UDR-SIW has a $0.76\lambda^2_0$ equivalent radiating aperture when gain is 10 dBi. A big radiating aperture achieved by such a small UDR-SIW. The UDR-SIW has an unidirectional pattern with a FTBR over 20 dB form 27.5 GHz to 29 GHz, which is a significant improvement compared to a conventional SIW horn.

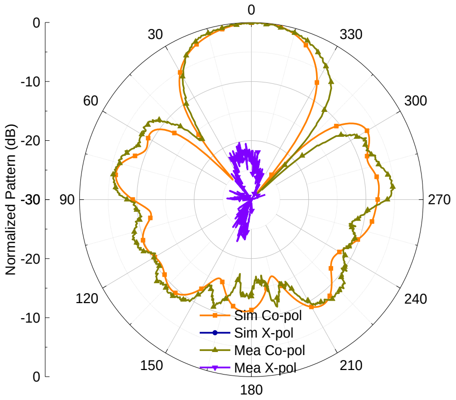
0
30
330
60
300
90
270
120
240
150
210
180
Normalized Pattern (dB)
0
-10
-20
-30
-20
-10
0
Sim Co-pol
Sim X-pol
Mea Co-pol
Mea X-pol

(a)

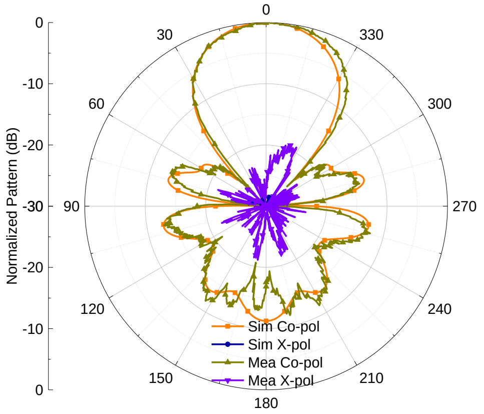
0
30
330
60
300
90
270
120
240
150
210
180
Normalized Pattern (dB)
0
-10
-20
-30
-20
-10
0
Sim Co-pol
Sim X-pol
Mea Co-pol
Mea X-pol

(b)

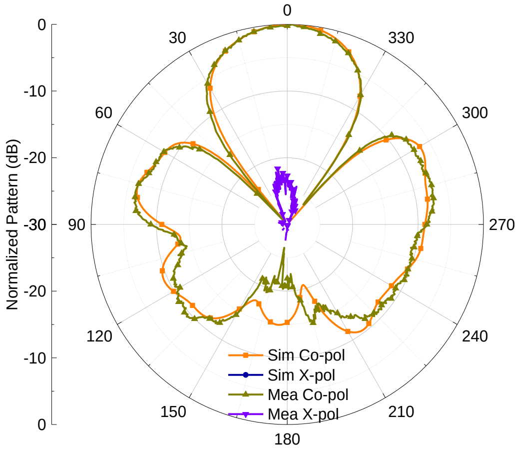
0
30
330
60
300
90
270
120
240
150
210
180
Normalized Pattern (dB)
0
-10
-20
-30
-20
-10
0
Sim Co-pol
Sim X-pol
Mea Co-pol
Mea X-pol

(c)

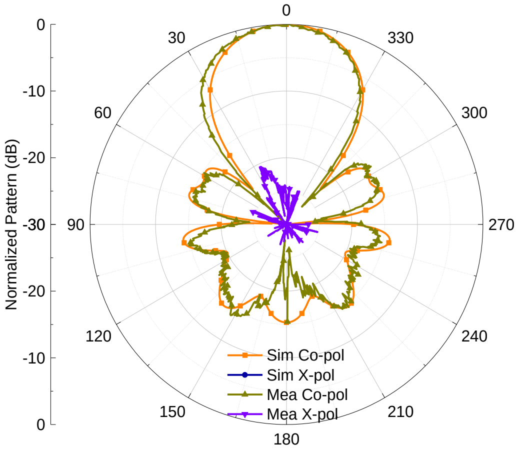
0
30
330
60
300
90
270
120
240
150
210
180
Normalized Pattern (dB)
0
-10
-20
-30
-20
-10
0
Sim Co-pol
Sim X-pol
Mea Co-pol
Mea X-pol

(d)

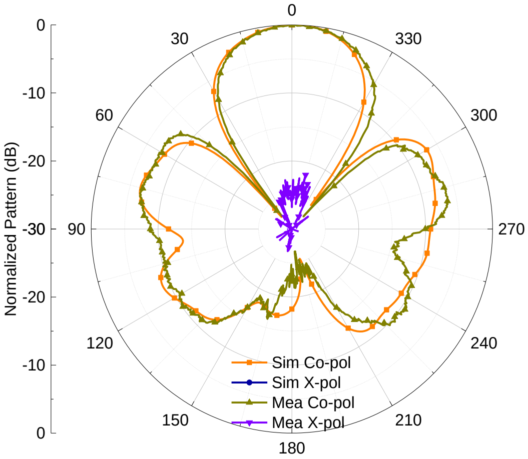
0
30
330
60
300
90
270
120
240
150
210
180
Normalized Pattern (dB)
0
-10
-20
-30
-20
-10
0
Sim Co-pol
Sim X-pol
Mea Co-pol
Mea X-pol

(e)

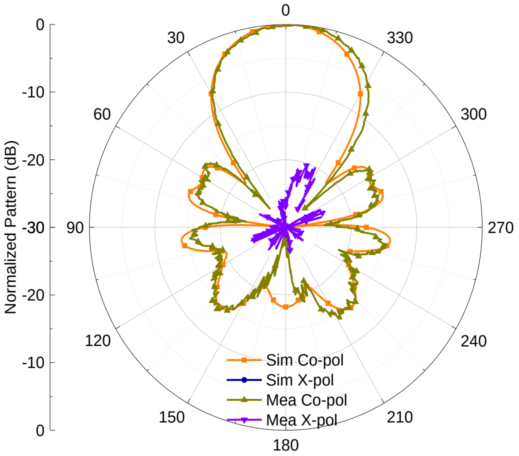
0
30
330
60
300
90
270
120
240
150
210
180
Normalized Pattern (dB)
0
-10
-20
-30
-20
-10
0
Sim Co-pol
Sim X-pol
Mea Co-pol
Mea X-pol

(f)

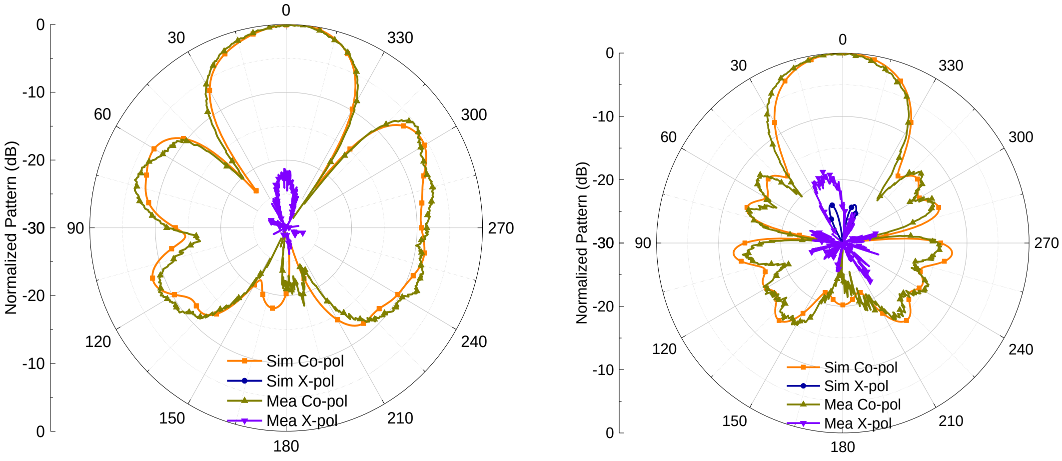

(g) (h)

Figure 3.15: Simulated and measured radiation pattern of UDR-SIW on

(a) E-plane at 26.8 GHz, (b) H-plane 26.8 GHz, (c) E-plane at 27.5 GHz, (d) H-plane 27.5 GHz, (e) E-plane at 28 GHz, (f) H-plane 28 GHz, (g) E-plane at 29 GHz and (h) H-plane 29 GHz

Figure 3.15 gives the simulated and measured radiation patterns at 26.8 GHz, 27.5 GHz, 28GHz and 29 GHz, which agree well with one another. The radiation pattern of a conventional SIW horn is asymmetric. The beam on the E-plane is much wider than that on the H-plane especially if a thin substrate is used. The patterns of the UDR-SIW are symmetric on both the E-plane and H-plane. The simulated and measured patterns on the E-plane and H-plane and the simulated 3-D radiation pattern in Figure 3.16 all show that the antenna has a nearly perfect circularly symmetric main lobe. Therefore, the UDR-SIW is also suitable to be a feeder of compact planar reflected array or lens.

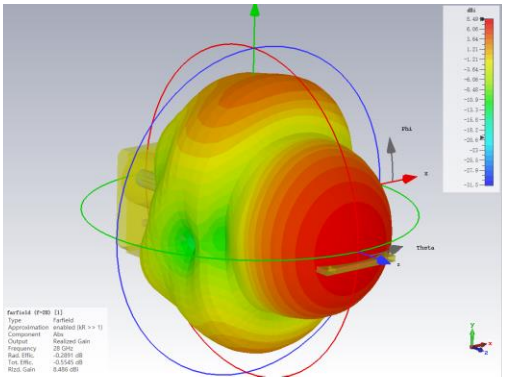

farfield (f=28) [1]

Type	Farfield
Approximation	enabled (kR >> 1)
Component	Abs
Output	Realized Gain
Frequency	28 GHz
Rad. Effic.	-0.2891 dB
Tot. Effic.	-0.5545 dB
Rlzd. Gain	8.486 dBi

Figure 3.16: 3-D pattern of the UDR-SIW

The proposed UDR-SIW antenna demonstrates its compact size, large FTBR, and symmetric radiation pattern. Different from a conventional UDR antenna, the UDR-SIW has a VP radiation pattern which is the same as an SIW H-plane horn or an open-end SIW. When its gain is required to be high, an SIW H-plane horn must flare in the H-plane largely due to the limitation of the thickness of the SIW. In turn, it leads to a big transverse size and an asymmetric radiation pattern on both the E-plane and H-plane. The UDR-SIW presents a smart mingled multilayer substrate structure that makes it possible to not only use a thick dielectric substrate to narrow the E-plane pattern, but also use a thin embedded feeding SIW to facilitate its integration with RF subsystems. Therefore, the proposed UDR-SIW would be a competitive candidate to replace the SIW H-plane horn in certain applications.

3.2 UDR-ALTSA End-fire CP Antenna fed by a very thin Slotted SIW

3.2.1 Introduction

Up to now, to the knowledge of the author, the feeding layers of end-fire CP planar antennas are not made thin enough. The end-fire CP composite antennas based on SIW H-plane horn could be designed as fully planar structures but still use thick substrates [44], [76]-[79]. In [44],[78], SIW end-fire dual CP antennas made use of two-layer substrate. In the transition section of the SIW, a sloping open slot is set to transform the TE_{10} mode into two orthogonal modes, namely TE_{10} and TE_{01}. To radiate these two orthogonal modes in a common horn of the SIW, the antenna must use two thick substrates. The total thickness is more than $0.6\lambda_0$. In [79], the end-fire CP planar composite antenna is composed of ALTSA and SIW horns. The ALTSA is fed by the SIW, and it produces HP radiation. The open aperture of the SIW produces VP radiation. Consequently, the substrates used in the SIW must be thick for the equality of the two orthogonally polarized components. It resulted with a thickness of more than $0.127\lambda_0$ in [79]. Again, the development of end-fire CP planar helical antennas is also based on a thick substrate to achieve CP radiation [42],[47],[143].

Dielectric rod antennas are one kind of end-fire antennas, which have been used to enhance the performance of gains and/or bandwidth, for instance, in end-fire antennas [77] [131]-[134]. The shapes of dielectric rods and their positions in the antennas are not fit for the requirement of a fully planar integration with RF circuits. Among these antennas, the reported work in [77] is the only end-fire CP planar antenna. Although the waveguide transitions in [77] could be replaced by planar transitions, these planar transitions are actually not practical for an easy integration with a related RF subsystem. To further increase the gain and FTBR of the antenna, a thick three-layer tapered dielectric rod is placed in front of the antenna. The ALTSA in [77] must first produce CP radiation because the dielectric rod enhances both the VP and HP radiations equally. Therefore, the substrate of an ALTSA-based CP antenna could not be thinner than the limiting case. The current works show that the limitation of thickness is about $0.12\lambda_0$. The CP antenna in [77] uses a substrate of $0.15\lambda_0$ to ensure an equal amplitude of two orthogonally polarized radiations. On the other hand, a dielectric rod is usually placed in front of its feeding radiator for an effective excitation, and it would increase the length of the whole antenna.

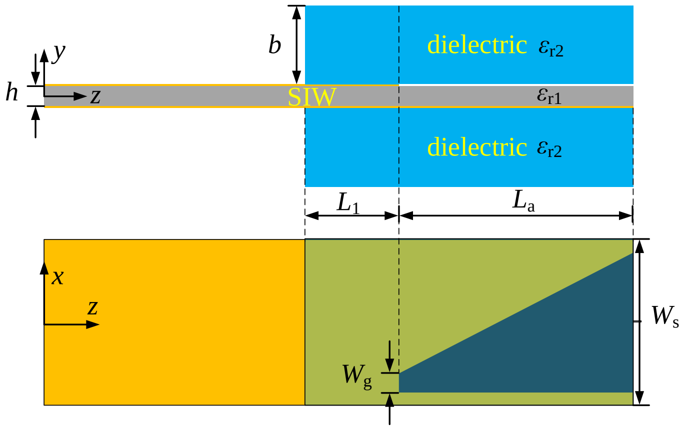

Figure 3.17: Configuration of UDR-ALTSA end-fire CP antenna

(L_1=5.72 mm, L_a=10.1 mm, W_S=7.4 mm, W_g=1.3 mm, h=0.508 mm, b=1.524 mm, ε_{r1}=2.2, ε_{r2}=3.55)

This work devises and presents UDR-ALTSA end-fire CP planar composite antenna, as shown in Figure 3.17. The proposed UDR-ALTSA antenna consists of a UDR and an ALTSA fed by an SIW. The UDR is a pair of dielectric substrate blocks placed symmetrically on the top and bottom sides of the feeding substrate which has a thickness of $0.05\lambda_0$. The open aperture of the SIW and the ALTSA could excite a VP field in the UDR, and in turn the UDR would produce the enhanced

VP end-fire radiation. The open aperture would also feed the ALTSA to produce HP radiation, though the UDR would not enhance the original HP radiation of the ALTSA. The selective enhancement of the VP radiation ensures an equal amplitude of VP and HP radiations so that a CP end-fire radiation is realized in the end.

The proposed UDR-ALTSA end-fire CP planar composite antenna has the following new features:

(1) The unique UDR enhances only the VP radiation rather than the HP radiation of the ALTSA. It also provides a way to modify the VP-to-HP ratio of the anticipated radiations.

(2) The fully planar end-fire CP antenna has a thin feeding layer of $0.05\lambda_0$. Its high performance, compact size, and easy integration with an RF subsystem make it a good option for building element antennas used in developing a large array.

(3) The UDR antenna is fed by a novel feeding structure.

(4) The multi-function SIW feeding structure can feed both the ALTSA and URD simultaneously.

3.2.2 Mechanism of UDR-ALTSA End-fire CP Radiation

3.2.2.1 Operating Modes in UDR of a UDR-ALTSA

The proposed UDR-ALTSA antenna, shown in Figure 3.17, consists of an ALTSA fed by an SIW on a feeding substrate, and two dielectric blocks placed symmetrically on the top and bottom sides of the feeding substrate. The two dielectric blocks are actually a UDR that is fed by the open aperture of the SIW and the ALTSA. The open aperture is set to excite a TM_{mn}^{y} mode in the UDR. The UDR would in turn produce VP end-fire radiation. On the other hand, the ALTSA could excite the TM_{mn}^{x} mode in the UDR. Both the UDR and the ALTSA can jointly produce HP radiation so that the CP end-fire radiation can be achieved.

How to enhance VP radiation and make it equal to HP radiation is crucial to end-fire CP radiation of an ALTSA on a thin substrate. An ALTSA produces both the HP and VP radiation, however, the VP radiation usually is too weak to match its HP counterpart. This scenario becomes much more pronounced when the substrate is thin. Therefore, when the substrate is thin, it would be impossible for an ALTSA to produce CP radiation. This is why all the presented ALTSA-based

CP antennas make use of substrates with thicknesses greater than $0.12\lambda_0$. In fact, the open aperture of the feeding SIW in an ALTSA also produces VP radiation. The simulated results show that the ALTSA would weaken the original VP radiation produced by the open aperture of the SIW. Therefore, enhancing the VP radiation to make it equal or comparable to the HP radiation is crucial to realize an end-fire CP radiation of ALTSA on a thin substrate. When an ALTSA is loaded with a UDR, since the initial HP radiation is much stronger, the UDR should then be used to enhance the VP radiation rather than the HP radiation.

To clearly understand how a UDR affects the HP and VP radiation of an ALTSA differently, one should examine the modes of the UDR and how the ALTSA excites these modes.

The TM^y_{mn} mode in a dielectric with ground plane has been introduced in Section 3.1.2. For TM^x_{mn} in Figure 3.2 (c), there is $H_x = 0$, and E_x and H_y are main components of propagating modes. The other field components of TM^x_{mn} can be expressed with H_y as follows:

$$E_x = \frac{\omega\mu}{\beta} H_y + \frac{1}{\omega\varepsilon\beta}\frac{\partial^2 H_y}{\partial x^2} \tag{3.34}$$

$$E_y = \frac{1}{\omega\varepsilon\beta}\frac{\partial^2 H_y}{\partial x \partial y} \tag{3.35}$$

$$E_z = \frac{j}{\omega\varepsilon}\frac{\partial H_y}{\partial x} \tag{3.36}$$

$$H_z = -\frac{j}{\beta}\frac{\partial H_y}{\partial y} \tag{3.37}$$

As an approximation, one could ignore the fields in region IV, and H_y in other regions are as follows

$$H_y = H_1 \cos(k_x x)\cos(k_y y + \eta_y) e^{-j\beta z}, \quad (|x| < 0.5a, |y| < b) \qquad \text{in region I} \tag{3.38}$$

$$H_y = H_2 \cos(k_x x) e^{-\alpha_y |y|} e^{-j\beta z}, \quad (|y| \geq b) \qquad \text{in region II} \tag{3.39}$$

$$H_y = H_3 \cos(k_y y + \eta_y) e^{-\alpha_x |x|} e^{-j\beta z}, \quad (|x| \geq 0.5a) \qquad \text{in region III} \tag{3.40}$$

To use similar method as Section 3.1.2, one can have following eigen equations

$$k_x a = m\pi - 2\arctan(\frac{k_x}{\varepsilon_r \alpha_x}),(m=1,2,3,\cdots) \tag{3.41}$$

$$\alpha_x = \sqrt{k_0^2(\varepsilon_r - 1) - k_x^2} \tag{3.42}$$

$$N^2 = \varepsilon_r - \left(\frac{k_x}{k_0}\right)^2 \tag{3.43}$$

$$\alpha'_y = \sqrt{k_0^2(\varepsilon_r - 1) - k_x^2 - k_y^2} \tag{3.44}$$

$$2k_y b = n\pi - 2\arctan(\frac{k_y}{\alpha'_y}),(n=1,2,3\cdots) \tag{3.45}$$

$$\beta = \sqrt{k_0^2\varepsilon_r - k_x^2 - k_y^2} \tag{3.46}$$

The electric fields and magnetic fields of TM_{mn}^{x} in a rectangle dielectric rod, shown in Figure 3.2 (c), are as follows:

$$E_x = H_1 \cos(k_x x)\cos(k_y y + \eta_y)(\frac{\omega\mu}{\beta} - \frac{k_x^2}{\omega\varepsilon\beta})e^{-j\beta z} \tag{3.47}$$

$$E_y = \frac{H_0 k_x k_y}{\omega\varepsilon\beta}\sin(k_x x)\sin(k_y y + \eta_y)e^{-j\beta z} \tag{3.48}$$

$$E_z = \frac{jk_x H_0}{\omega\varepsilon}\sin(k_x x)\cos(k_y y + \eta_y)e^{-j\beta z} \tag{3.49}$$

$$H_x = 0 \tag{3.50}$$

$$H_y = H_1 \cos(k_x x)\cos(k_y y + \eta_y)e^{-j\beta z} \tag{3.51}$$

$$H_z = \frac{jk_y H_1}{\beta}\cos(k_x x)\sin(k_y y + \eta_y)e^{-j\beta z} \tag{3.52}$$

The main field components of TM_{mn}^{y} are E_y and H_x, and H_y=0. Therefore, a TM_{mn}^{y} mode is associated with a VP field in the UDR-ALTSA antenna. After a TM_{mn}^{y} is rotated by 90-degree to the z-axis, it will become a TM_{mn}^{x}. A TM_{mn}^{x} is associated with an HP field in the UDR-ALTSA antenna. One can deduce each field components of TM_{mn}^{x} mode using formulas (3.47)-(3.52). When η_y=0, TM_{mn}^{x} mode reaches the maximum E_x on y=0 plane, and Figure 3.18 is a sketch picture of the field configuration of TM_{11}^{x} on cross sections of dielectric.

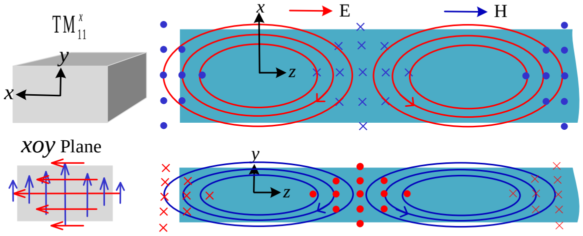

Figure 3.18: Sketch picture of the field configuration of TM_{11}^{x}

3.2.2.2 Mechanism of CP radiation

To achieve CP radiation, it is important that the UDR in a UDR-ALTSA should enhance the original VP radiation much more than the HP radiation from the ALTSA and ideally even equalize the VP radiation to the HP radiation. How could this be achieved? The following is an explanation for such a procedure based on modes in the UDR.

A UDR fed by an ALTSA could be divided into four regions as shown in Figure 3.19 (a). A TM_{11}^{y} mode could exist in region I, II and III, almost the whole UDR. The two flaring metal plates of the ALTSA act as a PEC in Figure 3.2 (b) and do not suppress TM_{11}^{y}. A TM_{11}^{x} mode could exist only in region II where have a maximum E_x on y=0 plane. On the other hand, TM_{11}^{x} could not appear in region I, III, and IV where E_x=0 due to the two flaring metal plates.

When a TE10 mode in an SIW is feeding into the ALTSA, the E_y in region I would excite a TM_{11}^{y} mode in the whole UDR. Consequently, the UDR can effectively enhance the original VP radiation in the ALTSA.

On the other hand, the HP component of the ALTSA would excite the TM_{11}^{x} mode only in Region II of the UDR. Region II, as shown in Figure 3.19 (b), is a dielectric rod with a tapered width, which could be treated as several cascading dielectric rods with different uniform widths. The smaller the width is, the higher the cut-off frequency of TM_{11}^{x} is.

The TM_{11}^{x} could not be excited in the left red area of Region II where the cut-off frequency of TM_{11}^{x} is higher than the operating frequency. However, it can only be excited in the right green area where the cut-off frequency of TM_{11}^{x} is lower than the operating frequency. Therefore, the ALTSA excites TM_{11}^{x} only in a small area of the UDR, and the UDR cannot effectively enhance the original HP radiation from the ALTSA. Moreover, because the propagating area of TM_{11}^{x} is at the tail end of the UDR-ALTSA, most of the power is used to excite the TM_{11}^{y} mode before it reaches the propagating area of TM_{11}^{x}. Consequently, the power used to excite the TM_{11}^{x} mode is much lower than the power used to excite the TM_{11}^{y} mode in the UDR-ALTSA. From a power distribution network viewpoint, the VP radiator takes up a bigger portion of power than the HP radiator.

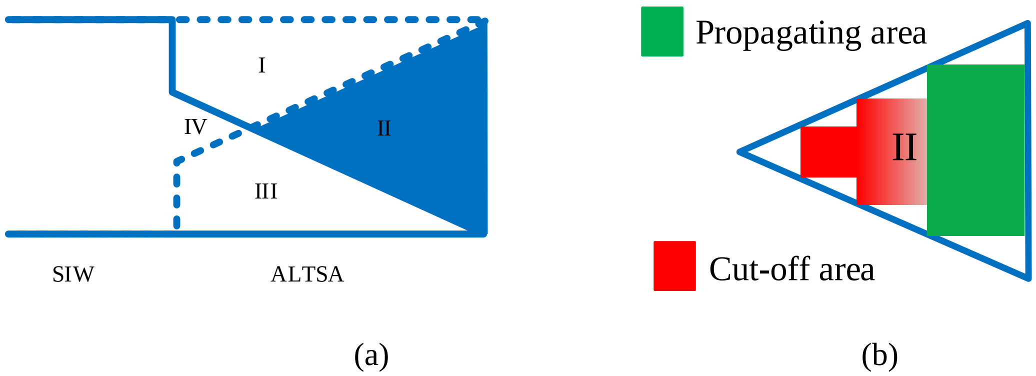

(a) (b)

Figure 3.19: (a) Four regions and (b) Region II and its cascaded dielectric rods

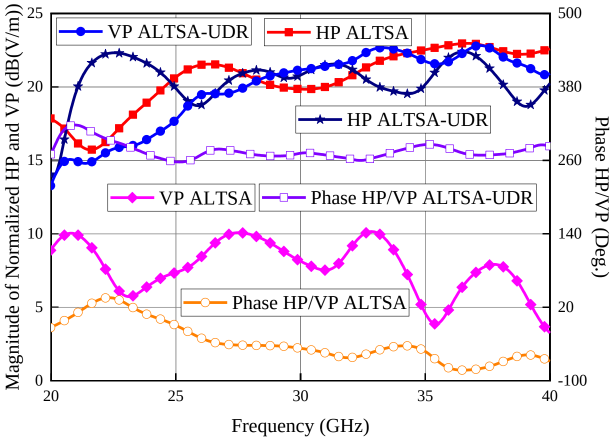

Figure 3.20: Radiation comparison（HP/VP）and phase difference of ALTSA and UDR-ALTSA vs frequency in far zone

The UDR-ALTSA uses two modes of TM_{11}^{y} and TM_{11}^{x} in the UDR together with a smart exciting structure, thus achieving a CP radiation. It is important to note that the UDR in the UDR-ALTSA antenna can affect the VP and HP radiations in different ways.

To numerically evaluate the effects on the HP and the VP radiations of a UDR loaded on an ALTSA, the ratios of HP to VP radiations from the ALTSA with a 0.508 mm thick substrate and the UDR-ALTSA of Figure 3.17 have been simulated at *z*=1000 mm for the end-fire direction, where the far zone is for both antennas. The thickness and the relative permittivity of the dielectric substrates in the UDR-ALTSA are chosen to ensure the effective propagation of the TM_{11}^{y} mode. The dielectric blocks are the same width as ALTSA’s. This would benefit its fabrication in the future. To remove the reflection effect on the radiation strength, both the HP and the VP radiating fields are all normalized using $(1-|S_{11}|^2)$. Figure 3.20 shows that the original VP radiation produced only by an ALTSA without a UDR are much weaker than the HP radiation. It also shows that the UDR in the UDR-ALTSA does mainly enhance the VP radiation rather than the HP radiation of the ALTSA. Moreover, the phase difference between the HP and VP radiations of a UDR-ALTSA becomes smoother than a single ALTSA. It would be benefit from a wider axial ratio (AR) bandwidth.

3.2.2.3 Parameter Study

The length, gap width, dielectric substrate thickness, and dielectric permittivity of an ALTSA are key influential parameters in the performances of an UDR-ALSTA. Parametric studies are implemented to explore the effects of these parameters on CP performances. When a parameter changes in the following simulations, the other parameters will remain the same as in the caption of Figure 3.17.

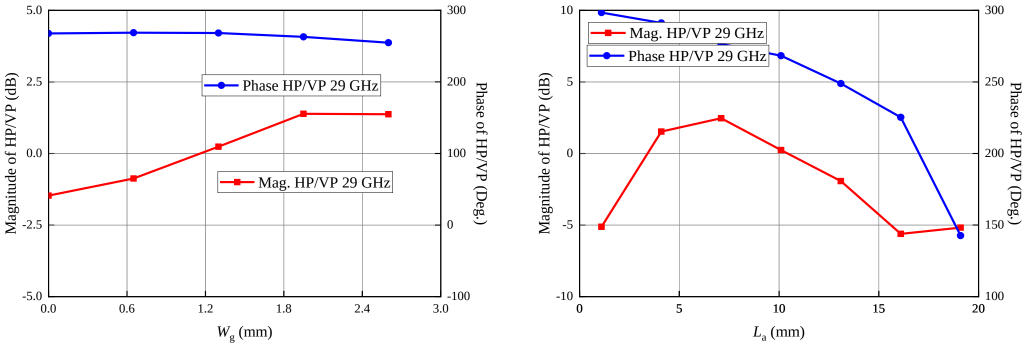

(a) (b)

Figure 3.21: Ratio of HP to VP radiations from ALTSAs in far zone at 29 GHz with different (a) the gap widths and (b) lengths of ALTSA

Figure 3.21 presents the ratios of HP to VP radiation from the UDR-ALTSAs in the far zone at 29 GHz with different gap widths W_g and lengths L_a of the ALTSA. It shows that both parameters could be used to tune the magnitude ratio of HP to VP radiation, and the length of ALTSA could be also used to turn the phase difference between the HP and VP radiation. The results are important to provide an appropriate design guideline for the UDR-ALTSA CP antenna.

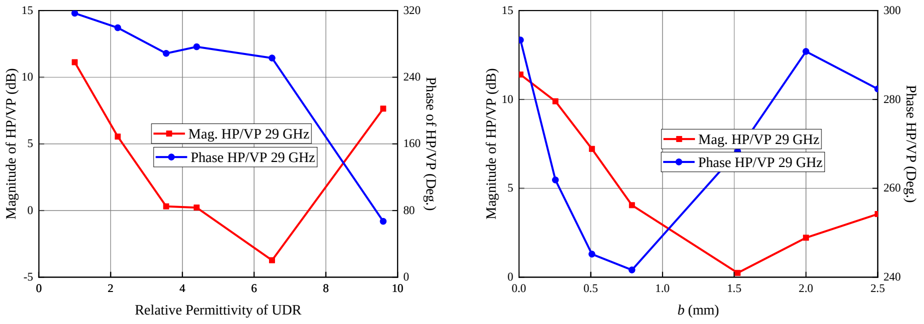

(a) (b)

Figure 3.22: Ratio of HP to VP radiations from ALTSAs in far zone at 29 GHz with different (a) dielectric permittivity and (b) the thickness of UDR

On the other hand, Figure 3.228 depicts the ratios of HP to VP radiation in the far zone at 29 GHz with different dielectric permittivity and thicknesses of UDR. It suggests that the permittivity should have large effects on the ratio of HP to VP radiation. When the permittivity is very low, e.g. $\varepsilon_r = 2.2$, the TM_{11}^y cannot exist so that the VP radiation enhancement is not available. When the permittivity is modest, e.g. $\varepsilon_r = 3.55$ or $\varepsilon_r = 6.6$, the TM_{11}^y can exist, and the VP radiation can be enhanced effectively, even exceeding the HP radiation. When the permittivity is high, e.g. $\varepsilon_r = 9.8$, not only can TM_{11}^y be excited effectively but also TM_{11}^x; then, the magnitude ratio increases again. When the permittivity changes but is not very high, the phase difference between the HP and VP radiation remains smooth. When the permittivity becomes high, however, the phase difference would change drastically. It is due to the improper excitation of TM_{11}^x.

The thickness effects of the UDR could be also explained by its modes. When a UDR is thin, e.g. 0.254 mm, the TM_{11}^y is in a cut-off state, and the VP radiation enhancement is not available. When a UDR is very thick, e.g. 2.54 mm, the TM_{11}^y does not synchronize well with the exciting E_y in the ALTSA, and the VP radiation enhancement does not occur very well.

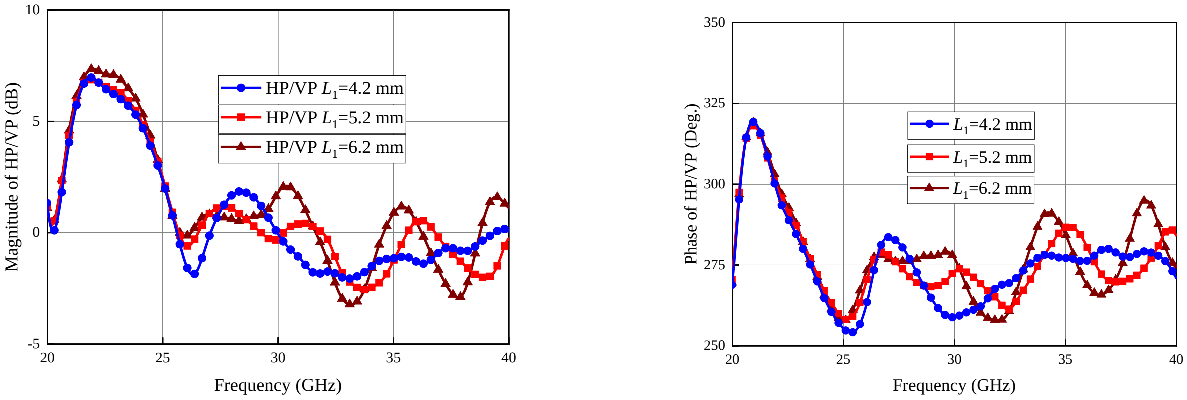

(a) (b)

Figure 3.23: Ratios of HP to VP radiations from ALTSAs in far zone with different backward lengths of UDR: (a) magnitude and (b) phase

Figure 3.23 describes the ratios of HP to VP radiations from ALTSAs in the far zone with different backward lengths of the UDR. It shows that when frequency exceeds 27 GHz, both the magnitude and phase curves are smooth, which means that the effects of the length are relatively small.

The results plotted in Figure 3.21 to 3.23 suggest that the phase difference between the VP and HP radiation is not so sensitive to the UDR parameters. The ALTSA and the feeding SIW are also travelling-wave structures generally with wide bandwidths. All those features would be beneficial for a CP antenna with a wide bandwidth.

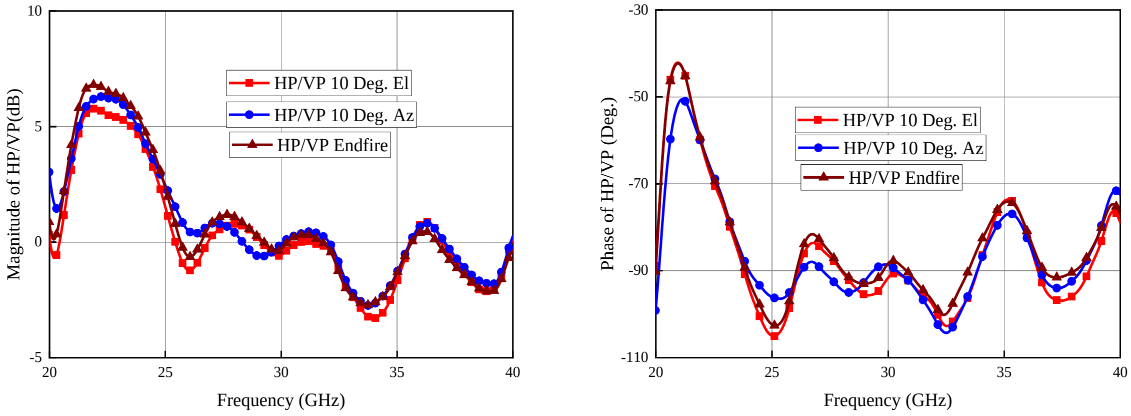

(a) (b)

Figure 3.24: Ratios of HP to VP radiations in far zone in far zone vs frequency at end-fire direction, 10^{o} azimuth angle and 10^{o} elevation angle

To examine how well the UDR-ALTSA could satisfy the CP radiation conditions, Figure 3.24 shows the ratios of HP to VP radiation at three spatial angles in the far zone at different frequencies. The magnitude and phase conditions remain stationary when frequency exceeds 27 GHz. The little difference observed in the curves of different spatial angles also implies a wide AR beam width.

3.2.2.4 Design Guide

Based on the mechanism of the proposed UDR-ALTSA antenna and its parametric study, a design guideline can be summarized as follows.

(1) Choose a dielectric substrate. The substrate should be thick enough to ensure a TM_{11}^{y} propagation in the substrate. The accurate relationship between the dielectric thickness and the cut-off frequency of the TM_{11}^{y} mode is indirect and complex. A simulation tool can be used to extract information related to such a relationship; the formula (3.26) can be used for a primary design. For practical design, the thickness and permittivity of a dielectric substrate are usually specified. The width of the dielectric can be used to tune the propagation constant of TM_{11}^{y} in the dielectric.

(2) Consider the SIW substrate. The substrate should be thin enough to ensure a reasonable performance and an easy integration with an RF subsystem. Usually its thickness should be less than $0.05\lambda_0$ in the millimeter wave range.

(3) Determine the width of the SIW and dielectrics. The width should ensure the TE_{10} propagation in the SIW. Usually, the width is larger than the thickness of the dielectrics so that the TM_{11}^{y} is also a propagating mode in the dielectric after the TE_{10} propagates in the SIW.

(4) Select the lengths of the UDR and ALTSA. The longer the UDR and ALTSA are, the higher the gain of the CP antenna becomes. Besides, the parameters of the UDR and ALTSA can be used to tune the magnitude ratio and the phase difference between the HP and VP radiations.

(5) Optimize the above-mentioned parameters using a full-wave simulation tool to ensure good matching, wide impedance and AR bandwidth, and desired gain. It also helps to balance performance and size.

3.2.3 Simulation and Measurement Results

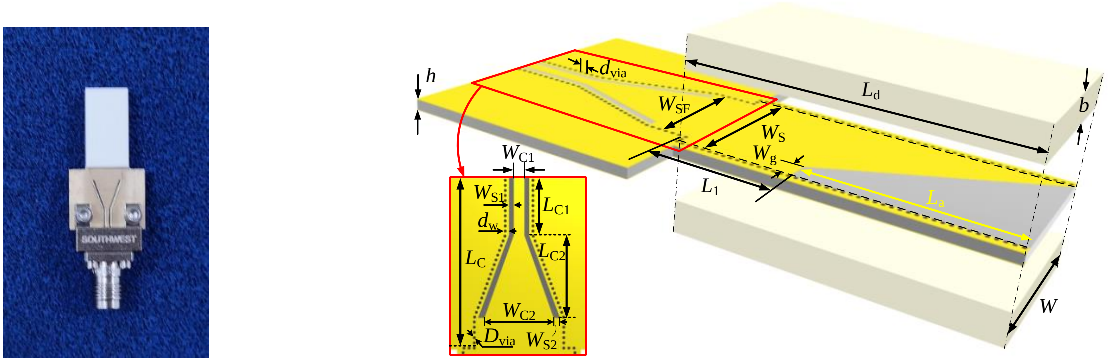

(a) (b)

Figure 3.25: (a) Prototype of UDR-ALTSA and (b) its structure diagram

(h=0.508, b=1.524, D_{via}=0.2, d_{via}=0.35, d_w=0.35, L_1=5.72, L_a=10.1, L_d=15.3, L_C=11.7, L_{C1}=4, L_{C2}=5.7, W_{S1}=0.33, W_{S2}=0.435, W_{C1}=0.72, W_{C2}=4.7, W_g=1.3, W_S=7.4, W_{SF}=5.9, W=8.4. unit: mm)

To verify the discussed mechanism and design considerations, an experimental prototype of the proposed UDR-ALTSA, as shown in Figure 3.25, has been designed, fabricated and measured. The operating frequency of the prototype is set at 28 GHz and above so that it can be applied in 5G or

B5G systems. Most of the parameters of a UDR-ALTSA can be determined by the design guideline in the previous section. A connector and a CPW-SIW transition, however, must be added to the UDR-ALTSA for measurement. Because the UDR-ALTSA is smaller and thinner than the connector, the connector has strong effects on the radiation performances of the UDR-ALTSA. It actually degrades its AR. As a result, the parameters of the prototype in Figure 3.21 are determined only after co-simulations of the whole prototype, including the connector and the CPW-SIW transition.

The prototype of the UDR-ALTSA, including the CPW-SIW transition, is only $2.57\lambda_0*0.78\lambda_0*0.33\lambda_0$ at 28 GHz. Thanks to its compact size and fully planar structure, the UDR-ALTSA end-fire CP antenna is a suitable candidate for the antenna element of a large array. When used as an element antenna, the UDR-ALTSA will be fed with an SIW feeding network, which does not need a connector or a transition of CPW-SIW for measuring. Also, the two margins between two element antennas would be unnecessary. Therefore, the size of the UDR-ALTSA in an array is actually $1.48\lambda_0*0.73\lambda_0*0.33\lambda_0$, and the thickness of its feeding substrate is only $0.047\lambda_0$. The thin feeding substrate would also bring certain benefits to the mingled multilayer feeding network of a large array. For a scanning array with a modest scanning angle, the size is also acceptable, and grating lobes would not exist.

Figure 3.26 depicts the simulated and measured reflection coefficients and realized gains of the UDR-ALTSA. The measured impedance bandwidth for $|S_{11}| < -15dB$ is 15% from 26.65 GHz to 31 GHz, and the bandwidth for $|S_{11}| < -10\,dB$ is 72% or 2.13:1 from 26.15 GHz to 55.8 GHz. The measured gain is over 9 dBi from 27.5 GHz to 34 GHz, and the maximum gain is 11 dBi. Without a connector, the UDR-ALTSA is expected to have a much wider impedance bandwidth. The simulated results with a wave-port in Figure 3.26 have indeed verified the presented proposition.

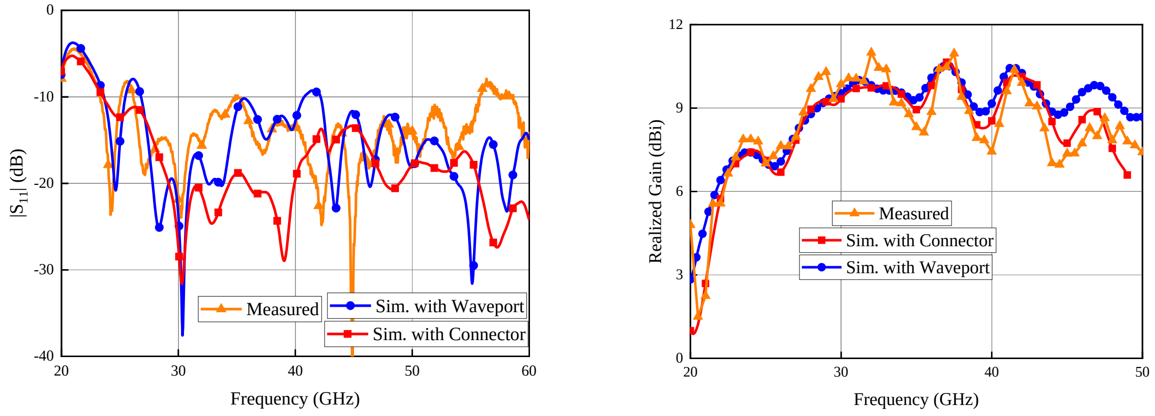

(a) (b)

Figure 3.26: (a) Reflection coefficient and (b) gains of UDR-ALTSA

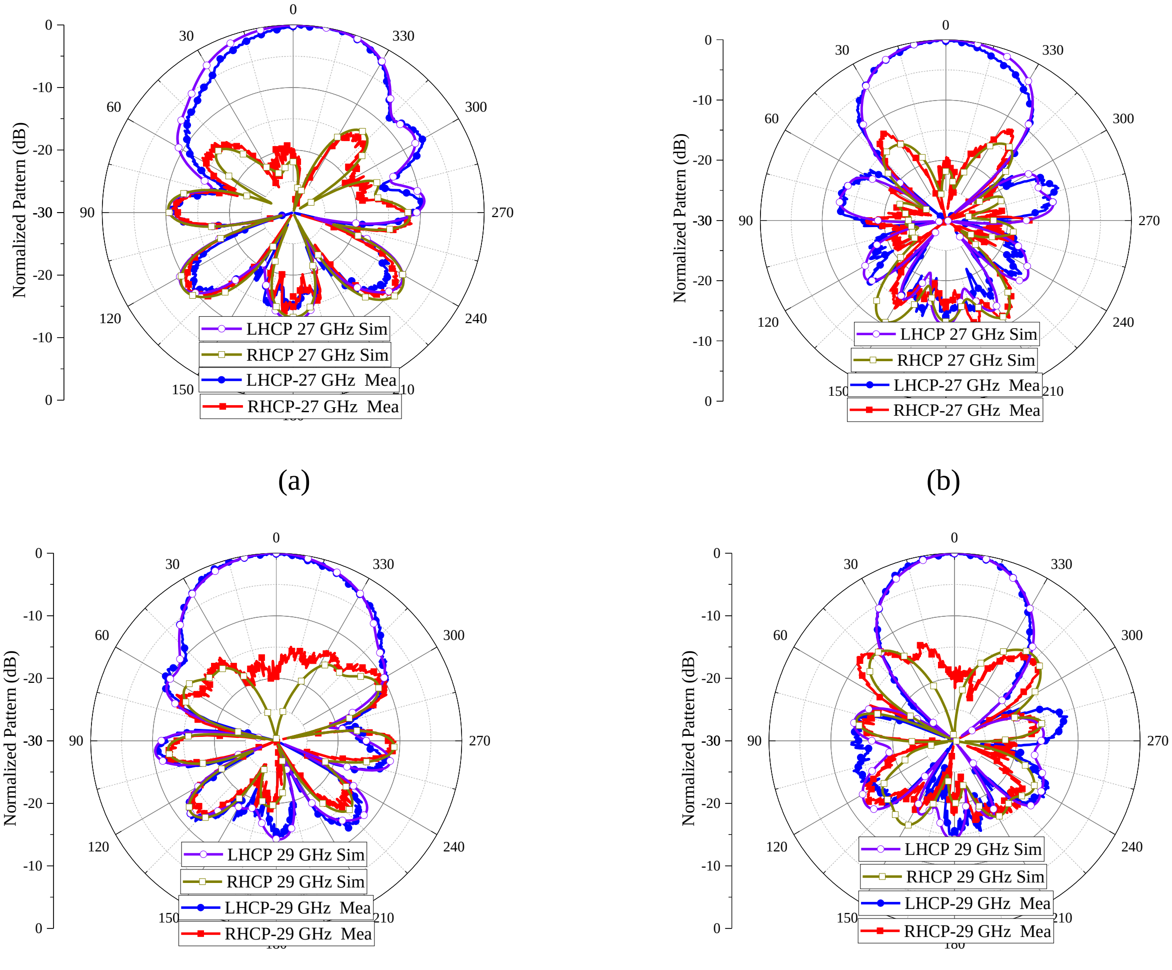

(a) (b)

(c) (d)

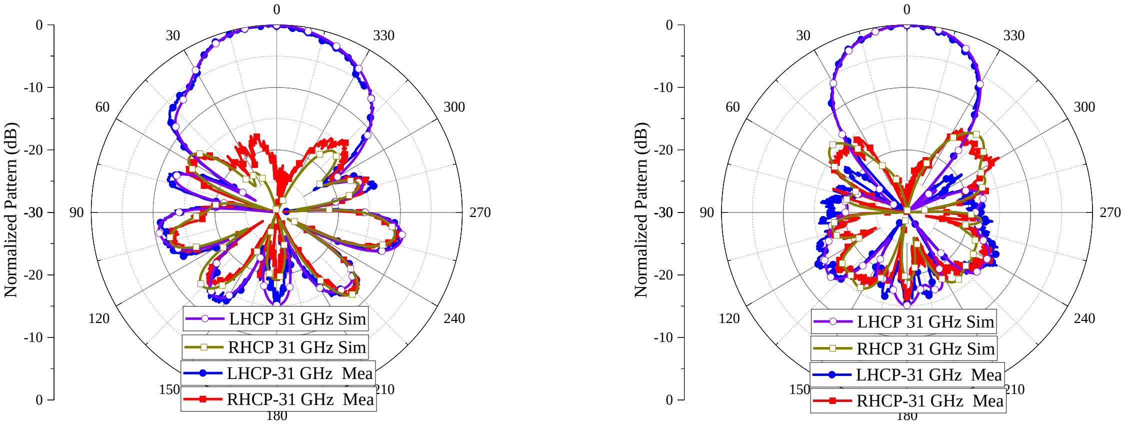

(e) (f)

Figure 3.27: Simulated and measured radiation pattern of UDR-ALTSA

on (a) xoz plane at 27 GHz, (b) yoz plane 27 GHz, (c) xoz plane at 29 GHz, (d) yoz plane 29 GHz, (e) xoz plane at 31 GHz and (f) yoz plane 31 GHz

Figure 3.27 shows the simulated and measured radiation patterns at three different frequencies. Both simulated and measured results suggest that the proposed UDR-ALTSA has a wide AR beam width, which is almost the same as the width of its main lobe. The pattern has a moderate FTBR and symmetry.

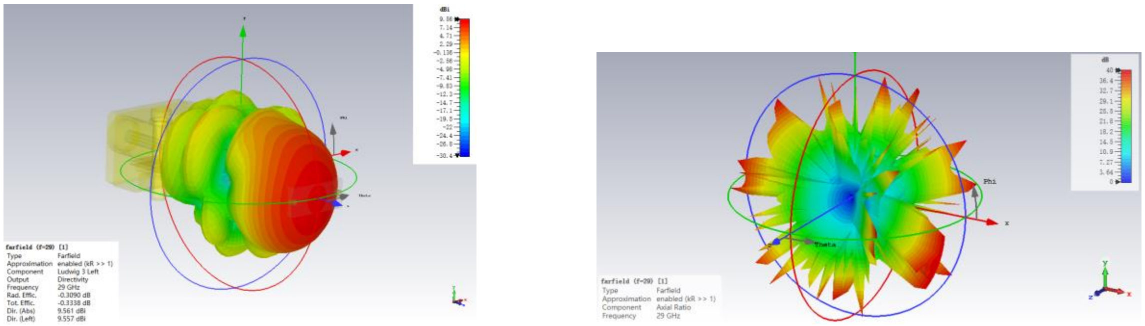

```
farfield (f=29) [1]
Type            Farfield
Approximation   enabled (kR >> 1)
Component       Ludwig 3 Left
Output          Directivity
Frequency       29 GHz
Rad. Effic.     -0.3090 dB
Tot. Effic.     -0.3338 dB
Dir. (Abs)      9.561 dBi
Dir. (Left)     9.557 dBi
```

```
farfield (f=29) [1]
Type            Farfield
Approximation   enabled (kR >> 1)
Component       Axial Ratio
Frequency       29 GHz
```

(a) (b)

Figure 3.28: 3-D pattern of UDR-ALTSA (a) radition pattern and (b) AR pattern

Figure 3.28 plots the simulated 3-D radiation pattern and AR pattern of the UDR-ALTSA prototype antenna. It also shows a nice end-fire left hand CP pattern, which has a modest symmetric radiation and AR patterns.

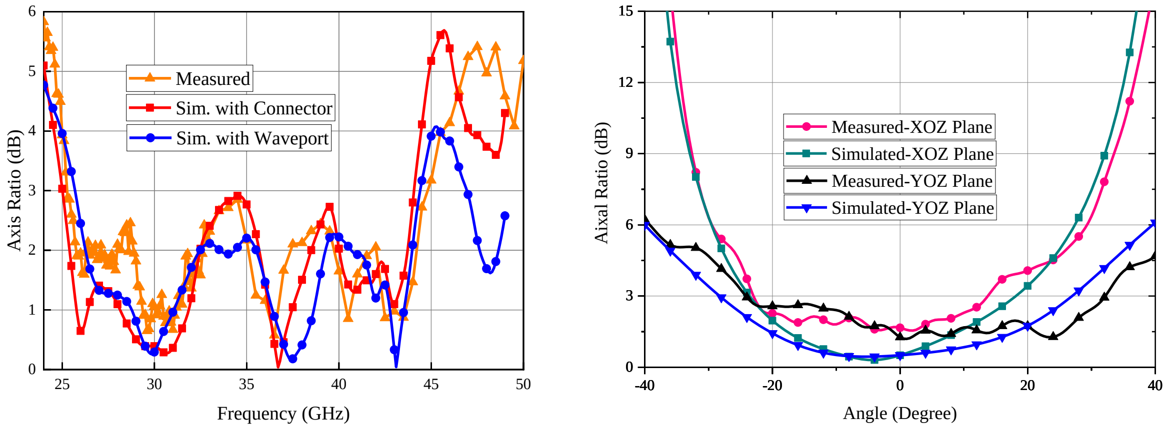

(a) (b)

Figure 3.29: (a) AR vs frequency and (b) AR vs azimuth and elevation angles

Figure 3.29 shows the simulated and the measured AR, which are found to agree well with each other. The measured 3-dB AR bandwidth is 19.7 GHz from 25.3 GHz to 45 GHz, and it is covered almost by the whole impedance bandwidth of $|S_{11}|<-10dB$. The measured AR is larger than the simulated AR, which may root from the influence of the connector for measurement. During simulation, a wave port can be used to replace the connector. The simulated AR with a wave port shows that the AR is actually much lower than with a connector. Therefore, in a practical application, the UDR-ALTSA is expected to have a better AR performance. The measured AR beam width on the azimuth plane is 37° from -23° to 14°, and on the elevation plane it is 56° for -24° to 32°, which are almost the same as the width of its main lobe.

3.3 Comparison and Discussion of Planar End-fire CP Antennas

Table 3.2 summarizes and compares the features of the state-of-the-art end-fire CP antennas in the thesis and other end-fire CP antennas in [30], [53], [56], [76]-[79] in terms of 3dB AR beamwidth, 3 dB AR bandwidth, impedance bandwidth, gain, and size. These antennas could be roughly divided into two groups: low gain with thin substrates, and high gain with thick substrate.

These antennas of low gain with thin substrates consist of electric and magnetic dipoles placed in end-fire direction [30], [53], [56]. Both the two types of dipoles have an omnidirectional pattern and not an end-fire pattern, although these antennas have wide AR bandwidth. Therefore, the gains of these antennas are very low. Moreover, these antennas use vertically mounted cable probes for feeding, and thus are not fully planar structures. Using a Yagi array could improve the gain of the dipole type of CP antennas, though these antennas still use cable probes.

These high gain antennas with a thick substrate are usually the ALTSAs fed by SIWs [76]-[77], thick SIW horn [78], or ALTSA-SIW composite antenna [79]. The ALTSA-SIW composite antenna in [79] has a similar structure with the horn-ALTSA, but the phase centers of the ALTSA and the SIW horn are separated by a long distance, thus degrading its AR beam width on the substrate plane. The proposed horn-ALTSA antenna in Section 2.2 has a compact feeding structure, and the phase centers of ALTSA and SIW horn is very close. These features would benefit to a wide AR beamwidth and a large CP array.

The antenna in [78] is actually a 4-element array, and has switchable beams. It must use thick two-layer substrate and is not a fully planar structure because of a vertically mounted cable probe for feeding. The substrates used in antennas in [76]-[77] are still relatively thick to produce enough VP radiation to realize a CP antenna. The proposed slot-ALTSA composite antenna in Section 2.3 uses extra slots to enhance VP radiation, and the approach could be expected to be available to a thinner substrate than in Section 2.3. As a unique property, the proposed antennas in Section 2.2 and 2.3 actually provide practical solutions of planar single-layer end-fire CP composite antenna arrays with high gains. Moreover, the two solutions in in Section 2.2 and 2.3 could be combined to form a generalized array solution to a higher gain CP antenna. The solution is flexible to choose the number and structures of antenna elements, so the gain and radiation pattern of the element can be adjusted to meet diverse requirements for practical applications.

When a substrate is thick, the transition of SIW to other planar transmission lines or components are low performance, and it will suffer from a high loss due to radiation and surface waves. Accordingly, the antennas in [76]-[77] use the transitions of SIW to waveguide to achieve good performances, and are not fully planar structures. Although the waveguide transitions could be replaced by planar transition, the planar transitions are actually not practical. Modern RF systems usually use mingled multilayer substrate PCB technology for good performances. The substrate of RF circuits in a mingled multilayer substrate must be very thin, e. g. 0.508 mm in Ka band. Therefore, the feeding substrate of the planar end-fire CP antennas must be as thin as the substrate of RF circuits for an easy integration.

Compared to high gain CP antennas in [76]-[79], the proposed UDR-ALTSA antenna has the thinnest feeding substrate and the smallest size with good performances comparable to any other antennas. These features make SIW-based UDR-ALTSA the first option for realizing high gain planar end-fire CP antennas. Moreover, the novel dielectric and excitation structures and mechanism of only VP radiation enhancement developed in the UDR-ALTSA would expand the applications of UDR antennas.

Table 3.2: Comparison of planar end-fire CP antenna

Related Papers	3dB AR Bandwidth (%)	3dB AR Beamwidth	Impedance Bandwidth (%)	Gain (dBi)	Size (λ_0)
[30]	9.2	92°	2.4	3.2	0.74*0.60*0.039
[53]	14.5	80°	1.9	2.3	0.74*0.65*0.048
[56]	8	250°	22.2	1.5	0.66*0.97*0.04
[76]	34.5	N.A	32	6.2-9.6	3.5*1.5*0.25
[77]	42.9	N.A	53（1.7:1）	10.1-12.9	5.88*0.71*0.441/0.147
[78]	23	N.A	29	10.4-12.8	20*3*0.38
[79]	8.9	N.A	20	8.4	7.2*5.4*0.13
Horn-ALTSA	5.9	20°	5	8.5	7.5*4.4*0.13
Slot-ALTSA	5	26° /15°	32	8.0	3.8*1.25*0.13
UDR-ALTSA	56	56/37	72(2.1:1)	9.1-11	2.66*0.81*0.34/0.05

CHAPTER 4 SIW PERIODIC CHARACTERISTICS AND CALCULATION FORMULAS

Transmission lines are not only basic microwave components but also constituent parts of antennas. As a kind of planar transmission line, SIWs have been applied to various microwave/millimeter wave systems and antennas. When operating frequency is high and the periodicity of via array in an SIW is comparable to the operating wavelength, the SIW should be treated as a periodic rather than a uniform structure. When the periodic characteristics of an SIW are concerned, however, there are still obscure to be clarified. This chapter concentrates on the SIW characteristic associated with its periodicity and calculation method related to SIW, emphasizing on the differences between an SIW and a uniform transmission line.

Section 4.1 is a brief description of SIW. Section 4.2 discusses the modes in an SIW, emphasizing on the differences between the modes in a periodic structure ans the eigenmode in a uniform structure. Section 4.3 demonstrates that the wave impedance in a periodic transmission line, such as SIW, is not uniform, emphasizing that only normalized impedances in an SIW is available. Then defines a kind of equivalent impedance of SIW. Section 4.4 proposes and examines closed-form formulas of characteristic parameters in a periodic structure (FPPS) based on field-distribution. Section 4.5 investigates the reflection characteristics in a periodic structure using the FPPS.

4.1 Structure Description and Parameter of SIW

4.1.1 Structures of SIW and Its Equivalent Dielectric Filled Waveguide

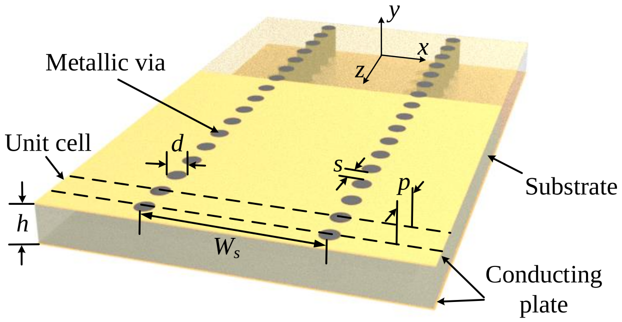

Figure 4.1: Structure of SIW

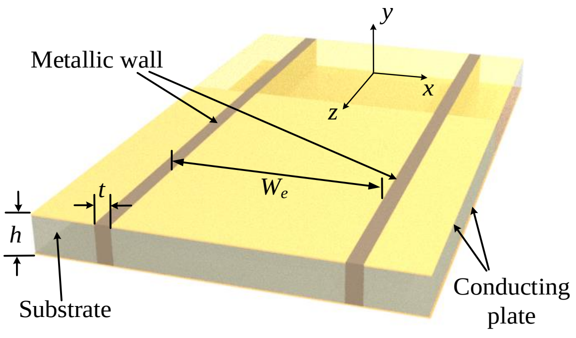

Figure 4.2: Equivalent DFW of SIW

An SIW, shown in Figure 4.1, is similar to a rectangle dielectric-filled waveguide (DFW), and its two rows of periodic metallic via arrays act as two narrow walls of the rectangle waveguide. Although an SIW is a periodic transmission line, we can roughly treat it as an equivalent DFW, as shown in Figure 4. 2, because its periodicity is usually much smaller than a wavelength. The equivalent DFW has the same substrate as the SIW. The width of the DFW is chosen so that it has the same propagation constant or impedance as the associated SIW. At a primary design, one usually uses an equivalent DFW to replace an SIW to improve design efficiency.

Because an SIW is a periodic transmission line where there are a fundamental mode and space harmonics. Usually, the propagation constant of the fundamental mode is regarded as the propagation constant of the SIW.

4.1.2 Equivalent Width of SIW

An SIW has the same propagation constant as its equivalent DFW. Under the criterion, the width of the equivalent DFW of an SIW can be determined. Following are the typical formulas of the equivalent width of SIW [2].

$$W_e = W_s - \frac{d^2}{0.95 \times p} \tag{4.1}$$

When the d / W_s is large, the above formula is modified as [4]

$$W_e = W_s - 1.08 \times \frac{d^2}{p} + 0.1 \times \frac{d^2}{W_s} \tag{4.2}$$

The formulas (4.1) and (4.2) is accurate when the following conditions hold true [4, 5].

$$\begin{aligned} & p > d \\ & p / \lambda_c < 0.25 \\ & \alpha / k_0 < 1 \times 10^{-4} \\ & p / \lambda_c > 0.05 \end{aligned} \tag{4.3}$$

where k_0 is the wavenumber in air, α is the attenuation constant and λ_c is the cutoff wavelength respectively.

4.1.3 Losses in SIW

The losses in an SIW roots from three different mechanisms: conductor, dielectric and radiation. The dissipations from conductor and dielectric in SIW are similar to that in a DFW. The thinner the substrate is, the larger the conductor loss is. Dielectric losses are due to the dissipation in the substrate material, and roughly independent of the geometry of SIW. The calculation of conductor and dielectric losses in an SIW can be based on the equations derived for the classical rectangular waveguide [144]-[145]. However, no equation in a classical rectangular waveguide is available to calculation of the radiation loss in SIW due to its open structure.

The attenuation constant, associated with dielectric loss, is related to the propagation constant k_z, the wavenumber k in the dielectric and the loss tangent $\tan\delta$, and is as follow [38]

$$\alpha_d = \frac{k^2 \tan\delta}{2k_z} (NP/m) \tag{4.4}$$

When the attenuation constant, α_c, associated with conductor loss is small, it can be calculated using a well-known perturbation method [39]. For the dominant mode TE10, the attenuation constant is as follow

$$\alpha_c = \frac{R_s}{h\eta} \frac{1+2\frac{h}{W_e}\left(\frac{\lambda}{\lambda_c}\right)^2}{\sqrt{1-\left(\frac{\lambda}{\lambda_c}\right)^2}} \tag{4.5}$$

where $R_s = 1/(\sigma\delta_f)$ is the surface resistance of the conducting plates of the SIW, and δ_f is the skin depth of a conductor plate with a thickness *t*, which is introduced by Hiraoka [146] as a modification to the skin depth of a half-infinite conductor.

$$\delta_f = \delta(1 - e^{-t/\delta}) \tag{4.6}$$

$$\delta = \frac{1}{\sqrt{\pi f \mu\sigma}} \tag{4.7}$$

The radiation loss in a properly designed SIW is usually much smaller than conductor and dielectric losses. The radiation from the grid of metallic vias in an SIW leads to losses, and M. Pasian gives a formula of radiation loss in an SIW as follows [147]

$$\alpha_r = \frac{\frac{1}{W_e}\left(\frac{d}{W_e}\right)^{2.84}\left(\frac{p}{d}-1\right)^{6.28}}{4.85\sqrt{\left(\frac{2W_e}{\lambda}\right)^2 - 1}} \text{（dB/m）} \tag{4.8}$$

When all the three types of losses are small, the total attenuation constant α, is the summation of all the three types of attenuation constants.

$$\alpha = \alpha_d + \alpha_c + \alpha_r \tag{4.9}$$

4.2 Modes in SIW

Although the modes in an SIW are similar to the TE_{mo} modes in its equivalent DFW and are regarded as quasi-TE_{mo} modes, the modes in an SIW are certainly different from the eigenmodes in the DFW because SIW is a periodic transmission line. When the periodicity of SIW is comparable to the operating wavelength, the differences would become obvious.

4.2.1 Modes in Uniform Transmission Line

A uniform transmission line, such as a DFW, has the same cross sections at any longitudinal positions so that the $\mathbf{E}_0^{uni}(x, y)$, which is also called as the transverse shape of the eigenmode, is independent of the longitudinal coordinate *z*. It means that each eigenmode in a uniform transmission line has a constant transverse shape. In a uniform transmission line, the field of any eigenmode can be written as follows [38]

$$\mathbf{E}^{uni}(x,y,z)=\mathbf{E}_0^{uni}(x,y)e^{-jk_z^{uni}z} \tag{4.10}$$

$$\nabla_T^2\mathbf{E}_0^{uni}(x,y)+[k^2-(k_z^{uni})^2]\mathbf{E}_0^{uni}(x,y)=0 \tag{4.11}$$

where any eigenmode function $\mathbf{E}_0^{uni}(x,y)$, representing transverse shape of field distribution, satisfies individually the transverse boundary conditions in the any cross section of a uniform transmission line. It should be noted that the equation (4.11) is a transverse two-dimensional partial differential equation. After solving the equation (4.11), one has an eigen equation like Pythagorean theorem about propagation constant and transverse wavenumbers of the eigenmode as follow

$$(k_z^{uni})^2=k^2-(k_x^{uni})^2-(k_y^{uni})^2 \tag{4.12}$$

where k_x^{uni} and k_y^{uni}, called as transverse wavenumbers, are eigenvalues of x-direction and y-direction respectively. In the eigen equation in (4.12) the propagation constant is related to the transverse wavenumbers which are determined by solving a transverse two-dimensional partial differential equation. Therefore, the propagation constant of any eigenmode is only related to the shape, size and boundary conditions of the cross section in a uniform transmission line.

4.2.2 Modes in Periodic Transmission Line

In a periodic transmission line, its cross section changes along with its propagation direction and is not uniform. Different cross sections must lead to different transverse shapes of a mode and different transverse “wavenumbers” of the field mode. It means that it is impossible for a periodic transmission line to have a mode that keeps a constant transverse shape along with its propagation direction. For a periodic transmission line like an SIW, one has [38]

$$\mathbf{E}(x,y,z)=\mathbf{E}_0(x,y,z)e^{-jk_z z} \tag{4.13}$$

$$\mathbf{E}_0(x,y,z+p)=\mathbf{E}_0(x,y,z) \tag{4.14}$$

where $\mathbf{E}_0(x,y,z)$, the function of fundamental mode, is a periodic function with a periodicity *p*.

Substituting (4.13) into a wave equation, one has

$$\nabla_T^2\mathbf{E}_0(x,y,z)+\frac{\partial^2\mathbf{E}_0(x,y,z)}{\partial z^2}-2jk_z\frac{\partial\mathbf{E}_0(x,y,z)}{\partial z}-k_z^2\mathbf{E}_0(x,y,z)+k^2\mathbf{E}_0(x,y,z)=0 \tag{4.15}$$

Rather than two-dimensional, the equation (4.15) is a three-dimensional partial differential equation. The transverse shape of fundamental mode $\mathbf{E}_0(x,y,z)$ is not constant, and depends on z-coordinate. As a result, in a periodic transmission line, the fundamental mode is different from eigenmode in a uniform transmission line. According to Floquet theorem, $\mathbf{E}_0(x,y,z)$ is a periodic function, and can be expanded into space harmonics as follow

$$\mathbf{E}_0(x,y,z)=\sum_n \mathbf{E}_{n0}(x,y)e^{-j\frac{2n\pi}{p}z} \tag{4.16}$$

and (4.13) can be expressed as follow

$$\mathbf{E}(x,y,z)=\sum_n \mathbf{E}_{n0}(x,y)e^{-j\left(k_z+\frac{2n\pi}{p}\right)z} \tag{4.17}$$

The space harmonic $\mathbf{E}_{n0}(x,y)$ is also called as Floquet mode. It should be noticed that any space harmonics $\mathbf{E}_{n0}(x,y)$, even the fundamental space harmonic $\mathbf{E}_{00}(x,y)$, does not satisfy the boundary conditions of any cross sections of the periodic transmission line individually, and any single space harmonic does not exist alone in a periodic transmission line. Accordingly, as for k_{zn} of any space harmonic, even the k_z of its fundamental mode, there is not an eigen equation similar to equation (4.12).

For simplicity, the propagation constant of the fundamental mode in SIW is usually regarded as the propagation constant of SIW. It should be keep in mind that the fundamental mode in a periodic SIW and the TE_{10} mode in the DWF have different definition and characteristics.

4.3 Impedance Characteristics of SIW

Wave impedance characteristics of uniform and periodic transmission lines are different. The former is uniform and independent of positions, and the latter is not uniform and related to both longitudinal coordinate *z* and transverse coordinates (*x*,*y*). It is difficult to rigorously define a kind of impedance in a periodic transmission line, because its cross sections change along with its propagation direction. Consequently, the impedance in a periodic transmission line is usually defined only at the interface between two unit cells. Based on the periodicity in a periodic transmission line, a kind of normalized impedance can be defined as in [39]. To obtain an impedance from the normalized impedance, however, one must specify a standard impedance. How to define a standard impedance is still ambiguous, especially in a periodic transmission line, such as an SIW.

In [39] the normalized impedance can be defined on the reference interfaces of the unit cell in a periodic transmission line. Consequently, the standard impedances could be the impedance of a transmission line that is connected to the reference interfaces. The definition of a unit cell in a periodic transmission line, however, is not unique. Figure 4.3 shows two different definitions of a unit cell in an SIW. On the reference interface of unit cell A, the cross section is like a rectangle waveguide. On the reference interface of unit cell B, however, the cross section is like a parallel-plate waveguide. The impedances of the rectangle waveguide and the parallel-plate waveguide are different. Therefore, the standard impedances of the two different kinds of unit cells are also obviously different.

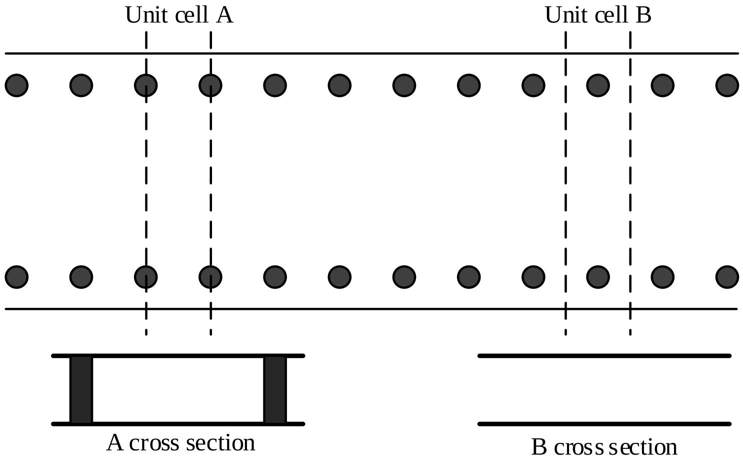

Figure 4.3: Two types of unit cells of SIW

Even after a unit cell is specified, the wave impedance in an SIW cannot be regarded as a standard impedance. The characteristics of wave impedances in a periodic transmission line will be examined.

4.3.1 Wave Impedance in Periodic Transmission Line

The wave impedance in a periodic transmission line is complex and depends on positions in the transmission line. One can write electromagnetic fields in a periodic transmission line as follow

$$\mathbf{E}(x,y,z)=\mathbf{E}_0(x,y,z)e^{-jk_z z}=[E_{x0}(x,y,z)\mathbf{e}_x+E_{y0}(x,y,z)\mathbf{e}_y+E_{z0}(x,y,z)\mathbf{e}_z]e^{-jk_z z} \tag{4.18}$$

$$\mathbf{H}(x,y,z)=\mathbf{H}_0(x,y,z)e^{-jk_z z}=[H_{x0}(x,y,z)\mathbf{e}_x+H_{y0}(x,y,z)\mathbf{e}_y+H_{z0}(x,y,z)\mathbf{e}_z]e^{-jk_z z} \tag{4.19}$$

where both $\mathbf{E}_0(x,y,z)$ and $\mathbf{H}_0(x,y,z)$ are periodic functions about the argument *z*. To expand Maxwell electric field curl equation into scalar equations, for TE modes, $E_{z0}=0$, and we have

$$-\frac{\partial E_y}{\partial z}=-j\omega\mu H_x \tag{4.20}$$

$$\frac{\partial E_x}{\partial z}=-j\omega\mu H_y \tag{4.21}$$

Substituting (4.18) and (4.19) into (4.20) and (4.21), we have

$$\frac{E_{y0}}{-H_{x0}}=\frac{\omega\mu}{k_z}-j\frac{1}{k_z(-H_{x0})}\frac{\partial E_{y0}}{\partial z} \tag{4.22}$$

$$\frac{E_{x0}}{H_{y0}}=\frac{\omega\mu}{k_z}-j\frac{1}{k_z H_{y0}}\frac{\partial E_{x0}}{\partial z} \tag{4.23}$$

We can deduce the wave impedance of TE mode in a periodic transmission line as follow

$$Z_{TE}=\frac{E_{y0}}{-H_{x0}}=\frac{\omega\mu}{k_z}-j\frac{1}{k_z(-H_{x0})}\frac{\partial E_{y0}}{\partial z} \tag{4.24}$$

To determine characteristics of the wave impedance, we can first assume that the wave impedance is independent of variable *z*, which is just the case in a uniform transmission line. Accordingly, we can set

$$E_{y0}(x,y,z)=-Z_{TE}(x,y)H_{x0}(x,y,z) \tag{4.25}$$

Substituting (4.25) into (4.24), we can deduce

$$Z_{TE} = \frac{\omega\mu}{k_z + j\frac{\partial H_{x0}(x,y,z)}{\partial z}\Big/ H_{x0}(x,y,z)} \tag{4.26}$$

Because $H_{x0}(x,y,z)$ is a periodic function about the argument *z*, $\frac{\partial H_{x0}(x,y,z)}{\partial z} \neq 0$. Moreover, $\frac{\partial H_{x0}(x,y,z)}{\partial z}\Big/ H_{x0}(x,y,z)$ must be a function about the argument *z* unless the $H_{x0}(x,y,z)$ is an exponential function about the argument *z*, which will not happens in a periodic transmission line. Therefore, the equation (4.26) contradicts the assumption in equation (4.25). Accordingly, we must set

$$E_{y0}(x,y,z) = -Z_{TE}(x,y,z)H_{x0}(x,y,z) \tag{4.27}$$

Substituting (4.27) into (4.24), we can deduce

$$Z_{TE}\left[1 + j\frac{1}{k_z H_{x0}(x,y,z)}\frac{\partial H_{x0}(x,y,z)}{\partial z}\right] + j\frac{1}{k_z}\frac{\partial Z_{TE}}{\partial z} = \frac{\omega\mu}{k_z} \tag{4.28}$$

Similarly, based on (4.23) the wave impedances of TE mode in a periodic transmission line also meets the following equation

Because both the differential equations (4.27) and (4.28) have complex and position-dependent coefficients, one can draw out the following conclusions.

(1) The wave impedance of TE mode in a periodic transmission line changes along its propagation direction and is not constant or uniform on its cross section.

(2) The wave impedance of TE mode in a periodic transmission line is a complex one. A complex impedance means that there is stored energy and reflected waves at inner points in a periodic transmission line.

Similarly, the wave impedance of TM mode in a periodic transmission line has the same characteristics. These characteristics of the wave impedance in a periodic transmission line are different from those in a uniform transmission line, and it narrows the availabilities of wave impedance in a periodic transmission line. Therefore, the wave impedance in SIW cannot be regarded as a standard impedance.

4.3.2 Equivalent Wave Impedance of SIW

Although wave impedance in a periodic transmission line cannot be determined only based on the propagation constant of the fundamental mode, we can still use the propagation constant of the fundamental mode to define an equivalent wave impedance. Following is the formula of equivalent wave impedance for quasi-TE modes in an SIW

$$Z_{TE} = \frac{\omega\mu}{k_z} \tag{4.29}$$

where k_z is the propagation constant of the fundamental mode of the SIW. The definition of the equivalent wave impedance of SIW is consistent with the definition of equivalent propagation constant of SIW. The consistency not only holds true in quasi-TE_{10} modes but also keeps in quasi-TE_{mo} modes in an SIW.

4.4 Formulas of Characteristic Parameters in Periodic Structures

4.4.1 Why Need a Calculation Method of Characteristic Parameter

Bloch waves, which are also called as Floquet waves or Floquet modes in 1-D case, exist in the periodic structures. Wave phenomena in a periodic structure, no matter a periodic transmission line or a leaky wave antenna, differ from that in a uniform structure and are much complex than a uniform structure. These complexities bring various constitutive parameters to characterize wave phenomena in a periodic structure. On the other hand, the characterizations of wave phenomenon in a periodic structure and the calculation of Bloch parameters are also much complex.

Both the eigenmode solver method and the equivalent network methods only involve the unit cell in a periodic structure and are independent of exciting signals. These methods cannot obtain the number and amplitudes of the Bloch/Floquet modes and cannot be use to calculate wave reflections in a practical periodic structure.

Usually both the forward waves and backward waves exist in a practical periodic structure simultaneously. When multiple exciting signals in different directions or some discontinuous boundaries exist in a practical periodic structure, big inner wave reflections would arise. The total wave at an arbitrary point is the sum or superposition of the forward waves and backward waves. To characterize the wave reflection in a practical periodic structure, a reflection coefficient is necessary, which is defined as the ratio of the backward wave to the forward wave. To extract the forward waves or backward waves from the total wave is critical to calculate reflection coefficients or Floquet modes in a practical periodic structure. However, conventional electromagnetic full-wave simulation tools, such as CTS or HFSS, also have not such a function of the separation of the forward waves and backward waves.

4.4.2 Close-form Formulas of Characteristic Parameters in Periodic Structure

The FPPS is based on field distribution calculated by a driven-mode solver, achieves the separation of the forward waves and backward waves from the total wave in a practical periodic structure, and calculates reflection coefficient, propagation constant and amplitudes of the Bloch/Floquet modes. Here FPPS are proposed.

In a 1-D periodic structure with a periodicity of p, a forward wave propagates along z direction, and the forward wave of any field, for example $\mathbf{E}^{+}\left(x,y,z\right)$, can be written as follow

$$\mathbf{E}^{+}\left(x,y,z\right)=e^{-j\beta z}e^{-\alpha z}\mathbf{P}^{+}\left(x,y,z\right) \tag{4.30}$$

where β is phase constant, α is attenuation constant, and the forward wave magnitude, $\mathbf{P}^{+}\left(x,y,z\right)$, is a periodic function which means

$$\mathbf{P}^{+}\left(x,y,z+p\right)=\mathbf{P}^{+}\left(x,y,z\right) \tag{4.31}$$

Usually in a practical periodic structure there would be a forward wave and a backward wave simultaneously, namely

$$\mathbf{E}\left(x,y,z\right)=\mathbf{E}^{+}\left(x,y,z\right)+\mathbf{E}^{-}\left(x,y,z\right) \tag{4.32}$$

One can write a backward wave as follow

$$\mathbf{E}^{-}\left(x,y,z\right)=e^{j\beta z}e^{\alpha z}\mathbf{P}^{-}\left(x,y,z\right) \tag{4.33}$$

Accordingly, the field components, $\mathbf{E}\left(x,y,z\right)$, inside the periodic structure is

$$\mathbf{E}\left(x,y,z\right)=e^{-j\beta z}e^{-\alpha z}\mathbf{P}^{+}\left(x,y,z\right)+e^{j\beta z}e^{\alpha z}\mathbf{P}^{-}\left(x,y,z\right) \tag{4.34}$$

For simplification, the arguments *x* and *y* is no longer written in the following deduction, and (4.32) and (4.34) are rewritten as

$$\mathbf{E}\left(z\right)=\mathbf{E}^{+}(z)+\mathbf{E}^{-}(z) \tag{4.35}$$

$$\mathbf{E}\left(z\right)=e^{-j\beta z}e^{-\alpha z}\mathbf{P}^{+}\left(z\right)+e^{j\beta z}e^{\alpha z}\mathbf{P}^{-}\left(z\right) \tag{4.36}$$

From (4.36), one can write

$$\begin{aligned}\mathbf{E}\left(z+p\right)&=e^{-j\beta z}e^{-j\beta p}e^{-\alpha p}e^{-\alpha z}\mathbf{P}^{+}\left(z+p\right)+e^{j\beta z}e^{j\beta p}e^{\alpha p}e^{\alpha z}\mathbf{P}^{-}\left(z+p\right)\\&=e^{-j\beta z}e^{-j\beta p}e^{-\alpha p}e^{-\alpha z}\mathbf{P}^{+}\left(z\right)+e^{j\beta z}e^{j\beta p}e^{\alpha p}e^{\alpha z}\mathbf{P}^{-}\left(z\right)\\&=e^{-j\beta p}e^{-\alpha p}\mathbf{E}^{+}\left(z\right)+e^{j\beta p}e^{\alpha p}\mathbf{E}^{-}\left(z\right)\end{aligned} \tag{4.37}$$

To set

$$u=e^{j\beta p}e^{\alpha p} \tag{4.38}$$

and one can write the (4.37) as

$$\mathbf{E}\left(z+p\right)=u^{-1}\mathbf{E}^{+}\left(z\right)+u\mathbf{E}^{-}\left(z\right) \tag{4.39}$$

Similarly, one can write

$$\mathbf{E}\left(z-p\right)=u\mathbf{E}^{+}(z)+u^{-1}\mathbf{E}^{-}(z) \tag{4.40}$$

From the equations (4.35), (4.39) and (4.40), we have

$$u^{2}\mathbf{E}\left(z\right)-u\left[\mathbf{E}\left(z-p\right)+\mathbf{E}\left(z+p\right)\right]+\mathbf{E}\left(z\right)=0 \tag{4.41}$$

$$\mathbf{E}^{+}(z)=\frac{u^{2}\mathbf{E}\left(z\right)-u\mathbf{E}\left(z+p\right)}{u^{2}-1},\quad \mathbf{E}_{0}^{+}(z)=\mathbf{E}^{+}(z)u^{\frac{z}{p}} \tag{4.42}$$

$$\mathbf{E}^{-}(z)=\frac{u\mathbf{E}\left(z+p\right)-\mathbf{E}\left(z\right)}{u^{2}-1},\quad \mathbf{E}_{0}^{-}(z)=\mathbf{E}^{-}(z)u^{-\frac{z}{p}} \tag{4.43}$$

We can use any field components of **E** or **H** to obtain solutions of u in equation (4.41), and the pair of conjugate solutions are

$$u_1=\frac{\left(E_i\left(z-p\right)+E_i\left(z+p\right)+\sqrt{\left[E_i\left(z-p\right)+E_i\left(z+p\right)\right]^2-4E_i^2\left(z\right)}\right.}{2E_i(z)}, \tag{4.44}$$

$$(i=x,y,z)$$

$$u_2=\frac{\left(E_i\left(z-p\right)+E_i\left(z+p\right)-\sqrt{\left[E_i\left(z-p\right)+E_i\left(z+p\right)\right]^2-4E_i^2\left(z\right)}\right.}{2E_i(z)}, \tag{4.45}$$

$$(i=x,y,z)$$

Based on (4.38), one can write the phase constant and the attenuation constants in a periodic transmission line respectively as follow

$$\beta_n=\frac{phase(u)}{p} \tag{4.46}$$

$$\alpha=\frac{\ln|u|}{p} \tag{4.47}$$

To calculate the phase constants and the attenuation constant at any point, we need to know the field components at only three points.

Based on (4.42) and (4.43), one can obtain the space harmonics of forward waves or backward waves as follows

$$\mathbf{E}_0^+(x,y,z)=\sum_n\mathbf{E}_{n0}^+(x,y)e^{-j\frac{2n\pi}{p}z} \tag{4.48}$$

$$\mathbf{E}_{n0}^+(x,y)=\frac{1}{p}\sum_i\mathbf{E}_0^+(x,y,z_i)e^{j\frac{2n\pi}{p}z_i} \tag{4.49}$$

Also based on (4.42) and (4.43), using any available component of **E** or **H**, we can write the reflection coefficient R_i as follow

$$R_i(x,y,z)=\frac{E_{0i}^-(x,y,z)}{E_{0i}^+(x,y,z)}=\frac{uE_i\left(x,y,z+p\right)-E_i\left(x,y,z\right)}{u^2E_i\left(x,y,z\right)-uE_i\left(x,y,z+p\right)}u^{-\frac{2z}{p}} \tag{4.50}$$

It should keep in mind that the reflection coefficient, $R_i(x,y,z)$, is also a function with argument x and y. Therefore, the reflection coefficient $R_i(x,y,z)$ in equation (4.50) is regarded as a point reflection coefficient to distinguish a conventional port reflection coefficient defined on port. In a uniform transmission line, the point reflection coefficient is the same as a port reflection coefficient because the point reflection coefficient is uniform in the whole uniform transmission line. On the other hand, an inhomogeneous $R_i(x,y,z)$ would imply an inhomogeneous wave impedance, as deduced in Section 4.3, due to the relationship between the reflection coefficient and the wave impedance.

It should be noticed that above FPPS is also available to a uniform structure although a periodicity is used during its derivation process. In fact, a uniform structure is also actually a periodic structure, and any value can be its periodicity.

Figure 4.4 shows the implementation flowchart of the FPPS. In the implementation, one can use any other electromagnetic simulation tools to replace CST in Figure 4.4.

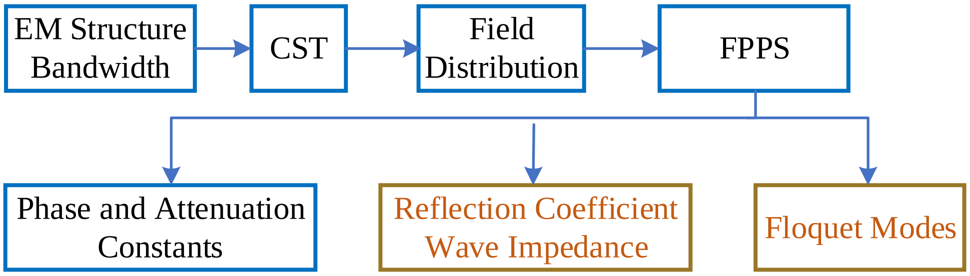

Figure 4.4: Flowchart of FPPS

4.4.3 Verification of FPPS

To examine the validity of FPPS, the FPPS is applied to several cases and is compared to other methods. The field values required by the FPPS can be calculated with a driven-mode solver in commercial electromagnetic full-wave simulation tools, such as CTS or HFSS. The field component used in the FPPS is E_y except a special note.

For clear comparisons, besides Eigenmode Slover in CST, other methods to calculate characteristic parameters are briefly described as follows.

The analytical formulas of phase constant and reflection coefficient in a uniform lossless rectangle waveguide are shown as follows

$$\beta_0=\frac{2\pi}{\lambda_0}\sqrt{\varepsilon_r-\left(\frac{\lambda_0}{2a}\right)^2} \tag{4.51}$$

$$|R|=\frac{\sqrt{\varepsilon_r-\left(\frac{\lambda_0}{2a}\right)^2}-\sqrt{1-\left(\frac{\lambda_0}{2a}\right)^2}}{\sqrt{\varepsilon_r-\left(\frac{\lambda_0}{2a}\right)^2}+\sqrt{1-\left(\frac{\lambda_0}{2a}\right)^2}} \tag{4.52}$$

where λ_0 is operating wavelength, ε_r is relatively permittvity of the filled dielectric inside the waveguide, and a is the waveguide width.

The attenuation constants in a transmission structure can be also determined with scattering parameters by

$$\alpha=-\frac{1}{2L}\ln\frac{|S_{21}|^2}{1-|S_{11}|^2} \tag{4.53}$$

where L is the length between two ports.

The phase constants in a periodic structure can be calculated by

$$\beta=\frac{\Delta\varphi_{21}}{p} \tag{4.54}$$

where $\Delta\varphi_{21}$ is the phase variation of the S_{21} when the periodic structure increases a unit cell, and p is the periodicity of the periodic structure.

The attenuation constant calculated by the formulas (4.53) is an average value along the whole the structure. On the other hand, the formulas (4.53) and (4.54) are not accurate when strong reflection exist in the structure. Moreover, the formula (4.54) is not always available. When the transmission coefficient of a calculated structure is very small, the out-wave at port 2 is too weak to obtain an accurate $\Delta\varphi_{21}$.

In principle, the shapes and sizes of structures in the following cases could be chosen arbitrarily. We use these specific parameters in the following cases just to verify the FPPS comprehensively.

Case 1: A lossless periodically membraned-loaded air rectangle waveguide.

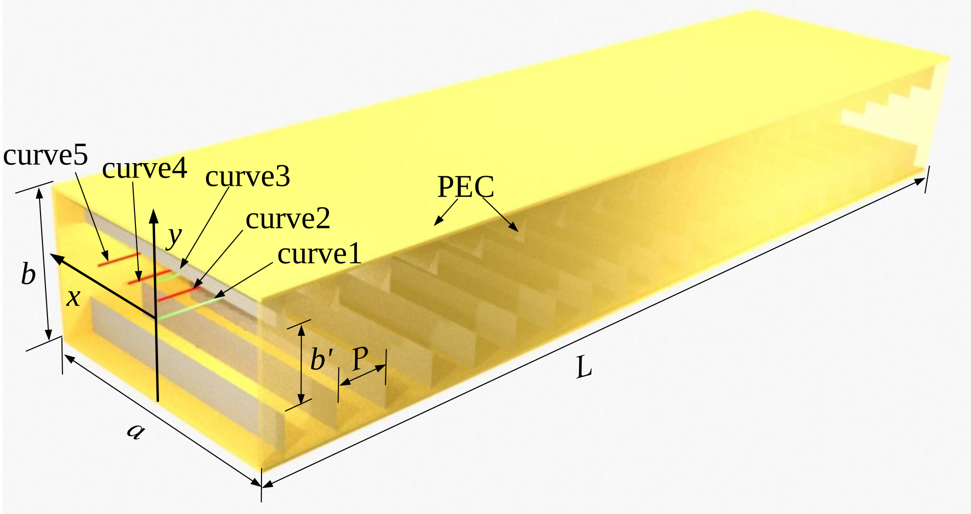

Figure 4.5: Structure of membraned-loaded air waveguide

(*a*=8 mm, *b*=4 mm, *L*=134 mm and *p*=6 mm. C 1: *x*=0, *y*=0, 31mm<*z*<103mm; C 2: *x*=0, *y*=*b*/8, 31mm<*z*<103mm; C 3: *x*=0, *y*=*b*/4-0.5mm, 31mm<*z*<103mm; C 4: *x*=*a*/6, y=*b*/8, 31mm<*z*<103mm; C 5: *x*=*a*/3, *y*=*b*/8, 31mm<*z*<103mm.)

The Case 1 is used to examine performances of the FPPS in a closed periodic structure, as shown in Figure 4.4. The 19 infinitely thin membranes are loaded in the waveguide to form a uniform spacing array. The heights of upper and lower membranes are *b*/4, and the periodicity of the membrane array is 6 mm. The waveguide has a passband from 19 GHz to 28 GHz, as shown in Figure 4.5.

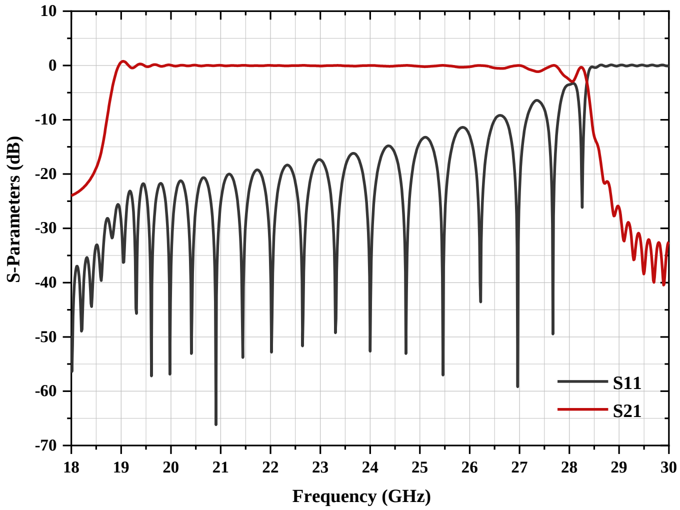

Figure 4.6: Scattering parameters of periodic membraned-loaded air waveguide

To test the FPPS comprehensively, five curves, as shown in Figure 4.4, have been chosen to calculate propagation constants along with themselves. Figure 4.6 (a) shows that calculated phase constants by FPPS are almost the same at different points in C1 to C5 inside the waveguide. Figure 4.6 (b) plots the calculated phase constants with E_y , H_x and H_z along C4 at 25 GHz. The fluctuations of phase constants with different field components are about 0.0003 (1/mm) inside the waveguide, which is only 10^{-3} of the average phase constant. These results show that the FPPS can use any component of electric or magnetic fields to calculate propagation constant.

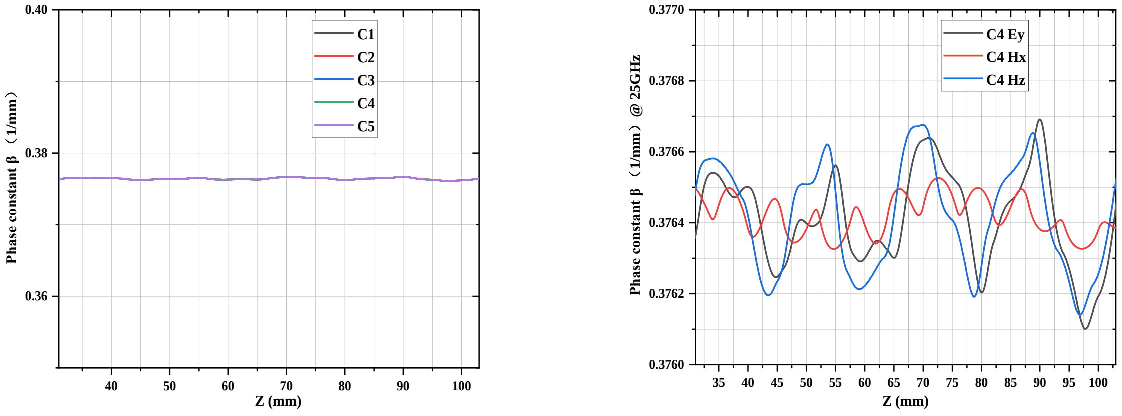

(a) (b)

Figure 4.7: Phase constants of the membrane-loaded waveguide at 25 GHz

(a) along C1 to C5 with *Ey* and (b) along C4 with E_y, H_x and H_z components

Along each curve, 466 points from z=31mm to z=103mm are chosen to calculate phase constants at 25 GHz by FPPS. Table 4.1 exfibits the statistical performances of FPPS along each curves and with different field components at 25 GHz. It shows that the random errors of the result by FPPS are very low, which indicates FPPS can be implemented at any point and hold a high accuracy when applying to a closed lossless periodic structure.

Table 4.1: Statistical performances of FPPS

Curves	$\overline{\beta_0}$ (1/mm)	σ_β (1/mm)	CST (1/mm)
C1	0.3764	1.340×10-4	0.379
C2	0.3764	1.338×10-4	0.379
C3	0.3764	1.336×10-4	0.379
C4	0.3764	1.338×10-4	0.379
C5	0.3764	1.338×10-4	0.379
Field component	$\overline{\beta_0}$ (1/mm)	σ_β (1/mm)	CST (1/mm)
Ey	0.3764	1.34×10-4	0.379
Hx	0.3764	5.50×10-5	0.379
Hz	0.3764	1.52×10-4	0.379

A comparison among FPPS, formula (4.54) and the Eigenmode Solver of CST from 19 GHz to 28 GHz is shown in Figure 4.7.

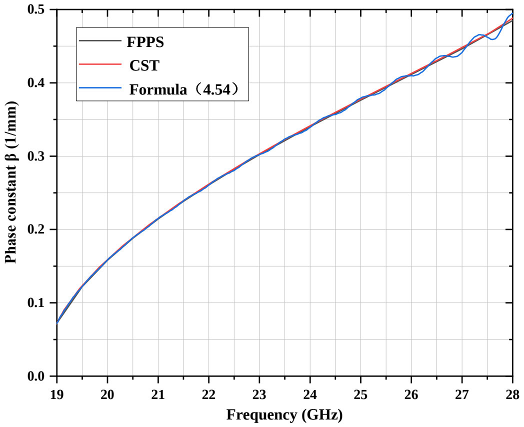

Figure 4.8 Comparison of phase constants among FPPS, formula (4.54) and Eigenmode Solver of CST

Case 2: A loss periodically membrane-loaded dielectric-filled waveguide.

Case 2 is used to check performances of FPPS when it is applied to loss closed periodic structures. The waveguide in Case 2 is the same as Case 1 but filled with different loss dielectrics to replace the air. The relative permittivity of all the filled dielectrics is 2.2, and loss tangents are 0.0, 0.03, and 0.05. For clear comparisons, the results of loss tangent zero are also calculated.

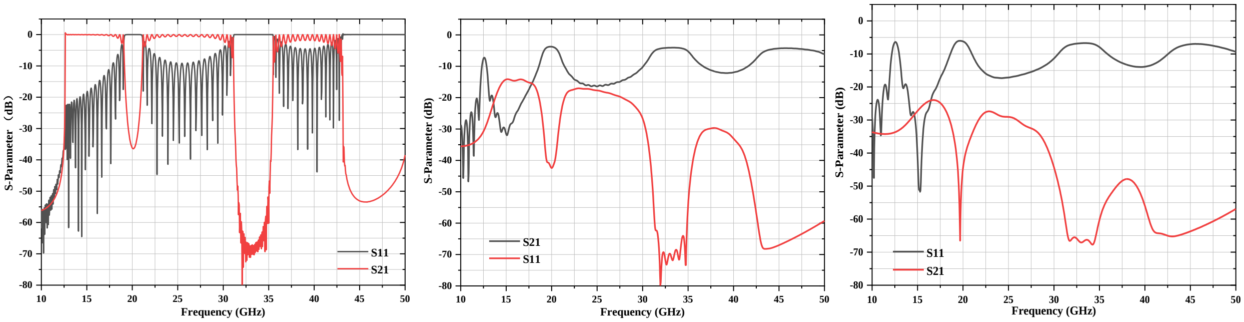

(a) (b) (c)

Figure 4.9: S-Parameters of membrane periodically loaded loss waveguide

(a) $tg\delta = 0$, (b) $tg\delta = 0.03$, and (c) $tg\delta = 0.05$

Figure 4.8 depicts the simulated S-parameters of these membrane-loaded waveguides. When the lossless dielectric is filled, Figure 4.8 shows that the membrane-loaded waveguide has obvious passbands and stopbands. The first passband is from 12.6 GHz to 19.2 GHz, and the second passband is from 21 GHz to 31.2 GHz. The first stopband is from 19.2 GHz to 21 GHz, and the second is from 31.2 GHz to 35.5 GHz. When loss dielectrics are filled, there are not obvious passbands and stopbands, and the transition between a stopband and a passband is not so sharp as lossless dielectrics. A loss associated with tangent of 0.03 is actually very big, and the transmitting coefficient $|S_{21}|$ is small both in the passband and the stopband. It would affect the performances of formulas (4.52) and (4.53).

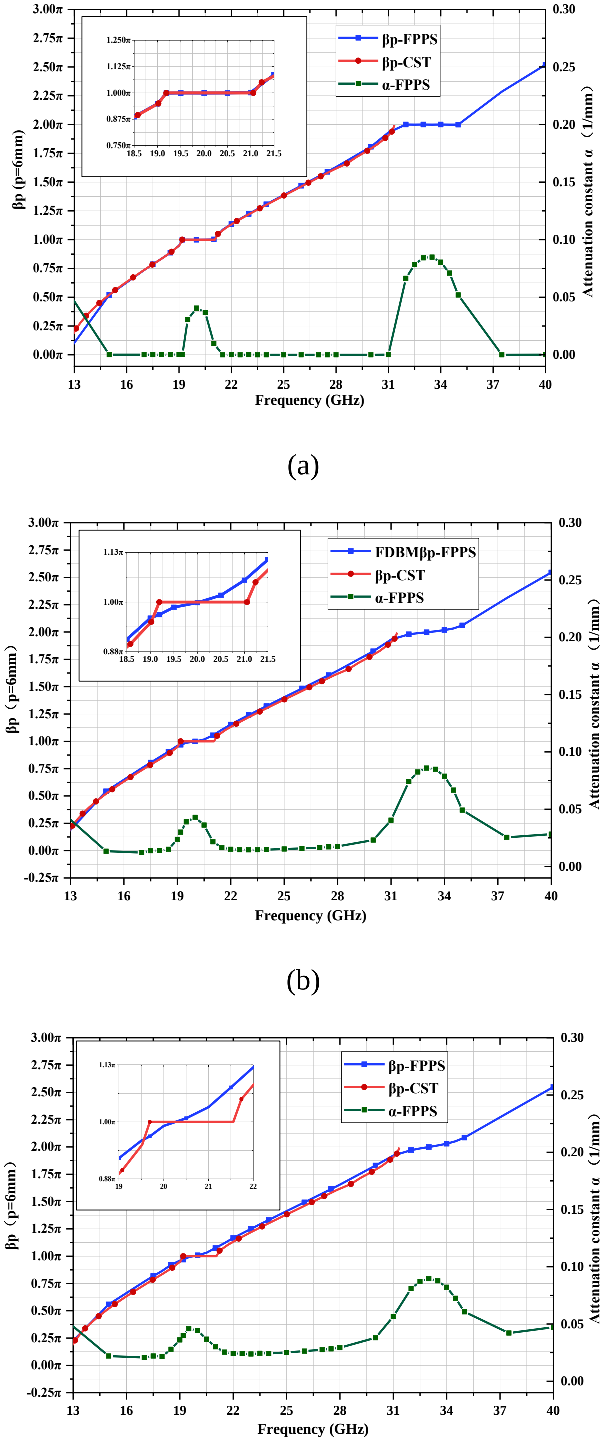

Figure 4.10: Calculated phase and attenuation constants of membrane-loaded waveguide

(a) $tg\delta = 0$, (b) $tg\delta = 0.03$, and (c) $tg\delta = 0.05$

Figure 4.9 (a) shows the calculated phase constants of the membrane-loaded waveguides with different filled dielectrics. When the filled dielectric is lossless, the phase constants using the FPPS agree well with that using CST both in passbands and stopbands. When the filled dielectric is loss, however, the FPPS agree well with CST only in passband. In stopbands, the phase constant using CST keeps constant, but the phase constant using FPPS is no longer a constant value. Because of dielectric loss, the transition of S-parameters from a passband to a stopband, as shown in Fig. 4 (b), is smooth and not sharp. Similarly, the phase constants in a stopband would be no longer constant due to loss. Therefore, the phase constant by FPPS would be more reasonable.

Different the eigen-mode solver, the FPPS can be used to calculate the attenuation constant. When the filled dielectric is lossless, Figure 4.9 (a) shows that the attenuation constants by the FPPS are zero in passbands, and have values more than zero in stopbands. When the filled dielectric is loss, Figure 4.9 (b) and (c) show that the attenuation constants by the FPPS have values more than zero in both the passband and the stopbands. Therefore, the the attenuation constants by the FPPS is also reasonable.

When a structure has a big loss, the accuracies of the formulas (4.53) and (4.54) will decrease. Figure 4.10 shows the comparison of the phase constants by the FPPS and the formula (4.54), and the comparison of the attenuation constants by the FPPS and the formula (4.53). When the filled dielectric are loss, the loss of the membrane-loaded waveguide is big. The magnitude of out-going wave at port 2 is too weak to accurately calculate the changes of both the phase and magnitude of the out-going wave when an extra unit cell is added the waveguide. The scenario becomes worse when the transmitting coefficient $|S_{21}|$ is very small, and it is demonstrated clearly in Figure 4.10.

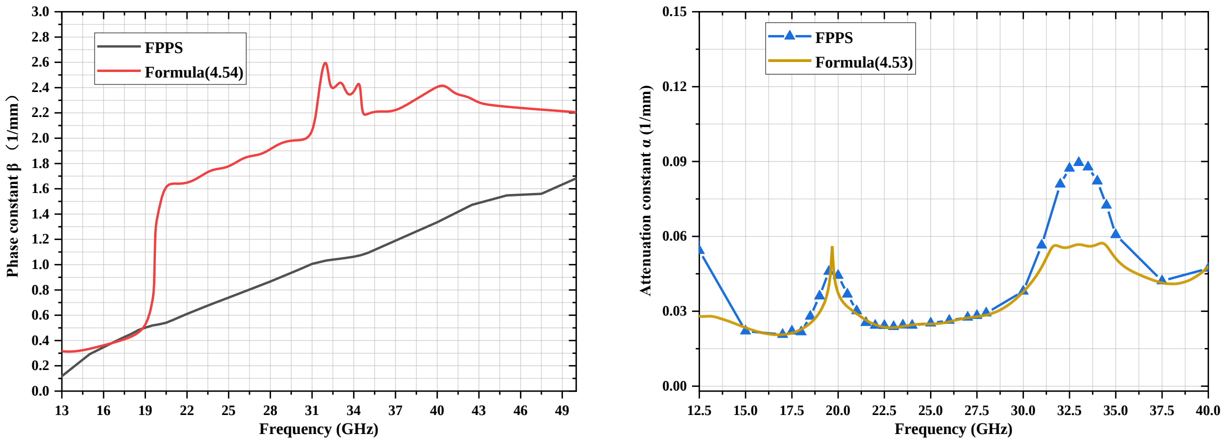

(a) (b)

Figure 4.11: Comparison of propagation constants with FPPS and S-Parameter based formulas (a) phase constant and (b) attenuation

Case 3: Periodic slotted dielectric-filled DFW.

The Case 3 is chosen to examine performances of FPPS in an open periodic structure. The periodic slotted DFW, as shown in Figure 4.11, is 92 mm long, and 13 pairs of identical transverse slots, etched on both broad walls of the DFW symmetrically, forms a uniform spacing periodic leaky wave antenna.

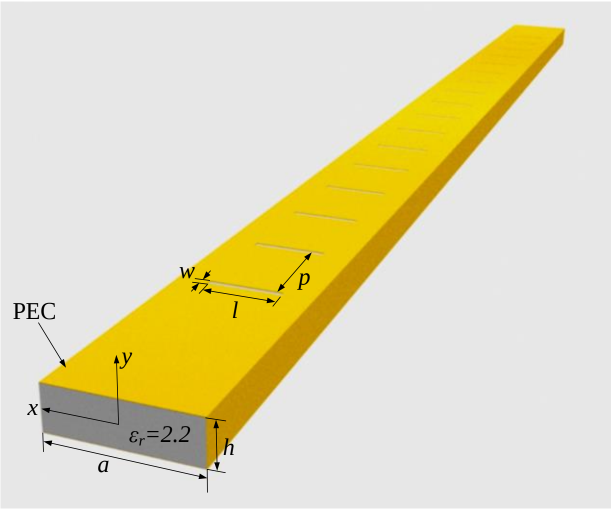

Figure 4.12: Periodic slotted dielectric-filled waveguide

(*a*=8 mm, *h*=1.52 mm, *l*=6 mm, *w*=0.4 mm, *p*=6 mm.)

Figure 4.12 shows the reflection coefficient and the radiation efficiency of the slotted DFW, and it indicates that the sltted DFW has a relatively high radiation efficiency at about 14.1 GHz. A large radiation efficiency means a big loss, and it will degrade the accuracies of formulas (4.53) and (4.54).

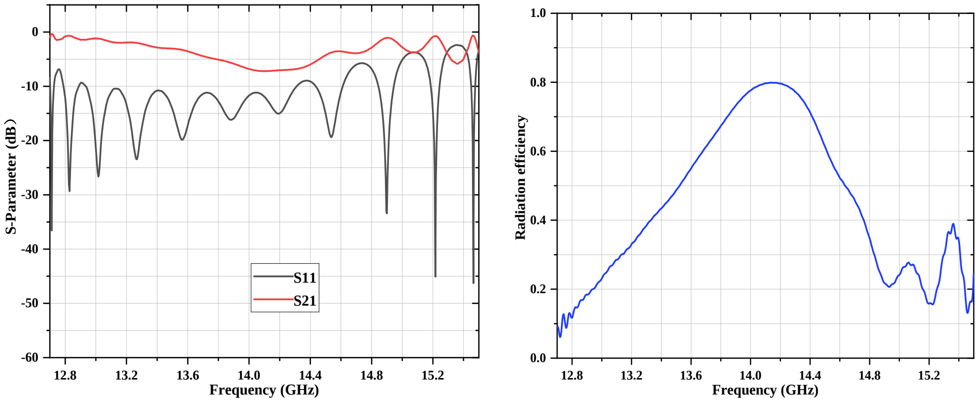

(a) (b)

Figure 4.13: Simulated (a) S-parameter and (b) radiation efficiency of periodic slotted DFW

Figure 4.13 (a) shows the calculated phase constants by the FPPS and the eigen-mode solver of CST. When an eigen-mode solver is applied to an open structure, the boundary size and boundary condition could be optional, as shown in Figure 4.13 (b). Therefore, the calculated phase constants by an eigen-mode solver are different with different boundary configuration. The slotted DFW is an open radiating structure, and a kind of absorbing boundary condition should be enforced on the boundaries of the unit cell during simulation. In the eigen-mode solver, however, only PEC, PMC or periodic boundary conditions are available. When using the eigen-mode solver, two kinds of boundary conditions: CST-1 and CST-2, are used. The boundary condition in CST-1 is a PMC boundary enforced on outside planes close to the broad walls, namely H=h. The boundary condition in CST-2 is a PMC boundary enforced on outside planes far from the broad walls, namely H>>h. Figure 4.13 (a) shows that the phase constants by CST-1 and CST-2 are obviously different. Therefore, it is not convenient and not accurate to use an eigen-mode solver to calculate phase constants of a periodic radiating structure.

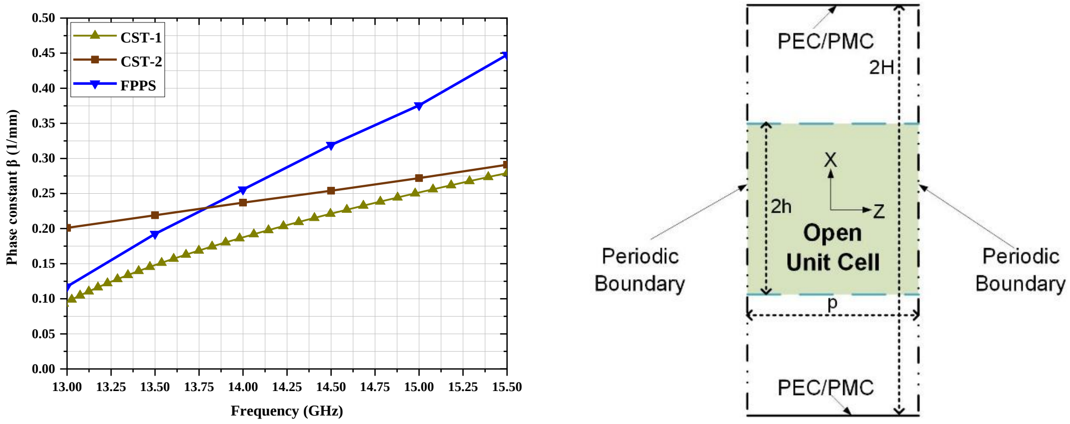

(a) (b)

Figure 4.14: Calculated phase constants of (a) slotted DFW by FPPS and CST, and (b) the boundary condition of an open unit cell in eigen-mode solver of CST

Because of the open radiating structure and the big radiation loss, both the eigen-mode solver and the formulas (4.54) are not available, and we must use other method to examine the accuracy of the FPPS. Figure 4.14 (a) shows the simulated magnitude and phase distributions of E_y at 14.1 GHz along z-axis inside the slotted DFW. It is clear that the phase delay in a short range less than a periodicity does not hold a linear relation with position along propagation direction, and it means the phase velocity and phase constant is not uniform. Across a long distance, however, the phase delay has a linear relation with position. Therefore, one can use the phase delay of E_y across a long distance to calculate phase constant. Figure 4.14 (b) shows the phase constant calculated by FPPS and the phase distribution of E_y, and the results by the two method agree well each other. Therefore, the FPPS can be applied to open radiating structures.

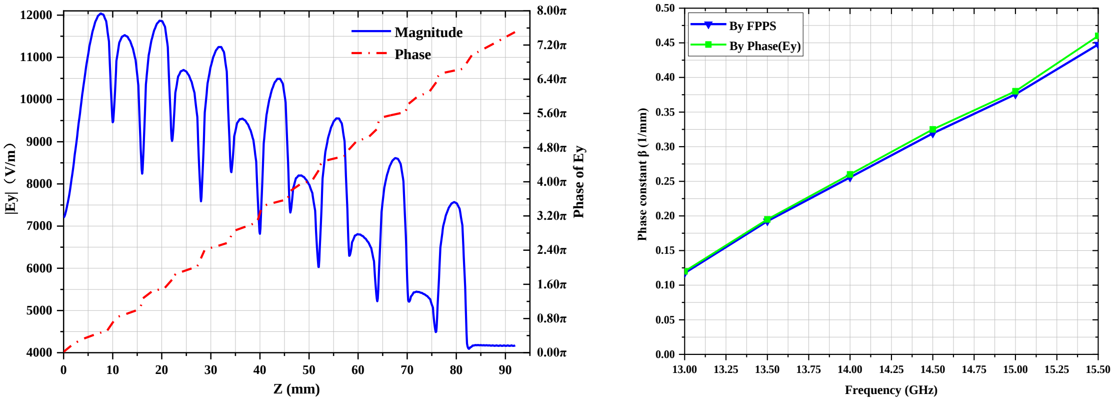

(a) (b)

Figure 4.15: (a) Magnitude and phase distributions of Ey at 14.1 GHz along z-axis of periodic slotted DFW, (b) phase constants by FPPS and phase of E_y

The performances of theFPPS have been examined with diverse periodic structures, including closed and open/radiating, and lossless or loss. Simulated results and the comparisons to other results show that the FPPS is accurate formulas for wave impedance, phase and attenuation constants, even strong reflections exist. After obtaining the required field values, the calculations of all the parameters are analytical and direct processe

4.4.4 FPPS in 2-D Periodic Structure

The field in a practical 2-D periodic structure can be written as

$$\begin{aligned}\mathbf{E}(x,y,z) = \mathbf{E}_0^{++}(x,y,z)e^{-jk_x x}e^{-jk_y y} + \mathbf{E}_0^{+-}(x,y,z)e^{-jk_x x}e^{jk_y y}\\ + \mathbf{E}_0^{-+}(x,y,z)e^{jk_x x}e^{-jk_y y} + \mathbf{E}_0^{--}(x,y,z)e^{jk_x x}e^{jk_y y}\end{aligned} \tag{2-55}$$

where all the $\mathbf{E}_0^{++}(x,y,z)$, $\mathbf{E}_0^{+-}(x,y,z)$, $\mathbf{E}_0^{-+}(x,y,z)$, and $\mathbf{E}_0^{--}(x,y,z)$ are periodic functions with periodicity p_x about the argument x and periodicity p_y about the argument y. For simplicity, we can use the following short forms to denote fields

$$\mathbf{E} = \mathbf{E}(x,y,z) \tag{4.56}$$

$$\mathbf{E}_{m,n} = \mathbf{E}(x+mp_x, y+np_y, z) \tag{4.57}$$

The (4.55) can be write as

$$\mathbf{E} = \mathbf{E}^{++} + \mathbf{E}^{+-} + \mathbf{E}^{-+} + \mathbf{E}^{--} \tag{4.58}$$

To set $u_x = e^{jk_x p_x}$ and $u_y = e^{jk_y p_y}$. Based on Bloch theorem, we have

$$\mathbf{E}_{1,0} = (\mathbf{E}^{++} + \mathbf{E}^{+-})u_x^{-1} + (\mathbf{E}^{-+} + \mathbf{E}^{--})u_x \tag{4.59}$$

$$\mathbf{E}_{-1,0} = (\mathbf{E}^{++} + \mathbf{E}^{+-})u_x + (\mathbf{E}^{-+} + \mathbf{E}^{--})u_x^{-1} \tag{4.60}$$

$$\mathbf{E}_{0,1} = (\mathbf{E}^{++} + \mathbf{E}^{-+})u_y^{-1} + (\mathbf{E}^{+-} + \mathbf{E}^{--})u_y \tag{4.61}$$

$$\mathbf{E}_{0,-1} = (\mathbf{E}^{++} + \mathbf{E}^{-+})u_y + (\mathbf{E}^{+-} + \mathbf{E}^{--})u_y^{-1} \tag{4.62}$$

Based on the equations (4.58) to (4.62), and to use any component of $E_i(i = x, y, z)$, one can obtain the solution of u_x and u_y as follows

$$u_x = \frac{E_{i,-1,0} + E_{i,1,0} \pm \sqrt{(E_{i,-1,0} + E_{i,1,0})^2 - 4E_i^2}}{2E_i} \tag{4.63}$$

$$u_y = \frac{E_{i,0,-1} + E_{i,0,1} \pm \sqrt{(E_{i,0,-1} + E_{i,0,1})^2 - 4E_i^2}}{2E_i} \tag{4.64}$$

With u_x and u_y, it is easy to calculate k_x and k_y. When u_x and u_y is known, one can easily obtain the solutions of $\mathbf{E}^{++}$, $\mathbf{E}^{+-}$, $\mathbf{E}^{-+}$, and $\mathbf{E}^{--}$ from the linear equations (4.59) to (4.62), and then determine their space harmonics.

In the above description of 2-D FPPS, the two axes of periodicity are assumed orthogonally, but the formulations still hold in the case of generally skewed axes.

Similarly, the formulas for a multi-dimension periodic structure cauld be deduced, and the FPPS could be applied to multi-dimension periodic structures.

The FPPS can also apply to uniform structures, because the formulas (4.55) to (4.64) hold no matter the structures are periodic or uniform. Even if for a quasi-periodic structure with only three unit cells, the FPPS is still available, and it can give the average values of the phase and attenuation constants over the three unit cells.

4.5 Reflection Characteristics in Periodic Structure

With the FPPS, it might be easier to reveal the physical mechanism of the periodic structures.

In a lossless uniform transmission structure, the amplitude of the reflection coefficient is uniform, and the phase of the reflection coefficient is a periodic function with argument z. The reflection characteristics in a lossless periodic transmission structure, however, are much complex. The FPPS can extract the forward wave and the backward wave from the total wave in a practical periodic structure and calculate the reflection coefficients at any point inside a structure rather than only on the port of the structure. Therefore, the FPPS could be a powerful tool to examine reflection characteristics in periodic structures.

The structure to be examined is a 13-membrane loaded air rectangle waveguide, and it is almost the same as the waveguide in Figure 4.4 except for a=40.39 mm, b=20.19 mm, p=8 mm, and L=160 mm. We use formula (4.50) to calculate the amplitudes of the reflection coefficients along C1 to C5 in the membrane-loaded waveguide. The Figure 4.15 (a) shows the amplitudes of the reflection coefficients at 6 GHz. The reflection coefficients are not uniform. The fluctuation of the amplitudes along each curve could not totally be attributed to the errors during calculations, because it is not random and displays certain periodic characteristics along the propagation direction. Therefore, the fluctuation of the reflection coefficient might be relative to the periodic structure. Among C1 to C5, the closer to the membrane a curve is, the more inhomogeneous the field distribution in the curve is, and the more fluctuation the point reflection coefficients in the curve have.

Although the fluctuation of the amplitudes of the reflection coefficient at different points is small, it should not be totally attributed to the contribution of the errors during numerical calculation, and it embodies the inhomogeneous characteristic of the reflection in a periodic structure. To extract the periodicity effect on reflection, the magnitude order of the error from numerical calculation should be evaluated.

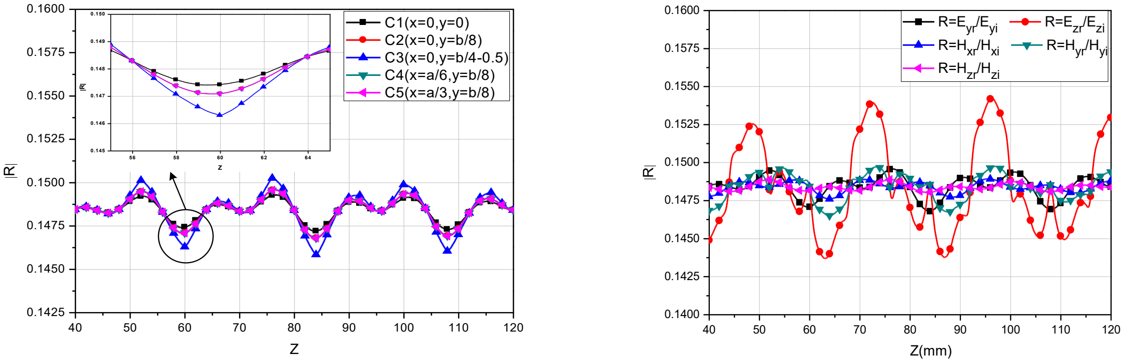

(a) (b)

Figure 4.16: (a) Point reflection coefficients of the membrane-loaded waveguid at 6 GHz

(a) calculated with E_y along C1 to C2, and (b) calculated with different field components along C4

When the membrane-loaded waveguide is excited with TE10 mode, the reflection is independent of *x*-coordinate inside the waveguide due to the structure symmetry, and so that the reflection coefficients along the C2, C4, and C5 should be exactly the same theoretically, because the three curves have the same *y*-coordinate *y*=*b*/8. Figure 4.15 (a) shows the expected uniformity of the reflection coefficients along the *x*-coordinate. Therefore, one can use the calculated reflection coefficients at different points where the *y*-coordinate and *z*-coordinate is the same and *x*-coordinates are different, to evaluate the error of the numerical calculation.

The reflection coefficients at the 101 points have been calculated with the formula (4.50) at 6 GHz. The 101 points are on the cross section of *z*=60 mm, have the same *y*-coordinate *y*=*b*/8, and are uniformly distributed from *x*=0 to *x*=0.5*a*. The statistical standard deviation of the calculated reflection coefficients at the 101 points is $3.14 \times 10^{-6}(1/mm)$. Accordingly, the error of the numerical calculation is the order of $10^{-6}(1/mm)$.

The inset in Figure 4.15 (a) shows that the difference of reflections between the C1 and C3 at *z*=60 mm at 6 GHz is around $8 \times 10^{-4}(1/mm)$. It is much larger than the error order of the numerical calculation. Therefore, the reflection coefficient on the cross section of a periodic structure is not uniform. The difference of reflection coefficients between the C1 and C3 embodies the inhomogeneous characteristic of the reflection in a periodic structure.

Because the reflection coefficients are inhomogeneous inside a periodic transmission structure, the reflection coefficient is position-dependent, such a reflection coefficient can be regarded as a kind of point reflection coefficient, to distinguish it from the conventional port reflection.

In Figure 4.15 (a), E_y is used to calculate reflection coefficients, and we can also use other field components to calculate them. In a uniform transmission structure, the reflection coefficients of all the field components will be the same. In a periodic transmission structure, however, the point reflection coefficients with the different field components could be different. Figure 4.15 (b) displays the reflection coefficients of the different field components at 6 GHz along C4 in the membrane-loaded waveguide. The results in Figure 4.15 (b) shows that the point reflection coefficients of the different polarized components of the field are not the same. The difference between the results with E_y and H_x exceeds 0.001 (1/mm), and the difference is much larger than the numerical calculation error. In addition, the difference between the results with E_z and any other field component are even larger, and the reason behind it might be that E_z does not exist on the port of the membrane-loaded waveguide and is excited by the membranes so that E_z is fully affected by the periodicity of the membrane array.

Due to the intrinsic discontinuities in a periodic structure, the reflections of different field components are different. The difference indicates that a tensor point reflection coefficient might be necessary to characterize the reflection phenomenon inside a periodic structure.

A tensor point reflection coefficient can be defined as following

$$\mathbf{E}_0^-(\mathrm{x},\mathrm{y},z)=\overleftrightarrow{\mathbf{R}}(x,y,\mathrm{z})\cdot\mathbf{E}_0^+(\mathrm{x},\mathrm{y},z) \tag{4.65}$$

The formula (4.65) can be also written in a matrix form as follow

$$\begin{bmatrix} E_{0x}^- \\ E_{0y}^- \\ E_{0z}^- \end{bmatrix} = \begin{vmatrix} R_{xx} & R_{xy} & R_{xz} \\ R_{yx} & R_{yy} & R_{yz} \\ R_{zx} & R_{zy} & R_{zz} \end{vmatrix} \begin{bmatrix} E_{0x}^+ \\ E_{0y}^+ \\ E_{0z}^+ \end{bmatrix} \tag{4.66}$$

Compared to the reflection phenomenon in a uniform transmission structure, the reflection phenomenon in a periodic structure is much complex, and the point reflection coefficient is an inhomogeneous tensor.

It should be noticed that a point reflection coefficient in the periodic transmission structure is different from a port reflection coefficient. Even the port reflection is little, the point reflection coefficient could be large. To observe how the point reflection coefficient approaches the associated port reflection coefficient, the membrane-loaded waveguide is extended with a uniform waveguide of 48 mm long, to prolong the distance between port 1 to membrane array. The starting point of the C1 is reset to port plane z=0, such the first left membrane is at z=52 mm.

We calculate the point reflection coefficients R_{yy} using formula (4.50) along C1 at 6 GHz, 8.504 GHz, 9 GHz and 10 GHz, respectively. The results are shown in Figure 4.16 (a). The port reflection coefficients calculated by CST at the four frequencies are 0.245, 0.000257, 0.0482 and 0.649, respectively. The results in Figure 4.16 (a) shows that the port reflection is very small at 8.504 GHz, about 0.000257, but the point reflection coefficients R_{yy} inside membrane region are about 0.217, which are much larger than the port reflection coefficient.

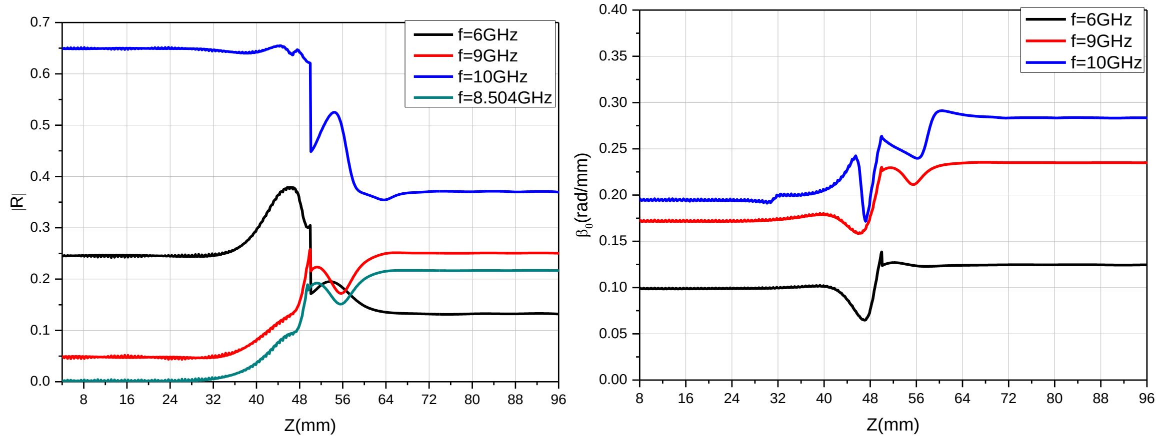

(a) (b)

Figure 4.17: Point reflection coefficients and phase constants along Curve 1

(a) Reflection coefficients and (b) Phase constants

Figure 4.16 (a) also shows that the point reflection coefficient has not an obvious relationship with the port reflection coefficient. However, the point reflection coefficients approach the associated port reflection coefficients when the calculated point goes away from the membrane region. When a point is far away the membrane region about two times of the periodicity length, the point reflection coefficient at the point is almost the same as the port reflection coefficient, and it also indicate that the FPPS can be applied to uniform structures.

The variation of point reflection coefficients in the transition region is due to the transition from the Floquet mode in a periodic waveguide to the eigen mode in a uniform waveguide. The formula (4.50) itself, however, might also lead to the fluctuation. To calculate a point reflection coefficient using formula (4.50), we must use field values at three sampling points spanning two periodicity lengths. When calculating the reflection coefficients in the transition region, there are certain sampling points outside the periodic region, and the formulas (4.39) and (4.40) are not available. When calculating point coefficients in the uniform waveguide, we can use any p value. The results in Figure 4.16 (a) use p=2 mm.

We also examine the transition of phase constants from the periodic waveguide to the uniform waveguide. The results are shown in Figure 4.16 (b). It shows that the lower the frequency is, the smaller the difference of the phase constants of the two waveguides is, and the shorter the transition region is. As a comparison, the length of the transition region of the two kinds of reflection coefficients in Figure 4.16 (a) is independent of the difference between the two reflection coefficients. The results in Figure 4.16 (b) show that the error due to the formulas (4.39) and (4.40) affects the phase constants only in the region from z=40 mm to z=56 mm at 6 GHz. Therefore, the error due to formulas (4.39) and (4.40) should affect only in the region from z=40 mm to z=56 mm at 6 GHz. The results of the reflection coefficients in Figure 4.16 (a), however, show that its transition region at 6 GHz is from z=32 mm to z=64 mm. Accordingly, the transition of reflection from z=32 mm to z=40 mm and from z=56 mm to 64 mm must be attributed to the difference between the Floquet mode and the eigen mode rather than the errors from formulas (4.39) and (4.40).

Although a periodic transmission structure with many unit cells could be almost all-pass between two ports without any port reflection, there could be strong point reflection inside any unit cell in the periodic transmission structure. Based on its reflection phenomenon, a periodic transmission structure in fact can actually be regarded as a cascaded multi-order filter.

CHAPTER 5 RADIATION OF SLOTS ON BROAD WALLS OF SIW

The slots on broad walls of an SIW could be used to improve performances of an SIW-based planar composite antenna. To design an SIW-based planar composite antenna with slots properly, one must have a comprehensive understanding of the radiation mechanism of the slots. When operating frequency is high, the dominating modes in an SIW would be slow wave. How about the radiation efficiency of slots is? Could a slow wave produce radiation?

This chapter is organized as follows. Section 5.1 examines the radiation characteristics for a two-slot array on the broad wall of an SIW, addressing a radiation produced by a slow wave in a non-periodic structure. Section 5.2 examines the radiation of a PLWA, addressing that the radiation could and should be explained with its fundamental mode even if the fundamental mode is a slow wave.

5.1 Radiation from Slow waves in Structures without Space Harmonics

5.1.1 Radiation from Slow Waves in a Two-slot DFW and SIW

To investigate the radiation from slow waves in more general cases, the radiation of a two-slot width-uniform SIW and its equivalent DFW, as shown in Figure 5.1(a) and(b), is examined. The prototype of the two-slot SIW, as shown in Figure 5.1(c), is fabricated and measured. The total length of the two-slot SIW is 75.4 mm. These proposed two-slot SIW/DFW is modeled and designed on Rogers RO4003 dielectric substrate (ε_r=3.55, tan δ = 0.0022, and thickness of metal = 0.017 mm). To simplify the following simulations with CST, without otherwise specified, all the substrates are treated as lossless and the metal is treated as PEC (perfect electric conductor).

When the two transverse slots in the two-slot SIW are etched on its broad wall, the two slots form a two-slot array, and the two-slot SIW becomes a slotted SIW. Both the two-slot SIW/DFW here are non-uniform and non-periodic structures, and there is not any space harmonic in the two-slot DFW/SIW. When a dominating mode TE_{10} is excited in a DFW without slot, its phase constant β is as follow,

$$\beta = k_0\sqrt{\varepsilon_r - \left(\frac{\lambda_0}{2W}\right)^2} \qquad (5.1)$$

When operating frequency exceed 5.22 GHz the dominating mode is a slow wave.

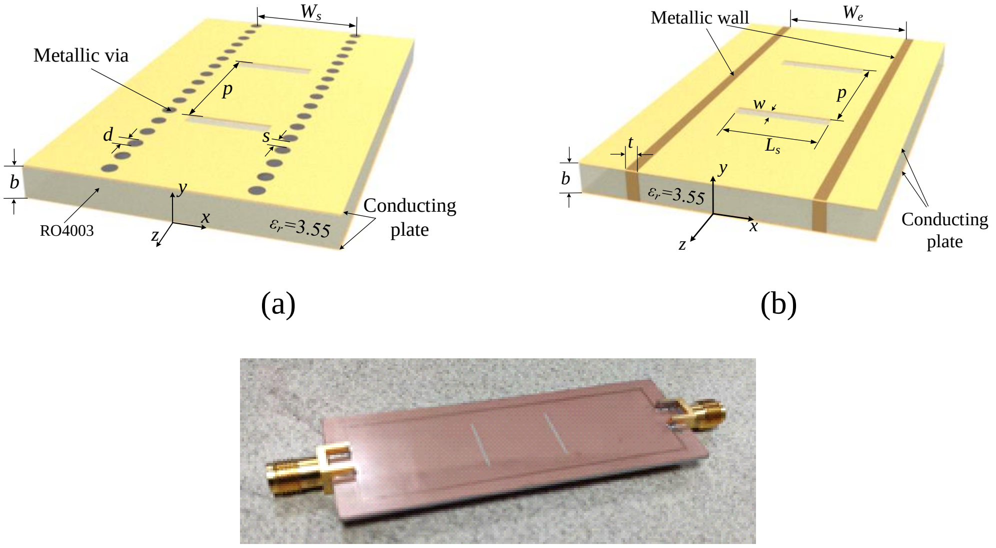

(a) (b)

(c)

Figure 5.1: Two-slot SIW

(a) width-uniform SIW, (b) its equivalent width-uniform DFW and (c) the prototype of the two-slot SIW. (*W*s=18 mm, *s*=0.3 mm, *d*=0.6 mm, *W*e=17.9 mm, *b*=0.813 mm, *w*=0.4 mm, *L*s=12 mm, *p*=15 mm. and *t*=0.6 mm)

The radiation patterns of the two-slot DFW/SIW are related to the feeding phase delay between the two slots. The directions of the main lobe and null radiation in the pattern could be explanted based on the phase delay. The radiation pattern of the two-slot array can be written as

$$F_\theta = F_0(\theta)e^{-j(kr+0.5\beta p)}\cos[0.5p(k_0\cos\theta-\beta)] \tag{5.2}$$

where θ is the elevation angle from z coordinate axis, and $F_0(\bullet)$ is the radiation pattern of a single slot on DFW/SIW. Because the DFW/SIW has a definite length, the $F_0(\bullet)$ will decrease when θ tends to end-fire or backfire direction

The radiation pattern of a two-slot DFW antenna depends on both the pattern of the two-slot array and the pattern of one individual slot. The pattern of the two-slot array depends on the feeding phase delay of the two slots, so it is possible to determine the feeding phase delay based on the directions of either the main lobe or the null radiation. The main lobe of the two-slot DFW/SIW is very wide, so that it is difficult to accurately determine the main lobe direction. On the other hand, because the radiation strength is more sensitive to space angle near a hollow than a peak value, so it is more accurate to determine the direction of null radiation than a main lobe. When $0.5p(k_0 \cos\theta - \beta) = m\pi \pm \pi/2$, the two-slot array will be a null radiation in the direction θ. If the direction of null radiation is 0.5π which is the broadside direction, the needed phase delay is $\beta p = 2m\pi \mp \pi$.

Once the radiations from the two slots become almost the same, a deep valley in its pattern will appear at broadside. Weak radiation of the two slots is favorable to equal-amplitude feeding and in turn equal-amplitude radiation of the two slots, and thus would benefit for an accurate determination of the direction of null radiation. When the radiation from the slots is large, the two slots would be fed with unequal-amplitudes. It would lead to unequal-amplitude radiations of the two slots, and in turn makes the simulated and measured radiations at null radiation direction to be large.

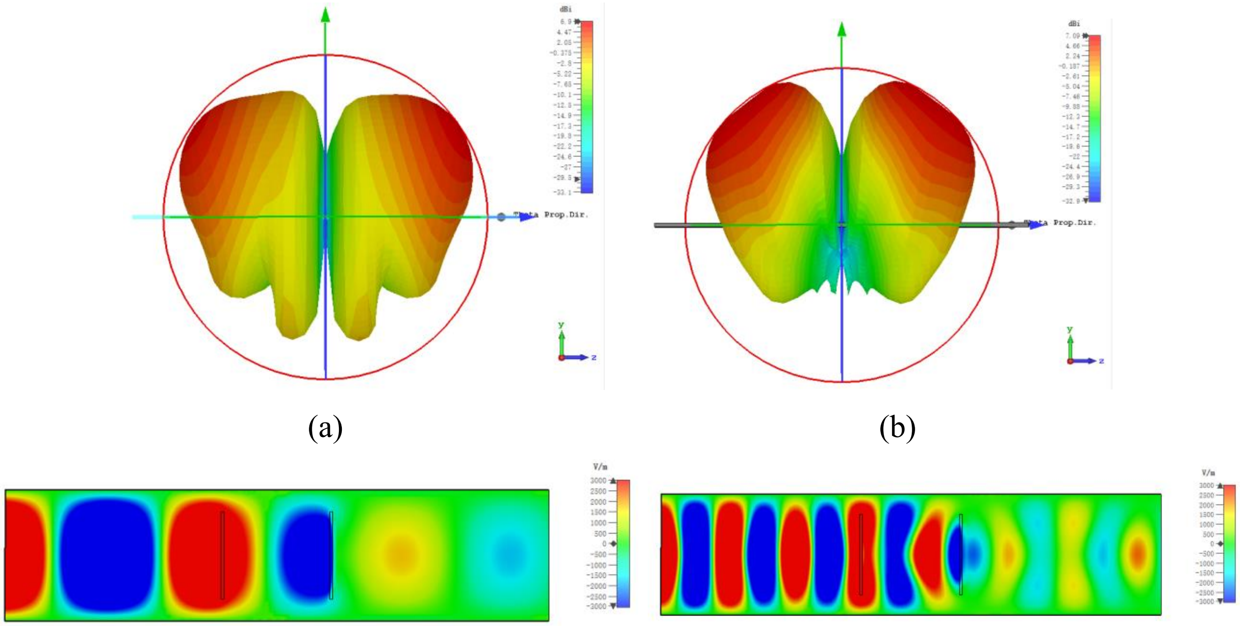

(a) (b)

(c) (d)

Figure 5.2: Simulated radiation patterns and electric fields of the two-slot DFW

(a) pattern at 6.9 GHz, (b) pattern at 16.5 GHz, (c) E-field at 6.9 GHz and (d) E-field at 16.5 GHz

Watching the simulated radiation patterns of the two-slot DFW, one can find that the first two frequencies with the null radiation at broadside are 6.9 GHz and 16.5 GHz respectively. Figure 5.2 (a) and (b) shows the simulated 3-D radiation patterns at 6.9 GHz and 16.5 GHz respectively, and all the two patterns have a hollow at broadside. Figure 5.2 (c) and (d) are E-field distribution on a broad wall inside the two-slot DFW at 6.9 GHz and 16.5 GHz respectively. Based on the E-field distribution, one can know the modes inside the two-slot DFW are slow waves at 6.9 GHz and 16.5 GHz.

A deep hollow in a simulated E-plane pattern is actually null radiation in theory, and so that the feeding phase delays between the two slots at 6.9 GHz and 16.5 GHz should be π and 3π respectively. When p=15 mm, the phase delays of π and 3π determine the two phase constants of $66.7\pi m^{-1}$ and $200.0\pi m^{-1}$ respectively. On the other hand, using the formula (5.1), one is also able to calculate the phase constants of the dominating mode at the two frequencies of 6.9 GHz and 16.5 GHz, and the two phase constants are $66.5\pi m^{-1}$ and $199.7\pi m^{-1}$ respectively, which agree well with the results from the simulated radiation patterns. The consistency indicates that it is the slow wave in the two-slot DFW that produces radiation.

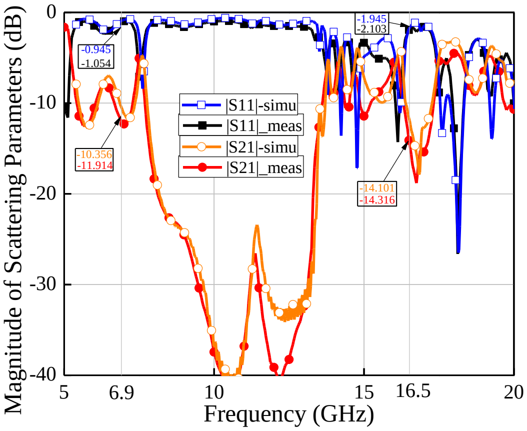

Figure 5.3: Simulated and measured S-parameter of two-slot SIW

To verify the radiation explanation based on a slow wave concept experimentally, a prototype of associated two-slot SIW, as shown in Figure 5.1 (c), is fabricated and measured. The two-slot SIW has a 17.9 mm equivalent width. Figure 5.3 exhibits the comparison between the simulated and measured S-parameters, it shows a good agreement between them. The S-parameters show that the slow waves in the two-slot SIW can produce radiations. Figure 5.4 (a) and (b) plot the simulated and measured radiation patterns on E-plane of the two-slot SIW at 6.9 GHz and 16.5 GHz respectively, all the two patterns have a hollow at broadside. The phase constants based on formula (5.1) at the two frequencies are 66.3πm^{-1} and 199.5πm^{-1} respectively, which agree well with the results from simulated radiation patterns.

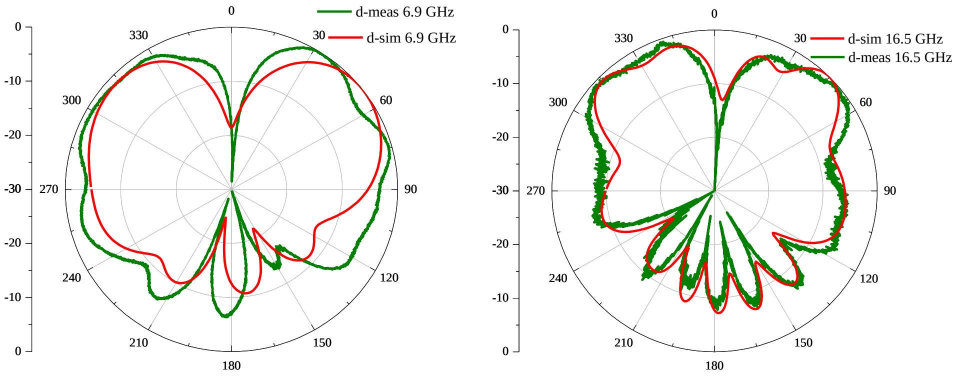

(a) (b)

Figure 5.4: E-plane radiation patterns of two-slot SIW at (a) 6.9 GHz and (b) 16.5 GHz

To further check whether the modes at 6.9 GHz and 16.5 GHz are slow waves, the E-fields on plane y=0.5b of the two-slot SIW at the two frequencies have been simulated and are shown in Figure 5.5. Figure 5.5 shows that the wavelength of the guided wave at 6.9 GHz and 16.5 GHz are roughly 30 mm and 10 mm respectively, which is also in accordance with the results based on the simulated and measured radiation patterns.

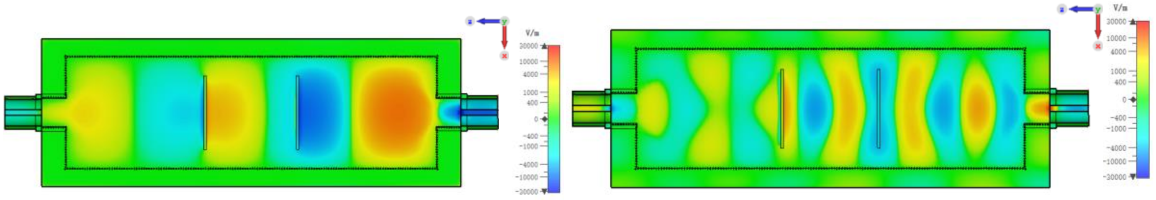

(a) (b)

Figure 5.5: Simulated electric fields inside the two-slot SIW at (a) 6.9 GHz and (b) 16.5 GHz

5.1.2 Radiation from a Slow Wave in a Two-slot Width-tapered DFW

To investigate the radiation produced by slow waves in more complex cases, a two-slot width-tapered DFW, as shown in Figure 5.6, is investigated with simulation. The width-tapered DFW has a width of a linear profile, and the substrate is the same as two-slot width-uniform DFW in Section 5.1.1. The two-slot width-tapered DFW here is still a non-uniform and non-periodic structure, and there is no any space harmonic. During simulations, the two-slot width-tapered DFW is treated as a lossless structure.

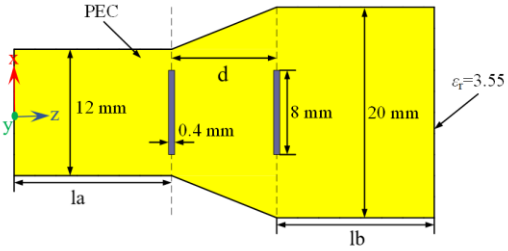

Figure 5.6: Two-slot width-tapered DFW (*l*a=15 mm, *l*b=15 mm, *d*=10 mm)

The phase delay between the two slots can be calculated as follow

$$\varphi=\int_{la}^{la+d}[\frac{2\pi}{\lambda_0}\sqrt{\varepsilon_r-\left(\frac{\lambda_0}{2W(z)}\right)^2}]dz \tag{5.3}$$

where $W(z)$ is the profile of the width of the two-slot width-tapered DFW.

Figure 5.7 shows the simulated 3-D radiation patterns of the two-slot width-tapered DFW at 9.89 GHz and 24.9 GHz. All the patterns have a hollow at broadside, which means the phase delays between the two slots must be π and 3π respectively. On the other hand, using the formula (5.3), one can calculate the phase delays of the two slots at 9.89 GHz and 24.9 GHz are 1.06π and 3.06π respectively, which agree well with the results from simulated radiation patterns.

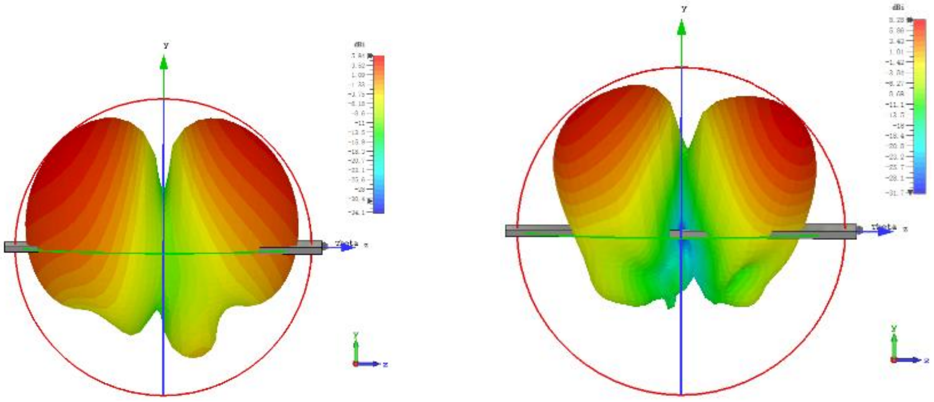

(a) (b)

Figure 5.7: Radiation patterns of two-slot width-tapered DFW at (a) 9.89 GHz and (b) 24.9 GHz

To further ensure that the modes inside the width-tapered DFW at 9.89 GHz and 24.9 GHz are slow waves, the electric fields on plane *y*=0.5*b* have been simulated and are shown in Figure 5.8. Figure 5.8 shows that the phase delays between the two slots at 9.89 GHz and 24.9 GHz are roughly π and π respectively, which is also in accordance with the results based on the simulated radiation patterns and formula (5.3).

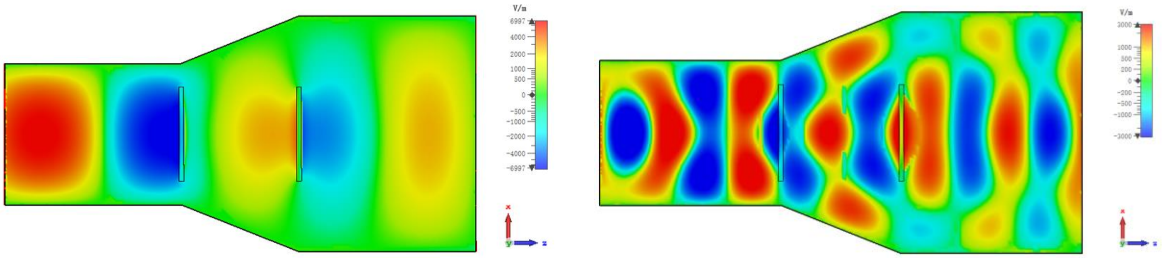

(a) (b)

Figure 5.8: Simulated electric field at (a) 9.89 GHz and (b) 24.9 GHz

All the above results show that the radiation patterns of the structures without space harmonics can be fully interpreted with the concept of slow wave radiation.

5.2 Radiation Produced by Slow Wave in a Periodic Leakage Wave Antenna

Although the two-slot array in Section 5.1 has not any space harmonics, it has been verified that the radiation patterns of the two-slot array can be fully interpreted based on a concept of slow wave. Consequently, it is a reasonable inference that a slow wave in a periodic leaky-wave antenna (PLWA) could also produce a leaky wave radiation. In a PLWA there is a fundamental mode and many space harmonics (Floquet modes). It has always been thought of the fact that only fast waves in a PLWA do produce leaky wave radiation. When the fundamental mode is a slow wave, the radiation pattern of a PLWA is usually interpreted with its space harmonics rather than its fundamental mode [37], [94]-[95], [148]-[153]. In fact, it is possible and reasonable to interpret the radiation pattern of a PLWA with its fundamental mode even if the fundamental mode is a slow wave.

For a PLWA both the fundamental mode and the space harmonics have the feeding phases delays between any two adjacent radiating elements, and there are relations among these phase delays, namely [38]

$$\beta_n p = \beta_0 p + 2n\pi \tag{5.4}$$

where β_0 is the phase constant of the fundamental mode, β_n is the phase constant of the nth space harmonic, and *p* is the periodicity of the PLWA. For an antenna array with *N* elements, the array pattern is as follow

$$F(u) = \left| \frac{\sin(0.5Nu)}{\sin(0.5u)} \right| \tag{5.5}$$

$$u = k_0 p \cos\theta - \beta p \tag{5.6}$$

where u is the total phase difference of two radiating fields from adjacent two element antennas, and F(u) is a periodic function with a periodicity of 2π.

The phase difference based on space harmonics is as follow

$$u_n = k_0 p \cos\theta - \beta_n p \tag{5.7}$$

Due to (5.4), one has

$$u_n = k_0 p \cos\theta - \beta_0 p - 2n\pi \tag{5.8}$$

Therefore, we have

$$u_n = u_0 - 2n\pi \tag{5.9}$$

where u_0 is the phase difference based on the fundamental mode. Based on the periodic characteristic of F(u), one has

$$F(u_n) = F(u_0) \tag{5.10}$$

Therefore, the phase difference of $2n\pi$ among each two adjacent elements does not product any difference in the pattern of the array [37]. Therefore, if one can interpret an array patterns well with a space harmonic, one can also interpret the array patterns well with the fundamental mode, even if the fundamental mode is a slow wave.

For an eigenmode in a uniform structure, for instance, a uniform LWA, there is an eigen equation as follow

$$k_z^2 = k_0^2 - k_x^2 - k_y^2 \tag{5.11}$$

where k_z is the propagation constant of the eigenmode, and k_x and k_y are its transverse wavenumbers. When the eigenmode is a slow-wave, namely $k_z > k_0$, $k_x^2+k_y^2$ must be negative. Therefore, the slow-wave cannot produce radiation. As a result, one can identify whether an eigenmode produces radiation or not based on its propagation constant. However, it would be not true for the fundamental mode and space harmonics in a periodic structure since there are not equations like (5.11). Therefore, whether a periodic structure produces a radiation or not, it can not be identified based on the propagation constant of its fundamental mode.

One can write the field in a periodic structure as follows [38]

$$\mathbf{E}(x,y,z) = \mathbf{E}_0(x,y,z)e^{-j\beta_0 z} \tag{5.12}$$

$$\mathbf{E}_0(x,y,z+p) = \mathbf{E}_0(x,y,z) \tag{5.13}$$

where $\mathbf{E}_0(x,y,z)$, the function of fundamental mode, is a periodic function. The fundamental mode satisfies a three-dimensional partial differential equation as follow

$$\nabla_T^2\mathbf{E}_0(x,y,z) + (k^2-\beta_0^2)\mathbf{E}_0(x,y,z) + \frac{\partial^2\mathbf{E}_0(x,y,z)}{\partial z^2} - 2j\beta_0\frac{\partial\mathbf{E}_0(x,y,z)}{\partial z} = 0 \tag{5.14}$$

The wavenumber β_0 depends on the boundary condition on the whole boundary of a unit cell rather than the boundary condition only on its cross section. Due to generally

$$(\frac{\partial^2}{\partial z^2} - 2j\beta_0\frac{\partial}{\partial z})\mathbf{E}_0(x,y,z) \neq 0 \qquad (5.15),$$

the three-dimensional partial differential equation cannot be reduced into a two-dimensional partial equation as follow.

$$(\nabla_T^2 - \beta_0^2 + k_0^2)\mathbf{E}_0(x,y,z) = 0 \tag{5.16}$$

Consequently, the $\mathbf{E}_0(x,y,z)$ cannot be characterized with only a pair of transverse eigen parameters of k_x and k_y, which are determined only by the transverse boundary condition. Therefore, there is an inequation as follow

$$\beta_0^2 \neq k_0^2 - k_x^2 - k_y^2 \tag{5.17}$$

As a result, in a periodic structure the β_0 associated with a fundamental mode has not a meaning like that associated with an eigenmode in a uniform transmission line. If the fundamental mode is a slow wave, namely $\beta_0 > k_0$, based on formula (5.17), the value of $k_x^2+k_y^2$ cannot be determined to be negative, and the value of $k_x^2+k_y^2$ could be positive. Consequently, when the fundamental mode propagates in a periodic structure, whether the fundamental mode radiates or not, it cannot be identified only based on the longitudinal wavenumber of the fundamental mode.

Although β_0 is also associated with the fundamental space harmonic $\mathbf{E}_{00}(x,y)$, the inequation (5.17) still holds. $\mathbf{E}_0(x,y,z)$ can be expand to space harmonics, and the field in the periodic structure can be expressed as follows

$$\mathbf{E}(x,y,z)=\sum_n \mathbf{E}_{n0}(x,y)e^{-j\beta_n z} \tag{5.18}$$

$$\beta_n=\beta_0+\frac{2n\pi}{p}, \quad (n=0,\pm1,\pm2,\cdots) \tag{5.19}$$

where $\mathbf{E}_{n0}(x,y)$ are space harmonics. It should be noticed that any space harmonics $\mathbf{E}_{n0}(x,y)$, even the fundamental space harmonic $\mathbf{E}_{00}(x,y)$, does not satisfy the boundary conditions on any cross sections of a periodic structure individually, so that any a single space harmonic does not exist alone in a periodic structure [95]. Therefore, the space harmonics have not physical significance.

On the other hand, a field distribution or a mode could be expand with eigenmodes, only if the field distribution or the mode also satisfies the same boundary condition as the eigenmodes. Therefore, any space harmonics $\mathbf{E}_{n0}(x,y)$, including the fundamental space harmonic $\mathbf{E}_{00}(x,y)$, can not be expand with eigenmodes. Consequently, for the fundamental mode and any Floquet modes, there are inequations as follows

$$k^2-\beta_n^2 \neq k_x^2+k_y^2 \quad (n=0,\pm1,\pm2,\cdots) \tag{5.20}$$

As for a PLWA, a slow wave condition, $\beta_0 > k_0$, does not mean that the fundamental mode must decay exponentially in transverse dimensions and cannot produce leaky wave radiations. Therefore, it is reasonable to interpret the radiation in a PLWA with its fundamental mode, even if the fundamental mode is a slow wave.

CHAPTER 6 CONCLUSION AND FUTURE WORK

6.1 Conclusions

The scope of this Ph.D. thesis focuses on diverse fully planar SIW-based end-fire CP composite antennas, and the characteristics and research method of periodic structures. The major contribution from this work can be concluded as the followings:

- To devise and demonstrate three kinds of fully planar high gain SIW-based end-fire CP composite antenna: horn-ALTSA, slot-ALTSA, and UDR-ALTSA. The three composite antennas are actually three kinds of two-element heterogeneous linear arrays, stretching in the three orthogonal space dimensions respectively. The horn-ALTSA also includes a compact planar feeding network with flexible configurations of phase and magnitude, and it could be also used to form a big array with slot-ALTSA, UDR-ALTSA or other end-fire CP antennas. The slot-ALTSA is also a heterogeneous array of a frequency-scanning beam and an end-fire fixed beam, and it supposed to be difficult to design. Besides, the slot-ALTSA also demonstrates an application of slow wave radiation in a slotted SIW, and it would open a way to novel applications associated with slow wave radiation in diverse leaky wave antennas. The UDR-ALTSA has wide impedance and AR bandwidths, and a very small size with a very thin feeding substrate whose thickness is less than $0.05\lambda_0$, and these features make the antenna a good candidate for the element antenna of a big array. Moreover, the UDR-ALTSA includes a smart UDR, fed by a novel feeding structure, to enhance only VP rather than HP radiation of ALTSA. The novel polarization-selective enhancement could be applied to other CP antennas.
- To explore two fully planar VP composite antennas: a UDR-SIW fed by an SIW and an SIW-based slot-horn. The UDR-SIW can be fabricated with a mingled multilayer PCB technology, is fed with an SIW on a very thin substrate of $0.05\lambda_0$. It applies a generalized Fabry-perot principal to achieve a unidirectional radiation, has a compact size, a high gain, a large FTBR and a symmetric pattern, and could be a competitive replacement for an SIW H-plane horn. The slot-horn could have an E-plane omnidirectional pattern and a frequency response of gain similar to a high-selectivity filter, and could be also used to improve the radiation performance of a thin SIW H-plane horn.

- Comprehensive closed-form formulas of characteristic parameters in a periodic structure (FPPS) are proposed. The FPPS can be used to separate the forward waves and backward waves from the total wave at any point inside a practical structure, and calculate reflection coefficients, wave impedances, phase constants, attenuation constants, and the number and amplitudes of the Bloch/Floquet modes. The FPPS can be applied to 1-D and multi-dimensional structures, and not only to electromagnetics but also to acoustics and solid physics.
- To explore the reflection and wave impedance in a periodic structure with the FPPS and/or theory analysis respectively. The reflection inside a periodic structure is inhomogeneous, polarization-dependant, and different from the conventional port reflection coefficient, and should be characterized with a tensor reflection coefficient. The wave impedance of a mode in a periodic transmission line is complex and inhomogeneous, so that there is stored energy and reflected waves inside an unit cell of the periodic transmission line, which are all different from a uniform transmission line.
- To demonstrate radiation produced by slow waves in non-periodic antennas with simulations and experiments, interpret the radiation pattern of a PLWA with its fundamental mode even if the fundamental mode is a slow wave, and to clarify that whether a mode propagating in a periodic structure produces radiation or not, it cannot be identified based on only the longitudinal wavenumber of the mode. The work will also help to understand the radiation phenomena in a periodic transmission line such as SIW, CRLH and SSPP.

The work of the thesis expands SIW-based antennas to various composite antennas of multi-type radiators, and would provide a conceptual foundation and a comprehensive method for the researches and applications relative to periodic structures.

6.2 Future Works

Subsequent to studies described in this doctoral dissertation, a number of technical issues should be addressed in future investigations:

- The applications and performances of the FPPS in 2-D periodic structures should be explored and examined with simulations and experiments.

- An experiment should be designed to show wave that slow waves in periodic structures can produce leaky wave radiations.
- The performances, especially FTBR, bandwidth and beamwidth of AR, of the slot-ALTSA antenna should be improved.
- The performances of slotted width-tapered slot-horn antennas should be improved.

REFERENCES

[1] D. Deslandes and K. Wu, "Integrated microstrip and rectangular waveguide in planar form," IEEE Microwave and Wireless Components Letters, vol. 11, no. 2, pp. 68-70, Feb. 2001.

[2] Y. Cassivi, L. Perregrini, P. Arcioni, M. Bressan, K. Wu, and G. Conciauro,“Dispersion characteristics of substrate integrated rectangular waveguide,” in IEEE Microwave Wireless Compon. Lett., vol. 12, Sep. 2002, pp. 333–335.

[3] Deslandes D, Wu K. Single-substrate integration technique of planar circuits and waveguide filters[J]. IEEE Transactions on Microwave Theory and Techniques, 2003, 51(2): 593-596

[4] Xu, F., Wu, K. Guided-wave and leakage characteristics of substrate integrated waveguide, IEEE Trans. Microw. Theory Tech., 2005, 53, (1), pp. 66–73

[5] Deslandes, D., Wu, K. Accurate modeling, wave mechanisms, and design considerations of a substrate integrated waveguide, IEEE Trans. Microw. Theory Tech., 2006, 54, (6), pp. 2516–2526

[6] Deslandes D, Wu K. Millimeter-Wave Substrate Integrated Waveguide Filters[C]. Canadian Conference on Electrical and Computer Engineering, 2003. 1917-1920

[7] Germain S, Deslandes D, Wu K. Development of Substrate Integrated Waveguide Power Dividers[C]. Canadian Conference on Electrical and Computer Engineering, 2003. 1921-1924

[8] Che W Q, Yung E K, Wu K. Millimeter-wave ferrite phase shifter in substrate integrated waveguide (SIW)[C]. IEEE AP-S International Symposium, 2003. 887-890

[9] D. Stephens, P. R. Young and I. D. Robertson, "W-band substrate integrated waveguide slot antenna," Electronics Letters, vol. 41, no. 4, pp. 165-167, 17 Feb. 2005.

[10] Hao Z C, Hong W, Chen J X, et al. Compact super-wide bandpass substrate integrated waveguide (SIW) filters[J]. IEEE Transactions on Microwave Theory and Techniques, 2005, 53(9): 2968-2977

[11] Hao Z C, Hong W, Chen X P, et al. Multilayered substrate integrated waveguide (MSIW) elliptic filter[J]. IEEE Microwave and Wireless Components Letters, 2005, 15(2): 95-97

[12] Mojica J F, Cassivi Y, Wu K. Low-cost RF and microwave source design using substrate integrated waveguide technique[C]. IEEE Radio and Wireless Conference, RAWCON, 2004. 447-450

[13] Luo G Q, Hong W, Hao Z C, et al. Theory and experiment of novel frequency selective surface based on substrate integrated waveguide technology[J]. IEEE Transactions on Antennas and Propagation, 2005, 53(12): 4035-4043

[14] Xu X Y, Bosisio R G, Wu K. A new six-port junction based on substrate integrated waveguide technology[J]. IEEE Transactions on Microwave Theory and Techniques, 2005, 53(7): 2267-2273

[15] Chen J X, Hong W, Hao Z C, et al. High isolation sub-harmonic up-converter using substrate integrated waveguide[J]. Electronics Letters, 2005, 41(22): 1225-1226

[16] Abdolhamidi, M., Shahabadi, M.: ‘X-band substrate integrated waveguide amplifier’, IEEE Microw. Wirel. Compon. Lett., 2008, 18, (12), pp. 815–817

[17] Chen, J.-X., Hong,W., Hao, Z.-C., Li, H., Wu, K.: ‘Development of a low cost microwave mixer using a broad-band substrate integrated waveguide (SIW) coupler’, IEEE Microw.Wirel.Compon. Lett., 2006, 16, (2), pp. 84–86

[18] Hao Z C, Hong W, Chen J X, et al. Planar diplexer for microwave integrated circuits[C]. IEE Proceedings on Microwaves, Antennas and Propagation, 2005. 455-459

[19] Deslandes, D., Wu, K.: ‘Substrate integrated waveguide leaky-wave antenna: concept and design considerations’. Proc. Asia-Pacific Microwave Conf. (APMC’05), Suzhou, China, 2005

[20] Samanta, K.K., Stephens, D., Robertson, I.D.: ‘Design and performance of a 60-GHz multi-chip module receiver employing substrate integrated waveguides’, IET Microw., Antennas Propag., 2007, 1, (5), pp. 961–967

[21] Vincenti Gatti, R., Marcaccioli, L., Sbarra, E., Sorrentino, R.: ‘Flat array antennas for Ku-band mobile satellite terminals’, Hindawi Int. J. Antennas Propag., 2009, pp. 1–5.

[22] Yan L, Hong W, Hua G, et al. Simulation and experiment on SIW slot array antennas. IEEE Microwave and Wireless Components Letters, 2004, 14(9): 446-448.

[23] A. R. Mallahzadeh and S. Esfandiarpour, “Wideband H-plane horn antenna based on ridge substrate integrated waveguide (RSIW),” IEEE Antennas and Wireless Propagation Letter, vol. 11, pp. 85-88, 2012.

[24] Hao Wang, D. G. Fang, B. Zhang and W. Q. Che, “Dielectric loaded substrate integrated waveguide (SIW) H-plane horn antennas,” IEEE Trans. Antennas and Propagation, vol. 58, no. 3, pp. 640-947, 2010.

[25] M. Esquius-Morote, B. Fuchs, J. F. Zürcher and J. R. Mosig, "Novel thin and compact H-plane SIW horn antenna," IEEE Trans. Antennas Propagat., vol. 61, no. 6, pp. 2911-2920, Jun. 2013.

[26] M. Esquius-Morote, B. Fuchs, J. F. Zürcher and J. R. Mosig, "A printed transition for matching improvement of SIW horn antennas," IEEE Trans. Antennas Propagat., vol. 61, no. 4, pp. 1923-1930, Apr. 2013.

[27] Y. Cai, Z. Qian, Y. Zhang and W. Cao, "A compact wideband SIW-fed dielectric antenna with end-fire radiation pattern," IEEE Trans. Antennas Propagat., vol. 64, no. 4, pp. 1502-1507, Apr. 2016.

[28] L. Wang, X. Yin, S. Li, H. Zhao, L. Liu and M. Zhang, "Phase corrected substrate integrated waveguide H-plane horn antenna with embedded metal-via arrays," IEEE Trans. Antennas Propagat., vol. 62, no. 4, pp. 1854-1861, Apr. 2014.

[29] Y. Zhao, Z. Shen and W. Wu, "Wideband and low-profile h-plane ridged SIW horn antenna mounted on a large conducting plane," IEEE Trans. Antennas Propagat., vol. 62, no. 11, pp. 5895-5900, Nov. 2014.

[30] W. J. Lu, J. W. Shi, K. F. Tong and H. B. Zhu, "Planar end-fire circularly polarized antenna using combined magnetic dipoles," IEEE Antennas and Wireless Propagation Letters, vol. 14, pp. 1263-1266, 2015.

[31] Z. Y. Zhang and K. Wu, " A Broadband Substrate Integrated Waveguide (SIW) Planar Balun," IEEE Microwave and Wireless Components Letters., vol. 17, no. 12, pp. 843-845, Dec. 2007.

[32] Y. LUO AND J. BORNEMANN, "SUBSTRATE INTEGRATED WAVEGUIDE CIRCULARLY POLARIZED HORN-DIPOLE ANTENNA WITH IMPROVED GAIN," MICROW. AND OPTIC. TECHNOL. LETT., 2016, 58(12): 2973-2977.

[33] J. LIU, D. R. JACKSON, AND Y. LONG, "MODAL ANALYSIS OF DIELECTRIC-FILLED RECTANGULAR WAVEGUIDE WITH TRANSVERSE SLOTS," IEEE TRANS. ANTENNAS PROPAG., VOL. 59, NO. 9, PP. 3194–3203, SEP. 2011.

[34] Y. J. CHENG, W. HONG, K.WU, AND Y. FAN, "MILLIMETER-WAVE SUBSTRATE INTEGRATED WAVEGUIDE LONG SLOT LEAKY-WAVE ANTENNAS AND TWO-DIMENSIONAL MULTIBEAM APPLICATIONS," IEEE TRANS. ANTENNAS PROPAG., VOL. 59, NO. 1, PP. 40–47, JAN. 2011

[35] M. OHIRA, A. MIURA, AND M. UEBA, "60-GHZ WIDEBAND SUBSTRATE-INTEGRATED-WAVEGUIDE SLOT ARRAY USING CLOSELY SPACED ELEMENTS FOR PLANAR MULTISECTOR ANTENNA," IEEE TRANS. ANTENNAS PROPAG., VOL. 58, NO. 3, PP. 993–998, MAR. 2009.

[36] J. LIU, D. R. JACKSON, AND Y. LONG, "SUBSTRATE INTEGRATED WAVEGUIDE (SIW) LEAKY-WAVE ANTENNA WITH TRANSVERSE SLOTS," IEEE TRANS. ANTENNAS PROPAG., VOL. 60, NO. 1, PP. 20–29, JAN. 2012.

[37] A. SUTINJO, M. OKONIEWSKI, AND R. H. JOHNSON, "RADIATION FROM FAST AND SLOW TRAVELING WAVES," IEEE ANTENNAS PROPAG. MAG., VOL. 50, NO. 4, PP. 175–181, AUG. 2008.

[38] R. E. COLLIN, FIELD THEORY OF GUIDED WAVES. NEW YORK, NY, USA:MCGRAW-HILL, 1960.

[39] D. M. POZAR, MICROWAVE ENGINEERING, 4TH ED., NEW YORK: WILEY, 2012.

[40] M. BAGHERIASL, O. QUEVEDO-TERUEL, AND G. VALERIO, "BLOCH ANALYSIS OF ARTIFICIAL LINES AND SURFACES EXHIBITING GLIDE SYMMETRY," IEEE TRANS. MICROW. THEORY TECH., VOL. 67, NO. 7, PP. 2618–2628, JULY 2019.

[41] J. D. KRAUS, "HELICAL BEAM ANTENNAS FOR WIDE-BAND APPLICATIONS," PROC. IRE, VOL. 36, NO. 10, PP. 1236–1242, OCT. 1948.

[42] Z. Z. Chen, and Z. X. Shen, "Planar helical antenna of circular polarization," IEEE TRANSACTIONS ON ANTENNAS AND PROPAGATION, VOL. 63, NO. 10, PP. 4315-4323, OCT. 2015.

[43] S. LIN, A. ELSHERBINI, S. YANG, A. FATHY, A. KAMEL, AND H. ELHENNAWY, ''EXPERIMENTAL DEVELOPMENT OF A CIRCULARLY POLARIZED ANTIPODAL TAPERED SLOT

antenna using SIW feed printed on thick substrate,’’ in Proc. IEEE Antennas Propag. Soc. Int. Symp., pp. 1533-1536, Jun. 2007.

[44] Y. Cai, Y. Zhang, Z. Qian, W. Cao, and S. Shi, ‘‘Compact wideband dual circularly polarized substrate integrated waveguide horn antenna,’’ IEEE Trans. Antennas Propag., vol. 64, no. 7, pp. 3184–3189, Jul. 2016.

[45] Mao Ye, Xin-Rong Li, and Qing-Xin Chu, “Planar End-fire Circularly Polarized Antenna With bidirectional CP radiation of the same sense,” IEEE ANTENNAS AND WIRELESS PROPAGATION LETTERS, VOL. 16, pp621-624, 2017.

[46] Y. Yao, F. Zhang and F. Zhang , “Microstrip fed planar end-fire circularly polarised antenna with enhanced bandwidth , ” ELECTRONICS LETTERS 30th Vol. 53 No. 7 pp. 445–446, Mar. 2017.

[47] S. H. Zainud-Deen, H. A. El-A. Malhat , N. A. A. S. El-Shalaby, and S. M. Gaber, “Circular Polarization Bandwidth Reconfigurable High Gain Planar Plasma Helical Antenna,” IEEE TRANSACTIONS ON PLASMA SCIENCE, VOL. 47, NO. 9, pp. 4274-4280, Sept. 2019.

[48] H. Yagi, ‘‘Beam transmission of ultra short waves,’’ Proc. IRE, vol. 16, no. 6, pp. 715–740, Jun. 1928.

[49] J. Huang and A. C. Densmore, ‘‘Microstrip Yagi array antenna for mobile satellite vehicle application,’’ IEEE Trans. Antennas Propag., vol. 39, no. 7, pp. 1024–1030, Jul. 1991.

[50] J. Huang, ‘‘Planar microstrip Yagi array antenna,’’ in IEEE Antennas Propag. Soc. Int. Symp. Dig., vol. 2, Jun. 1989, pp. 894–897.

[51] A. Wang, L. Yang, Y. Zhang, X. Li, X. Yi, and G. Wei, “A Novel Planar Dual Circularly Polarized End-fire Antenna,” IEEE Access, Vol. 7, pp. 64297-64302, 2019.

[52] X. Lv , W. Cao , Z. Zeng , and S. Shi, “Circularly Polarized Frequency Beam-Scanning Antenna Fed by a Microstrip Spoof SPP Transmission Line,” IEEE ANTENNAS AND WIRELESS PROPAGATION LETTERS, VOL. 17, No. 7, pp. 1329-1333, JULY 2018.

[53] W. H. Zhang, W. J. Lu, and K. W. Tam, “A planar end-fire circularly polarized complementary antenna with beam in parallel with its plane,” IEEE Trans. Antennas Propag., vol. 64, no. 3, pp. 1146-1152, Mar. 2016.

[54] B. Xue, M. You, W. J. Lu, and L. Zhu, “Planar end-fire circularly polarized antenna using concentric annular sector complementary dipoles,” Int. J. RF Microw. Comput.-Aided Eng., vol. 26, no. 9, pp. 829-838, Aug. 2016.

[55] J. Zhang, W. J. Lu, L. Li, L. Zhu, and H. B. Zhu, “Wideband dual-mode planar end-fire antenna with circular polarisation,” Electron. Lett., vol. 52, no. 12, pp. 1000-1001, June 2016.

[56] M. You, W. J. Lu, B. Xue, L. Zhu, and H. B. Zhu, “A novel planar end-fire circularly polarized antenna with wide axial-ratio beamwidth and wide impedance bandwidth,” IEEE Trans. Antennas Propag., vol. 64, no. 10, pp. 4554-4559, Oct. 2016.

[57] H.-Q. Yang, M. You, W.-J. Lu, L. Zhu, and H.-B. Zhu, ‘‘Envisioning an end-fire circularly polarized antenna: Presenting a planar antenna with a wide beamwidth and enhanced front-to-back ratio,’’ IEEE Antennas Propag. Mag., vol. 60, no. 4, pp. 70–79, Aug. 2018.

[58] W. J. Lu, K. Wang, S. S. Gu, L. Zhu, and H. B. Zhu, “Directivity enhancement of planar end-fire circularly polarized antenna using V-shaped 1.5-Wavelength dipoles,” IEEE Antennas Wireless Propag. Lett., vol. 18, no.7, pp. 1420-1423, July 2019.

[59] M. N. Chen, W. J. Lu, L. J. Wang, M. Yang, and L. Zhu, “Design approach to a novel planar bisensing circularly polarized antenna,” IEEE Trans. Antennas Propag., vol. 67, no. 11, pp. 6839-6846, Nov. 2019.

[60] W. H. Zhang, P. Cheong, W. -J. Lu, K. -W. Tam, “Planar end-fire circularly polarized antenna for low profile handheld RFID reader,” IEEE J. Radio Freq. Identification, vol. 2, no. 1, pp. 15-22, Mar. 2018.

[61] W. L. Zhou, J. H. Liu, and Y. L. Long, “A broadband and high-gain planar complementary Yagi array antenna with circular polarization,” IEEE Trans. Antennas Propag., vol. 65, no. 3, pp. 1446-1451, Mar. 2017.

[62] M. Li et al., “A low-profile wideband CP end-fire magnetoelectric antenna using dual-mode resonances,” IEEE Trans. Antennas Propag., vol. 67, no. 7, pp. 4445-4452, July 2019.

[63] H.-Q. Yang, M. You, W.-J. Lu, and Y. Cheng, “Conceptual design of a dual-band circularly polarized antenna,” in Proc. IEEE Int. Conf. Ubiquitous Wireless Broadband (ICUWB), Nanjing, China, Oct. 2016, pp. 1–3.

[64] W. Fan, K. M. Luk, “A Compact and Reconfigurable Circularly Polarized Complementary Antenna,” IEEE Antennas Wireless Propag. Lett., vol. 16, pp. 1188-1191, 2017.

[65] M. Ye, X. R. Li, and Q. X. Chu, “Planar Circularly Polarized End-fire Antenna Based on Superposition of Complementary Dipoles,” 2016 IEEE International Symposium on Antennas and Propagation (APSURSI), Fajardo, Puerto Rico, 26 June-1 July 2016, DOI: 10.1109/APS.2016.7695963.

[66] M. Ye, X. R. Li, and Q. X. Chu, “Planar End-fire Circularly Polarized Antenna With unidirectional pattern,” 2017 IEEE International Symposium on Antennas and Propagation & USNC/URSI National Radio Science Meeting, San Diego, CA, USA, 9-14 July 2017, DOI: 10.1109/APUSNCURSINRSM.2017.8073199.

[67] L. Wang and Y. C. Jiao, “Planar Reconfigurable Circularly Polarized Complementary Antenna for End-fire Radiation,” 2019 International Symposium on Antennas and Propagation (ISAP), Xi'an, China, China, 27-30 Oct. 2019.

[68] S. S. Gu, and W. J. Lu, “Preliminary Design of Helix-Loaded, High Gain Planar End-fire Circularly Polarized Antenna,” 2019 International Symposium on Antennas and Propagation (ISAP)， Xian， 27-30 Oct. 2019

[69] J. Liu, Y. Li, Z. Liang, and Y. Long, “A Planar Quasi-Magnetic–Electric Circularly Polarized Antenna,” IEEE TRANSACTIONS ON ANTENNAS AND PROPAGATION, VOL. 64, NO. 6, pp. 2108-2114, JUNE 2016.

[70] M. Ye, X. R. Li, and Q. X. Chu, “Single-Layer Circularly Polarized Antenna With Fan-Beam End-fire Radiation,” IEEE ANTENNAS AND WIRELESS PROPAGATION LETTERS, VOL. 16, pp. 20-23, 2017.

[71] Y. Gao, Z. Xue, W. Li and W. Ren, “Wide-beam Planar End-fire Circularly Polarized antenna based SIW,” 2019 International Conference on Microwave and Millimeter Wave Technology (ICMMT), Guangzhou, China, China, 19-22 May 2019, DOI: 10.1109/ICMMT45702.2019.8992474.

[72] R. M. Cox and W. E. Rupp, "Circularly polarized phased array antenna element," IEEE Trans. Antennas Propag., vol. 18, no. 6, pp. 804-807, Nov. 1970.

[73] A. Dupressoir, F. Salvat, “Circularly polarized electromagnetic radiators,” US4502053, 1985.

[74] Y. Cheng, and Y. Dong, “A Directive Circularly Polarized Planar Yagi Array Antenna,” IEEE International Symposium on Antennas and Propagation and USNC-URSI Radio Science Meeting, Atlanta, GA, USA, 7-12 July, 2019, DOI:10.1109/APUSNCURSINRSM.2019.8888768.

[75] K. Lertsakwimarn, and T. Fukusako, “A Circularly Polarized Bi-directional Surface Wave Antenna with Low-profile,” 2017 International Symposium on Antennas and Propagation (ISAP). Phuket, Thailand, 30 Oct.-2 Nov. 2017.

[76] X. Cheng, Y. Yao, J. Yu, and X. Chen, ‘‘Circularly polarized substrate integrated waveguide tapered slot antenna for millimeter-wave applications,’’ IEEE Antennas Wireless Propag. Lett., vol. 16, pp. 2358–2361, 2017.

[77] J. Wang , Y. Li, L. Ge, J. Wang, M. Chen, Z. Zhang , and Z. Li, “Millimeter-Wave Wideband Circularly Polarized Planar Complementary Source Antenna With End-fire Radiation,” IEEE TRANSACTIONS ON ANTENNAS AND PROPAGATION, Vol. 66, No. 7, pp. 3317-3326, JULY 2018.

[78] Q. Wu , J. Hirokawa, J. Yin, C. Yu, H. Wang , and W. Hong, “Millimeter-Wave Multibeam End-fire Dual-Circularly Polarized Antenna Array for 5G Wireless Applications,” IEEE TRANSACTIONS ON ANTENNAS AND PROPAGATION, vol. 66, no. 9, pp. 4930-4935, Sept. 2018.

[79] S. S. Hesari and J. Bornemann, ‘‘Wideband circularly polarized substrate integrated waveguide end-fire antenna system with high gain,’’ IEEE Antennas Wireless Propag. Lett., vol. 16, pp. 2262–2265, 2017.

[80] F. Y. Xia, Y. J. Cheng, Y. F. Wu, and Y. Fan, “V-Band Wideband Circularly Polarized Endfire Multibeam Antenna With Wide Beam Coverage,” IEEE Antennas Wireless Propag. Lett., vol. 18, no. 8, pp. 1616-1620, Aug. 2019.

[81] X. Ruan and C. H. Chan, “An Endfire Circularly Polarized Complementary Antenna Array for 5G Applications,” IEEE Trans. Antennas Propag., vol. 68, no. 1, pp. 266-274, Jan. 2020.

[82] X. Cheng, Y. Yao, T. Tomura, J. Hirokawa, T. Yu, J. Yu, and X. Chen, "Compact Multi-Beam End-Fire Circularly Polarized Septum Antenna Array for Millimeter-Wave Applications," IEEE Access, no. 6, pp. 62784–62792, 2018.

[83] K. Al-Amoodi, R. Mirzavand, M. M. Honari, J. Melzer, D. G. Elliott, and P. Mousavi, "A Compact Substrate Integrated Waveguide Notched-Septum Polarizer for 5G Mobile Devices," IEEE Antennas Wireless Propag. Lett., vol. 19, no. 12, pp. 2517-2521, Dec. 2020.

[84] K. Al-Amoodi, M. M. Honari, R. Mirzavand, J. Melzer, D. G. Elliott, and P. Mousavi, "Circularly-polarised end-fire antenna and arrays for 5G millimetre-wave beam-steering systems," IET. Microw., Antennas Propag., vol. 14, no. 9, pp. 980–987, Jul. 2020.

[85] L. Brillouin, "Wave Propagation in Periodic Structures, " McGraw-Hill Book Co., Inc., New York, N. Y.; 1946.

[86] G. A. Campbell, "On loaded lines in telephonic transmission, " Phil. Msg., vol. 5, p. 319; 1903.

[87] E. L. Chu and W. W. Hansen, "The theory of disk-loaded waveguides, " J. A$fil. Phys., vol. 18, pp. 996; 1947.

[88] A. W. Lines, G. R. Nicoll, and A. M, Woodward, "Some properties of waveguides with periodic structures, " PYOG. IEE,VOi 97, pt. III, pp. 263-276~ July, 1950.

[89] J. C. Slater, "Microwave Electronics, " D. Van Nostrand Co. Inc.. New York. N. Y.: 1950.

[90] R. E. Vowels, "Matrix methods in the solution of ladder networks, " J. IEE, vol. 95, pp. 40–50; January, 1948.

[91] L. Brillouin,Wave Propagation in Periodic Structures. New York, NY: Dover, 1953.

[92] A.A. Oliner, "The impedance properties of narrow radiating slots in the broad face of rectangular waveguide: Part I – Theory," IRE Trans. Antennas Propag., vol. 5, 1, pp. 4-11, 1957.

[93] T. Tamir and A.A. Oliner, "Guided complex waves: Part 1 – Fields at an interface," Proc. IEE, vol. 110, 2, pp. 310-324, 1963.

[94] A.A. Oliner, "Leakage from higher modes on microstrip line with application to antennas," Radio Sci., vol. 22, 6, pp. 907-912, Nov. 1987.

[95] R. E. Collin and F. J. Zucker, Antenna Theory. New York: McGraw- Hill, 1969.

[96] S. T. Peng, T. Tamir, and T. L. Bertoni, “Theory of periodic dielectric waveguides,” IEEE Trans. Microw. Theory Tech., vol. 23, pp. 123–133, Jan. 1975.

[97] D. Sievenpiper, L. Zhang, R. F. J. Broas, N. G. Alexopolous, and E. Yablonovitch, “High-impedance electromagnetic surfaces with a forbidden frequency band,” IEEE Trans. Microw. Theory Tech., vol. 47, pp. 2059–2074, Nov. 1999.

[98] Hines J N, Rumsey V H, Walter C H, “Traveling-wave slot antenna, Proceedings of the IRE, 1953,41(11):1624-1631

[99] Yunjie Geng and Junhong Wang, “Non-uniform slotted leakage wave antenna array broad-beam radiation based on substrate integrated waveguide ”, 2016 11th International Symposium on Antennas, Propagation and EM Theory (ISAPE) , Guilin, China ,18-21 Oct. 2016, DOI: 10.1109/ISAPE.2016.7833909.

[100] Cheng Jin ; Arokiaswami Alphones, “Leaky-Wave Radiation Behavior From a Double Periodic Composite Right/Left-Handed Substrate Integrated Waveguide”, IEEE Trans. Antennas Propagat., vol. 60, no. 4, pp. 1727–1735, Apr. 2012.

[101] C. A. Balanis, Antenna Theory: Analysis and Design, 2nd ed. New York: Wiley, 1996, pp. 688.

[102] Y. Yin, B. Zarghooni, and K. Wu, “Single-layered circularly polarized substrate-integrated waveguide horn antenna array,” IEEE Trans. Antennas Propag., vol. 65, no. 11, pp. 6161–6166, Nov. 2017.

[103] S. Sugawara, Y. Maita, K. Adachi, K. Mori, and K. Mizuno, “A mm-wave tapered slot antenna with improved radiation pattern,” in IEEE-IMS, Denver, CO, pp. 959–962, 1997.

[104] M. Clenet, J. Litzenberger, D. Lee,S.Thirakoune, G. Morin, and Y. Antar, “Laminated waveguide as radiating element for array applications,” IEEE Trans. Antennas Propag., vol. 54, no. 5, pp. 1481 –1487, May 2006.

[105] Yufan Cao, Yang Cai, Lei Wang, Zuping Qian, Lei Zhu, "A Review of Substrate Integrated Waveguide End-fire Antennas", Access IEEE, vol. 6, pp. 66243-66253, 2018.

[106] B. Pan, Y. Li, G. E. Ponchak, J. Papapolymerou and M. M. Tentzeris, "A 60-GHz CPW-fed high-gain and broadband integrated horn antenna," IEEE Trans. Antennas Propagat., vol. 57, no. 4, pp. 1050-1056, Apr. 2009.

[107] Y. Zhao, Z. Shen and W. Wu, "Conformal SIW H-plane horn antenna on a conducting cylinder," IEEE Antennas and Wireless Propagation Letters, vol. 14, pp. 1271-1274, 2015.

[108] Z. L. Li and K. Wu, “A new approach to integrated horn antenna,” Proc. Int. Symp. on Antenna Technology and Applied Electromagnetics, Jul. 2004, pp. 535–538.

[109] W. Che, B. Fu, P. Yao, and Y. L. Chow, “Substrate integrated waveguide horn antenna with dielectric lens,” Microw. Optic. Technol. Lett., vol. 49, no. 1, pp. 168–170, Jan. 2007.

[110] S. B. Yeap, X. Qing, M. Sun and Z. N. Chen, "140-GHz 2×2 SIW horn array on LTCC," Antennas and Propagation (APCAP), 2012 IEEE Asia-Pacific Conference on, Singapore, 2012, pp. 279-280.

[111] L. Wang, X. Yin and H. Zhao, "A planar feeding technology using phase-and-amplitude-corrected SIW horn and its application," IEEE Antennas and Wireless Propagation Letters, vol. 14, pp. 147-150, 2015.

[112] P. J. Gibson, “The Vivaldi aerial,” in Proc. EuMC, Brighton, U.K., 1979, pp. 101-105.

[113] GAZIT E. Improved design of the Vivaldi antenna [J]. IEE Proceedings: Part H: Microwaves, Antennas & Propagation, 1988, 135(2): 89.

[114] Z. C. Hao, W. Hong, J.X. Chen, X. P. Chen, K. Wu, “A novel feeding technique for antipodal linearly tapered Slot Antenna Array”, in IEEE MTT-S Int. Microwave Symp. Dig. 2005, pp. 1641 – 1643.

[115] S. N. Parasad and S. Mahapatra, “A novel MIC slot-line antenna,” in Proc. EuMC, Brighton, U.K., 1979, pp. 120–124.

[116] H. Nakajima, T. Kosugi, and T. Enoki, “Hyperbolic tangent tapered slot antenna,” Electron. Lett., vol. 46, no. 21, pp. 1422-1424, 2010.

[117] X. Qing, Z. N. Chen, and M. Y. W. Chia, “Dual elliptically tapered antipodal slot antenna loaded by curved terminations for ultrawideband applications,” Radio Science, vol. 41, no. 6, 2006.

[118] K. Ebnabbasi, D. Busuioc, R. Birken, and M. Wang, “Taper design of Vivaldi and co-planar tapered slot antenna (TSA) by Chebyshev transformer,” IEEE Trans. Antennas Propag., vol. 60, no. 5, pp. 2252–2259, May. 2012.

[119] K. S. Yngvesson et al., “End-fire tapered slot antennas on dielectric substrates,” IEEE Trans. Antennas Propag., vol. 33, pp. 1392-1400, 1985.

[120] K. S. Yngvesson, T. L. Korzeniowski, Young-Sik Kim, E. L. Kollberg, and J. F. Johansson, “The tapered slot antenna- A new integrated element for millimetre-wave applications,” IEEE Trans. Microwave Theory Tech, vol. 37, No.2, pp. 365-374, 1989.

[121] Y.-S. Kim, and K. S. Yngvesson, “Characteristics of tapered slot antenna feeds and feed array,” IEEETrans. Microwave Theory Tech., vol. 37, pp. 1559-1564, 1990.

[122] Bee Yen Toh, Robert Cahill, and Vincent F. Fusco "Understanding and measuring circular polarization," IEEE Transactions on Education, vol. 46, no. 3, pp. 313-318, Aug. 2015.

[123] Rengarajan S R. “Compound radiating slots in a broad wall of a rectangular waveguide”, IEEE Trans. Antennas Propag., vol. 37, no. 9, pp. 1116-1123, Sept. 1989.

[124] Josefsson L. “A waveguide transverse slot for array applications”, IEEE Trans. Antennas Propag., vol. 41, no. 7, pp. 845-850, July 1993

[125] Josefsson L. “Analysis of longitudinal slots in rectangular waveguides”, IEEE Trans. Antennas Propag., vol. 35, no. 12, pp. 1351-1357, Dec. 1987.

[126] Rengarajan S R, Steinbeck M., “Longitudinal slots in dielectric filled rectangular waveguides” Antennas and Propagation Society International Symposium (Digest), AP-S, 1991, 2: 1276-1279.

[127] K. M. Luk and K. W. Leung, Dielectric Resonator Antenna. Baldock, U.K.: Research Studies, 2003.

[128] R. K. Mongia and A. Ittipiboon, “Theoretical and experimental investigations on rectangular dielectric resonator antennas,” IEEE Trans. Antennas Propag., vol. 45, no. 9, pp. 1348–1356, Sep. 1997.

[129] M. Ranjbar Nikkhah, J. Rashed-Mohassel, and A. A. Kishk, “Highgain aperture coupled rectangular dielectric resonator antenna array using parasitic elements,” IEEE Trans. Antenna Propag., vol. 61, no. 7, pp. 3905–3908, Jul. 2013.

[130] Wael M. Abdel-Wahab, Dan Busuioc, and Safieddin Safavi-Naeini, “Millimeter-Wave High Radiation Efficiency Planar Waveguide Series-Fed Dielectric Resonator Antenna (DRA) Array: Analysis, Design, and Measurements,” IEEE TRANSACTIONS ON ANTENNAS AND PROPAGATION, VOL. 59, NO. 8, pp. 2834-2843, AUG. 2011

[131] N. Ghassemi and Ke Wu, “Planar Dielectric Rod Antenna for Gigabyte Chip-to-Chip Communication,” IEEE TRANSACTIONS ON ANTENNAS AND PROPAGATION, vol. 60, no. 10, pp. 4924-4928, Oct. 2012.

[132] R. Kazemi, A. E. Fathy, and R. A. Sadeghzadeh, “Dielectric Rod Antenna Array With Substrate Integrated Waveguide Planar Feed Network for Wideband Applications,” IEEE TRANSACTIONS ON ANTENNAS AND PROPAGATION, vol. 60, no. 3, pp. 1312-1319, Mar. 2012.

[133] M. Nasir, Y. Xia, M. Jiang, and Q. Zhu, “A Novel Integrated Yagi–Uda and Dielectric Rod Antenna With Low Sidelobe Level,” IEEE TRANSACTIONS ON ANTENNAS AND PROPAGATION, vol. 67, no. 4, pp. 2751-2756, Apr. 2019.

[134] C. Lugo, R. A. Ramirez, J. Wang, and T. M. Weller, “Multilayer Dielectric End-fire Antenna With Enhanced Gain Denise,” IEEE ANTENNAS AND WIRELESS PROPAGATION LETTERS, vol. 17, no. 12, pp. 2213-2217, Dec. 2018.

[135] Ke Wu, Ji Li, and Renato G. Bosisio, “A Low-Loss Unidirectional Dielectric Radiator (UDR) for Antenna and Space Power Combining Circuits,” IEEE TRANSACTIONS ON MICROWAVE THEORY AND TECHNIQUES. vol. 42. no. 2, pp. 339-341, FEB. 1994.

[136] Hongming An, Ke Wu, and Renato G. Bosisio, “Analytical and Experimental Investigations of Aperture Coupled Unidirectional Dielectric Radiator Arrays (UDRA),” IEEE TRANSACTIONS ON ANTENNAS AND PROPAGATION, vol. 44, no. 9, pp. 1201-1207, SEPT. 1996.

[137] Mekki Belaid, Jean-Jacques Laurin, and Ke Wu, “Integrated Active Antenna Array Using Unidirectional Dielectric Radiators,” IEEE TRANSACTIONS ON MICROWAVE THEORY AND TECHNIQUES, vol. 48, no. 10, pp. 1628-1634, OCT. 2000

[138] Hongming An, Ke Wu, and Renato G. Bosisio, "Radiation Pattern Prediction of the Unidirectional Dielectric Radiator (UDR)," IEEE MICROWAVE AND GUIDED WAVE LETTERS. VOL. 4. NO I I, pp. 367-369, NOV. 1994.

[139] T. Yoneyama and S. Nishida, "Nonradiative dielectric waveguide for millimeter-wave integrated circuits," IEEE Trans. Microw. Theory Tech., vol. 29, pp. 1188–1192, 1981.

[140] Feng Xu, and Ke Wu, "Substrate Integrated Nonradiative Dielectric Waveguide Structures Directly Fabricated on Printed Circuit Boards and Metallized Dielectric Layers," IEEE TRANSACTIONS ON MICROWAVE THEORY AND TECHNIQUES, VOL. 59, NO. 12, pp. 3076-3086, DEC. 2011.

[141] T. Tamir, "Integrated Optics," 2nd ed. Berlin, Heidelberg, New York: Springer-Verlag, 1979.

[142] K. Okamoto, "Fundamentals of Optical Waveguides," New York: Academic Press, 2000.

[143] Igor Syrytsin, Shuai Zhang, and Gert Frø, lund Pedersen, "Circularly Polarized Planar Helix Phased Antenna Array for 5G Mobile Terminals," 2017 International Conference on Electromagnetics in Advanced Applications (ICEAA), Verona, Italy, 11-15 Sept. 2017, DOI: 10.1109/ICEAA.2017.8065458.

[144] R. Garg, I. Bahl, and M. Bozzi, Microstrip Lines and Slotlines, Third ed. : Artech House, 2013.

[145] R. E. Collin, Foundations for Microwave Engineering. NewYork, NY, USA: McGraw-Hill, 1966.

[146] T. Hiraoka, T. Tokumitsu, and M. Aikawa, "Very small wide band MMIC magic T's using microstrip on a thin dielectric film," IEEE Trans. Microw. Theory Tech., vol. 37, no. 10, pp. 1569–1575, 1989.

[147] M. Pasian, M. Bozzi, and L. Perregrini, "A Formula for Radiation Loss in Substrate Integrated Waveguide" IEEE TRANSACTIONS ON MICROWAVE THEORY AND TECHNIQUES, VOL. 62, NO. 10, OCTOBER 2014.

[148] A. A. Oliner and R. C. Johnson, "Leaky-Wave Antennas," in Antenna Engineering Handbook, 3rd ed. New York: McGraw-Hill, 1993, ch. 10.

[149] M. Guglielmi and D. R. Jackson, “Broadside radiation from periodic leaky-wave antennas,” IEEE Trans. Antennas Propag., vol. 41, no. 1, pp. 31–37, Jan. 1993.

[150] S. Majumder and D. R. Jackson, “Radiation characteristics of one-dimensional periodic leaky-wave antennas,” in AP-S Dig., vol. 1, 1997, pp. 452–455.

[151] F. Xu, K. Wu, and X. Zhang, “Periodic leaky-wave antenna for millimeter wave applications based on substrate integrated waveguide,” IEEE Trans. Antennas Propag., vol. 58, no. 2, pp. 340–347, Feb. 2010.

[152] L. Goldstone and A. A. Oliner, “Leaky-wave antennas I: Rectangular waveguides,” IRE Trans. Antennas Propag., vol. 7, no. 4, pp. 307–319, Oct. 1959.

[153] P. Baccarelli, S. Paulotto, D. R. Jackson, and A. A. Oliner, “A New Brillouin Dispersion Diagram for 1-D Periodic Printed Structures,” IEEE Trans. Microw. Theory Tech., vol. 55, no. 7, pp. 1484-1495, July 2007.